Modélisation SPH et validation expérimentale des processus de remplissage et de solidification de la coulée rapide par gravité d'AlSi13

Mohammad Zarbini Seydani

HESAM UNIVERSITÉ

Arts Sciences et Technologies et Métiers

ÉCOLE DOCTORALE SCIENCES DES MÉTIERS DE L'INGÉNIEUR
[Laboratoire de MSMP & LIFSE – Campus de Aix-En-Provence et Paris]

THÈSE

présentée par : **Mohammad ZARBINI SEYDANI**
soutenue le : **03 February 2023**

pour obtenir le grade de : **Docteur d'HESAM Université**
préparée à : **École Nationale Supérieure d'Arts et Métiers**
Spécialité : **Mécanique des matériaux et des fluides**

Smoothed particle hydrodynamics (SPH) modelling and experimental validation of filling and solidification processes of rapid gravity casting of AlSi13

THÈSE dirigée par :

Professeur Mohamed EL MANSORI

et co-encadrée par :

Professeur Sofiane KHELLADI

Docteur Marie BEDEL

Jury

M. Dermot BRABAZON, Professor, School of Mechanical & Manufacturing Engineering, Glasnevin Campus, Dublin City University	Rapporteur
M. Xesús NOGUEIRA, Professor, Campus de Elviña, Universidade da Coruña	Rapporteur
M. Said AHZI, Professor, ICUBE Laboratory-CNRS, University of Strasbourg	Président
Mme. Marie BEDEL, Associate Professor, MSMP-EA7350, Arts et Métiers	Co-encadrante
M. Mohamed EL MANSORI, Professor**,** MSMP EA7350, Arts et Métiers	Directeur
M. Sofiane KHELLADI, Professor**,** LIFSE, Arts et Métiers	Co-encadrant

THÈSE

`Smoothed particle hydrodynamics (SPH) modeling and experimental validation of filling and solidification processes of rapid gravity casting of AlSi13

Acknowledgments

This research was a collaboration between two laboratories of École Nationale Supérieure d'Arts et Métiers (ENSAM) in Paris: MSMP and LIFSE. I would like to acknowledge all the individuals who have accompanied me in recent years during the preparation of my thesis.

First and foremost, I want to give a special thanks to Prof. Mohamed EL MANSORI and Prof. Sofiane KHELLADI for being excellent examples of scientists, engineers, advisors, and supervisors. They have been helpful, considerate, kind, and patient with me, and I am incredibly grateful for the opportunity to work with them. They provided me with guidance throughout my entire research period and for this PhD thesis. My sincere appreciation goes to Dr. Marie BEDEL, who supervised my thesis, for her commitment, support, guidance, and integrity, all of which had a significant impact on the outcome of this work. I would like to express my heartfelt gratitude to the members of my jury for accepting and evaluating my PhD thesis. In addition, I would like to express my special thanks to Dr. Morgan DAL, Dr. Abdelkader KRIMI, and Dr. Mohammad KALTEH for all their help during my academic career. Furthermore, I would like to thank Prof. Abbas TCHARKHTCHI and Dr. Mohammadali SHIRINBAYAN for supporting me during my thesis. I also extend my sincere thanks to all the researchers and PhD students at the MSMP and LIFSE laboratories who assisted me during my thesis. I give the most thanks to my father, sisters, and the memory of my late mother for their support.

I dedicate this thesis to the brave women of my country, Iran.

Women, life, freedom

Résumé

La simulation du processus de coulée en sable par gravité est complexe et implique des phénomènes multi-échelles et multi-physiques. Même si certains logiciels commerciaux sont disponibles, il est difficile de prévoir la dynamique de remplissage lorsqu'elle est couplée au refroidissement, à la solidification et aux défauts causés. En particulier, la prédiction de l'oxydation nécessite de suivre le front de fluide où se forme l'oxydation, donc leur mouvement par la suite dans la masse fondue est complexe avec les méthodes basées sur le maillage. La méthode "smoothed particle hydrodynamics" (SPH) est une approche de simulation lagrangienne qui est particulièrement bien adaptée pour modéliser l'étape de remplissage de la coulée. Le métal est modélisé par des particules en mouvement libre dans l'approche SPH, ce qui permet une prédiction fiable des écoulements fluides incorporant des mouvements complexes de surface libre. Cette thèse a pour objectif de développer l'approche SPH pour examiner les phases de remplissage, de refroidissement et de solidification de la coulée rapide par gravité d'AlSi13. Les résultats numériques SPH du remplissage, du refroidissement et de la solidification sont validés expérimentalement et comparés avec un logiciel commercial (ProCAST).

L'étape initiale pour atteindre l'objectif de cette thèse est le développement du code SPH de coulée en 2D, qui a été développé initialement par le laboratoire LIFSE. Tout d'abord, ce code SPH est développé au cours de cette thèse en 2D pour modéliser les processus de remplissage, de refroidissement et de solidification de la coulée par gravité en sable. Pour analyser le code SPH de la coulée par gravité en 2D pour un système fermé, un cas test expérimental est spécifiquement désigné. Ensuite, le code SPH est amélioré en 3D, et les résultats numériques du remplissage, du

refroidissement et de la solidification sont étudiés dans le cas d'une coulée 3D plus réaliste et comparés à l'expérience. Enfin, le code SPH validé en 2D et 3D fournit la base pour la prédiction future des défauts de coulée tels que l'oxydation.

Abstract

The simulation of gravity sand casting process is complex and involves multiscale and multiphysics phenomena. Even though some commercial software is available, it is difficult to predict the filling dynamic when coupled with cooling, solidification, and the induced defects. In particular, oxidation prediction requires tracking the fluid front where oxidation forms, so their motion afterward in the melt is complex with mesh-based methods. Smoothed particle hydrodynamics (SPH) is a Lagrangian simulation approach that is particularly well adapted to model the filling step of casting. Metal is modeled by free-moving particles of SPH approach, allowing reliable prediction of fluid flow incorporating complex free surface motion. This thesis aims to develop SPH approach to examine the filling, cooling, and solidification phases of rapid gravity casting of AlSi13. SPH numerical results of filling, cooling and solidification are validated experimentally and compared with commercial software (ProCAST).

The initial step in achieving this thesis's goal is developing 2D casting SPH code, which was developed initially by LIFSE laboratory. Firstly, this SPH code is developed during this thesis in 2D to model the filling, cooling, and solidification processes of sand gravity casting. In order to analyze 2D gravity casting SPH code for a closed system, an experimental test case is specifically designed. Secondly, the SPH code is upgraded to 3D, and the numerical results of filling, cooling and solidification are studied in the case of a more realistic 3D casting and compared to experiment. Finally, the upgraded 2D and 3D validated SPH code provides the basis for future prediction of casting defects such as oxidation.

Table of Contents

List of Tables

List of Figures

Chapter 1: State of the art

Contents

Introduction of thesis

Motivation

The foundry process is important for a wide range of scientific and industrial processes. Today, the significant growth in the casting components is linked to the development of automated sand mold printing and casting procedures, as well as digital casting simulation software. Figure (A) represents the several steps of producing components with these tools.

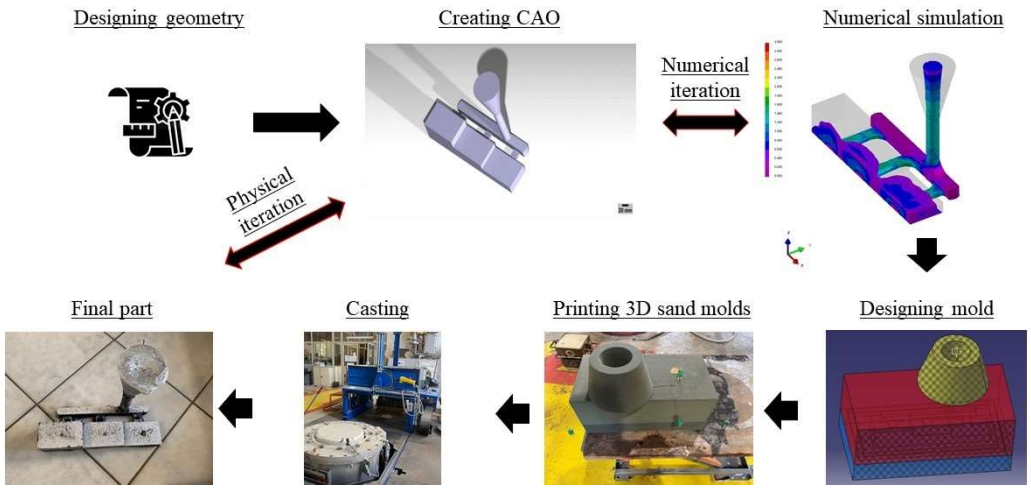

Figure A - A representation of multiple casting methods to produce components at the ENSAM in Aix-en-Provence.

The past thirty years have seen increasingly rapid advances in the field of casting processes, particularly gravity and low-pressure casting. With the difference that in low-pressure casting, the process of filling the mold is done from the bottom and is controlled by adjusting the pressure, whereas in sand gravity casting, the process of filling the mold is done from the top and is typically filled manually. A key aspect of low-pressure casting is controlling pressure and thus velocity to

avoid defects during filling step of casting. Gravity casting is more extensively used than low-pressure casting because it is less expensive and simple. It is interesting to note that they have a number of same features, such as the order of magnitude of velocity during the filling stage.

The casting process has been facing a tough and highly disputed challenge related to the formation, transfer, and eventual detection of oxidation, and its location in the final experiment. Experimentally characterizing oxidation generation and transport is exceedingly expensive because the casting process takes place in an enclosed space.

On an industrial scale, the number of physical iterations can be reduced by doing numerical simulations of filling and solidification processes. It would permit modify of cooling parameters to avoid defects prior to manufacturing. In order to predict defects such as oxidation and investigate multiphase flows, methodologies using Eulerian and Lagrangian approaches are utilized to monitor and track the interaction of phases. Even if there is a lot of software based on volume of fluid (VOF) method, it is very difficult to anticipate exactly the filling, solidification, and defects like oxidation. This is a tough topic in computational fluid dynamics based on Eulerian methods since there is no history to explain where the fluid was and where it oxides.

The focus of this thesis is to investigate the optimal techniques for controlling the filling, transportation of metal, cooling, and solidification processes during the gravity casting of light alloys using 3D printed molds. The investigation is carried out through both experimental and numerical methods, including the use of commercial software and the SPH approach.

This work lays the framework for anticipating and modeling oxidation in order to define new casting rules adapted to low-pressure casting in terms of avoiding/reducing oxides. In addition,

there is often a gap between modeling and practical tests, which is why the thesis is being done in partnership with two ENSAM (École Nationale supérieure d'arts et métiers) laboratories. This thesis is established taking into consideration the presence of specialists in the MSMP (Laboratoire Mécanique, Surfaces, Matériaux & Procédés) laboratory who deal with casting processes and professionals in the LIFSE (Laboratoire Ingénierie de Fluids Systems Énergétiques) laboratory who are knowledgeable in fluid dynamics. This thesis is divided into five topic chapters.

Thesis objectives

The main objective of this thesis is to improve an existing SPH code that was originally created in the LIFSE laboratory. The previous version of the code was able to qualitatively replicate the physics of casting in a 2D configuration. The focus of this thesis is to improve the SPH code so that it can model the physics of gravity casting for AlSi13 in 2D, utilizing a resin-bonded sand mold. To validate the accuracy of the 2D numerical results for the filling and solidification steps of the sand gravity casting process, an experimental test case is introduced. Additionally, the results of the SPH approach are compared with a commercial software to evaluate the strengths of each method.

The SPH code is then further developed for a 3D configuration, which is more realistic to explore the physics of rapid gravity casting. Two experiments were conducted, one using transparent glass and the other without glass, to validate the morphology of the filling process and temperature evolution.

Ultimately, the goal of this thesis is to create a strong and reliable SPH code that can precisely model the casting process, from filling to cooling and solidification, in both 2D and 3D configurations. This code will provide a foundation for predicting oxidation.

Thesis outline

In Chapter 1, the focus is on providing a comprehensive overview of the gravity casting process and the defects associated with it, with particular emphasis on oxidation. The chapter explores the state-of-the-art numerical approaches that have been developed to predict oxidation defect and improve the casting process. In addition, the chapter evaluates the state-of-the-art SPH methodology to determine whether it is suitable for modeling the casting process and predicting oxidation.

Chapter 2 presents a detailed description of the methodologies that have been utilized in this thesis. This includes the experiment methodology, ProCAST Software, and the SPH code that has been developed by the LIFSE laboratory over the past 10 years. The SPH code has been developed for this thesis with the aim of modeling the filling, cooling, and solidification of gravity casting in 2D and 3D configurations

Chapter 3 focuses on the 2D gravity casting study, where the aim is to improve the SPH code to model the physics of gravity casting for AlSi13. The chapter discusses the validation of the 2D numerical results for the filling and solidification steps of sand gravity casting process through an experimental test case. The chapter also includes a comparison of the results obtained through the SPH approach with those obtained using a commercial software, which highlights the strengths of each method.

Chapter 4 deals with the 3D gravity casting study, which is more realistic to explore the physics of rapid gravity casting. The chapter discusses the two experiments that were conducted using transparent glass and without glass to validate the morphology of the filling process and temperature evolution. The chapter presents the results obtained from the experiments and the corresponding numerical simulations.

Finally, Chapter 5 presents the conclusions of the thesis, summarizing the results obtained from the numerical simulations and experiments. The chapter also discusses the limitations of the SPH approach and suggests future research directions to improve the accuracy of the numerical simulations.

Introduction de la thèse

Motivation

Le procédé de fonderie est important pour une large gamme de processus scientifiques et industriels. Aujourd'hui, la croissance significative des composants de fonderie est liée au développement de l'impression automatisée de moules en sable et des procédures de coulée, ainsi qu'aux logiciels de numérique simulation de coulée.

Les trente dernières années ont vu des progrès de plus en plus rapides dans le domaine des procédés de coulée, en particulier la coulée par gravité et la coulée basse pression. Dans la coulée par basse pression, le procédé de remplissage du moule se fait par le bas et est contrôlé par le réglage de la pression, alors que dans la coulée par gravité, le procédé de remplissage du moule se fait par le haut et est généralement effectué manuellement. Un aspect essentiel de la coulée basse pression est le contrôle de la pression et donc de la vitesse pour éviter les défauts pendant l'étape de remplissage. La coulée par gravité est plus largement utilisée que la coulée à basse pression car elle est moins coûteuse et plus simple. Il est intéressant de noter qu'elles présentent un certain nombre de caractéristiques identiques, comme l'ordre de grandeur de la vitesse pendant l'étape de remplissage. Le procédé de coulée a été confronté à un défi difficile et hautement controversé lié à la formation, au transfert et à la détection éventuelle de l'oxydation, ainsi que de son emplacement dans l'expérience finale. La caractérisation expérimentale de la formation et du transport de l'oxydation est extrêmement coûteuse car le procédé de coulée se déroule dans un espace clos.

À l'échelle industrielle, le nombre d'itérations physiques peut être réduit en effectuant des simulations numériques des procédés de remplissage et de solidification. Cela permettrait de modifier les paramètres de refroidissement pour éviter les défauts avant la fabrication. Afin de prévoir les défauts tels que l'oxydation et d'étudier les écoulements multiphasiques, des méthodologies utilisant des approches eulériennes et lagrangiennes sont utilisées pour observer et suivre l'interaction des phases. Même s'il existe de nombreux logiciels basés sur la méthode du volume de fluide (VOF), il est très difficile de prévoir exactement le remplissage, la solidification et les défauts tels que l'oxydation. C'est un sujet difficile dans la dynamique des fluides numérique basée sur les méthodes eulériennes, car il n'y a pas d'histoire pour expliquer où était le fluide et où il s'oxyde. Cette thèse examine comment maîtriser les procédés de remplissage, de transport du métal, de refroidissement et de solidification pendant le procédé de remplissage de la coulée par gravité d'alliages légers dans des moules imprimés en 3D, à la fois expérimentalement et numériquement (logiciel commercial et approche SPH). Ce travail pose le cadre pour anticiper et modéliser l'oxydation afin de définir de nouvelles règles de coulée adaptées à la coulée basse pression en termes d'évitement/réduction des oxydes. Par ailleurs, il y a souvent un décalage entre la modélisation et les essais pratiques, c'est pourquoi la thèse se fait en partenariat avec deux laboratoires de l'ENSAM (École Nationale supérieure d'arts et métiers). La thèse est définie en partenariat entre des spécialistes du laboratoire MSMP (Laboratoire Mécanique, Surfaces, Matériaux & Procédés) qui travaillent sur les procédés de fonderie et des professionnels du laboratoire LIFSE (Laboratoire Ingénierie de Fluides Systems Énergétiques) qui travaillent sur la dynamique des fluides. Cette thèse est divisée en cinq chapitres thématiques.

Objectifs de la thèse

L'objectif principal de cette thèse est d'améliorer un code SPH existant qui a été créé à l'origine dans le laboratoire LIFSE. La version précédente du code était capable de reproduire qualitativement la physique de la coulée dans une configuration 2D. L'objectif de cette thèse est d'améliorer le code SPH afin qu'il puisse modéliser la physique de la coulée par gravité de l'AlSi13 en 2D, en utilisant un moule en sable imprimé. Afin de valider la précision des résultats numériques 2D pour les étapes de remplissage et de solidification du processus de coulée par gravité du sable, un cas test expérimental est introduit. De plus, les résultats de l'approche SPH sont comparés à ceux d'un logiciel commercial afin d'évaluer les points forts de chaque méthode.

Le code SPH est ensuite développé pour une configuration 3D, qui est plus réaliste pour explorer la physique de la coulée rapide par gravité. Deux expériences ont été menées, l'une avec du verre transparent et l'autre sans verre, pour valider la morphologie du processus de remplissage et l'évolution de la température.

En conclusion, l'objectif de cette thèse est de créer un code SPH solide et fiable qui peut modéliser précisément le procédés de coulée, du remplissage au refroidissement et à la solidification, dans des configurations 2D et 3D. Ce code fournira une base pour la prédiction de l'oxydation.

Plan de la thèse

Dans le premier chapitre, l'accent est mis sur la caractérisation du procédé de coulée par gravité et des défauts qui y sont associés, en mettant l'accent particulièrement sur l'oxydation. Le chapitre explore les approches numériques qui ont été développées pour prédire les défauts d'oxydation et améliorer le processus de coulée. En outre, le chapitre évalue la méthodologie SPH afin de

déterminer si elle est adaptée à la modélisation du processus de coulée et à la prédiction de l'oxydation.

Le chapitre 2 présente une description détaillée des méthodologies qui ont été utilisées dans cette thèse. Cela comprend la méthodologie expérimentale, le logiciel ProCAST et le code SPH qui a été développé par le laboratoire LIFSE au cours des 10 dernières années. Le code SPH a été développé pour cette thèse dans le but de modéliser le remplissage, le refroidissement et la solidification de la coulée par gravité dans des configurations 2D et 3D.

Le chapitre 3 se concentre sur l'étude de la coulée par gravité en 2D, où l'objectif est d'améliorer le code SPH pour modéliser la physique de la coulée par gravité pour AlSi13. Le chapitre discute de la validation des résultats numériques 2D pour les étapes de remplissage et de solidification du processus de coulée par gravité du sable à travers un cas test expérimental. Le chapitre comprend également une comparaison des résultats obtenus par l'approche SPH avec ceux obtenus à l'aide d'un logiciel commercial, ce qui met en évidence les points forts de chaque méthode.

Le chapitre 4 traite de l'étude de la coulée par gravité en 3D, qui est plus réaliste pour explorer la physique de la coulée rapide par gravité. Le chapitre aborde les deux expériences qui ont été menées en utilisant du verre transparent et sans verre pour valider la morphologie du procédé de remplissage et l'évolution de la température. Le chapitre présente les résultats obtenus à partir des expériences et des simulations numériques correspondantes.

Enfin, le chapitre 5 présente les conclusions de la thèse, en résumant les résultats obtenus à partir des simulations numériques et des expériences. Le chapitre discute également des limites de

l'approche SPH et suggère des directions de recherche futures pour améliorer la précision des simulations numériques.

1.1 Introduction to the state of the art

Metal castings, because of their three-dimensional integral forms, are essential components in almost all other manufacturing industries [1]. Numerous alloys (steel, cast iron, aluminum, magnesium, etc.) can be combined with a variety of mold materials (silicon-clay sand, chemical sand, lost wax, 3D printing, metal mold, etc.) and casting methods (gravity, high-pressure, low-pressure, centrifugation, etc.) [2] [3] [4]. To have qualified casting components, several sub-operations such as alloying, melting, molding, pouring, solidification, and finishing should be mastered (Figure(1-1)).

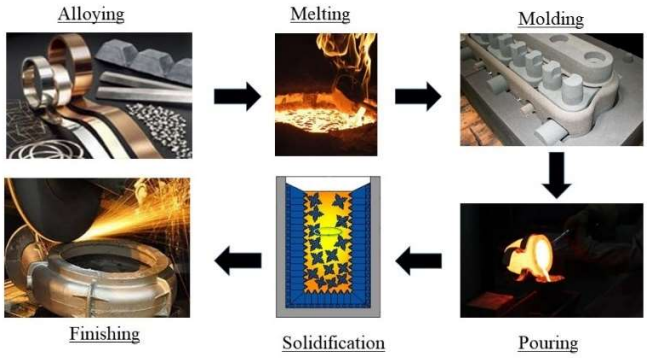

Figure 1-1 - Several sub-operation of usual casting process

Failure of even one of these steps will almost certainly result in the casting failing [4]. Molding, filling, and solidification are key steps in the foundry process. Although there are numerous aspects to consider in order to complete the casting process, we only examine the concerns that are relevant to the objective of the thesis in the following part. The next part provides a general description of

the issues that must be considered when designing an appropriate casting process, as well as various molding techniques.

1.2 Casting design, molding and filling

1.2.1 General casting design consideration

The design of the casting consists of modifying the geometry of the part to adapt it to the process than adding the appendages necessary for filling and solidifying the cavity [5] [6]. Many casting problems, according to Choudhari et al [7], can be ascribed to the poor design of the component in terms of manufacturability, which cannot be removed by making modifications to tooling and process parameters. When designing a casting component, it is crucial to consider gradual and progressive section changes, as well as limiting them [8]. Sections having tapers should be reduced in size to avoid stress concentrations and to simplify section feeding without intensifying turbulence in the metal flow [8].

Low liquid metal flow velocity into a mold cavity is regarded as an advantageous feature of a running system [8]. However, until Campbell offered a concept, the crucial value of mold entrance velocity was not precisely specified [4]. He argued that reducing the velocity in the ingate to below the threshold velocity at which surface entrainment can occur was one of the most essential criteria of an effective operating system [4]. This idea has gained widespread acceptance, and it has been well verified by several researchers who have validated the damage to castings and their characteristics when a critical ingate velocity is exceeded [4] [8] [9].

Shrinkage porosity is typical casting defect that may be minimized or eliminated by employing an appropriate design [10]. To compensate for the shrinkage of the liquid metal as it solidifies in the

mold cavity, a portion of fresh molten metal should be supplied [10]. However, because new molten metal cannot be supplied to an isolated non-solidified metal that is entirely surrounded by solidified metal, porosity defects like cavities and other void regions occur [10]. Feeders are attached to the casting to compensate for solidification shrinkage by providing directed solidification, which directs the final solidification points to the feeders [11]. The following describes the main molding process.

1.2.2 Main molding process

Permanent and nonpermanent molds are the two main types of molds used in casting process [12] [13]. Permanent mold casting is usually constructed of steel or cast iron and can be reused thousands of times [14]. Permanent mold casting is frequently utilized in high-volume manufacture of small, basic metal components with consistent wall thickness [13] [14]. Aluminum alloys, magnesium alloys, and copper alloys are common non-ferrous metals utilized in this procedure [13] [14]. Gears and gear housings, pipefittings, and various automotive and aeronautical components such as pistons, impellers, and wheels are all common permanent mold parts [13] [14].

In nonpermanent molding, a temporary mold is utilized, and it is destroyed after each cycle. The nonpermanent mold is usually created using green or resin-bonded sand from permanent models which are often made of wood or resin. The draft angle should be designed into the model in order to extricate it from the mold after molding. Green sand molds are traditionally made by mixing water with siliceous sand, clay, and black carbon. The amount of water manually poured in has an impact on the thermophysical characteristics of molds. Molds made using 3DP, on the other hand,

allow for the creation of many molds with identical thermophysical properties. Density, heat capacity, and thermal conductivity are all thermophysical properties of mold. As a result, the repeatability experiment could be used to assess the reliability and validity of the casting experiments.

1.2.3 Filling in gravity casting

Gravity casting is a method of pouring molten metal from a crucible into a mold using only gravity as a force [15]. It is the oldest, casting technique thanks to great adjustability and versatility [16]. It can produce complex high-integrity components like wheels, cylinder heads and engine blocks [17]. It is worth mentioning that this process has several issues, such as exposing the molten metal to air and causing oxidation [18]. Product quality and process productivity may both be improved through better design by filling system. The filling step and related defects are examined in detail in the following sections. Figure (1-2) displays a schematic of gravity casting process.

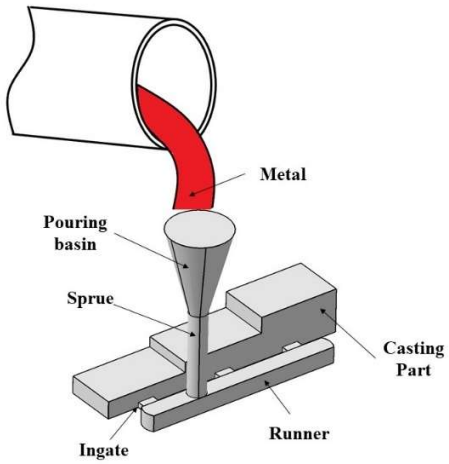

Figure 1-2 - Schematic of gravity casting

The design and development of a gating system influence sand casting quality, which necessitates an understanding of the physics of filling and solidification [19]. A well-designed gating system should fill the mold rapidly, quietly, and with little turbulence; encourage directed solidification; and limit air aspiration, decreasing re-oxidation and slag formation [20]. Prior to the entry of molten metal into the cavity, it should also prevent mold/core erosion [19] [21]. In gravity casting, molten metal is usually poured manually into the mold from a vessel or ladle. The mold cavity fills with no force other than gravity [22]. The filling velocity control in manual filling is not particularly accurate, which can result in turbulent flow [22]. Turbulence, which is responsible for the incorporation of oxide bi-films into the melt, is one of the most critical reasons leading to poor castings. Although turbulence cannot be completely eliminated, especially in gravity casting, it can be greatly reduced by developing efficient gating systems and managing metal velocity effectively [19] [22].

To obtain exact and trustworthy results, forecasting and assessing the behavior of molten metal through the gating system requires a careful combination of computational modeling and physical experimentation [23]. This will offer the benefit of being able to analyze the internal flow and learn more about the behavior of flow. Several simulation studies have been conducted to optimize the filling step by making improvements to the gating system design. John Campbell [24] argued for some running and gating system designs that result in fewer entrainment defects and higher-quality castings. The need for installing filters across the runner to avoid backflow and ensure consistent priming of the runner was emphasized by the author. Furthermore, Campbell identified two gating system designs: the Trident Gate and the Vortex Gate, both of which have the ability to eliminate entrainment defects [25]. Jezierski et al. [26] presented a gating system that combines

trident gates, a spin trap, and a bubble trap that appears to be a cost-effective (optimized) method for casting.

1.2.4 Filling in Low-Pressure casting

Among the processes of casting, low-pressure casting (LPC) is certainly worth mentioning; in several cases, it provides a compromise between quality, cost, efficiency and geometric feasibility [15]. In LPC, a mold is connected to a furnace containing molten metal by a tube. A schematic view of a LPC setup is shown in Figure (1-3) [27].

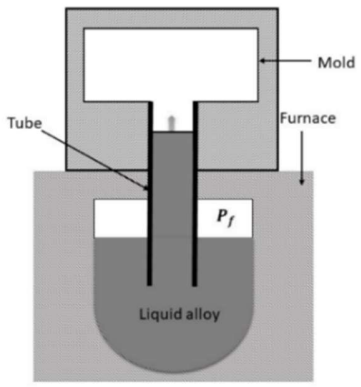

Figure 1-3 - Low-pressure casting setup

LPC has two main advantages. Firstly, the velocity can be controlled during filling in order to decrease oxidation entrapment and avoid misrun. Therefore, the risk of oxidation in the low-pressure casting process is lower than in gravity casting process [28] [29] [30]. Secondly, applying pressure during solidification phase can potentially reduce shrinkage defects. Metals shrink during the solidification step, so the filling process does not stop, overpressure is applied to prevent shrinkage defects. The filling step of LPC process starts by setting the air pressure inside the

hermetically sealed furnace. Generally, applying pressure during low-pressure casting filling is divided into four stages to control velocity inside the mold. Figure (1-4) illustrates an example of an industrial pressure-fill-curve [31].

The first step (1) corresponds to the filling of the tube is generally similar and the filling of the part which depends on its geometry. The second stage (2) corresponds to pressure holding at the end of filling. In phase (3), the purpose is to improve feeding during solidification by applying an overpressure. After considering constant overpressure until the end of solidification of the part, in the final stage (4), the pressure is released [31]. The remaining liquid metal in the tube and at the bottom of the filling system return to the furnace [32].

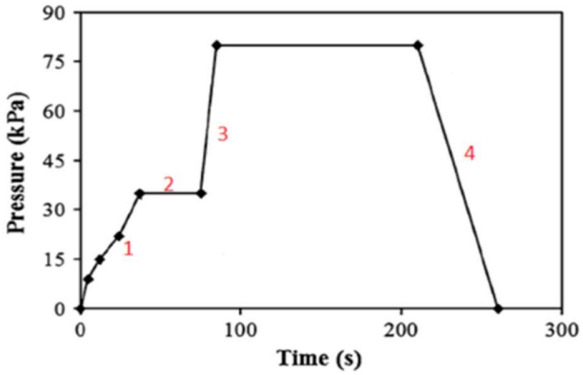

Figure 1-4 - Set pressure in low-pressure casting [31]

1.3 Filling step defects in aluminum sand casting

The filling process, as the first stage of casting, has a significant impact on the quality of the final casting products. If defects such as gas porosity, inclusion, oxide inclusion, cold shut, or misrun are not properly handled throughout the filling process, they can form [33].

1.3.1 Main defect induced by filling

In the aerospace and automotive sectors, the fluidity of aluminum foundry alloys is critical, especially when casting components with thin walls [34] [35]. When the velocity of the molten metal is too low to fully fill the mold before solidification, some parts of the mold are left unfilled, which is called a misrun defect [36]. Misrun prediction is difficult for modeling the casting process of thin-walled components [37]. This defect is fairly simple to identify and it is observable experimentally. Jakumeit et al. [38] simulated misrun formation in aluminum alloy and titanium aluminide alloy castings and found that the simulation and actual findings were in good accord. Humphreys et al. [39] also noticed that their misrun simulation findings using PHYSICA for the casting of titanium aluminide blades were quite close to the experimental data. It is important to use suitable thermal characteristics for the materials to achieve good agreement between the experimental and simulated results [40]. The interface heat transfer coefficient between the casting and the mold and the critical solid fraction at which the alloy flow in the mold channel stops are two of the most significant factors for misrun simulations for castings [41]. Therefore, to avoid misrun defects, usually, the casting process is done with high superheat and high filing velocity in industrial parts [32].

In addition, one of the most common casting defects is called inclusion, which is caused by the abrasion of the mold surface by passing the molten metal and is combined with thermomechanical stresses [42]. Besides, the flow may damage the mold by wresting sand, therefore inducing sand inclusions in metal and a bad geometry [30]. Inclusion appears as small or medium holes with grains of sand on the inner part formed on the surface [36].

A cold shut is a defect that occurs when two streams of metal in the mold cavity fail to fuse properly, resulting in a discontinuity [36]. With smooth rounded edges, the defect may look like a crack, hole, or seam. The following factors contribute to a cold shut defect: (i) inconsistent metal pouring, (ii) delayed pouring, (iii) inappropriate gating, (iv) pouring at low temperatures, (v) wrong metal composition, (vi) core print design and core assembly, and (vii) molten metal lack of fluidity [43]. The schematics of misrun, inclusion and cold shut faults are shown in Figure (1-5).

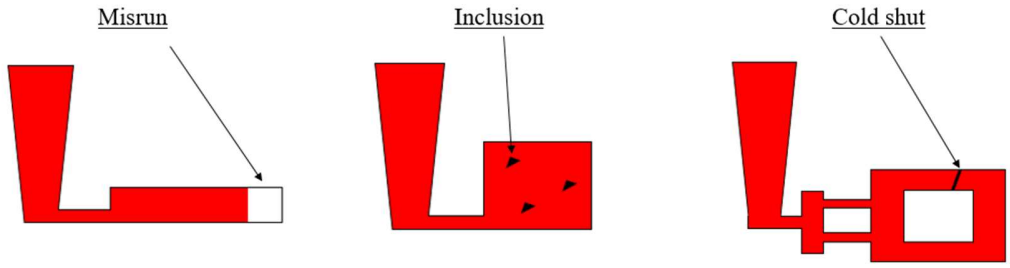

Figure 1-5 - Filling steps defects: Misrun, Inclusion, and cold shut

1.3.2 Oxidation defect

In molten aluminum and its alloys, oxidation occurs rapidly due to its reactivity by forming a thin oxide film on the exposed surface of the molten metal. Liquid metal is transferred from various crucibles and furnaces to a casting process in cast houses [44]. These transfers may include pouring a crucible into a furnace, emptying a furnace into a launder trough, or flowing from a launder to a casting process, depending on the procedure [44]. During these procedures, the oxide layer formed on top of the molten aluminum breaks apart, exposing fresh melt to air, resulting in further oxide production and the development of dross, a combination of oxide and un-oxidized melt [44] [45].

Defects such as small porosity are easily created due to the tiny oxide and involved gas generated by the disturbance of molten metal during the pouring stage. If the filling is done rapidly, the flow could be turbulent, and air could be mixed with metal, inducing oxidation. Turbulence flow during the filling step leads to entering a portion of this film into the cast metal and causes the formation of different defects and pull down mechanical properties [32] [46]. The micrograph of oxidation is shown in Figure (1-6).

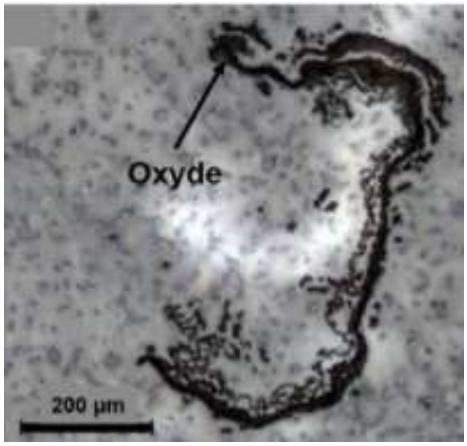

Figure 1-6 - Micrograph of oxidation [47]

Geometry and associated oscillation, as well as falling velocity, are the most important factors that induce oxidation.

1.3.3 Good filling analytical criteria

Here are presented the existing criteria for oxidation formation based on dimensionless numbers.

Maximum velocity criteria: This criterion represents the limitation of speed for aluminum alloys which is about 0.5 m/s, regardless of the geometry. Campbell [48] [49] proposed a maximum

velocity criterion that depends on the melt density and surface tension to decrease the oxidation defect. It should be noted that turbulent flow is the main reason for the entrainment of the surface oxide film [29]. By comparing experimental results with this criterion, the authors concluded that when the velocity is more than 0.5 m/s, the final part properties like bending strength drop sharply [50]. Liu et al. [29] mentioned that when the area ratio is smaller than 0.5, rising the pressurizing speed could avoid surface cracks [29]. Sun et al. [51] by simulating the mold filling step by using MAGMA and Flow-3D showed that when the metal gets into the waterfall structure area, gating velocity is greater than the crucial value (0.5 m/s), which causes oxidation because of the sudden expansion of the geometry.

Weber: Weber number indicates the ratio of inertial forces of the flow to surface tension [42]. When the local velocity of the liquid surface is higher than 0.5 m/s, the inertia force is slightly higher than the surface tension [52]. Campbell proposed that surface turbulence starts when the value of the Weber number is between 0.2 and 0.8 [48]. This surface turbulence causes increasing oxidation defects. Cuesta et al. [53] represented that the surface entrainment is much more related to the Weber number than to melt velocity for pure aluminum and pure iron. It is suggested that for channel thickness between 3 mm and 25 mm, the critical velocity should be in the interval of 0.3-0.5 m/s. Jakumeit et al. [54] developed two models by considering geometrical aspects and dynamic Weber numbers to detect locations where folding or breaking of the metal/gas interface brings oxide entrapment. The results showed different oxide film distributions during the early phase of the filling step depending on geometry.

Reynolds: The Re is a dimensionless number, called Reynolds number [55]. Kuo et al. [56] developed a numerical simulation for prediction of occurrence of gas porosity, and they

determined the proper velocity gate for every part of casting by considering Reynold's number. In some cases, considering the principle of dynamic theory, water can be used instead of metal to perform the filling step [55]. Liu et al. used the Reynolds criterion for principal similarity:

$$\mathrm{Re}_a = \mathrm{Re}_w \tag{1-2}$$

Ohnesorge number: In laminar flow, inertial forces do not play a significant role. On the other hand, viscosity can restore the flat surface. So the balance between the actions of viscosity and surface tension is represented by using a non-dimensional Ohnesorge number that includes the Reynolds number and the Weber number [42].

$$Oh_{\max} = \frac{We^{\frac{1}{2}}}{\mathrm{Re}} \tag{1-3}$$

Van der Graaf et al. [42] mentioned that instabilities are associated with low values of the Ohnesorge number. They claimed that surface tension provides the driving force for surface instabilities, and viscosity is like the damping force. They obtained results that conflicted with the results of Campbell that claimed higher Weber numbers induce stronger instability [42].

As previously noted, there are challenges with evaluating the casting filling process due to its indoor nature and the experimental approaches used to examine it. As a result, using numerical simulations reduces costs while also avoiding trial-and-error and allowing for a more complete analysis.

1.4 Experimental casting tests

Experiments used to validate numerical modeling should reveal if numerical results properly represent physical processes and whether the process factors and material qualities can be

effectively taken into consideration [57]. Standard physical testing can provide answers to these fundamental issues. The laboratory benchmarks for the mold filling process, solidification within full containers, and coupling of filling and solidification were established by the combination of experiment and numerical analysis [57].

1.4.1 Experimental characterization filling

Several research has been carried out over the last decades to experimentally validate the relationship between gating factors and casting quality [32]. Various physical models are employed to characterize the flow characteristics since the simulated findings must be verified [19]. The water analogy [55] [58] [59] was one of them, and it was utilized to investigate the flow properties of basic castings. The metal flow pattern may also be observed throughout the gating system and mold cavity using an open mold or a temperature-resistant transparent quartz glass window [60]. This technique is best for studying thin section cast specimens in an experimental setting. The development of high-intensity X-rays led to a novel way of capturing the mold filling procedure in an opaque sand mold using X-rays and a high-speed camera [61] [62]. This approach is appropriate for experimental investigation, but it is restricted by the size and thickness of the casting, as well as costs and safety concerns [61] [62]. Contact time technique approach in another method that detects the melt flow front and calculates the filling velocity using a series of sensor wires linked to a circuit [2]. By attaching it to a computerized data gathering system, the temperature of the metal may also be monitored using thermocouples in relation to time and solidification rate, as well as direction. However, too many wires might pose problems in the manufacturing process [2].

1.4.2 Casting benchmarks

Several benchmarks have been used to validate filling, transport, cooling, and solidification modeling results for various casting processes. In terms of the filling step of the casting process, Tol et al. [63] used Particle Image Velocimetry (PIV) to estimate flow patterns and interface shapes of horizontal horseshoe filling to confirm numerical findings from Flow-3D software. Abdullah et al. [64] established two experimental case studies ((a) a semi-cylindrical cavity, (b) the gravity sand benchmark casting). One is based on flow visualization, while the other is based on an experiment in which a brief shot approach is used to create a picture of a metal flow pattern in a pressure die cast part. When a turbulent flow model was used to compare numerical data with experimental data, there was a lot of agreement. Bublk et al. [65] aimed the purpose of providing novel experimental data for the validation of well-established mathematical models within the context of the lattice Boltzmann method (LBM), which is used in casting processes in complicated mold cavities. The benchmark tests demonstrate the developed algorithm's ability to deliver a trustworthy solution when surface tension effects become prominent.

Regarding solidification, a three-dimensional cellular automaton-finite element solidification model was used by Carozzan et al. [66] to mimic a solidification benchmark experiment. It comprises a FE solution for heat and mass transport in the presence of fluid flow, including differentiation of total mass and solute mass, as well as grain structure prediction and thermodynamic property computation. B. Sirrel et al. [67] developed a benchmark evaluating the flow and solidification modeling of Al Castings that appears to be good in its macroscopic capabilities when turbulence is correctly taken into consideration. Chandra [68] provided a systematic set of benchmark issues aimed to evaluate models of latent heat release during

solidification in pure metals and super alloys. These issues were analyzed utilizing a 2-dimensional and 3-dimensional finite element code for illustrative objectives. Im et al. [69] developed a unified model for two-dimensional filling and solidification of a square cavity with simultaneous filling and solidification. In order to evaluate the linked effects of filling and natural convection on solidification, the mixed natural-convection flow and residual flow arising from the completion of filling were included in the study.

1.5 Numerical approach

Foundry engineers are increasingly recognizing numerical modeling as a way to improve quality and reduce energy consumption while shortening the trial period and lowering costs [70]. The complicated physics involved in casting processes makes it tough to simulate, including fluid mechanics with phase changes, macrosegregation in alloys, and heat transfer between the casting and the mold. Modeling the filling and solidification and predicting the relevant behaviors via numerical simulations can reveal the underlying fundamentals and design/optimize the process. Eyres et al. [71] established the groundwork for numerical modeling of casting processes back in 1946. Since then, computational models for simulating the filling process, estimating temperature profiles during solidification, and diagnosing the causes of defects such as misrun, shrinkage, and oxidation have been developed [10] [72] [73]. The numerical simulation of melting transportation during filling and cooling and solidification steps must be carried out with perfect accuracy in order to accurately estimate oxidation generation, transportation, and location. Multiphase flows and mechanisms for recording or tracking the interaction phases are generally required to forecast defects like oxidation. The most prevalent strategies for detecting interaction phases in the Eulerian

approach are the VOF (Volume of Fluid) approach [74], the LS (level set) method [75], and the front tracking method explained in the next sections [76] [77].

1.5.1 VOF (Volume of fluid)

Hirt and Nichols [78] proposed the VOF (Volume of Fluid) approach, which uses a fractional function (usually a Heaviside function) to describe the volume of each fluid in each computational cell. This fractional function is determined as an integral of the characteristics of fluid functions in a cell [79]. If the cell is empty (i. e., there is no fluid), the fractional function equals 0. If the cell is filled, the fractional function represents one. The derivative of fractional function must be equal to zero. The interface is generated using the cell volume fraction and its nearest neighbors for each time step [79] [80]. Because the fractional function discontinuities represent the interfaces, they are susceptible to numerical diffusion and numerical oscillations [79]. They may also suffer from sophisticated interfacial processes like fragmentation and coalescence. Nevertheless, for mold filling simulation, the VOF approach remains the most popular and extensively used method [79]. The key reasons for this employment are the relative ease of implementation and its foundation in volume fractions, which lends itself well to the absorption of other physics.

Concerning the casting process utilizing this approach, Im et al. [69] investigated the complete casting process with a numerical approach that employs the implicit volume of fluid (VOF) technique for filling and an implicit, source-based method for solidification. Yang et al. [81] proposed an algorithm, Oxide Film Entrainment Tracking (OFET, 2-D) for numerical modeling of casting process. The proposed algorithm is able to model the metal flow behavior and oxide film defect entrainment in the filling of aluminum castings using the VOF approach. Using the VOF

technique, Minaie et al. [58] estimated the flow pattern in the filling stage of the die cavity. The results showed that flow patterns for a range of geometries are consistent with experimental data, however further experiments are needed to clarify the flow's entire nature. The VOF technique is used by certain commercial software packages for casting simulation and analysis, such as MAGMAsoft, Flow-3D, ProCAST, etc.

Iqbal et al. [82] used MAGMAsoft Software to explore the influence of design parameters such as filling pattern, pressure and velocity, cooling rate, solidification, and defects such as air entrapment, hot spot, and porosity on complicated geometries in the sand casting process. The Oxide Film Entrainment Model (OFEM) was developed by Reilly et al. [83] in the Flow-3D software to evaluate entrainment events as well as mark and track entrained oxide films. This enables the location(s) of the ultimate defect(s) to be determined. Liu et al. [84] used fluent software considering the VOF method to investigate the filling step of low-pressure casting by considering the two-phase model (gas, fluid) of flow with the sudden expansion section in three different values of pressurizing speed and oxide film entrainment. They represented that high gate velocity causes melt falling back and relative rotating vortex, which are the main causes of oxide film entrainment. Huang et al. [85] used the Anycasting software package using the VOF approach to simulate the low-pressure die-casting processes of A356 aluminum in order to better understand the evolution of mold flow, temperature field, and solidification. To reduce the number of defects in wheel products, various casting parameters were paired with flow channel and overflow designs. Water simulation with a Plexiglas mold was used by Liu et al. [55] to investigate the filling of a progressive expansion structure in low-pressure casting using the two-phase flow model's the VOF (Volume of Fluid) algorithm and the FLUENT computational fluid dynamics (CFD) code. A

mathematical model was developed between the pressurizing speed, expansion angle, and the height of the progressive expansion structure to avoid the entrainment of oxide filling [55]. Wu et al. [86] examined the distribution of gas entrainment, the evolution of temperature, and surface defects in the filling stage for a copper motor rotor by numerically optimizing process parameters utilizing the VOF method (Flow-3D).

1.5.2 Level set method

LSMs (level-set methods) are a conceptual model for numerical surface and shape analysis. The level-set approach has the benefit of allowing numerical computations involving curves and surfaces to be performed on a fixed Cartesian grid without the need to parameterize these objects. Osher and Sethian [87], first introduced this technique to simulate interfacial development in the normal direction. The notion of implicit surfaces is used to describe the liquid–solid interface in LSM, where a function is specified in a domain with a fixed value at the interface. LSM and its applications have been described in great detail by Sethian [88], Osher and Fedkiw [89]. Du et al. [90] proposed using LSM to capture the interface during the process of casting a second alloy into a mold, largely displacing the first to generate a casting with a distinct alloyed skin. They discovered that the stability of the interface is affected by the density ratio and inflow velocity, but not by the viscosity ratio. For solidification modeling, Ji et al. [91] presented a hybrid extended FEM–LSM model. It makes use of recent advances in enriched finite-element approximations to show a sharp interface on a fixed grid. Xia et al. [92] developed a level-set based technique for casting part optimization and explored casting part performance and molding restriction.

1.5.3 Front tracking method

Front tracking is a numerical approach that uses surfaces or lower-dimensional manifolds as computational degrees of freedom. Its purpose is to improve the resolution of discontinuities or steep gradients in solution variables, as well as the physical laws that control them. Thermal or concentration discontinuities, and thermodynamic phase discontinuities, may benefit from front tracking, which is often poorly handled by Eulerian advection systems [93].

Kreziak et al. [94] used SIMULOR software to model low-pressure casting in the permanent mold by using free-surface tracking to examine the solidification and filling phase of molten metal in thin wall cross-member. The results of the simulation in temperature evolution, filings step, predicting misrun and shrinkage defect, and the influence of pouring temperature are all in good agreement with the full experimental test when using the two-phase approach in free-surface tracking. Hetu and Ilinca [95] proposed a technique that uses a front-tracking model for predicting velocity, pressure, and temperature fields as well as the position of the interface during the filling of a 3D mold. Physical phenomena such as highly deformable free surface flows and gravity-induced flows were predicted by the model. It has been demonstrated to be capable of resolving gravity casting's highly convective fluxes and nonlinear material behavior. The solidified grain structure (macrostructure) of castings is predicted by McFadden and Browne using a newly extended front-tracking technique that models the growth of solid dendritic fronts through undercooled liquid during metallic alloy solidification [96]. Fic et al. [97] used a novel BEM front tracking algorithm to simulate the unknown location of the solid–liquid interface and temperature field during continuous casting. Klimes et al. [98] studied the use of graphics processing units (GPUs) to improve the computational efficiency of the front tracking approach for simulating

phase transition processes. The front tracking approach is roughly two orders of magnitude more accurate than interface capture methods, according to the computational accuracy assessment.

Other approaches, such as classical metaballs, the Point set method, the marching cube algorithm, the level contour reconstruction method, and the screen space mesh approach, have not been examined since they are less commonly used in casting operations [86]. The approaches based on the Lagrangian method are detailed in the next section.

1.5.4 Lagrangian methods

Eulerian techniques are incapable of directly capturing the surface and interface of fluid. The incorrect forecast of interface phase evolution leads to an incorrect estimate of its curvature and normal vector, causing inaccuracies in terms of prediction free surfaces. These mistakes can be reduced by employing adaptive mesh refinement methods [99]. For predicting free surfaces and oxidation defects, the Lagrangian method is more accurate than the Eulerian techniques. Besides that, Eulerian methods take too long to compute and generate grid cells. The easiest way to define and monitor a free surface is to build a Lagrangian grid that is embedded in the fluid and moves with it. This technique is used in several finite-element approaches. The grid follows free surfaces automatically since the grid and fluid move together. At a surface, the approximation equations must be modified to account for the suitable boundary conditions and the fact that fluid exists only on one side of the boundary. If this is not done, asymmetries will develop, eventually destroying the accuracy of the simulation. Lagrangian techniques have a major drawback in that they cannot follow surfaces that break apart or cross. Without regrading techniques like the Arbitrary-

Lagrangian-Eulerian (ALE) approach, even high amplitude surface movements can be difficult to track.

There are varieties of Lagrangian perspective approaches to consider. More study is needed to determine which of these techniques is more efficient in anticipating defects such as oxidation, which occurs during the casting process when the molten metal comes into contact with air. There have been over ten meshless systems or schemes created, some of which are included in Table (1-1) [100].

Table 1-1 - Meshless methods [100]

Method	System equation to be solved	Method of function approximation	Need background cell	Need integral
Diffuse element method	Weak form	MLS approximation, Galerkin method	Yes	Yes
Element Free Galerkin (EFG) method	Weak form	MLS approximation, Galerkin method	Yes	Yes
Meshless Local Petrov-Galerkin (MLPG) method	Local weak form	MLS approximation, Petrov-Galerkin method	No	Yes
Finite Point Method (FPM)	Strong form	Finite differential representation (Taylor series), MLS	No	No
Smooth particle hydrodynamics	Strong form	Integral representation	No	No
Reproducing kernel particle method	Strong form or weak form	Integral representation (RKPM)	Yes	Yes
hp-Clouds	Weak form	Partition of unity, MLS	Yes	Yes
Partition of unity FEM	Weak form	Partition of unity, MLS	Yes	Yes

Meshless techniques are often classified depending on how the approximation of the unknown field function is generated, i.e. the test function is chosen, and the system equation is solved. When the background cell integral is required in one of these meshless approaches, the complexity, and difficulty of solution increase. The Meshless Local Petrov-Galerkin (MLPG) approach [101] [102], the Finite Point Method (FPM) [103] and Smoothed particle hydrodynamics (SPH) are meshless methods that simply need nodes. As demonstrated in Table (1-1), two of them (FPM and SPH) are also straightforward to implement since they do not even require a background cell or an

integral. The numerical stability, on the other hand, might be a concern. For example, concerning the heat transfer equation, the Neumann boundary condition is convection-dominated. Solving the equations of substituting the approximation with variable weighting function usage into a non-symmetric finite difference format of the temperature derivative, can lead to inaccuracy and instability problems [100]. As a result, specialized treatment is required to resolve the issue.

The background cell integral is not required for the smooth particle hydrodynamics (SPH) approach, although it is very useful in handling unbounded problems [104]. **Furthermore, because of earlier work done at the LIFSE laboratory on the SPH approach and its advantages, which are explained in detail in the next part, the SPH method was chosen to replicate rapid gravity casting in this thesis.** The word "rapid gravity casting" is taken into consideration for the gravity casting procedure using resin-bonded sand molds. The SPH approach and its advantages, which were employed in this thesis, are covered in detail in the next section.

1.6 SPH method

Smoothed particle hydrodynamics (SPH) is the earliest contemporary mesh free particle technique since it is a "really" mesh free particle method initially intended for continuous scale applications [44]. Unlike traditional Eulerian methods, the SPH method takes the continuum fluid as a set of Lagrangian properties. SPH is a type of theory that is primarily based on interpolation, with a weight function controlling the interaction between each particle [44]. Interpolation formulae and finite difference approximations for second-order derivatives are utilized to convert parabolic partial differential equations into ordinary differential equations to obtain the motion of particles and change their properties [44]. The conservation laws of continuum dynamics, which are partial

differential equations, are transformed into integral equations using the kernel function of the field variables at each point [105]. It is worth noting that with this technique, each particle has its own set of material characteristics. The neighboring particles determine each particle's position and properties [105].

The kernel function determines how much the bordering particles influence the center particle. Neighboring particles have a greater impact when they are closer to the central particle. By utilizing the kernel function of the field variables at each location, the conservation laws of continuum dynamics, which are partial differential equations, have been converted into integral equations [105]. As a result, information is only available at discrete locations, and integrals are computed over nearby particles. Figure (1-7) shows the interpolation between the particles.

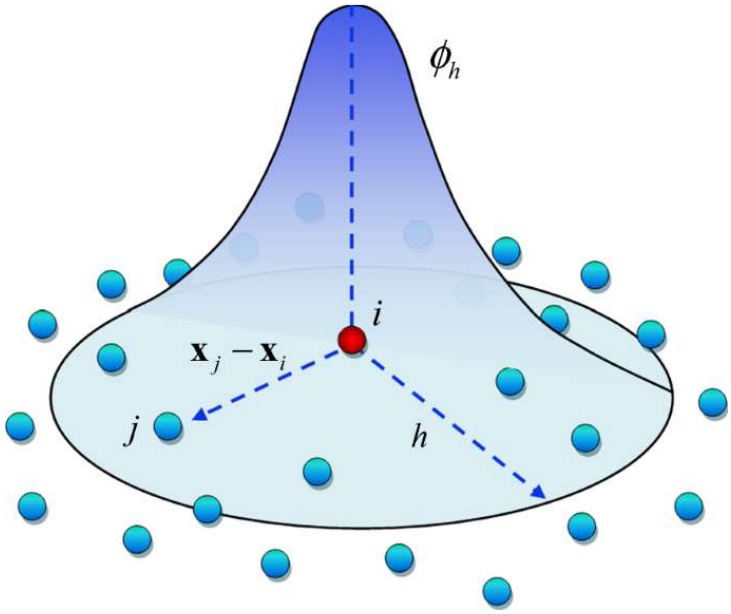

Figure 1-7 - Effect of kernel function on the neighboring particles [106]

1.6.1 Advantages

SPH has a variety of advantages over grid-based numerical methods, which are discussed in the following [107].

1. SPH is a Lagrangian particle technique whose methodology is Galilean invariant. It could acquire the time history of material particles. The advection system and transport could therefore be estimated [107].

2. The free surfaces, material interfaces, and moving boundaries can all be tracked naturally in the simulation process independent of the complicity of the particle movement, which has proven difficult for many Eulerian techniques. As a result, SPH is an excellent choice for simulating free surface and interfacial flow [107].

3. SPH is a particle technique that does not rely on a grid or mesh. The mesh-free property of the SPH approach allows for straightforward handling of very large deformations. Because the link between particles is generated as part of the computation and can vary over time. SPH applications in high-energy events such as explosions, underwater explosions, high-velocity impacts, and penetrations are typical examples [107].

4. A particle in the SPH technique represents a finite volume in a continuum scale. This is comparable to the conventional molecular dynamics (MD) approach [108] [109], which uses a particle to represent an atom or molecule at the nanoscale. Furthermore, it is analogous to the dissipative particle dynamics (DPD) technique [110] [111], which employs a particle to represent a mesoscale cluster of molecules. As a result, it is only logical to generalize or extend SPH to

lower scales, or to combine SPH with molecular dynamics and dissipative particle dynamics for multiscale applications.

5. SPH is appropriate for issues involving objects that are not continuous. This is especially true at the micro and nanoscales in bio- and Nano engineering, as well as at the astronomic scale in astrophysics. SPH is a logical choice for numerical simulations in such cases [107].

6. SPH is easier to apply numerically than grid-based techniques, and it is more natural to construct three-dimensional numerical models [107].

1.6.2 Previous studies on casting

The SPH technique was originally used to tackle astrophysical issues in three-dimensional open space because the collective movement of those particles is comparable to that of a liquid or gas flow and can be described using the governing equations of classical Newtonian hydrodynamics [112] [113]. For incompressible enclosed flows, SPH was developed lately [114]. Low-speed incompressible flow, viscous flow, underwater explosion, and galaxy formation may all be modeled using SPH. Heat conduction, natural convection in a cavity and Rayleigh–Benard convective instability, and high-pressure die-casting are examples of further uses [107]. Monaghan and coworkers have provided examples of validation of basic free surface flows [107]. During the past 20 years, much more information has become available on simulating casting processes using the SPH method especially high-pressure die casting [107].

Cleary et al. [115] and Ha and Cleary [116] reported on the application of SPH to HPDC in two dimensions and the favorable comparison of these SPH results with water analog experiments. Ha and Cleary [116] did isothermal SPH and VOF fluid simulation of high-pressure die-casting, and

both numerical results were compared with water flow tests for three different geometries. The SPH method was able to predict separation from the corners, the time of vanishing of separation voids, and the smoothness and shape of the free surfaces of primary jets better [116]. For three-dimensional isothermal numerical simulation, Cleary et al. [117] developed a modeling of the high-pressure die casting (HPDC) process. The flow separation and considerable fragmentation of the free surfaces resulted in the huge transient void creation. To compare SPH methodology with commercial software, Cleary et al. [118] contrasted the findings of MAGMAsoft simulation and SPH methodology with a single servo position water analog experiment for high-pressure die-casting. They discovered that, unlike MAGMAsoft simulation, the SPH model exhibited extraordinarily good agreement with fill pattern, speed prediction, and void trapping timings. Furthermore, by adopting an enthalpy formulation for solidifying metals, heat transfer and solidification using SPH are in good agreement with the experiment. He et al. [119] examined the two- and three-dimensional modeling filling stage of high pressure die casting (HPDC) using smoothed particle hydrodynamics and artificial viscosity, as well as the moving least squares method to address pressure oscillation. When the findings of SPH and the finite difference method (FDM) were compared to the results of the experiments, it was discovered that the SPH results were more in line with the FDM. Cleary et al. [120] demonstrated that SPH could be used as a computational tool to predict die-filling behavior of high pressure die casting in complicated thin walls, and the findings were compared to water analog studies using similar Reynolds numbers. The relative rate of flow movement, the shapes and positions of voids in early filling, and the location and relative rate of the backfilling process were all found to be perfectly matched. Hu et al. [121] employed smoothed particle hydrodynamics to create a three-dimensional simulation of

high-pressure die-casting (HPDC) for a realistic die. The experimental findings confirmed the SPH model's excellent stability and dependability in evaluating molten metal flow rate during the cavity filling process. Tokunaga et al. [122] described a particle method simulation for the generation and flow of cold flakes in a high-pressure die casting process in their study.

It should be noted that SPH has been used in other casting methodologies, such as gravity and low-pressure casting. Ha et al. [123] reported using smoothed particle hydrodynamic (SPH) to model the filing process of gravity die-casting in two dimensions by considering isothermal conditions and thermophysical properties of water in two different shapes. Besides, the results have good agreement with experiments to predict the overall structure of the filling step. The SPH simulations were able to capture the free surface wave behavior and the fine details of the flow. Based on the work of Cleary [124], the developed the SPH approach for predicting shrinkage defects in two-dimensional simulations of the low-pressure casting process of an engine block. They predict oxide production, feeding, solidification dynamics, and residual pressure distribution in solidified metal. The capacity to forecast the amount of liquid metal exposed to air and the length of that exposure is linked to the ability to anticipate oxide concentration, according to them. Cao et al. [59] proposed a novel methodology based on composite solid boundary treatment and created numerical models based on the SPH method to simulate the foundry-filling process. The solidification model was created using a traditional method. This method used viscosity, which varies with temperature, however, the findings were unsatisfactory. The SPH approach was used to simulate the filling and crystallization of low-pressure casting by Lysenko et al. [125] The SPH approach has been demonstrated to be quite accurate in simulating the filling process, and it may be used in foundry

manufacturing. They stated that due to super cooling, crystallization under high pressure lowers the time it takes for aluminum alloys to solidify.

Although various studies have been conducted to model filling, solidification, and the prediction of oxidation defects, there has been relatively limited investigation into the simultaneous simulation of these processes in gravity and low-pressure casting.

According to these researches, the SPH approach is utilized to simulate filling, solidification, and defect prediction in various casting procedures. The results reveal that this technique has a high accuracy for modeling the filling process and replicating free surfaces when compared to commercial software and validation with experimental data. This is the reason why this approach is used to model the filling, cooling, and solidification steps of the gravity casting process, as is explained in more detail in the following chapter.

1.6.3 Oxidation prediction

This is a complicated issue in traditional grid or mesh based Eulerian CFD since information is only available for liquid metal that is currently at the free surface. There is no history available to show where the metal was previously or where the oxide created previously has moved. Each particle in SPH represents the same precise volume of fluid throughout the simulation and can contain information about the composition and history of particle. Small-scale research and case studies began to appear in the previous two decades, linking the SPH approach to forecasting oxidation throughout the casting process. Prakash et al. [126] studied numerically oxidation prediction in order to forecast preliminary cumulative internal and exterior oxide levels over time in a typical DC casting operation. The amount of inner oxide will reflect the influence of oxide on

the final metal microstructure, they said. The quantity of external oxide influences the billet's surface quality.

The capacity to forecast the quantity of liquid metal exposed to air (metal positioned at the free surface) and the length of that exposure, according to Cleary et al, [124] is required for predicting oxide content. When the temperature of a particle drops below the solidus temperature and more than two of its neighbors are solid metals, the equation for that particle should be changed. Setting the particle's velocity to zero and locking it in place is the simplest option. Furthermore, they stated that with the following crucial factors, the oxide prediction becomes quite straightforward in the Lagrangian framework employed by SPH [124]:

- Liquid metal particles oxidize for as long as they are in contact with the free surface. When they are not on the free surface, they do not oxidize. This necessitates determining which particles are on the surface at any given time and calculating their exposed surface area [124].
- In this Lagrangian framework, the rate of oxidation is described by a simple ordinary differential rate equation [124].
- The oxide that has already developed is transferred during filling of casting process by its host SPH particle. As a result, the approach automatically provides the subsequent distribution of oxide formed by the fluid flow [124].

A rate equation determines the oxide content of any particle (step 2). Baker et al. [127] proposed a simple linear oxide development model for pure aluminum, which we employ here:

$$\frac{dO_x}{dt} = \kappa_1 \tag{1-4}$$

In equation (1-4) κ_1 represents the rate constant and t shows the time. Briks and Meier [128] suggested the rate constant as follows:

$$\kappa_1 = 10.9 \times 10^{-3}\, kg/m^2 s \tag{1-5}$$

This model is designed for pure aluminum, which should melt completely during the pouring process. When the oxide model was implanted in the SPH code, some assumptions were taken into account. For more information, see [44]. Niu et al. [129] utilized the SPH technique at three different resolutions to forecast the amount of oxide formed during furnace tipping. The numerical and experimental tests were found to be in good agreement. In gravity die-casting, K.Ellingsen et al. [130] studied the modeling of oxide and the creation of oxide films. The SPH model was used to investigate the filling of gravity dies at two different filling velocities, including the generation of oxidation and how it is transmitted. The results show that low input velocity creates more oxides in the casting because it is exposed to the air for a longer period and has a longer filling time. It is worth mentioning that oxidation is more intense at the thicker stage. During the simulation by K.Ellingsen et al. [130], a strategy for identifying the oxide film is presented. A technique for detecting the free surface was developed by Marrone et al. [131] Oxide layers are said to be entrained with the flow when the normal oxidized surface points in opposing directions (as shown in Figure (1-8)). The surface normal and particle velocity may be used to identify each surface, and the algorithm can detect if a particle belongs to an oxide layer.

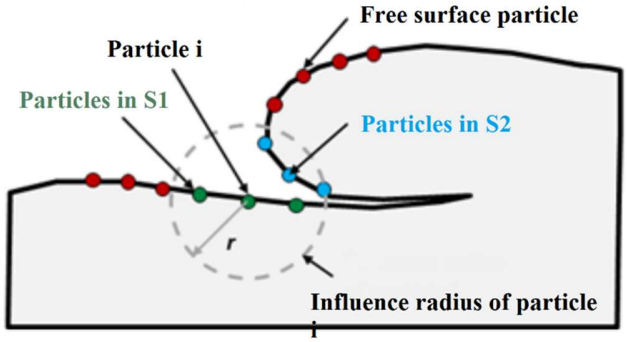

Figure 1-8 - Oxidized surfaces pointing against each other forming an oxide film [130]

As aforementioned, the SPH approach could be utilized to model the filling, solidification, and prediction of oxidation formation and transport. As a result, in the continuation of the work, the SPH approach is used to simulate rapid gravity casting, which is explained in detail in the following chapter.

1.7 Conclusion

Casting is used for a long time and it is still required for all industrial purposes, despite its numerous difficulties. Several sub-operations, including melting, alloying, molding, pouring, solidification, and finishing, must all be managed at the same time during the casting process. In every casting process, the filling and solidification processes are two of the most crucial steps. Different casting processes (gravity, high and low-pressure, etc.) are used on various metals (steel, aluminum, magnesium, etc.) using several molding techniques (chemical sand, silicon-clay sand, metal mold, lost wax, and 3D printing). The new introduction of the sand mold 3D printing process prefers to employ taking advantage of having undercuts for complicated parts. The gravity sand casting process is ensuring to achieve 20% low mechanical properties than that of permanent mold casting because of the low rate of solidification. It should be noted that, in contrast to gravity and

high pressure casting, low-pressure casting (LPC) has a controlled filling velocity. Moreover, the velocities during filling steps are the same for gravity and low-pressure casting, considering that gravity casting is easier and more practicable. As a result, the rapid gravity casting is investigated in this thesis. Defects, particularly oxidation that happens during the filling stage, are a serious issue in gravity casting. During the filling phase of aluminum alloy casting, certain general defects such as misrun, inclusion, cold shut, and oxidation are formed. Oxidation is a more difficult defect to treat since it occurs fast when exposed to air. Different parameters for dealing with the oxidation defect during the filling process are provided after a thorough examination. It should be mentioned that lowering velocity and oscillation during the filling stage have been documented by several researches could increase the rate of oxidation formation. To anticipate the oxidation defect throughout the casting process, the casting phases must be properly simulated, including filling, cooling, and solidification.

Numerical simulation techniques for simulating multiphase flows and systems for recording or tracking the interaction phases are often necessary to avoid the trial-and-error procedure and reduce costs. Volume of fluid (usually utilized in commercial software), the level set technique, and front tracking method were researched as approaches to track molten metals based on the Eulerian approach. These approaches, however, are capable of directly recording the surface and interface of fluids. Predicting oxidation defects using the Eulerian approach is challenging and time-consuming due to mesh quality and capturing the free surface of fluid.

Lagrangian approaches could foresee oxidation problems during the filling stage because they can carry the history of each particle to determine if it has been exposed to air during the filling phase. The finite point method (FPM) and Smoothed particle hydrodynamics are two meshless methods

that could be used to simulate the casting process since they are simple to apply and do not require background cells or integrals. Because of earlier work done at the LIFSE laboratory, the SPH approach is preferred over the FPM method. It has certain distinct advantages, such as the ability to model free surface flow, which might lead to oxidation prediction. Several studies were conducted utilizing the SPH approach to model filling and solidification of gravity, low-pressure and high-pressure casting, as well as oxidation prediction. However, little research has been conducted to model the casting process using the SPH approach, involving the filling and solidification processes, as well as the simultaneous prediction of oxidation defects.

To summarize, the goal of the thesis is to investigate and master the processes of filling, cooling, and solidification in sand gravity casting for light alloys, utilizing a 3D printing mold to establish the circumstances for oxidation prediction. **To achieve this purpose, basic 2D casting SPH code developed by LIFSE experts should be improved and upgraded to model filling, cooling and solidification of rapid gravity casting in 2D and 3D**. The comprehensive SPH technique description, as well as its multiple methodologies for 2D and 3D, is examined in chapter (2). One of the accomplishments of this thesis is the introduction and development of an experimental test case that can be used to replicate the two-dimensional filling and solidification process, which is addressed in depth in chapter (3). Furthermore, in order to validate the filling, cooling, and solidification results of numerical simulation of the 3D SPH code and the application of commercial software, a more realistic experiment using transparent glass that replicates the gravity casting process was carried out in the chapter (4).

Conclusion

La fonderie est utilisée depuis longtemps et elle est toujours nécessaire à toutes les fins industrielles. Plusieurs sous-opérations, dont la fusion, le moulage, la coulée, la solidification et l'ébarbage, doivent toutes être gérées au cours du procédé de coulée. Dans tout procédé de coulée, les procédés de remplissage et de solidification sont deux des étapes les plus importantes. Différents procédés de coulée (gravité, sous pression, basse pression, etc.) sont utilisés pour divers alliages (acier, aluminium, magnésium, etc.) à l'aide de plusieurs techniques de moulage (sable à prise chimique par impression 3D ou non, sable silico-argileux, moule métallique, cire perdue, ...). Le nouveau procédé d'impression 3D de moules en sable permet de négliger les problématiques de contre-dépouilles. Le procédé de coulée en sable par gravité permet d'obtenir des propriétés mécaniques inférieures de 20 % à celles de la coulée en moule permanent en raison de la faible vitesse de solidification. Il convient de noter que, contrairement à la coulée par gravité et sous pression, la coulée basse pression (LPC) a une vitesse de remplissage contrôlée. De plus, les vitesses pendant les étapes de remplissage sont les mêmes pour la coulée par gravité et par basse pression. Considérant que la coulée par gravité est plus facile et plus pratique à mettre en œuvre, la coulée rapide par gravité est étudiée dans cette thèse. Les défauts, en particulier l'oxydation qui se produit pendant l'étape de remplissage, sont un problème sérieux dans la coulée par gravité. Pendant la phase de remplissage de la coulée d'alliage d'aluminium, certains défauts généraux tels que le défaut de coulée incomplète, l'inclusion, le défaut de soudure froide et l'oxydation se forment. L'oxydation est un défaut plus difficile à traiter car les oxydes se forment lorsque est exposé à l'air. Différents paramètres pour traiter le défaut d'oxydation pendant le procédé de remplissage sont fournis après un examen approfondi. Il convient de mentionner que

la diminution de la vitesse et de l'oscillation pendant l'étape de remplissage a été documentée par plusieurs recherches et pourrait augmenter le taux de formation d'oxydation. Pour anticiper le défaut d'oxydation tout au long du procédés de coulée, les phases de coulée doivent être correctement simulées, notamment le remplissage, le refroidissement et la solidification.

Des techniques de simulation numérique des écoulements multiphasiques de de surface libre sont souvent nécessaires pour éviter la procédure d'essai-erreur et réduire les coûts. La méthode VOF (Volume Of Fluide - généralement utilisé dans les logiciels commerciaux), la technique du Level Set et la méthode du front tracking ont été étudiées pour suivre les métaux en fusion sur la base de l'approche eulérienne. Ces approches sont incapables d'enregistrer directement la surface et l'interface entre des fluides. La prédiction des défauts d'oxydation à l'aide de l'approche eulérienne est difficile et prend du temps en raison de la qualité du maillage et de la saisie de la surface libre du fluide.

Les approches lagrangiennes peuvent permettre de prédire les problèmes d'oxydation pendant la phase de remplissage car elles peuvent porter l'historique de chaque particule pour déterminer si elle a été exposée à l'air pendant la phase de remplissage. La méthode des points finis (FPM) et l'hydrodynamique des particules lissées sont deux méthodes sans maillage qui pourraient être utilisées pour simuler le procédé de coulée car elles sont simples à appliquer et ne nécessitent pas de cellules de fond ou d'intégrales. En raison de travaux antérieurs effectués au laboratoire LIFSE, l'approche SPH est préférée à la méthode FPM. Elle présente certains avantages distincts, tels que la capacité à modéliser l'écoulement à surface libre, ce qui pourrait permettre de prédire l'oxydation. Plusieurs études ont été menées en utilisant l'approche SPH pour modéliser le remplissage et la solidification de la coulée par gravité, basse pression et haute pression, ainsi

que la prédiction de l'oxydation. Cependant, peu de recherches ont été menées pour modéliser le procédé de coulée en utilisant l'approche SPH, impliquant les procédés de remplissage et de solidification, ainsi que la prédiction simultanée des défauts d'oxydation.

En résumé, l'objectif de la thèse est d'étudier et de maîtriser les procédés de remplissage, de refroidissement et de solidification dans la coulée gravitaire en sable pour les alliages légers, en utilisant un moule obtenu par impression 3D pour établir les circonstances de la prédiction de l'oxydation. *Pour atteindre cet objectif, le code SPH de la coulée en 2D développé par les experts de LIFSE doit être amélioré et mis à niveau pour modéliser le remplissage, le refroidissement et la solidification de la coulée rapide par gravité en 2D et 3D. La description complète de la technique SPH, ainsi que ses multiples méthodologies pour le 2D et le 3D, sont examinées dans le chapitre (2). L'un des accomplissements de cette thèse est l'introduction et le développement d'un cas test expérimental qui peut être utilisé pour reproduire le processus de remplissage et de solidification en deux dimensions, qui est abordé en profondeur dans le chapitre (3). En outre, afin de valider les résultats de remplissage, de refroidissement et de solidification de la simulation numérique du code SPH 3D et de l'application de logiciels commerciaux, une expérience plus réaliste utilisant du verre transparent qui reproduit le processus de coulée par gravité a été réalisée dans le chapitre (4).*

1.8 References

[1] R. Davami, P. Tavakoli, "Feeder growth: a new method for automatic optimal feeder design in gravity casting processes," *Structural and Multidisciplinary Optimization,* vol. 39, p. 519–530, 2009.

[2] A. Sanitas, M. Bedel, M. El Mansori, "Experimental and numerical study of section restriction effects on filling behavior in low-pressure aluminum casting," *Journal of Materials Processing Tech.,* vol. 254, pp. 124-134, 2018.

[3] F. Bonollo, N.Gramegna, G. Timelli, "High-Pressure Die-Casting: Contradictions and Challenges.," *JOM,* p. 901–908, 2015.

[4] J. Campbell, Castings, Butterworth-Heinemann: Oxford, 2003.

[5] C. M. Choudhari, B. E. Narkhede, S. K. Mahajan, "Casting Design and Simulation of Cover Plate using AutoCAST-X Software for Defect Minimization with Experimental Validation," *Procedia Materials Science,* vol. 6, p. 786 – 797, 2014.

[6] M. C. Choudhari, J. K. Padalkar, K. K. Dhumal., E. B Narkhede, K. S. Mahajan, "Defect free casting by using simulation software," *Applied Mechanics and Materials,* Vols. 313-314, pp. 1130-1134, 2013.

[7] C. M. Choudhari, B. E. Narkhede, S. K. Mahajan, "Finite Element Simulation of Temperature Distribution during Solidification in Cylindrical Sand Casting with Experimental Validation," in *4th International and 25th All India Machine Tool Design and Research*, Jadavpur University, Kolkata, India, 2012.

[8] F. Y. Hsu, M. R. Jolly and J. Campbell, "Vortex-gate design for gravity casting," *International Journal of Cast Metals Research,* vol. 19, no. 1, pp. 38-44, 2006.

[9] B. Sirrell, M. Holiday and J. Campbell, "Proc. 7th Conf on "Modeling of casting, welding and advanced solidification processes"," in *Warrendale, PA, TMS 1995*, 915-921, 1995.

[10] D. R. Gunasegaram, D.J. Farnsworth, T.T. Nguyen, "Identification of critical factors affecting shrinkage porosity in permanent mold casting using numerical simulations based on design of experiments," *journal of materials processing technology,* vol. 209, pp. 209-219, 2009.

[11] R.Hummer, "Relationship between Cooling and Dilatation Curves of Ductile-iron Melts and their Shrinkage Tendency," *Cast metals,* no. 2, pp. 62-68, 1988.

[12] A.W Ayoola, O.S Adeosun, O.S Sanni, O.S., A.Oyetunji,, "Effect of casting mould on mechanical properties of 6063 Aluminium alloy," *Journal of Engineering Science and Technology,* vol. 7, no. 1, 2012.

[13] Ajay Bhardwaj, Mahesh V. Rawlani, C.K Mukherjee, "Permanent Mold Casting" Excellent Casting Method for Manufacture of Automotive Components," *International Journal on Recent and Innovation Trends in Computing and Communication,* vol. 2, no. 8, p. 2254 – 2255.

[14] F. R. Elsayed, N. Hort, M.A. Salgado-Ordorica and K. Kainer, "Magnesium Permanent Mold Castings Optimization," *Materials Science Forum,* vol. 690, pp. 65-68, 2011.

[15] F. Bonollo, J. Urban, B. Bonatto, M. Botter, "Gravity and low pressure die casting of aluminium alloys: a technical and economical benchmark," *La Metallurgia Italiana,* 2005.

[16] Guofa MI, Hengtao ZHAO, Kuangfei WANG, Zhian XU, Jitai NIU, "Simulation of Mold Filling and Solidification on Gravity Casting of Al-Si Alloy (A357)," *Materials Science Forum,* Vols. 575-578, pp. 1204-1209, 2008.

[17] A. A.Lou, "Magnesium casting technology for structural applications," *ournal of Magnesium and Alloys 1,* pp. 2-22, 2013.

[18] Heqian Song, Lunyong Zhang, Fuyang Cao, Xu Gu, Jianfei Sun, "Oxide bifilm defects in aluminum alloy castings," *Materials Letters,* vol. 285, 2021.

[19] P. D. Ingle, B. E. Narkhede, "A Literature Survey Of Methods To Study And Analyze The Gating System Design For Its Effect On Casting Quality," *Materials Today: Proceedings,* vol. 5, pp. 5421-5429, 2018.

[20] Shashank V. Gulhane, Rahul M. Dahekar, "To Improve Productivity for Casting Technology By Reducing Weight of Gating System," *International Journal of Engineering Research & Technology,* vol. 3, no. 10, 2014.

[21] Ramsuddin Sulalman and Tram Chee Keen, "Flow analysis along the runner and gating system of a casting process," *Technology, Journal ofMaterials Processing,* vol. 63, pp. 690-695, 1997.

[22] R.A. Harding, M. Wickins, H. Wang, G. Djambazov, K.A. Pericleous, "Development of a turbulence-free casting technique for titanium aluminides," *Intermetallics,* vol. 19, pp. 805-813, 2011.

[23] Carlos E. Esparza, Martha P. Guerrero-Mata , Roger Z. Rı´os-Mercado, "Optimal design of gating systems by gradient search methods," *Computational Materials Science,* vol. 36, pp. 457-467, 2006.

[24] J. Campbell, , Mini Casting Handbook. (Aspect Design), 2018.

[25] M. Papanikolaou, E.Pagone, M.Jolly M and K.Salonitis, Numerical Simulation and Evaluation of Campbell Running and Gating Systems Metals, Basel, 2020.

[26] Jan Jezierski, Rafał Dojka and Krzysztof Janerka, "Optimizing the Gating System for Steel Castings," *Metals,* vol. 8 (4), no. 266, 2018.

[27] A. Sanitas, M. Bedel, S. Khelladi and M.El Mansori, "Mastering of the Filling Stage in Low Pressure Sand Casting Process," *Materials Science Forum,* vol. 941, pp. 2306-2312, 2018.

[28] F. J. Edler, G. Lagrené, R. Siepe, "Thin-walled Mg Structural Parts by a Low-pressure Sand Casting Process," *In book: Magnesium Alloys and their Applications,* 2006.

[29] Shan-Guang Liu, Fu-Yang Cao, Tao Ying, Xin-Yi Zhao, Jing-Shun Liu, Hong-Xian Shen, Shu Guo, And Jian-Fei Sun, "Formation Mechanism of Surface Crack in Low Pressure Casting of A360 Alloy," *Metallurgical and materials transactions B,* vol. 48, no. 6, pp. 1-10, 2017.

[30] Z.-T. Fan and S.Ji, "Low pressure lost foam process for casting magnesium alloys," *Materials Science and Technology,* vol. 21, no. 6, pp. 727-734, 2013.

[31] Jianglan Duan, Daan Maijer, Steve Cockcroft, and Carl Reilly, "Development of a 3D Filling Model of Low-Pressure Die-Cast Aluminum Alloy Wheels," *Metallurgical and Materials Transactions A,* vol. 44A, no. 12, 2013.

[32] Abhilash Viswanath, M.V. Manu, S. Savithric, U.T.S. Pillai, "Numerical simulation and experimental validation of free surface flows during low pressure casting process," *Journal of Materials Processing Technology,* vol. 244, pp. 320-330, 2017.

[33] M. Schmid , F.Klein, "Fluid flow in die-cavities: Experiments and numerical simulation," *Proceedings of the 18th International Die Casting Congress and Exposition,* pp. 93-97, 1995.

[34] D.Apelian, M. Di Sabatino L. Arnberg, "Progress on the understanding of fluidity of aluminium foundry alloys," *International Journal of Metalcasting,* vol. 2, pp. 17-27, 2008.

[35] M. Hartlieb, J. Major, "Advances in aluminum foundry alloys for permanent and semi-permanent mold casting," *International Journal of Metalcasting,* vol. 3, pp. 43-53, 2009.

[36] B.Sorte.Madhukar, "Defects, Root Causes in Casting Process and Their Remedies: Review," *Journal of Engineering Research and Application,* vol. 7, no. 3, pp. 47-54, 2017.

[37] V. E. Bazhenov, A. V. Petrova, and A. V. Koltygin, "Simulation of fluidity and misrun prediction for the casting of 356.0 aluminum alloy into sand molds," *International Journal of Metalcasting,* vol. 12, pp. 514-522, 2018.

[38] J. Jakumeit, E. Subasic, M. Bu¨nck, "Shape Casting: 5th International Symposium," (Wiley, San Diego), 2014.

[39] N.J. Humphreys, D. McBride , D.M. Shevchenko, T.N. Croft, P. Withey, N.R. Green, M.Cross, "Modelling and validation: Casting of Al and TiAl alloys in gravity and centrifugal casting processes," *Applied Mathematical Modelling,* vol. 37, pp. 7633-7643, 2013.

[40] T.O.Mbuya, , "Element effects on the fluidity of cast Al-Si alloys," *Trans. Am. Foundry Soc,* vol. 163, p. 114, 2006.

[41] M. Di Sabatino, L. Arnberg, "A review on the fludity of AL based alloys," *Metallurgical Science and Tecnology,* 2013.

[42] G.B. Van Der Graaf, H.E.A. Van Den Akker, And L. Katgerman, "A Computational and Experimental Study on Mold Filling," *Metallurgical and Materials Transactions B,* vol. 32, no. 1, pp. 69-78, 2001.

[43] Gowrishankar, J. Yokesh Kumar K. S. Amirthagadeswaran Sripriya, "Casting process optimization for reducing the cold shut defect in casting using response surface methodology," *Indian Journal of Engineering and Materials Sciences,* vol. 22, no. 2, pp. 187-194, 2015.

[44] Mahesh Prakasha, Paul Cleary, John Grandfield, "Modelling of metal flow and oxidation during furnace emptying using smoothed particle hydrodynamics," *journal of materials processing technology,* vol. 209, p. 3396–3407, 2009.

[45] Hua. Wu Haiming. Shi, Haifeng. Liu, Zhenjia.Xia, "Numerical Simulation of Flow Field and Temperature Field on Aluminium Alloy Engine Cylinder in Casting Process," *Materials Science Forum,* Vols. 704-705, pp. 50-57, 2012.

[46] B. Zhang, S.L. Cockcroft, D.M. Maijer, J.D. Zhu, and A.B. Phillion, "Casting Defects in Low-Pressure Die-Cast Aluminum Alloy Wheels," *JOM,* 2005.

[47] Antonin. Sanitas,, "Étude expérimentale et numérique de la coulée basse-pression de l'alliage de magnésium RZ5 dans des moules en sable imprimés en 3D," Ecole nationale supérieure d'arts et métiers-ENSAM, 2016.

[48] John Campbell,, Castings Practice, Butterworth-Heinemann, 2004.

[49] John Campbell, , Castings, Butterworth-Heinemann, 1991.

[50] J.Runyoro, S.M.A.Boutorabi, J.Campbell, "Critical gate velocities for filmforming casting alloys: a basis for process specification," *AFS Trans,* vol. 100, p. 225–234, 1992.

[51] Jingying Sun, Qichi Le, Li Fu, Jing Bai, Johannes Tretter, Klaus Herbold, Hongwei Huo, "Gas entrainment behavior of aluminum alloy engine crankcases during the low-pressure-die-casting process," *Journal of Materials Processing Tech.,* vol. 266, pp. 274-282, 2019.

[52] John Campbell, Complete casting handbook, metal casting processes, metallurgy, techniques and design, Elsevier Butterworth-Heinemann, 2011.

[53] Rafael Cuesta, Angel Delgado, Antonio Maroto, and David Mozo, "Numerically Modeling Oxide Entrainment in the Filling of Castings: The Effect of the Webber Number," *JOM,* vol. 5, pp. 58-62, 2006.

[54] J. Jakumeit, S. Jana, T. Waclawczyk, A. Mehdizadeh, A. Sadiki, J. Jouani, "Four-phase fully-coupled modelling and solidification simulation for gas porosity prediction in aluminum sand casting," *Materials Science and Engineering,* vol. 33, no. 1, 2012.

[55] Shan-guang Liu, Chuan-biao Luo, Guo-ai Li, Wen-lin Gao, Zheng Lu, Sheng-long Dai, "Effect of pressurizing speed on filling behavior of gradual expansion structure in low pressure casting of ZL205A alloy," *Research & Development,* vol. 15, no. 4, p. 276–282, 2018.

[56] Jer-Haur Kuo, Feng-Lin Hsu & Weng-Sing Hwang, "Development of an interactive simulation system for the determination of the pressure-time relationship during the filling in a low pressure casting process," *Science and Technology of Advanced Materials,* vol. 2, pp. 131-145, 2001.

[57] Maciej Kowalczyk* Tomasz A. Kowalewski, Andrzej Cybulski, Tomasz Michałek, "Selected laboratory benchmarks for validating numerical simulation of casting problems," *Numerical Heat Transfer ,* 2005.

[58] B. Minaie, K. A. Stelson , V. R. Voller, "Analysis of Flow Patterns and Solidification Phenomena in the Die Casting Process," *journal of engineering materials and technology,* vol. 113, pp. 296-302, 1991.

[59] Wen-Jiong Cao, Zhao-Yao Zhou, Fang-Ming Jiang, "Smoothed particle hydrodynamics modeling and simulation of foundry filling process," *Trans. Nonferrous Met. Soc. China,* vol. 25, pp. 2321-2330, 2015.

[60] M. Masoumi, H. Hu, J. Hedjazi, M.A. Boutorabi,, "Effect of gating design on mold filling," *AFS Trans,* vol. 152, pp. 1-12, 2005.

[61] Ictor Anjo and Reyaz Khan, "Gating System Design for Casting thin Aluminium Alloy (Al-Si) Plates," *Leonardo Electronic Journal of Practices and Technologies,* no. 23, pp. 51-62, 2013.

[62] Marek Bruna, Dana Bolibruchova , Richard Pastircak, and Anna Remisova, "Gating System Design Optimization for Investment casting process," *Journal of Materials Engineering and Performance,* vol. 28, p. 3887–3893, 2019.

[63] R.Van Tol, L.Katgerman and H.E.A Van den akker, "Experimental and numerical investigations of mould filling of thin wall horizontal aluminum casting," *Material science forum ,* Vols. 329-330, pp. 461-466, 2000.

[64] S Abdullah, D T Gethin and F Bell, "An experimental investigation of the filling of a thin section casting and simulation by the finite element method," *Proc instn mech engrs,* vol. 212 Part B, 1998.

[65] Ondrej Bublık, Libor Lobovsky, Vaclav Heidler, Tomas Mandys and Jan Vimmr, "Experimental validation of numerical simulation of free-surface flow within casting mold cavities," *Engineering Computations,* vol. 38, pp. 4024-4046, 2021.

[66] Tommy carozzani, charles-andre´ gandin, hugues digonnet, michel bellet, kader zaidat, and yves fautrelle, "Direct Simulation of a Solidification Benchmark Experiment," *Metallurgical and materials transactions a,* vol. 44A, 2013.

[67] B. Sirrell, M. Holliday, and J. Campbell, "Benchmark Testing the Flow and Solidification Modeling of AI Castings," *JOM,* vol. 48, pp. 20-23, 1996.

[68] U.Chandra, "Benchmark problems and testing of a finite element code for solidification in investment castings," *International Journal For Numerical Methods In Engineering,* vol. 30, pp. 1301-1320, 1990.

[69] Ik-Tae Im, Woo-Seung Kim, Kwan-Soo Lee, "A Unified analysis of filling and solidification in casting with natural convection," *International Journal of Heat and Mass Transfer,* vol. 44, pp. 1507-1515, 2001.

[70] K-O.Yu, Modeling for casting and solidification processing, CRC Press, 2001.

[71] N.R. Eyres, D.R. Hartree, J. Ingham, J.R. Sarjant and J.B Wagstaff , "The calculation of variable heat flow in solids," *Philos. Trans. R. Soc. London. Ser. A, Math. Phys. Sci,* vol. 240, pp. 1-57, 1946.

[72] S. Sulaiman, A.M.S. Hamouda, "Modelling and experimental investigation of solidification process in sand casting," *Journal of Materials Processing Technology,* Vols. 155-156, pp. 1723-1726, 2004.

[73] P.D. Lee, A. Chirazi, D. See, "Modeling microporosity in aluminum–silicon alloys: a review," *Journal of Light Metals 1,* pp. 15-30, 2001.

[74] C. W. Hirt and B.D.Nichols, "Volume of Fluid (VOF) Method for the dynamic of free boundaries," *Journal of computational physics,* vol. 39, no. 1, pp. 201-225, 1981.

[75] S. Osher and R. P.Fedkiw, "Level set methods: an overview and some recent results," *Journal of Computational physics,* vol. 169, no. 2, pp. 463-502, 2001.

[76] G. Tryggvason, B. Bunner, A. Esmaeeli, D. Juric, N. Al-Rawahi, W. Tauber, J. Han, S. Nas, and Y.-J. Jan, "A front-tracking method for the computations of multiphase flow," *Journal of Computational Physics,* vol. 169, no. 2, pp. 708-759, 2001.

[77] S. O. Unverdi and G.Tryggvason,, "A front-tracking method for viscous, incompressible, multi-fluid flows," *ournal of computational physics,,* vol. 100, no. 1, pp. 25-37, 1992.

[78] C.W. Hirt, B.D. Nichols, "Volume of fluid method for the dynamics of free boundaries," *J. Comp. Phys,* vol. 39, pp. 201-225, 1981.

[79] Paul Cleary, Joseph Ha, Vladimir Alguine, Thang Nguyen, "Flow modelling in casting processes," *Applied Mathematical Modelling,* vol. 26, pp. 171-190, 2002.

[80] Listy Stephen, Anoop Jose, "An Overview of Surface Tracking and Representation in Fluid Simulation," *International Journal of Advanced Computer Science and Applications,* vol. 11, no. 6, 2015.

[81] X.Yang, X. Huang, X. Dai, J. Campbell and J. Tatler, "Numerical modelling of entrainment of oxide film defects in filling of aluminium alloy casting," *International Journal of CastMetals Research,* vol. 17, no. 6, pp. 321-331, 2004.

[82] Hassan Iqbal, Anwar K. Sheikh, AbdulHadi Al-Yousef, and M. Younas, "Mold Design Optimization for Sand Casting of Complex Geometries Using Advance Simulation Tools," *Materials and Manufacturing Processes,* vol. 27, pp. 775-785, 2012.

[83] C. Reilly, N.R. Green , M.R. Jolly , J.-C. Gebelin, "The modelling of oxide film entrainment in casting systems using computational modelling," *Applied Mathematical Modelling,* p. 8451–8466, 2013.

[84] Shan-Guang Liu, Fu-Yang Cao, Xin-Yi Zhao, Yan-Dong Jia,Zhi-Liang Ning, Jian-Fei Sun, "Characteristics of mould filling and entrainment of oxide film in low pressure casting of A356 alloy," *Material and Scieb Engeeniring,* vol. 626, pp. 159-164, 2015.

[85] Pei-Hsing Huang, Wei-Jen Wu, Chung-Han Shieh, "Compute-Aided Design of Low Pressure Die-Casting Process of A356 Aluminum Wheels," *Applied Mechanics and Materials,* vol. 864, pp. 173-178, 2017.

[86] Ya'nan Wu, Guojie Huang Lei Cheng Daniel Liang, Wei Xiao, "Numerical Simulation on Filling Optimization of Copper Rotor for High Efficient Electric Motors in Die Casting Process," *Materials Science Forum,* vol. 898, pp. 1163-1170, 2017.

[87] S. Osher, J.A Sethian, "Fronts propagating with curvature-dependent speed:," *Journal of Computational,* vol. 79, pp. 12-49, 1988.

[88] J.A. Sethian, Level Set Methods and Fast Marching Methods, Cambridge: second ed. Cambridge University Press, part4, 1999.

[89] S.osher and R.Fedkiw, Level Set Methods and Dynamic Implicit Surfaces, New York: Springer-Verlag part 2 and 4, 2002.

[90] P.Du, Q.LI, D.Li, Y.Li, R.Li, P.Zhang, "Simulating a double casting technique using," *Computational Materials Science,* vol. 22, pp. 200-212, 2001.

[91] H.Ji, D.Chopp, J.E. Dolbow,, "A hybrid extended finite element/level set method for modelling phase transformations," *International Journal for Numerical Methods in Engineering,* vol. 54, pp. 1209-1233, 2002.

[92] Q. Xia, T.Shi, M.Y.Wang, S.Liu,, "A level set based method for the optimization of casting part," *Structural and Multidisciplinary Optimization,* vol. 41, pp. 737-747, 2010.

[93] D. She, R. Kaufman, H. Lim, J. Melvin, A. Hsu and J. Glimm, "Front-Tracking Methods," *Handbook of Numerical Analysis,* vol. 17, pp. 383-402, 2916.

[94] G. Kreziak, C. Rigaut and M. Santarini, "Low pressure permanent mould process simulation of a thin wall aluminium casting," *Materials Science and Engineering,* pp. 255-259, 1993.

[95] Jean-FrancoisHetu and Florin Ilinca, "A finite element method for casting simulations," *Numerical Heat Transfer, Part A,,* vol. 36, pp. 657-679, 1999.

[96] S. McFadden, D.J. Browne, "A front-tracking model to predict solidification macrostructures and columnar to equiaxed transitions in alloy castings," *Applied Mathematical Modelling,* vol. 33, pp. 1397-1416, 2009.

[97] A. Fic, A.J. Nowak, R. Bialecki, "Heat transfer analysis of the continuous casting process by the front tracking BEM," *Engineering Analysis with Boundary Elements,* vol. 24, pp. 215-223, 2000.

[98] Lubomír Klimes , Tomas Mauder, Pavel Charvat, Josef Stetina, "Front tracking in modelling of latent heat thermal energy storage: Assessment of accuracy and efficiency, benchmarking and GPU-based acceleration," *Energy,* vol. 155, pp. 297-311, 2018.

[99] M. J. Berger and P.Colella, "Local adaptive mesh refinement for shock hydrodynamics," *Journal of computational Physics,* vol. 82, no. 1, pp. 64-84, 1989.

[100] Lei Zhang, Hou-Fa Shen, Yiming Rong, Tian-You Huang, "Numerical simulation on solidification and thermal stress of continuous casting billet in mold based on meshless methods," *Materials Science and Engineering A,* vol. 466, pp. 71-78, 2007.

[101] S. N. Atluri, T. Zhu, "A new Meshless Local Petrov-Galerkin (MLPG) approach in computational mechanics," *Computational Mechanics 22,* pp. 117-127, 1998.

[102] S. N. Atluri, T.-L. Zhu, "The meshless local Petrov-Galerkin (MLPG) approach for solving problems in elasto-statics," *Computational Mechanics 25,* pp. 169-179, 200.

[103] E. Onate, S. Idelsohn, O.C. Zienkiewicz, R.L. Taylor, C. Sacco, "A stabilized finite point method for analysis of fluid mechanics problems," *Comput. Methods Appl. Mech. Engrg.,* vol. 139, pp. 315-346, 1996.

[104] L. B. Lucÿ, "A numerical approach to the testing of the fission hypothesis," *The astronomical journal,* vol. 82, 1977.

[105] G R Liu and M B Liu, , Smoothed Particle Hydrodynamics a meshfree particle method, National University of Singapore, 2003.

[106] Mohd Atif, Sheng-Wei Chi, Emanuele Grossi, Ahmed A. Shabana, "Evaluation of breaking wave effects in liquid sloshing problems: ANCF/SPH comparative study," *Nonlinear Dynamics volume,* vol. 97, pp. 45-62, 2019.

[107] M.B. Liu and G.R.Liu, , "Smoothed Particle Hydrodynamics (SPH): an Overview and recent developments," *Arch Comput Methods Eng,* vol. 17, pp. 25-76, 2010.

[108] MP Allen and DJ Tildesley, Computer simulation of liquids, Oxford University Press, Oxford, 1987.

[109] D.Frenkel , B.Smit , Understanding molecular simulation: from algorithms to applications, New York: Academic Press, 2002.

[110] PJ. Hoogerbrugge, J.Koelman, "Simulating microscopic hydrodynamic phenomena with dissipative particle dynamics," .*Europhys Lett,* vol. 19, no. 3, pp. 155-160, 1992.

[111] Warren, Robert D. Groot and Patrick B., "Dissipative particle dynamics: Bridging the gap between atomistic and mesoscopic simulation," *J Chem Phys,* vol. 11, no. 4423, p. 107, 1997.

[112] LB, Lucy, "A numerical approach to the testing of the fission hypothesis.," *Astron J,* vol. 82, no. 12, pp. 1013-1024, 1977.

[113] R.A. Gingold, JJ.Monaghan, "Smoothed particle hydrodynamics—theory and application to non-spherical stars," *Mon Not R Astron So,* vol. 181, pp. 375-389, 1977.

[114] JD, Anderson, Computational fluid dynamics: the basics with applications, New York: McGraw Hill, 2002.

[115] SR. Idelsohn, E. Onate, "To mesh or not to mesh? That is the question," *Comput Methods Appl Mech Eng,* vol. 195, pp. 4681-4696, 2006.

[116] Joseph Ha and Paul W.Cleary,, "Comparison of SPH simulations of high pressure die casting with the experiments and VOF simulations of Schmid and Klein," *International Journal of Cast Metals Research,* 2000.

[117] Paul W. Cleary, Joseph Ha, "Three-dimensional smoothed particle hydrodynamics simulation of high pressure die casting of light metal components," *Journal of light metlas,* pp. 169-183, 2002.

[118] P.W. Cleary, J. Ha , M. Prakash , T. Nguyen, "3D SPH flow predictions and validation for high pressure die casting of automotive components," *Applied Mathematical Modelling,* vol. 30, p. 1406–1427, 2006.

[119] He Yi, Zhou Zhao-Yao, Cao Wen-Jiong, Chen Wei-Ping, "Simulation of mould filling process using smoothed particle hydrodynamics," *Transactions of Nonferrous Metals Society of China,* vol. 21, no. 12, pp. 2684-2692, 2011.

[120] Paul W. Cleary, Gary Savage, Joseph Ha, Mahesh. Prakash, , "Flow analysis and validation of numerical modelling for a thin walled high pressure die casting using SPH," *Computational Particle Mechanics,* vol. 1, p. 229–243, 2014.

[121] M. Y. Hu, J. J. Cai, N. Li, H. L. Yu, Y. Zhang, B. Sun, and W. L. Sun, "Flow modeling in high-pressure die-casting processes using sph model," *International Journal of Metalcasting,* vol. 12, p. 97–105, 2018.

[122] Hitoshi Tokunaga, Yuichi Motoyama, and Toshimitsu Okane, "Particle method simulation for formation and flow of cold flakes in high-pressure die casting," *International Journal of Metalcasting,* vol. 13, p. 897–904, 2019.

[123] Joseph Ha, Paul Cleary, Vladimir Alguine and Thang Nguyen, "Simulation of die filling in gravity die casting using sph and magmasoft," *Second International Conference on CFD in the Minerals and Process Industries,* 1998.

[124] Paul W.Cleary, , "Extension of SPH to predict feeding, freezing and defect creation," *Applied Mathematical Modelling,* vol. 34, p. 3189–3201, 2010.

[125] Tatiana Lysenko, Yuriy Morozov, Kyryll Kreitser, Evgeny Kozishkurt, "Using the sph method for modeling the crystallization process of aluminum alloys," *Engineering Sciences,* vol. 3, no. 55, 2020.

[126] Mahesh Prakash, Joseph Ha, Paul W. Cleary And John Grandfield, "Preliminary sph modelling of oxide formation during the mould filling phase in dc casting of extrusion billets," in *Fifth International Conference on CFD in the Process Industries*, Melbourne, Australia, 2006.

[127] R. Baker, P.W. Nguyen, K. Kirkaldie, "Dross formation during metal transfer operations," *Aluminum Cast House Tech. 4th Australasian Asian Pacific,* p. 109–122, 1995.

[128] N. Birks, G.H.Meier,, Introduction to the high-temperature oxidation of metals, London, UK: Cambridge University Press, 1983.

[129] Xiaofeng Niu, Jingyu Zhao, Baojian Wang, "Application of smooth particle hydrodynamics (SPH) method in gravity casting shrinkage cavity prediction," *Computational Particle Mechanics,* vol. 6, pp. 803-810, 2019.

[130] K Ellingsen, T Coudert and M M'Hamdi, "SPH based modelling of oxide and oxide film formation in gravity die castings," *IOP Conf. Ser.: Mater. Sci. Eng.,* vol. 84, 2015.

[131] S. Marrone, A. Colagrossi, D. Le Touzé, G. Graziani, "Fast free-surface detection and level-set function definition in SPH solvers," *Journal of Computational Physics,* vol. 229, pp. 3652-3663, 2010.

Chapter 2: Experimental and numerical methodologies

Contents

2.1 Introduction

The goal of this chapter is to describe strategies for performing experiments and numerical modeling of the filling and cooling processes in casting, using the commercial program ProCAST and the SPH approach. First, the rapid gravity casting experiment process is presented, which includes alloy preparation, instrumentation, mold printing, and casting. These experiments are based on the foundry platform of ENSAM (École nationale supérieure d'arts et métiers) in Aix-en-Provence. After describing the experimental approach, the numerical simulation based on the ProCAST software is explained. The most important part of this chapter explains the SPH approach and how it is used to simulate the sand gravity casting process. The chapter develops the basic 2D SPH code, which was created by experts in the LIFSE laboratory at ENSAM University, to simulate the filling and solidification of the gravity casting process in both 2D and 3D. The fundamentals of SPH, its methodology, particle organization, integration into governing equations (continuity, momentum, and energy equations), and other SPH methods such as δ-SPH, are clearly explained. The governing equations used to apply SPH in this work are also discussed. Finally, the ProCAST simulation and SPH technique are compared in the last section of this chapter.

Introduction

L'objectif de ce chapitre est de décrire les stratégies de réalisation d'expériences et de modélisation numérique des processus de coulée et de refroidissement, en utilisant le logiciel commercial ProCAST et l'approche SPH. Tout d'abord, le processus d'expérimentation de la coulée gravitaire rapide présenté comprend la préparation de l'alliage, l'instrumentation, l'impression du moule et la coulée. Ces expériences sont basées sur la plateforme de fonderie de

l'ENSAM (École nationale supérieure d'arts et métiers) à Aix-en-Provence. Après avoir décrit l'approche expérimentale, la simulation numérique basée sur le logiciel ProCAST est expliquée. La partie la plus importante de ce chapitre explique l'approche SPH et la manière dont elle est utilisée pour simuler le processus de coulée gravitaire en sable. Le chapitre développe le code SPH 2D de base, qui a été créé par les experts du laboratoire LIFSE de l'Université ENSAM, pour simuler le remplissage et la solidification du processus de coulée par gravité en 2D et 3D. Les principes fondamentaux de SPH, sa méthodologie, l'organisation des particules, l'intégration dans les équations (équations de continuité, de quantité de mouvement et d'énergie), et les autres méthodes SPH telles que δ-SPH, sont clairement expliquées. Les équations utilisées pour appliquer le SPH dans ce travail sont également discutées. Enfin, la simulation ProCAST et la technique SPH sont comparées dans la dernière section de ce chapitre.

2.2 Experiment

When casting experiments are used to validate numerical simulations, they could be carried out in a way that demonstrates simply and perfectly the physics of the casting process. Two vital steps of these experiments are molding and casting, which are described in the following.

2.2.1 Molding

For complicated parts, the recent arrival of the sand mold 3D printing technique tends to replace traditional sand molding [1]. Four main steps are involved in the construction of resin-bonded sand mold with 3DP which are presented in Figure (2-1). The definition of the part in the computer-aided design (CAD) program is the first step (1) in the mold design process. After being designed, the various mold components are exported in STL format for printing. In the next step (2), a 3D

printing machine is used to make the mold using resin - bonded sand. The mold is printed with ExOne S-Print Furan machine with a job box size of $800 \times 500 \times 400 \ mm^3$ [2].

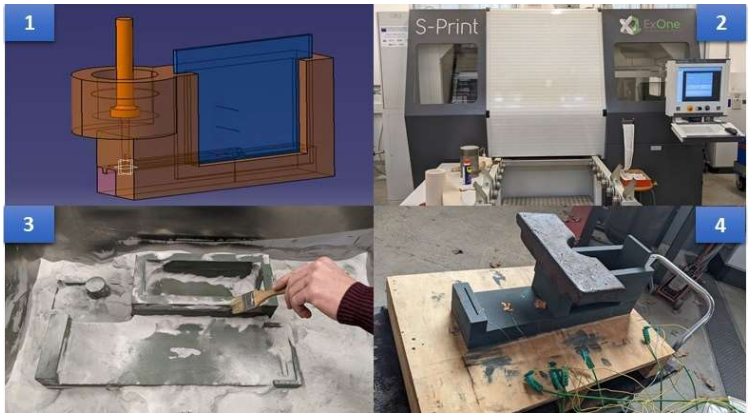

Figure 2-1 - Four main steps of resin - bonded sand molding using 3DP: 1) Design 2) 3DPrinting machine 3) De-molding 4) Instrumentation

The main manufacturing steps of 3D sand printing are shown in Figure (2-2). As a result, the printer produces the sand molds using the sand mixture in successive layers along the z-axis using silica sand with an AFS 97 grain size (average grain size 0.14 mm), also provided by ExoneTM.

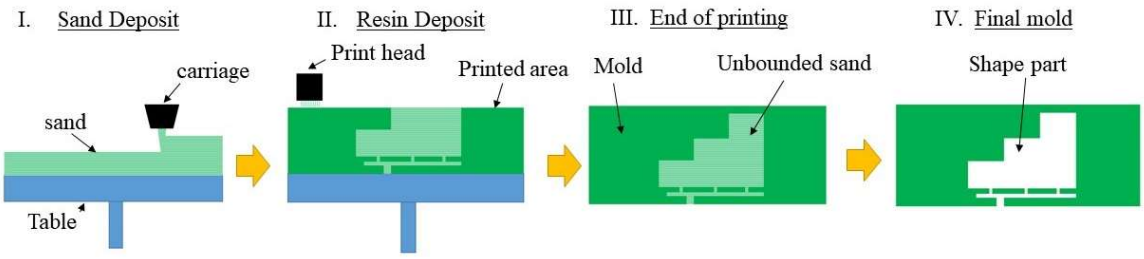

Figure 2-2 - Different steps of 3D printing sand mold [3]

Sand and resin are mixed to create the molds. Firstly, sand is sucked into the machine from the silo, mixed with the catalyst, and loaded into the recoater (sand removal trolley) [1] [4] [5]. After

that job box is installed in the machine with the plate raised, a layer of sand is deposited. In the following, the resin is printed in accordance with the CAD, the plateau is descended by one layer thickness, and the next layer is deposited. Then, the process is repeated as many times as necessary (in accordance with the CAD). The removal of the mold from the job box, which involves sucking up the sand without resin, is the last step. It is crucial to examine and record the filling time and liquid temperature at each individual point in the experiment carried out during the filling and solidification steps of casting process. Regarding instrumentation, Type K thermocouples with 0.5mm diameter are inserted into the molds to record the temperature fields during casting. The K-type thermocouples implemented have accuracy and frequency of $0.0075\times|T^{'}|$, 200Hz, respectively. It is worth noting that $\dot{T}$ refers to maximum temperature. Additionally, the electronic acquisition system was developed in the foundry for the collection of data on metal positions and filling time via electrical contacts placed in the mold. A card for data acquisition and Labview software were used to develop the acquisition system instrumentation. A cable with an initial voltage of 11 V connects metal contacts to the electronic system. A voltage curve representing the monitoring of the level of metal in the mold during filling is obtained by reducing the voltage by 0.05 V at each point where the metal contacts with a bar. Figure (2-3) illustrates the LabVIEW program's window and describes the acquisition principle.

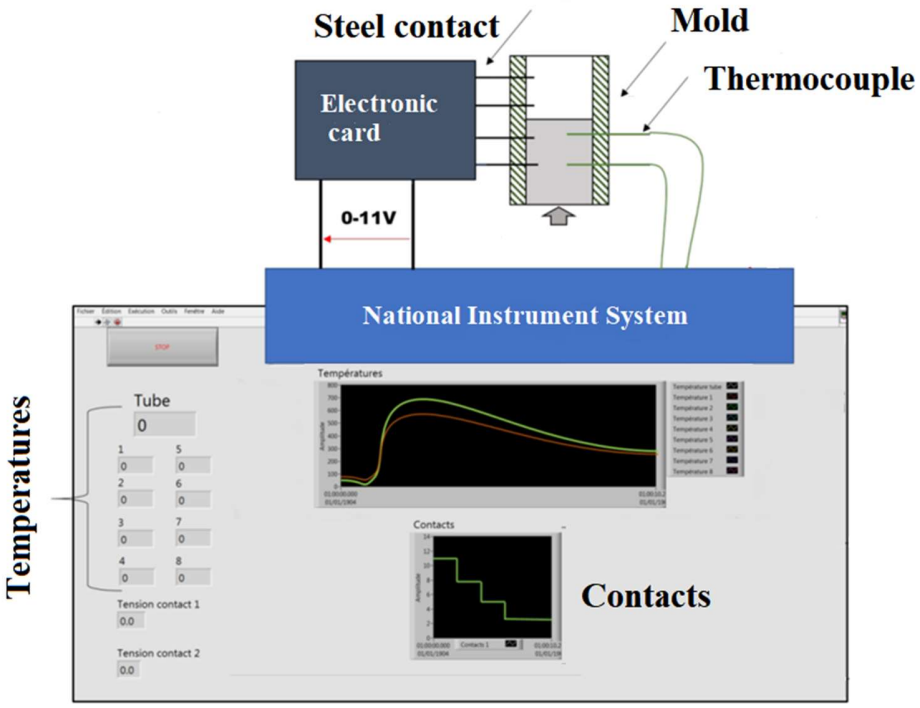

Figure 2-3 - Operating principle of the temperature and acquisition system

2.2.2 Alloy and casting

Casting tests were performed on the AlSi13(EN AC-4400: US designations of the Aluminum Association) alloy. AlSi13 is slightly hypereutectic according to the silicon content of 13 wt% (i.e., the eutectic point of the Al-Si is 12.6 wt%) [6]. The AlSi13 is commonly utilized in foundry because of fluidity, cast ability, corrosion resistance, and crack resistance [7]. Silicon is added to aluminum in order to improve stiffness, wear resistance, and melt fluidity during casting [3]. According to the equilibrium binary diagram, the Si concentration in cast Al-Si alloys changes depending on the alloy composition, which can be hypoeutectic, hypereutectic, or eutectic (Figure (2-4)). According to this figure, the eutectic temperature is 577°C degrees and a temperature

difference between liquidus and solidus temperature is only two degrees. As a result, the solidification process occurs at a reasonably constant temperature.

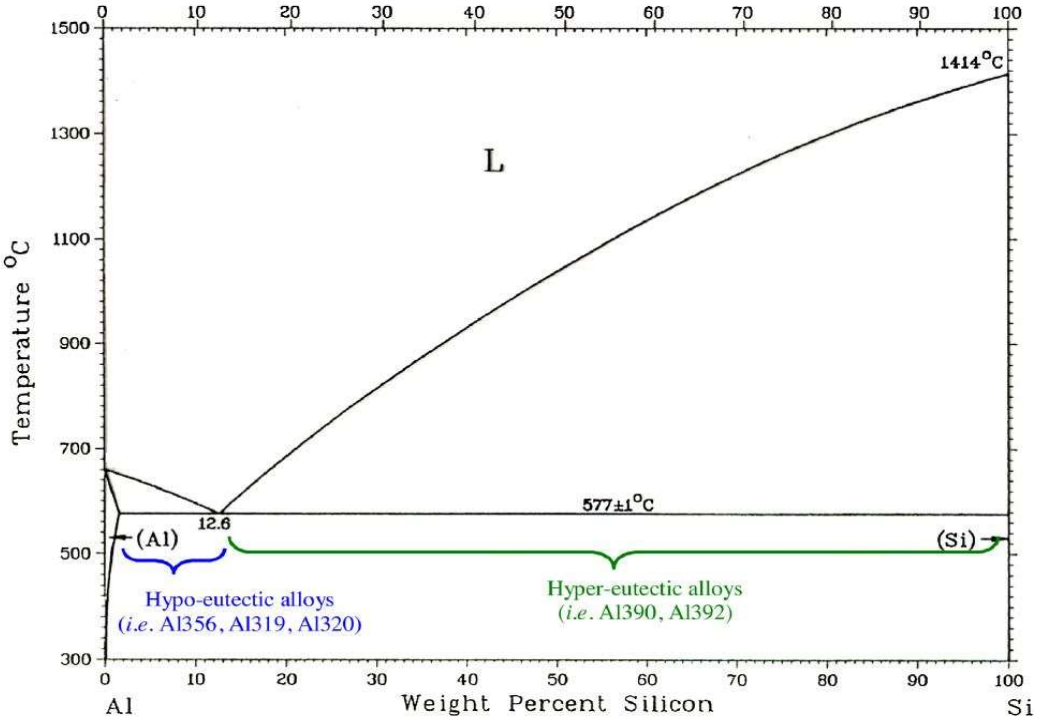

Figure 2-4 - Al-Si phase diagram showing hypo- and hyper-eutectic alloys [8]

In a 12Kw resistance furnace (type: NPG.45, voltage: 380 V, current: 19 A) at 750°C, AlSi13 is melted (Figure (2-5)). molten metal was extracted out of the furnace with a ladle and poured at a temperature between 650°C and 750°C. The filling step is then carried out manually using a ladle. The casting process's furnace and pouring step are represented in Figure (2-5).

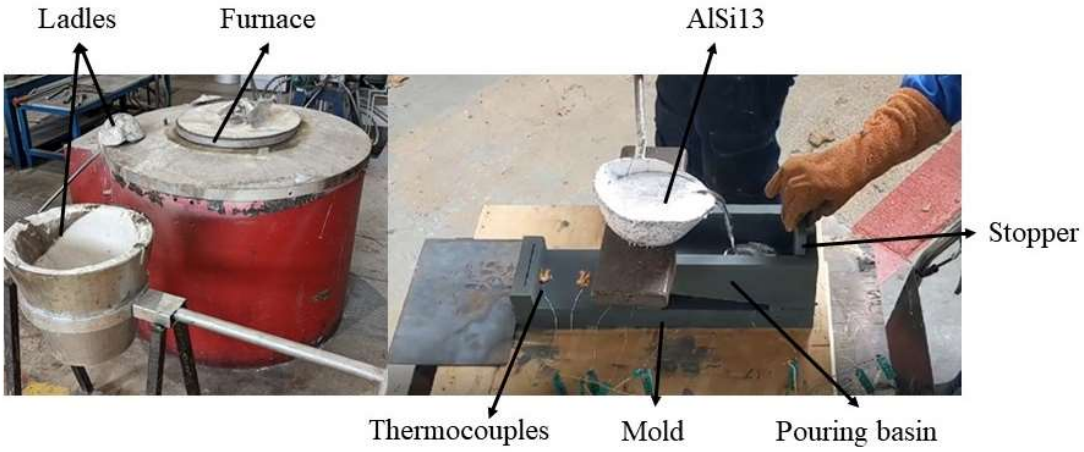

Figure 2-5 - Left) Furnace, Right) Manual pouring of casting process

2.3 ProCAST

ProCAST, a commercial software by ESI group, is a well-known user-friendly simulation tool for casting processes that are widely used in industrial companies and academic institutions around the world. ProCAST is based on finite element method to model casting process for most castable alloys and casting techniques such as sand casting, die casting, and investment casting. In this work, the simulations are using ProCAST version 2021 and Visual Environment 17.5.

2.3.1 ProCAST model

ProCAST is used to undertake a three-dimensional thermal-hydraulic simulation of AlSi13 alloy gravity casting in a resin-bonded sand mold [9] [10]. It should be highlighted to make a 2D simulation with ProCAST, one dimension must be addressed symmetrically, after which its impact can be ignored. Furthermore, the solidification process is applied to the momentum equation using the increasing viscosity method. In terms of thermal analysis, ProCAST employs temperature as

the major variable in modeling energy equations. Even though density changes with temperature, the flow of molten metal is incompressible since pressure has no impact on it [11] [12]. The liquid alloy of AlSi13 is a Newton fluid [11] [12]. The whole 3D continuity and Navier-Stokes equations were solved as well as heat conservation to model filling and solidification of gravity casting process [9] [10].

Continuity equation: $$\nabla.\vec{V} = 0 \quad (2\text{-}1)$$

Navier Stokes (Momentum equation): $$\rho\frac{D\vec{V}}{Dt} = \rho\vec{g} - \nabla p + \nabla.(\mu\nabla\vec{V}) \quad (2\text{-}2)$$

Energy equation: $$\rho c_p \frac{DT}{Dt} = \nabla.(k\nabla T) + \rho L\frac{\partial \phi_s}{\partial t} \quad (2\text{-}3)$$

Solidification Path: $$\phi_s = (\frac{T - T_l}{T_l - T_s}) \quad (2\text{-}4)$$

Where V is velocity, ρ is density, $\frac{D.}{Dt}$ is substantial derivative, t is time, g is gravitational acceleration component, P is pressure, μ is dynamic viscosity, c_p is heat capacity, T is temperature, k is thermal conductivity, L is latent heat, and ϕ_s is a solid fraction. The liquidus and solidus temperatures are represented by T_l and T_s, respectively. In ProCAST simulation the solidification path is considered to be linear. In terms of numerical simulation parameters, the minimum time step in ProCAST simulation is at 0.01s, while the maximum time steps in filling and solidification are 0.1s and 1s, correspondingly.

2.3.2 Material properties

To start the simulation for fluid flow and solidification analysis, aluminum alloy (AlSi13) was chosen using a gravity sand casting technique. Table (2-1) shows the thermal properties of the resin-bonded sand and the AlSi13 alloy in ProCAST database. It should be mentioned that the value of Latent heat of AlSi13 is $522kJ/kg$. Additionally, the ProCAST database's liquidus temperature and solidus temperatures are 572°C and 570°C, respectively. Moreover, the density of resin-bonded sand is assumed to be constant. At a temperature of 570 degrees and less than 100 kg.m/s, the quantity of viscosity of AlSi13 increases as molten metal reaches the mushy area. This method allows the viscosity term to take priority over the other terms, stopping fluid movement to simulate the solidification process.

Table 2-1 - Thermal properties of the resin-bonded sand and the AlSi13 alloy in ProCAST database

Temperature $(°C)$	Density $(kg.m^{-3})$	Specific heat $(J.kg^{-1}.K^{-1})$	Conductivity $(W.m^{-1}.K^{-1})$	Viscosity $(kg.m^{-1}.s^{-1})$
Resin-bonded sand properties				
20		670	0.71	
100		800	0.68	
200		920	0.64	
300		883	0.60	
400	1590	1006	0.56	
500		1006	0.53	
600		1006	0.50	
700		1006	0.60	
900		1006	0.73	
AlSi13 alloy properties				
300	2600	1020	151.6	100
450	2578	1130	147	100
550	2563	1200	144	100
570	2560	1210	143.5	100
572	2478	1210	80	0.001
750	2431	1210	80	0.001

2.4 SPH

The goal of this section is to introduce the SPH approach and show how to use it to solve partial differential equations of fluid mechanics. The fluid mechanic equations including continuity, momentum, and energy equations in SPH domain are explained. Additionally, a thorough explanation of how to use fluid mechanic equations in the SPH domain to simulate the filling and solidification steps of gravity casting in two and three dimensions is provided.

The primary objective of this thesis is to enhance the existing 2D SPH approach code developed by specialists from the LIFSE laboratory, which has demonstrated qualitative modeling capability for the casting process. The two-dimensional casting SPH code needs to be modified to effectively replicate the physical characteristics of the rapid gravity casting process for AlSi13, encompassing the various stages of filling, cooling, and solidification. The modification of the existing SPH approach code is initiated by modifying the energy equation to consider latent heat into specific heat. Subsequently, defining the thermophysical properties such as heat capacity, thermal conductivity, and density as a function of temperature for AlSI13 is necessary. The original version of the code employed the Boussinesq approximation in the momentum equation to apply gravity, which proved to be inadequate for simulation due to its unsuitability for compressible flow when temperature variation is wide. Therefore, only gravity was employed in the momentum equation. Different versions of the SPH approach, such as SPH, δ-LES-SPH, and δ-SPH, were employed to model the rapid gravity casting process, including filling, cooling, and solidification. Among the various options, δ-SPH produced the most favorable outcomes and was thus selected. For the 2D simulation, a Runge-Kutta fourth-order time integration method was used. The Matlab software is

used to generate solid and fluid particles in the desired geometry, and numerical parametric studies were conducted to run the simulation.

Converting the code from 2D to 3D is a crucial and intricate aspect of this thesis that necessitates multiple stages. Firstly, the third dimension must be added to all equations, including those of continuity, momentum, energy, displacement of particles, and initial and boundary conditions. Subsequently, kernel function and all mathematical operators, such as gradient, divergence, and Laplacian, must be upgraded to the 3D dimension. It is important to note that in the 3D version of the code, a predictor-corrector time integration method is utilized instead of the Runge-Kutta fourth-order method to reduce the computational time. The predictor-corrector method uses an initial approximation to predict the next step, and then corrects the approximation based on the actual results of the next step. This approach is more efficient for 3D simulations because it requires fewer function evaluations and lower-order approximations than the Runge-Kutta method. Additionally, the distribution of particles and the division of processors for running the code must be adapted for 3D. Ultimately, fluid and solid particles need to be generated using the Matlab software, and the code should be executed and simulated after conducting numerical parametric studies.

In summary, this thesis aims to enhance the SPH approach code to accurately model the casting process. Converting the code from 2D to 3D is a significant undertaking that requires careful attention to detail. By adding the third dimension, upgrading mathematical operators, and adapting particle distribution and processor division, the improved code will provide valuable insights into casting processes that were not previously possible with the 2D version.

The steps for adapting and creating 2D and 3D SPH codes to model the rapid gravity casting process are shown in Figure (2-6). It should be noted that the code is developed and written in C++.

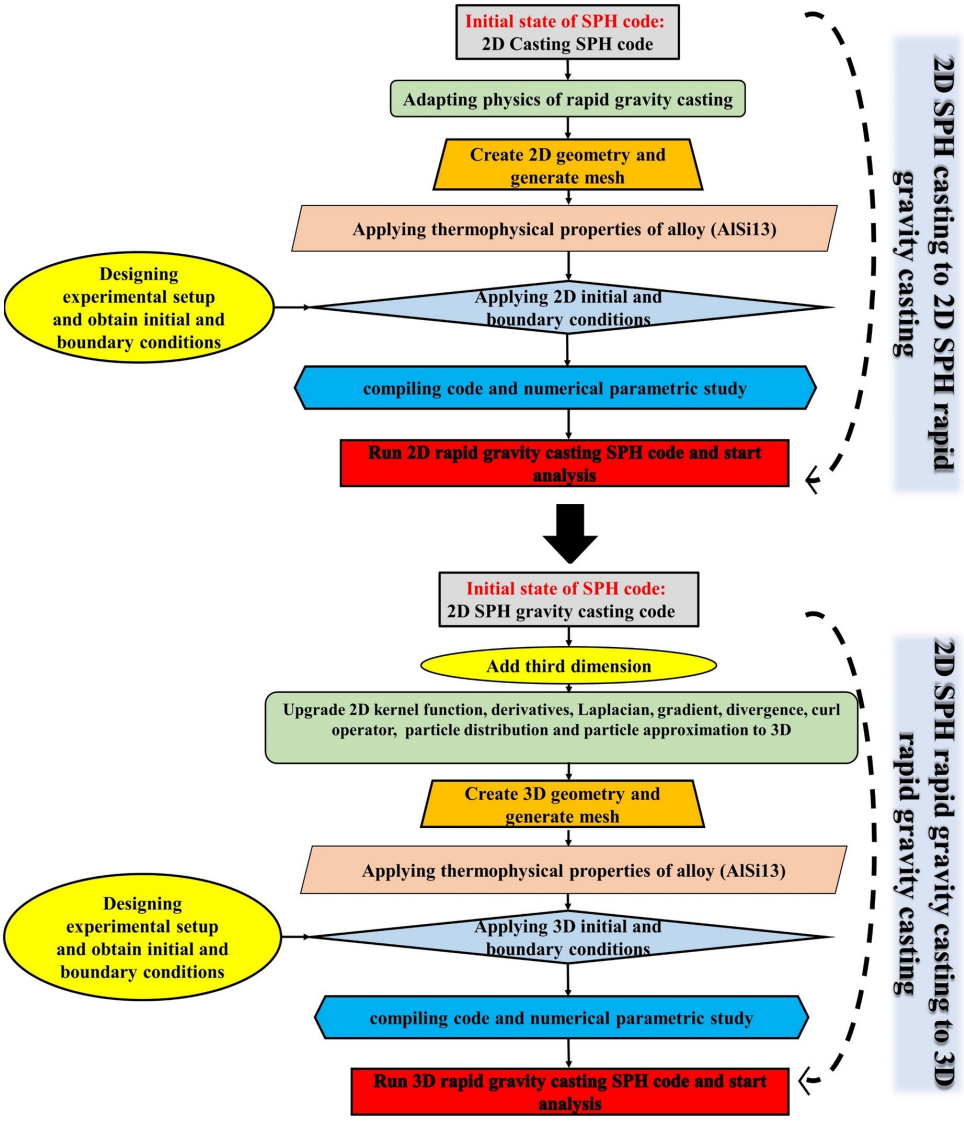

Figure 2-6 - Schematic of the steps to upgrade 2D casting SPH code to 2D and 3D rapid gravity casting SPH code.

2.4.1 SPH approximation techniques

The traditional SPH approach was created for hydrodynamics problems in which the governing equations are in the strong form of partial differential equations with field variables like density, velocity, energy, etc. [13]. In order to achieve SPH formulation, two essential steps are needed. The first step, known as kernel approximation, is to represent a function and/or its derivatives in continuous form as integral representation. The approximation of a function and its derivatives is based on the evaluation of the smoothing kernel function and its derivatives in this kernel approximation [14] [15]. Particle approximation is the term used to describe the second phase. The computational domain is initially discretized in this step by expressing it with a set of initial distributions of particles. Field variables on a particle are approximated after discretization by adding the values of the nearest neighbor particles [13].

2.4.1.1 Kernel approximation of a function

A smoothing function is used to represent a function and its derivatives in the kernel approximation of SPH method. The smoothing function is sometimes known as a kernel, smoothing kernel, smoothing kernel function, or weight function since it would satisfy certain fundamental features [13]. The SPH method begins with the following equation for the kernel approximation of a function $A(r)$.

$$A(r) = \int_{\Omega} A(r')\delta(r - r', h)dr' \tag{2-5}$$

It should be noted that A is a function of r and $\delta(r-r')$ which is the Dirac delta function given by [15]. r represents the position vector of a particle, while r' represents the position vector of a neighboring particle.

$$\delta(r-r')=\begin{cases}1 & r=r' \\ 0 & r\neq r'\end{cases} \tag{2-6}$$

The integral form of $A(r)$ function could be expressed using Equation (2-5). Given that the Dirac delta function is used, the integral formulation in (2-5) is accurate and rigorous as long as $A(r)$ is stated and continuous [13]. Equation (2-5) cannot be utilized to create discrete numerical models since the Delta function $\delta(r-r')$ has only a "point" support. The kernel approximation obtains when the Delta function $\delta(r-r')$ is replaced by a smoothing function $W(r-r',h)$ with a limited spatial dimension h [13].

$$<A(r)>=\int_{\Omega} A(r')W(r-r',h)dr' \tag{2-7}$$

W Represents the kernel function, while dr' showing a differential volume element in Equation (2-7). In addition, h define the influence or support area of the smoothing function W. Even function is the most used smoothing function [13]. Kernel function must meet certain conditions.

The first one is a normalizing condition [15].

$$\int_{\Omega} W(r-r',h)dr'=1 \tag{2-8}$$

As the smoothing length approaches zero, the presence of the delta function property is the second condition.

$$\lim_{h\to 0} W(r-r',h)=\delta(r-r') \tag{2-9}$$

The compact condition is the last one.

$$W(r-r',h)=0 \text{when} \mid r-r' \mid > \kappa h \tag{2-10}$$

κh defines the effective area of the smoothing function. This effective area is called the support domain for a point at r. Integration across the whole issue domain is localized as integration over the support domain of smoothing function. As a result, the integration domain and the support domain can be the same. The kernel approximation is frequently referred to as having h^2 accuracy or second-order accuracy in the SPH literature [13] [15].

2.4.1.2 Kernel approximation of derivatives

By simply substituting $\nabla.A(r)$ within Equation (2-7), the estimate for the spatial derivative is achieved [13].

$$<\nabla.A\ (r)>=\int_{\Omega}[\nabla.A(r')]W(r-r',h)dr' \tag{2-11}$$

Where the divergence of integral is calculated with respect to the primed coordinate [13]. Taking

$$[\nabla.A(r')]W(r-r',h)=\nabla.[(A(r')W(r-r',h)]-A(r').\nabla[W(r-r',h)] \tag{2-12}$$

The following equation can be found [13].

$$\nabla.A(r)=\int_{\Omega}\nabla.[(A(r')W(r-r',h)]-\int_{\Omega}A(r').\nabla[W(r-r',h)] \tag{2-13}$$

The divergence theorem could be used to convert the first integral on the right hand side (RHS) of (2-13) into an integral over the surface S of the domain of integration Ω, as follows:

$$<\nabla.A(r)>=\int_S A(r')W(r-r',h).\vec{n}dS-\int_\Omega A(r').\nabla[W(r-r',h)] \quad (2\text{-}14)$$

Where $\vec{n}$ is the normal to the surface S unit vector. In SPH, the value of W on the surface of the integral in (2-14) is zero because the smoothing function W is commonly designed to have compact support [13]. As a result, the right-hand side surface integral of (2-13) is zero. Hence, the derivatives kernel approximation could well be stated:

$$<\nabla.A(r)>=-\int_\Omega A(r').\nabla[W(r-r',h)] \quad (2\text{-}15)$$

The spatial gradient of a field function could be calculated using the values of function and the derivatives of the smoothing function W [13]. It should be mentioned that this equation is not verified close to the boundaries. The derivative kernel approximation is also of second-order accuracy [13]. By substituting $A(r)$ with the relevant derivatives in (2-7), utilizing integration by parts, the divergence theorem, and some basic transformations, kernel approximation of higher order derivatives could be produced in a similar fashion.

2.4.1.3 Particle approximation

The particle approximation is the second phase of the SPH technique, which entails describing the problem domain with a collection of particles and then estimating field variables using this set of particles. Figure (2-7) shows a two-dimensional problem domain with a collection of randomly distributed particles [13].

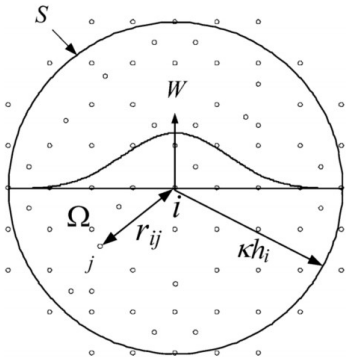

Figure 2-7 - SPH particle approximations in a two-dimensional problem domain with a surface S . W is the smoothing function used to estimate the field variables at particles i using averaged summations across particles j inside the support domain with a cut-off distance of κh [13] .

The state of the system is composed of these particles, each of which has a unique set of field characteristics. These particles can be used to represent the material as well as for integration, interpolation, and differences. The volume of a subsection is lumped on the particle that corresponds to it. As a result, one particle i is linked to a fixed lumped volume ΔV_i that has no set form [13]. When it comes to particle mass and density, the lumped volume can alternatively be substituted by the mass to density ratio m_i / ρ_i . The mass $m = \rho_{0Phase} V_0$ of each particle is considered constant during all of the simulation time. Hence, the particle approximation in the SPH approach adds the mass and density of particles into the equations, which is a significant feature [13]. This is most likely one of the main reasons why the SPH approach is so popular for solving dynamic fluid flow issues. It is particularly useful in hydrodynamic issues where density is a crucial field variable [13]. The initial particle volume has been considered as:

$$V_0 = \delta x_0^{\,d} \tag{2-16}$$

In the above equation, δx_0 and d are initial inter-particle distance and space dimension numbers, respectively. After representing the computing domain with a limited number of particles the continuous version of kernel approximation given in (2-7) could be represented in discretized form as a summation of the surrounding particles as follows [13]:

$$< A\ (r) >= \sum_{j=1}^{N} \frac{m_j}{\rho_j} A(r_j) W(r - r_j, h) \tag{2-17}$$

Where N is the total number of particles in the effect region of particle at r. It is the total number of particles in the support domain with a cut-off distance defined by the smoothing length, h, multiplied by a scalar constant κ [13]. Particle approximation is the process of calculating the sum of nearby particles. It shows that the average of the values of the function at all the particles in the support domain, weighted by the smoothing function, can be used to estimate the value of a function at a particle. The particle approximation of a derivative can be derived using the same technique [13].

$$< \nabla . A\ (r) >= -\sum_{j=1}^{N} \frac{m_j}{\rho_j} A(r_j) . \nabla W(r - r_j, h) \tag{2-18}$$

Equation (2-18) indicates that the summation of the function values at all the particles in the support domain weighted by the gradient of the smoothing function could be used to approximate the value of the gradient of a function at a particle situated at r [13]. In Equation (2-17) and Equation (2-18), the particle approximation translates the continuous form of a kernel function field and its derivatives to discrete summations over a collection of particles. **The use of particle summations to approximate the integral is a critical approximation that makes the SPH**

technique easy without requiring the use of a background mesh for numerical integration. The particle approximation is linked to various numerical issues with the SPH approach, such as particle inconsistency and tensile instability, which are discussed in the next sections. The discrete summation is only applied to the particles themselves, for one thing (collocation). To ensure stability and accuracy in mesh free approaches, the number of sampling points for integration should be greater than the number of field nodes (particles).

In the context of SPH, there are also different ways to approximate the second derivative. Some of them are detailed as follows. Taking the first derivative into account, one of them is as follows [16]:

$$\begin{aligned} <\nabla.\nabla A\ (r)>&=-\sum_{j=1}^{N}\frac{m_j}{\rho_j}\nabla A(r_j).\nabla W(r-r_j,h) \\ <\nabla.\nabla A\ (r)>&=-\sum_{j=1}^{N}\frac{m_j}{\rho_j}(\nabla A(r_j)-\nabla A(r_i)).\nabla W(r-r_j,h) \\ <\nabla.\nabla A\ (r)>&=-\sum_{j=1}^{N}\frac{m_j}{\rho_j}(\nabla A(r_j)+\nabla A(r_i)).\nabla W(r-r_j,h) \end{aligned} \tag{2-19}$$

Physical viscosity astrophysical problems [17] [18], 2D heat conduction problems [19] and low-Reynolds number incompressible flows [17] [18] [19] [20] were all studied using these forms. The scheme was used for astrophysical problems by Flebbe et al. [17] and Watkins et al. [18]. Fatehi et al. [21] demonstrated that when these schemes are applied to a heat-like equation with a discontinuous initial condition, oscillatory solutions result. The second derivative of the kernel function can also be used to construct the second derivative.

$$< \nabla.\nabla A\ (r) >= \sum_{j=1}^{N} \frac{m_j}{\rho_j} A(r_j) \nabla.\nabla W(r - r_j, h)$$
$$< \nabla.\nabla A\ (r) >= \sum_{j=1}^{N} \frac{m_j}{\rho_j} (A(r_j) - A(r_i)) \nabla.\nabla W(r - r_j, h) \quad (2\text{-}20)$$
$$< \nabla.\nabla A\ (r) >= \sum_{j=1}^{N} \frac{m_j}{\rho_j} (A(r_j) + A(r_i)) \nabla.\nabla W(r - r_j, h)$$

Fatehi and coworkers [21] demonstrated that for monotonicity to be preserved, the kernel function's inflection point must be farther away from the nearest neighboring particle. Because most smoothing functions have inflection points between $_0$ and $_h$, satisfying the above condition in a complicated flow problem is difficult. It is worth noting that this discussion is only about ordered particles. The form of equation (2-20) is also very sensitive to particle distribution, according to Monaghan [14]. Brookshaw [22] proposed a finite-difference form for the first derivation and an SPH summation for the derivative as

$$< \nabla.\nabla A\ (r) >= \sum_{j=1}^{N} 2 \frac{m_j}{\rho_j} \frac{A(r_i) - A(r_j)}{r_{ij}} e_{ij}.\nabla W(r - r_j, h) \quad (2\text{-}21)$$

Where $r_{ij} = | r_{ij} |$ and $e_{ij} = \frac{r_{ij}}{r_{ij}}$ represents a unit vector in the inter particle direction. Basa et al. [23] demonstrated that this technique is the best for approximating the second derivatives among the available SPH schemes.

SPH discretization can also be used to correct approximations by using higher-order Taylor series approximations [24] [25] or by generating correction terms that require the discrete equations to reproduce linear fields [26] or polynomials up to a certain order [27]. Corrections to second-order derivatives, notably the Taylor series approximations, which entail the computation of all second-

order derivatives, require substantially more effort [28]. The paper presented by Zheng et al [29] summarizes a number of improved methods for modeling the second-order viscosity force term. Schwaiger [28]. proposed a new SPH formulation of the Laplacian operator, which improves the accuracy near free surface boundaries. **In this thesis, the Laplacian operator is applied to the energy equation using this method [28]**.

2.4.1.4 SPH formulation for continuity equation

The flow continuity equation for compressible and incompressible flow is shown in the equations below, respectively [30].

$$\frac{D\rho}{Dt} + \rho\nabla.\vec{V} = 0$$
$$\nabla.\vec{V} = 0 \qquad (2\text{-}22)$$

Where V represents velocity. $\frac{D(.)}{Dt}$ indicate substantial derivative and it is defined as follows in cartesian coordinates.

$$\frac{D(.)}{dt} = \frac{\partial(.)}{\partial t} + u\frac{\partial(.)}{\partial x} + v\frac{\partial(.)}{\partial y} + w\frac{\partial(.)}{\partial z} \qquad (2\text{-}23)$$

It is possible to derive SPH formulations for partial differential equations governing the physics of fluid flows by combining the aforementioned kernel and particle approximation approaches with the relevant numerical strategies. Particle distribution and smoothing length are both dependent on density, which is one of the most important parameters in the SPH approach. Two methods are most commonly used to calculate density. The first is summation density, which has been demonstrated as follows [13] :

$$\rho_i = \sum_{j=1}^{N} m_j W_{ij} \tag{2-24}$$

N shows the number of particles in the support domain of particle i and m_j displays the mas of j particle. In this equation, sub-indexes denote the quantities related to the generic $i-th$ or $j-th$ particle. For example ρ_i and ρ_j refer density of $i-th$ and $j-th$ particle. Another approach to show density is the continuity equation. The SPH continuity equation has been widely utilized because it clearly illustrates that density changes are connected to relative velocity between each particle and other particles in the support domain. For further information, read [15] [31].

$$\frac{D\rho_i}{Dt} = \sum_i m_j (V_i - V_j).\nabla_i W_{ij} \tag{2-25}$$

V_i and $V_j$refer velocity of $i-th$ and $j-th$ particle. Because the locations and velocities show only as differences, this type of continuity equation is known as Galilean invariant. The relative velocity of two particles approaching each other is negative (as is the gradient of the kernel), therefore $\frac{d\rho_i}{dt}$ is positive. If the rate of change is positive, the particle density grows, causing a positive pressure to drive the particles apart once more. When two particles move apart, their densities drop, resulting in a negative pressure that pulls them back together. This interaction of velocity and density/pressure guarantees that the particles are 'on average' evenly spaced. Therefore, the density is close to uniform, resulting in a fluid that is almost incompressible [32]. The summing method conserves very precisely, but the time required for computation is more than that required by the continuity equation, thus the continuity equation is preferred.

2.4.1.5 SPH formulation for momentum equation

Navier-Stokes equation

For Newtonian fluids and incompressible flow, the Navier-Stokes equation is represented by following equation [30]:

$$\rho\frac{D\vec{V}}{Dt}=-\nabla P+\rho\vec{g}+\mu\nabla^2\vec{V} \tag{2-26}$$

Where [30]

$$\nabla\equiv\frac{\partial^2}{\partial x^2}+\frac{\partial^2}{\partial y^2}+\frac{\partial^2}{\partial z^2} \tag{2-27}$$

It should be mentioned that P,g and μ show pressure, gravity, and viscosity, respectively. In component notation, equation (2-26) can be represented as [30]

$$\begin{aligned}
&\rho(\frac{\partial V_x}{\partial t}+V_x\frac{\partial V_x}{\partial x}+V_y\frac{\partial V_x}{\partial y}+V_z\frac{\partial V_x}{\partial z})=-\frac{\partial P}{\partial x}+\rho g_x+\mu\nabla^2V_x\\
&\rho(\frac{\partial V_y}{\partial t}+V_x\frac{\partial V_y}{\partial x}+V_y\frac{\partial V_y}{\partial y}+V_z\frac{\partial V_y}{\partial z})=-\frac{\partial P}{\partial y}+\rho g_y+\mu\nabla^2V_y\\
&\rho(\frac{\partial V_z}{\partial t}+V_x\frac{\partial V_z}{\partial x}+V_y\frac{\partial V_z}{\partial y}+V_z\frac{\partial V_z}{\partial z})=-\frac{\partial P}{\partial z}+\rho g_z+\mu\nabla^2V_z
\end{aligned} \tag{2-28}$$

The basic SPH model employed at the time did not conserve linear and angular momentum, and the SPH model was refined over time. As a result, several modifications to the original SPH technique have been presented. It is worthy to mention that a lot of work has gone into improving accuracy, stability, convergence, and efficiency. Monaghan [14], for example, proposes an SPH

method that preserves both linear and angular momentum. The momentum equation for particle i by adding viscous term shows as follows [31]

$$\frac{DV_i}{Dt} = -\sum_j m_j \left(\frac{p_i}{\rho_i^2} + \frac{p_j}{\rho_j^2} + \Pi_{ij}\right).\nabla_i W_{ij} + F_i \tag{2-29}$$

The summation is done over all of the particles and p , ρ and Π_{ij} represent pressure, density, and viscosity parameter. Body force has been shown by F_i, and it is usually gravity. To conserve linear and angular momentum, the pressure terms were derived from the pressure gradient and expressed in the symmetrized form.

Artificial viscosity

Artificial viscosity, suggested by Neumann-Richtmyer [33], is utilized to eliminate oscillation in hydrodynamic simulations. This artificial viscosity often adds to the pressure term and aids in the diffusion of rapid oscillations. The original SPH technique is used in situations with little or no dissipation. Monaghan and Gingold [31] introduce artificial viscosity to the SPH technique at this time. At the shock front, it transforms kinetic energy into heat and inhibits particle penetration. The viscous term has the general form [31]

$$\Pi_{ij} = \begin{cases} \dfrac{-\alpha c_{ij}\mu_{ij} + \beta\mu_{ij}^2}{\bar{\rho}_{ij}} & v_{ij}.r_{ij} < 0 \\ 0 & v_{ij}.r_{ij} > 0 \end{cases} \tag{2-30}$$

r_i shows the position vector and it is corrected with $\delta^+ - SPH$ method and r_{ij} defines like.

$$r_{ij} = r_i - r_j \tag{2-31}$$

Where

$$\mu_{ij} = \frac{hV_{ij}.r_{ij}}{r_{ij}^2 + \eta^2} \tag{2-32}$$

In these equations the notation A_{ij} and $\overline{A}_{ij}$ show as follows [31]

$$A_{ij} = A_i - A_j \tag{2-33}$$

$$\overline{A}_{ij} = \frac{A_i + A_j}{2} \tag{2-34}$$

Monaghan reported the value of β and α are 0.0 and 0.01 respectively [31]. The term involved α shows both shear and bulk viscosity in the incompressible flow.

2.3.1.6 SPH formulation for Energy equation

The following is the energy equation for incompressible flow without a source, assuming negligible viscous dissipation and constant fluid conductivity [34].

$$\rho c_p \frac{DT}{Dt} = k\nabla^2 T \tag{2-35}$$

Where c_p, k and T represent heat capacity per unit mass when the pressure has been considered constant, thermal conductivity coefficient and temperature. Monaghan demonstrated that the thermal energy per unit mass has altered in the following ways [14]:

$$\frac{Du_i}{Dt} = \frac{1}{2}\sum_j m_j \left(\frac{p_i}{\rho_i^2} + \frac{p_j}{\rho_j^2} + \Pi_{ij}\right) V_{ij}' \nabla_i W_{ij} \tag{2-36}$$

u shows internal energy. V_j presents the volume of $j-th$ particle. The following equation was generated by SPH, and another form of energy equation was developed with temperature directly without heat sources or sinks [14].

$$c_{p,i}\frac{DT_i}{Dt}=\sum_j \frac{m_j}{\rho_i\rho_j}(k_i+k_j)(T_i-T_j)F_{ij} \tag{2-37}$$

This equation can not guarantee that heat flux is continuous when k is discontinued. Cleary and Monaghan [35] represent that this problem could be solved if ($k_i + k_j$) is replaced by:

$$\frac{4k_ik_j}{k_i+k_j} \tag{2-38}$$

Therefore, Monaghan has shown the final SPH heat conduction

$$c_{p,i}\frac{DT_i}{Dt}=\sum_j \frac{m_j}{\rho_i\rho_j}\frac{4k_ik_j}{k_i+k_j}(T_i-T_j)F_{ij} \tag{2-39}$$

The accuracy of this type of SPH form, according to Cleary and Monaghan, is comparable to that of finite difference techniques [35].

2.4.1.7 Moving the particles

Particles are moved in one of two ways, according to Monaghan [14].

$$\frac{dr_i}{dt}=V_i \tag{2-40}$$

Or the XSPH variant (where "X" is the unknown factor) [36]

$$\frac{dr_i}{dt}=\hat{V}_i=V_i+\varepsilon\sum_j m_j(\frac{V_{ji}}{\bar{\rho}_{ij}})W_{ij} \tag{2-41}$$

It should be mentioned that $\bar{\rho}_{ij}=\left(\rho_i+\rho_j\right)/2$ and $\varepsilon(0\le\varepsilon\le1)$ as a constant. The XSPH variation drives a particle at a velocity that is closer to the neighborhood's average velocity. XSPH does not cause dissipation, although it does enhance dispersion. (which can be lowered by changing kernels). In the modeling of almost incompressible fluids like water, the XSPH variation has

proven effective in keeping the particles orderly in the absence of viscosity. In this thesis, Equation (2-40) is used for the moving of the particles.

2.4.1.8 Particle interaction

Only a finite number of particles exist inside the support domain of the relevant particle's dimension κh are used in the particle approximations because the smoothing function has a compact support domain in the SPH technique. These particles are referred to as nearest neighboring particles searching for the particle in issue (NNPS) [37]. Nearest neighboring particle searches (NNPS) is a method of identifying the closest nearby particles. In contrast to a grid-based numerical approach, the nearest adjacent particles in the SPH for a specific particle might change over time.

In SPH applications, three NNPS techniques are commonly used: **all-pair search, linked-list search algorithm, and tree search algorithm.** Only the technique linked-list is discussed here; for more information on alternative ways, see [37]. Figure (2-8) shows the principle of linked list algorithm. For cases when the smoothing length is spatially constant, the linked-list search technique works well. According to Monaghan and Gingold [33] employing cells as a calculation technique can save significant amounts of time in calculation. Because the NNPS procedure is only required for a small group of particles, the computing time may be considerably reduced if all of the particles are allocated to cells and identified using linked lists. Monaghan [38] introduced the linked-list approach for looking for the nearest adjacent particle. In their study of short-range forces in particle simulation approaches, Hockney and Eastwood [39] provided more details on the method. Rhoades [40] proposed a technique for finding the closest nearby particles that are said to be efficient, especially on vector computers. When it came to numerical methodologies for

three-dimensional SPH simulations applied to accretion, Simpson [41] went into great length on the linked-list algorithm. A temporary mesh is layered over the issue domain during the implementation of the linked-list method. The mesh spacing is chosen to fit the support dimensions of domain. The mesh spacing should be set to κh for smoothing kernels with compact support of κh. The nearest neighboring particles for a particular particle i can only be in the same grid cell or the cells directly next to it. As a result, the search for one, two, or three-dimensional space is limited to 3, 9 or 27 cells, respectively.

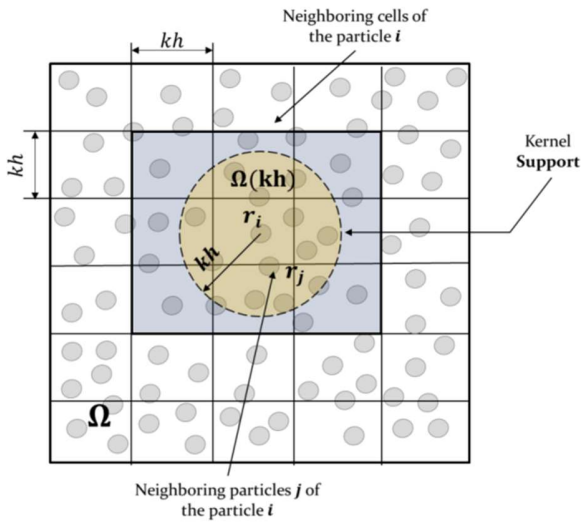

Figure 2-8 - The principle of linked list algorithm [42]

The linked-list technique assigns each particle to a cell and links all of the particles in that cell together for convenient access. The linked-list algorithm's complexity is of order $O(N)$ if the average number of particles per cell is small enough. The difficulty with linked-list approaches is that the mesh spacing may not be ideal for every particle when variable smoothing length is utilized. As a result, it may be less effective [37].

2.4.1.9 Equation of state

The particle pressure is computed using the equation of state and the local particle density to solve compressible flows. One of the most challenging aspects of incompressible flows is calculating the pressure term in the momentum equation. In theory, incompressible flow can be compressed, according to artificial compressibility. Artificial compressibility is used to generate the pressure time derivative [15]. The equation of state was used by Monaghan to simulate free surface flow.

$$P = B((\frac{\rho}{\rho_0})^{\gamma} - 1) \tag{2-42}$$

The value of γ is constant and for this investigation considers as:

$$\gamma = 1 \tag{2-43}$$

B is a parameter that regulates the greatest change in density and is sometimes referred to as starting pressure in some studies. The boundary impact is removed in free surface flows by subtracting 1 from this equation. It is significant to note that even little changes in density can have a significant impact on pressure outcomes.

$$p = c^2 \rho \tag{2-44}$$

The sound of speed is represented by the symbol c. One of the essential parameters in the artificial compressible method is sound speed. If the sound speed is the true value (1480 m/s), this value is enormous, and the Mach number drops to a very tiny value, resulting in little density fluctuation. As a result, the smaller number than the actual sound speed should be utilized to simulate a realistic fluid as an artificial compressible fluid. However, it must be large enough, and the time step must be increased enough. Monaghan proposes the following density variation value [15]:

$$\delta = \frac{\Delta\rho}{\rho_0} = \frac{|\rho - \rho_0|}{\rho_0} = \frac{V_b^2}{c^2} = M^2 \tag{2-45}$$

Where V_b and M refer bulk velocity and Mach number. The change in density is dependent on the bulk velocity, as shown by this equation. When the sound speed is set, the pressure field should be carefully approximated. Morris et al. presented an estimate for sound speed based on the balance of pressure, viscous force, and body force [15] [43].

2.4.1.10 Time integration

The discrete SPH equations, like other explicit hydrodynamic techniques, can be integrated with common methods such as the second order accurate Leap-Frog (LF), predictor-corrector, and Runge-Kutta (RK) schemes, and others. The Leap-Frog (LF) method has the feature of requiring less memory storage during calculation and allowing for one force evaluation per step. In some cases, if the smoothing lengths are very short, the time step might become prohibitively small. During such settings, the Runge-Kutta (RK) integrator with adaptive time-step has been proven to have an advantage [37]. In this approach, adaptive time stepping can be used, with the time step adjusted to minimize an estimate of the integration error within defined tolerances. The CFL requirement asserts that in a numerical simulation, the computational domain of dependence must cover the physical domain of dependence, or the maximum numerical propagation speed must reach the maximum physical propagation speed. The time step has to be proportionate to the shortest spatial particle resolution, which is represented by the smallest smoothing length in SPH applications [37].

$$\Delta t = \min\left(\frac{h_i}{c}\right) \tag{2-46}$$

In equation (2-46), h demonstrate smoothing length. When considering viscous diffusion, Morris et al. [43] proposed another equation for calculating time step.

$$\Delta t = 0.125\frac{h^2\rho}{\mu} \tag{2-47}$$

In this thesis, the two- and three-dimensional SPH simulations are carried out using the Runge-Kutta and predictor-corrector time integration methods, respectively. The issues with the generic SPH method and other methods that are preferable are discussed in the next section.

2.4.2 δ-SPH method

Much effort has been put towards improving the original SPH approach from both a theoretical and numerical standpoint during the previous few decades [44] [45] [46] [47]. As a result, a number of SPH variations have been developed, including the ISPH [44] [48] [49] [50], Riemann-based SPH [44] [51] [52] , higher-order SPH scheme [44] [53], and $\delta - SPH$ [44] [54]. The $\delta - SPH$ model is a weakly compressible SPH version that includes a diffusive term in the continuity equation as well as an artificial viscous term in the momentum equation. The parameters δ and α are used to tune the magnitudes of the two terms. **A good mix of these two coefficients improves the stability** [55]. In the simulation of complex free surface flows and fluid–solid interaction problems, $\delta - SPH$ has proven to be dependable and robust (see e.g. [44] ([56]). The $\delta - SPH$ scheme is simple to implement, and its key advantage over the normal SPH is that it stabilizes the scheme, preventing non-physical energy flux to high frequency modes. The $\delta - SPH$ strategy, as mentioned by Antuono et al. [44] [57], tends to keep the particles in more regular configurations than the normal SPH scheme. Despite the effectiveness of this formulation,

there are still numerous unanswered issues in this SPH model, particularly with regard to so-called tensile instability (see [44] [58]). Another issue is from the Lagrangian nature of SPH method, which causes fluid particles to create non-uniform spatial configurations in flow zones with significant velocity gradients. Morris [44] [59], who performed a stability analysis of the SPH under various pressure situations, came up with the concept of introducing a positive constant pressure to avoid tensile instability. small time steps, the magnitude of the particle shifting is relatively small (in comparison with the incompressible SPH).

2.4.2.1 Continuity equation

In the following lines, the general structure of the SPH scheme is discussed, taking into account the diffusive element in the continuity equation. The basic premise is that fluid is weakly compressible, which leads to the consideration of the linear equation of states. This theoretical analysis is completely universal and can be used for a variety of problems. Under the hypotheses that have been explained above, the continuity equations for $\delta - SPH$ a model are like the following [55].

$$\frac{D\rho_i}{Dt} = -\rho_i \sum_j (V_j - V_i).\nabla_i W_{ij} V_j' + hc_0 \sum_j \delta D_{ij}.\nabla_i W_{ij} V_j' \tag{2-48}$$

The symbol ∇_i represents the gradient taken, which is referred to as the coordinates of the particle i . V_j presents the volume of $j-th$ particle. $c_0$and h represents velocity of sound and smoothing length respectively. The diffusive term which has been shown with D_{ij} . The inclusion of the diffusive element in the continuity equation reduces numerical noise that influences density and, as a result, pressure.

$$D_{ij} = 2[(\rho_j - \rho_i) - \frac{1}{2}(<\nabla\rho>_j^L + <\nabla\rho>_i^L).(r_j - r_i)]\frac{(r_j - r_i)}{|r_j - r_i|^2} \tag{2-49}$$

The symbol $<\nabla\rho>_i^L$ indicates the renormalized density gradient that has been defined as [60]

$$<\nabla\rho>_i^L = \sum_j (\rho_j - \rho_i) L_i \nabla_i W_{ij} V_j' \tag{2-50}$$

$$L_i = [\sum_j (r_j - r_i) \otimes \nabla_i W_{ij} V_j']^{-1} \tag{2-51}$$

δ is a crucial parameter that determines the magnitude of density diffusion [55]. The range of this dimensionless parameter is limited and usually sets to 0.1 in $\delta - SPH$. It is worth noting that if this parameter approaches zero, the system reverts to the regular SPH model.

2.4.2.2 Momentum equation

The equation (2-52) represents momentum equation in $\delta - SPH$ methodology.

$$\frac{DV_i}{Dt} = f_i - \frac{1}{\rho_i}(p_i + p_j)\nabla_i W_{ij} V_j' + hc_0 \frac{\rho_0}{\rho_i} \sum_j \alpha \pi_{ij} \nabla_i W_{ij} V_j' \tag{2-52}$$

Monaghan and Gingold [33] introduced artificial viscosity to the momentum equation to improve stability.

$$\pi_{ij} = \frac{(V_j - V_i).(r_j - r_i)}{(r_j - r_i)^2} \tag{2-53}$$

The momentum equation will be modified to include a viscous dissipation term, with the magnitude of the dissipation indicated by the dimensionless parameter α. In $\delta - SPH$ the value of the α is constant locally, and it is in the range $[0.01 - 0.05]$.

2.4.3 2D and 3D governing equation of SPH methodology for filling, cooling and solidification of gravity casting

The $\delta - SPH$ [55] [61] technique was utilized to solve Navier-Stokes and continuity equations to improve the positions of particles, respectively. Weakly compressible and Newtonian assumptions have been applied to continuity, momentum, energy, and equation of state. It is indeed important to note that the interaction of the particles is **calculated using the linked-list algorithm**. The Runge kutta fourth order and predictor-corrector algorithm are used to integrate system in 2D and 3D, respectively. [62] . Within a radius of 2h and 1.02h, the interpolating Kernel function W controls the interaction between each particle in 2D and 3D, respectively. [63] [64]. It also is worth noting that the kernel functions for 2D and 3D simulation are as follows, respectively:

$$W(r,h)_{2D} = \alpha_{2d} \begin{cases} (1-\frac{r}{2h})^4 (2\frac{r}{h}+1) & 0 \le \frac{r}{h} < 2 \\ 0 & else \end{cases}$$

$$W(r,h)_{3D} = \alpha_{3D} \begin{cases} (3-\frac{r}{h})^5 - 6*(2-\frac{r}{h})^5 + 15(1-\frac{r}{h})^5 & 0 \le \frac{r}{h} < 1 \\ (3-\frac{r}{h})^5 - 6*(2-\frac{r}{h})^5 & 1 \le \frac{r}{h} < 2 \\ (3-\frac{r}{h})^5 & 2 \le \frac{r}{h} < 3 \\ 0 & \frac{r}{h} > 3 \end{cases} \quad (2\text{-}54)$$

Where α_{2D} and α_{3D} is equal to $\frac{7}{4\pi h^2}$ and $\frac{3}{359\pi h^3}$ for 2D and 3D simulation, respectively.

2.4.3.1 Continuity and Momentum equations

In this thesis, **the continuity equation (2-48)** mentioned in section $\delta - SPH$ will be applied directly. The basis of $\delta - SPH$ has been utilized for the momentum equation. It should be noted that solidification simulation requires **additional parameters** to be added to the right-hand side of the momentum equation.

$$\frac{DV}{Dt} = -\frac{\nabla p}{\rho} + \frac{1}{\rho}\nabla.(\mu \nabla V) + g + \frac{A(\phi)V}{\rho}$$
$$\frac{DV_i}{Dt} = -\frac{1}{\rho_i}\sum_j (p_i + p_j)\nabla_i W_{ij} V'_j + hc_0 \frac{\rho_0}{\rho_i}\sum_j \alpha \pi_{ij} \nabla_i W_{ij} V'_j + g_i + \frac{A(\phi_s)V_i}{\rho_i} \quad (2\text{-}55)$$

Enthalpy porosity is one method for simulating the solidification and melting processes [65]. The fluid in this model acts like a porous medium, with three separate zones: a solid area, a liquid section, and a mushy zone that contains both. The essential concept of solidification is that each velocity of each particle decreases progressively from a finite value in the liquid to zero in the solid state. This method assumes that the fluid acts as a porous medium with porosity $\phi =$ ‘‘element liquid fraction ’’. The equation is formulated as follows for all phase-changing particles and is added to the fluid momentum equation to behave in a porous medium, such as Carman-Kozney equations [66]. Brent et al. [65] defined this equation in the situation of solidification and melting under non-isothermal phase change.

$$A(\phi) = -C_A \frac{(1-\phi)^2}{\phi^3 + b} \quad (2\text{-}56)$$

b is a parameter with a small value that prevents division by zero. C_A represents a constant parameter which is 10^3 in this investigation. This constant coefficient controls the amount of

penetration parameter in the convection term. In the case of an isothermal phase change, Brent et al. [65] recommended linear function for A which is

$$A(\phi) = -C(1-\phi) \tag{2-57}$$

It should be mentioned that equation (2-57) is used in this thesis to apply solidification into momentum equation. This linear function has the benefit of having a cheap computing cost. The influence of the porosity function on the momentum equation is discussed in three phases in the following:

- In the full liquid region (i.e., when $\phi=1$), the function A vanishes and then has non-influence on the momentum equation.
- The porosity function has a gradual variation between the liquid and solid sections while in the mushy/regularization region (i.e., when $0<\phi<1$).

- In the full solid region (i.e., when $\phi=0$), the function A will take a tremendous value. As a result, it will swamp out all other terms in the momentum equation over the time variation of the velocity. Therefore, the new anticipated velocity is set to zero.

To complete the momentum equation, the gravity force should be substituted for the body force as a second term.

2.4.3.2 Energy equation

Based on the SPH approach, the following energy equation is developed to describe the cooling and solidification steps of the casting process. The total enthalpy formulation for conduction issue

papering in every single phase (solid, liquid, and mushy phases in the case of solidification of the alloy) of the material that undergoes phase change due to temperature difference is as follows [67]:

$$\frac{DH_i}{Dt} = \nabla.(k_i \nabla T_i) + S_{T_i} \tag{2-58}$$

In equation (2-58) k_i and T_i represent the thermal conductivity and temperature for each particle. S_{T_i} Serves the cooling or heating source term in the solidification and melting process. H_i is total enthalpy which is a function of temperature and it can be expressed in one equation that regroups all phases as a sum of sensible heat h_s and latent heat h_l following [68]

$$H(T) = h_s + h_L = \int_{T_r}^{T} < C > dT + \rho_l \phi L_h \tag{2-59}$$

$L_h$shows latent heat of metal or alloy. T_r represents reference temperature, and the value of it depends on the process type, which is isothermal or non-isothermal. If the phase change process is isothermal (pure material), the amount of reference temperature is equal to the melting temperature $(T_r = T_m)$, else if the phase change phenomena are non-isothermal, the value of T_r is obtained from the average of two liquidus and solidus temperatures $(T_r = \frac{T_s + T_l}{2})$.

This symbol $< . >$ defines as follows

$$< . >= (1-\phi)(.)_s + \phi(.)_l \tag{2-60}$$

C Indicates volumetric heat capacity, which is presented below:

$$C_i = \rho_i c_p \tag{2-61}$$

In equation (2-61), c_p and ρ_l are the specific heat capacity when the pressure is constant and density of each particle, respectively. Volumetric local liquid fraction has been shown by ϕ, and this parameter can be shown as a discontinuous Heaviside step function.

$$\phi(T) = \mathfrak{H}(T - T_m) \tag{2-62}$$

For isothermal phase change, a volumetric local liquid fraction can be employed, or for non-isothermal phase transition, it can be described as a function of temperature that varies smoothly within the melting temperature band. The use of a discontinuous Heaviside step function as a local liquid fraction for naive discretization in numerical simulations of phase transition issues can lead to the prediction of non-physical characteristics such as step-like movement and spurious temperature plateaus [67] [69]. The smooth approach of the fraction function can be utilized to solve both isothermal and non-isothermal phase transition issues [70] [71]. As a result, in the equation below, the regularize volumetric fraction is now stated as a function of temperature.

$$\phi(T) = \begin{cases} 0 & T < T_m - \varepsilon(solid) \\ \frac{1}{2}\{1 + \sin(\pi(\frac{T - T_m}{2\varepsilon}))\} & T_m - \varepsilon \le T \le T_m + \varepsilon(mushy) \\ 1 & T > T_m + \varepsilon(liquid) \end{cases} \tag{2-63}$$

Other functions, such as exponential [71] or hyperbolic-tangent functions [72], can also be used for the regularization of total enthalpy formulation instead of the equation. In equation (2-63), ε represents a smoothing parameter of a Heaviside step function within a region of 2ε . T_m is replaced by the average of T_s(solidus temperature) and T_l (liquidus temperature). By considering that the volumetric capacity C is constant in each phase, a derivative of equation (2-63) towards t has been shown as follows

$$\frac{DH}{Dt} = < C > \frac{DT}{Dt} + \rho_l L \frac{D\phi}{Dt} \tag{2-64}$$

By using the chain rule $\frac{d\phi}{dt}$ becomes an equation like the following:

$$\frac{D\phi}{Dt} = \frac{d\phi}{dT}\frac{DT}{Dt} \tag{2-65}$$

Therefore, the derivative system of equations (2-63) is derived as follows:

$$\frac{d\phi}{dT} = \begin{cases} 0 & T < T_m - \varepsilon(solid) \\ \frac{\pi}{4\varepsilon}\cos(\pi(\frac{T - T_m}{2\varepsilon})) & T_m - \varepsilon \le T \le T_m + \varepsilon(mushy) \\ 0 & T > T_m + \varepsilon(liquid) \end{cases} \tag{2-66}$$

The following is the consequence of substituting equation (65) into equation (64):

$$\frac{DH}{Dt} = \left\{ < C > + \rho_l L \frac{d\phi}{dT} \right\} \frac{DT}{Dt} = \tilde{C}\frac{DT}{Dt}$$

$$\tilde{C} = \left\{ < C > + \rho_l L \frac{d\phi}{dT} \right\} \tag{2-67}$$

$\tilde{C}$ is equivalent to volumetric heat capacity. Therefore, by using this entire hypothesis, then the enthalpy equation can be rewritten for all phases as:

$$\tilde{C}_i \frac{dT_i}{dt} = \nabla.(< k_i > \nabla T_i) \tag{2-68}$$

The following is the discrete form of the energy equation using the Laplacian operator:

$$\tilde{C} \frac{dT_i}{dt} = traceG.(-2\bar{k}_{ji} T_{ji} . \nabla_i W_{ij} V'_j - 2K_{ji} M' . B) \tag{2-69}$$

Where $\bar{k}_{ji} = \frac{k_j + k_i}{2}$, $T_{ji} = T_j - T_i$ and G is defined as follow:

$$G' = \nabla_i W_{ij} V'_j . \begin{bmatrix} (r_j - r_i)_x^2 & (r_j - r_i)_x (r_j - r_i)_y \\ (r_j - r_i)_y (r_j - r_i)_y & (r_j - r_i)_y^2 \end{bmatrix}$$
$$G = G' / \det G' \quad (2\text{-}70)$$

As well as M', which is written as:

$$M' = L \otimes O$$
$$L' = \nabla_i W_{ij} V'_j \begin{bmatrix} (r_j - r_i)_x (r_j - r_i)_x \\ (r_j - r_i)_y (r_j - r_i)_y \end{bmatrix}$$
$$L = L' / \det L' \quad (2\text{-}71)$$
$$O = T_{ij} \nabla_i W_{ij}$$

Finally, B is described this way:

$$B = \nabla_i W_{ij} V'_j \quad (2\text{-}72)$$

2.4.3.3 Equation of state

This study employed the weakly compressible smoothed particle hydrodynamics technique (WCSPH) [73] [74]. Instead of using the Poisson equation, it is necessary to utilize an equation of state (EOS) that clearly specifies the pressure from the density. The polytropic equation of state, which relates pressure, density, and temperature for a fluid, is commonly used in compressible flow applications where the process is adiabatic. However, in the case of the filling of casting process, the density of the fluid, AlSI13, does not undergo significant changes during the filling process. As a result, the use of the polytropic equation of state is still applicable in this context to calculate the pressure of the fluid. Despite the thermal exchange between the metal and the mold, the density of the fluid remains relatively constant, so the polytropic equation of state can still be

used to relate pressure and density [73] [75]. The polytropic equation of state used in this study is as follows:

$$P = P_r\left(\frac{\rho}{\rho_0} - 1\right) + P_b \tag{2-73}$$

Where ρ_0 indicates the reference density, P_r represents the reference pressure, and P_b means the background pressure. The reference pressure is a function of the reference density and reference sound speed c_0 for the linear constitutive equation of state provided by equation (2-74).

$$P_r = \rho_0 c_0^2 \tag{2-74}$$

According to the stability criteria, using the physical speed of sound as a reference results in a very tiny time step. As a result, it is common to utilize an artificial sound speed as a reference. As a consequence the value of $c_0$is found as follows:

$$c_0^2 \geq \max\left\{\frac{U_0^2}{\delta\rho}, \frac{\| g \| L_0}{\delta\rho}, \frac{\mu U_0}{\rho_0 L_0 \delta\rho}\right\} \tag{2-75}$$

The reference velocity, reference length and dynamic viscosity, respectively, are U_0 , L_0, and μ. $\delta\rho$ denotes the dimensionless density variation, which is set at 1% ($\delta\rho = 0.01$) [73]. The background pressure is usually set to zero $(P_b = 0)$ for numerical problems involving single-phase free surface fluid flows. Furthermore, in order to avoid tensile instability in simulations of single or multiphase restricted fluid flows, the pressure is selected as a positive value adequate to guarantee the positivity of the estimated pressure field through the equation of state [73] [76]. In

this thesis, the ideal background pressure P_b is determined as a function of the reference pressure a is proportional to $0.05P_r$ (i.e.: $P_b \propto 0.05P_r$).

2.4.3.4 Particle shifting

Particle shifting is a fundamental technique used in smoothed particle hydrodynamics (SPH) simulations to improve the accuracy of the results [37].. In SPH, the particles represent the fluid or material, and the simulation calculates the properties of the particles and their interactions with each other. Particle shifting is used to improve the quality of the particle distribution and avoid particle clumping, which can lead to inaccuracies in the simulation [37]. This technique involves moving particles to new positions to achieve a more uniform and balanced distribution. The goal is to ensure that the particles are evenly spaced and that their properties are smoothly interpolated across the simulation domain [38]. There are various particle shifting methods used in SPH, ranging from simple to more complex techniques [38]. Simple particle shifting methods involve adjusting the particle positions based on a fixed set of rules [38]. More complex methods, such as adaptive particle shifting, involve dynamically adjusting the rules based on the particle distribution and other simulation properties [38]. The effectiveness of particle shifting in improving simulation accuracy depends on the quality of the initial particle distribution. In some cases, more complex particle shifting methods may be necessary to achieve accurate results. However, for simulations with a uniform and balanced particle distribution, simple particle shifting methods can be sufficient to ensure accuracy.

For our simulation, the particle distribution quality is uniform and balanced enough so that the simple particle shifting technique is enough to ensure accurate outcomes. Furthermore, we have

decided to employ the simple particle shifting technique for the sake of computational efficiency and ease of implementation.

$$p_w = \frac{\sum_j^{n_f} p_j W_{ij} + g \sum_j^{n_f} \rho_j r_{wj} W_{wj}}{\sum_j^{n_f} W_{ij}} \tag{2-76}$$

2.4.3.5 Boundary condition

Fluid Boundary condition

In this thesis, we also propose a multiphase fluid flow adaptation of the generalized wall boundary condition approach suggested by [73] [77]. Three layers of dummy particles must be applied to the wall interface in the normal direction using this approach (see Figure (2-9)). The dummy particles are put to simulate the wall in such a way that the support of the kernel function is comprehensive, allowing for precise integration of field variables near the wall interface. This approach may be used to create free-slip or no-slip wall boundary conditions. In the computation of fluid viscous forces, the free-slip boundary condition is implemented by ignoring the viscous interaction between the fluid particle and the nearby dummy particles.

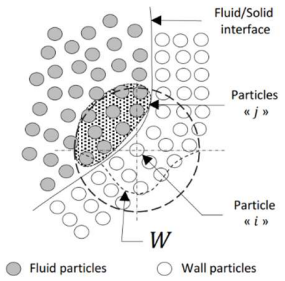

Figure 2-9 - Geometrical description of different parameters used in the generalized wall Boundary condition [73]

In the case of a no-slip wall boundary condition, the wall-dummy particle interacting with the fluid particle i is given a virtual velocity V_w [73].

$$V_w = 2V_i - \tilde{V}_i \tag{2-77}$$

Where $\tilde{V}_i$ signifies the interpolation of the smoothed velocity field of the fluid phase to the dummy particle location, and V is the specified velocity of wall particle i. The number of nearby fluid particles j of the wall particle i is referred to as n_f [73].

$$\tilde{V}_i = \frac{\sum_j^{n_f} V_j W_{ij}}{\sum_j^{n_f} W_{ij}} \tag{2-78}$$

According to [73] [77], the pressure in the dummy-wall particle is computed from the pressure in the nearby fluid particles j. This method is based on the theory that each fluid particle considers all of its wall-dummy neighbors as possessing similar properties, such as density, viscosity, and volume.

$$p_w = \frac{\sum_j^{n_f} p_j W_{ij} + g\sum_j^{n_f} \rho_j r_{wj} W_{wj}}{\sum_j^{n_f} W_{ij}} \tag{2-79}$$

Thermal Boundary condition

The temperature boundary conditions utilized to simulate the casting process must be such that the energy exchange between the liquid metal inside the mold and the mold is correctly represented to replicate the molten metal cooling and solidification. This study employs the non-homogeneous

thermal Neumann boundary condition $\nabla T.n=q$. The following values are interpolated on the material particles (liquid, mushy/regularization, and solid areas) by the relevant wall particles.

$$T_{wall_i}=\frac{q\sum_j^{nb} r_{ij}\frac{\partial W}{\partial r}V_j'+d\sum_j^{nb} T_jV_j'\nabla W.n_i}{d\sum_j^{nb} V_j'\nabla W.n_i} \tag{2-80}$$

Here q denote a heat flux ($q=0$ for the adiabatic conditions) and n_i is the normal vector to the wall.

2.4.3.5 Summary of governing equations for 2D and 3D casting simulation

Below is a summary of the governing equations used to simulate the filling and solidification steps of the casting process using $\delta - SPH$ approach.

$$\begin{cases}\dfrac{D\rho_i}{Dt}=-\rho_i\sum_j(V_j-V_i).\nabla_iW_{ij}V_j'+hc_0\sum_j\delta D_{ij}.\nabla_iW_{ij}V_j'\\ \dfrac{DV_i}{Dt}=-\dfrac{1}{\rho_i}\sum_j(p_i+p_j)\nabla_iW_{ij}V_j'+hc_0\dfrac{\rho_0}{\rho_i}\sum_j\alpha\pi_{ij}\nabla_iW_{ij}V_j'+g_i+\dfrac{A(\phi_s)V_i}{\rho_i}\\ \tilde{C}\dfrac{DT}{Dt}=\nabla.\left(<k>\nabla T\right)\\ \tilde{C}=<C>+\rho_lL\dfrac{d\phi}{dT}\\ <.>=(1-\phi)(.)_s+\phi(.)_l\\ P=\rho_0c_0^2(\dfrac{\rho}{\rho_0}-1)+0.05\rho_0c_0^2\\ r_i^*=r_i+dt*V_i\end{cases} \tag{2-81}$$

2.4.4 Comparison SPH/ProCAST

The fundamental distinction between the two approaches is that the SPH method is Lagrangian, whereas the commercial ProCAST software is Eulerian. The SPH approach is a meshless method, whereas the proCAST computation is mesh-based. Contrary to ProCAST, the SPH approach is able to get the temporal history of material particles. Free surfaces, material interfaces, and changing boundaries can all be tracked automatically in the SPH, regardless of particle movement complicity. The main equations of the WCSPH and ProCAST models, as well as the differences between them, are shown in Table (2-2).

Table 2-2 - Comparison of ProCAST and WCSPH model

WCSPH		**ProCAST software**
Weakly compressible flow		**Incompressible flow**
$\frac{\partial \rho}{\partial t} + \rho \nabla . V = 0$	**Continuity equation**	$\nabla . \vec{V} = 0$
$\rho \frac{D\vec{V}}{Dt} = \rho \vec{g} - \nabla p + \nabla . (\mu \nabla \vec{V}) + A(\phi_s)V$	**Momentum equation**	$\rho \frac{D\vec{V}}{Dt} = \rho \vec{g} - \nabla p + \nabla . (\mu \nabla \vec{V})$
$\tilde{C} \frac{DT}{Dt} = \nabla . (k \nabla T)$ $\tilde{C} = (1-\phi)\rho_s C_s + \phi \rho_l C_l + \rho_l L_f \frac{d\phi}{dT}$	**Energy equation**	$\rho C_p \frac{DT}{Dt} = \nabla . (k \nabla T) + \rho L \frac{\partial \phi_s}{\partial t}$
$\phi(T) = \begin{cases} 0 \\ \frac{1}{2}\{1 + \sin(\pi(\frac{T - T_m}{2\varepsilon}))\} \\ 1 \end{cases} \rightarrow \begin{bmatrix} T < T_m - \varepsilon(solid) \\ T_m - \varepsilon \leq T \leq T_m + \varepsilon(mushy) \\ T > T_m + \varepsilon(liquid) \end{bmatrix}$	**Solid fraction**	$\phi_l = \left(\frac{T - T_s}{T_l - T_s}\right)$

In terms of fluid flow distinction between these two methodologies, the SPH technique makes it challenging to calculate pressure for incompressible flow. As a result, the flow is defined as weakly compressible (WCSPH), allowing for the calculation of pressure using the equation of state.

In terms of solidification modeling in fluid flow, the ProCAST method employs the viscosity increase model, meanwhile, the SPH method uses the Carman-Kozeny equation to apply solidification to the momentum equation. The additional source term is added to the momentum equation in the Carman-Kozney equation, which sweeps all the other terms during the mushy area to prevent fluid flow from moving.

In terms of energy equation, latent heat is embedded inside the heat capacity in the WCSPH approach while it is provided as a source term in ProCAST software. In fact, the WCSPH technique employs equal heat capacity, which includes latent heat in the energy equation. It is worth noting that in ProCAST, solid fraction is a linear function, although, in the WCSPH technique, it is a sine function. ProCAST simulation is based on QuikCAST data set, as previously stated. The SPH approach defines thermal conductivity in the same way as the ProCAST simulation provides. In the case of density and heat capacity, the maximum and minimum values were taken from QuikCAST data set and computed using the equation below.

$$<.>=(1-\phi)(.)_s+\phi(.)_l \tag{2-81}$$

2.5 Conclusion

This chapter combines experimental methods with numerical simulation using commercial ProCAST software and the SPH approach. The design and 3D printing process for the sand molds that enable rapid gravity casting experimental tests of AlSi13 as well as data acquisition are described in the first section. The next section explained gravity casting modeling using commercial ProCAST software. It should be noted that the thermophysical properties of resin-bonded sand and AlSi13 are based on the ProCAST simulation data source. SPH approach is given in the third and most crucial part of this chapter in order to model the casting process, particularly the filling and solidification steps. To create an SPH formulation, two

steps must be taken. The kernel approximation process, which is the initial step, involves representing a function and/or its derivatives in continuous form as integrals. Particle approximation is the term used to describe the second phase. The computational domain is discretized at this point by presenting it as a set of initial particle distributions. $\delta - SPH$ is employed as well as adding a solidification term to the momentum equation in order to reproduce the filling and solidification steps of the gravity casting process. The solidification step was added to the momentum equation using the Carman-Kozney equation. Furthermore, to replicate the solidification stage involving the two values of latent heat and sensible heat, an equivalent heat capacity value is employed in the energy equation.

Conclusion

Ce chapitre combine les méthodes expérimentales avec la simulation numérique en utilisant le logiciel commercial ProCAST et l'approche SPH. La première section décrit la conception et le processus d'impression 3D des moules en sable, qui permettent de réaliser rapidement des essais expérimentaux de coulée par gravité d'AlSi13, ainsi que l'acquisition des données. La section suivante explique la modélisation de la coulée par gravité à l'aide du logiciel commercial ProCAST. Il convient de noter que les propriétés thermophysiques du sable lié à la résine et de l'AlSi13 sont basées sur la base de données de ProCAST. La troisième partie, la plus cruciale de ce chapitre, présente l'approche SPH pour modéliser le processus de coulée, en particulier les étapes de remplissage et de solidification. Pour créer une formulation SPH, deux étapes doivent être suivies. La première phase consiste à représenter une fonction et/ou ses dérivées sous forme continue comme des intégrales, et est appelée processus d'approximation par noyau. La deuxième phase est appelée approximation particulaire, et consiste à discrétiser le domaine de calcul en le

présentant comme un ensemble de distributions initiales de particules. Pour reproduire les étapes de remplissage et de solidification du processus de coulée par gravité, l'ajout d'un terme de solidification à l'équation de quantité de mouvement est utilisé. L'étape de solidification a été ajoutée à l'équation de quantité de mouvement en utilisant l'équation de Carman-Kozney. En outre, pour reproduire l'étape de solidification impliquant les deux valeurs de chaleur latente et de chaleur sensible, une valeur de capacité thermique équivalente est employée dans l'équation d'énergie.

2.6 References

[1] E. S. Almaghariz, B. P. Conner, L. Lenner, R. Gullapalli, G. P. Manogharan, B. Lamoncha, and M. Fang, "Quantifying the Role of Part Design Complexity in Using 3D Sand Printing for Molds and Cores," *International Journal of Metalcasting,* vol. 10, no. 3, pp. 240-252, 2016.

[2] Nicolas Coniglio, Tharmalingam Sivarupan, Mohamed El Mansori, "Investigation of process parameter effect on anisotropic properties of 3D printed sand molds," *The International Journal of Advanced Manufacturing Technology,* vol. 94, p. 2175–2185, 2018.

[3] Antonin. Sanitas,, "Étude expérimentale et numérique de la coulée basse-pression de l'alliage de magnésium RZ5 dans des moules en sable imprimés en 3D," Ecole nationale supérieure d'arts et métiers-ENSAM, 2016.

[4] R. Singh, "Three Dimensional Printing for Casting Applications : A State of Art Review and Future Perspectives," *Advanced Materials Research,* Vols. 83-86, pp. 342-349, 2009.

[5] G. Budzik, "Possibilities of utilizing 3DP technology for foundry mould making," *Archives of Foundry Engineering,* vol. 7, no. 2, pp. 65-68, 2007.

[6] M.Zamani, "Al-Si Cast Alloys -Microstructure and Mechanical Properties at Ambient and Elevated Temperature," Jönköping University, School of Engineering, Dissertation, 2017.

[7] Mariem Ben Saada, Mohamed El Mansori, "Assessment of the effect of 3D printed sand mold thickness on solidification process of AlSi13 casting alloy," *The International Journal of Advanced Manufacturing Technology,* vol. 114, pp. 1753-1766, 2021.

[8] Meysam Haghshenas, Jamal Jamali, "Assessment of circumferential cracks in hypereutectic Al-Si clutch housings," *Case Studies in Engineering Failure Analysis 8(C),* 2016.

[9] Peng Lan, Jiaquan Zhang, "Study on the mechanical behaviors of grey iron mould by simulation and," *Materials and Design,* vol. 53, pp. 822-829, 2014.

[10] Su-Ling Lu, Fu-Ren Xiao, Shuang-Jie Zhang, Yong-Wei Mao, Bo Liao, "Simulation study on the centrifugal casting wet-type cylinder liner based on ProCAST," *Applied Thermal Engineering,* vol. 73, pp. 512-521, 2014.

[11] Hua. Wu, Haiming. Shi, Haifeng. Liu, Zhenjia.Xia, "umerical Simulation of Flow Field and Temperature Field on Aluminium Alloy Engine Cylinder in Casting Process," *Materials Science Forum,* Vols. 704-705, pp. 50-57, 2012.

[12] Ning, Lin Panzhong and Li, "Low pressure casting technology and forming process analysis of metal mold based on ProCAST FEA procedure," *Mechanics of Advanced Materials and Structures,* 2020.

[13] M.B. Liu and G.R.Liu, , "Smoothed Particle Hydrodynamics (SPH): an Overview and recent developments," *Arch Comput Methods Eng,* vol. 17, pp. 25-76, 2010.

[14] J. J. Monaghan, "Smoothed Prticles Hydrodynamics," *Annu. Rev.,* vol. 30, pp. 543-574, 1992.

[15] G.R.Liu and M.B.Liu,, Smoothed Particle Hydrodynamics a meshfree particle method, National University of Singapore, 2003.

[16] R.Fatehi and M.T.Manzari, "Error estimation in smoothed particle hydrodynamics and a new scheme for second derivatives," *Computers & Mathematics with Applications,* vol. 61, no. 2, pp. 482-498, 2011.

[17] O.Flebbe, S.Muenzel, H.Herold, H.Riffer and H.Ruder,, "Smoothed Particle Hydrodynamics: Physical viscosity and the simulation of accretion disks," *The Astrophysical Journal,* vol. 431, no. 2, pp. 754-760, 1994.

[18] S. Watkins, A. Bhattal, N. Francis, J. Turner, A. Whitworth,, "A new prescription for viscosity in Smoothed Particle Hydrodynamics,," *Astronomy and Astrophysics,* vol. 119, pp. 177-187, 1996.

[19] J.H. Jeong, M.S. Jhon , J.S. Halow, J. van Osdol, "Smoothed particle hydrodynamics: Applications to heat conduction," *Computer Physics Communications,* vol. 153, pp. 71-84, 2003.

[20] J. Bonet , T.-S.L. Lok, "Variational and momentum preservation aspects of Smooth Particle Hydrodynamic formulations," *Comput. Methods Appl. Mech. Engrg,* vol. 180, pp. 97-115, 1999.

[21] R. Fatehi, M.A. Fayazbakhsh, M.T. Manzari, "On Discretization of Second-order Derivatives in Smoothed Particle Hydrodynamics," *World Academy of Science, Engineering and Technology,* vol. 40, 2008.

[22] L. Brookshaw, "A method of calculating radiative heat diffusion in particle simulations," *Astronomical Society of Australia, Proceedings,* vol. 6, pp. 207-210, 1985.

[23] Mihai Basa, Nathan J. Quinlan and Martin Lastiwka, "Robustness and accuracy of SPH formulations for viscous flow," *INTERNATIONAL JOURNAL FOR NUMERICAL METHODS IN FLUIDS,* vol. 60, pp. 1127-1148, 2009.

[24] J.K.Chen, J.E.Beraun, C.J.Jih, "A corrective smoothed particle method for transient elastoplastic dynamics.," *Computational Mechanics,* vol. 27, no. 3, pp. 177-187, 2001.

[25] M.B. Liu, G.R. Liu, "Restoring particle consistency in smoothed particle hydrodynamics," *Applied Numerical Mathematics,* vol. 56, pp. 19-36, 2006.

[26] J.Bonet, S.Kulasegaram , "A simplified approach to enhance the performance of smooth particle hydrodynamics method," *Applied Mathematics and Computation,* Vols. 2-3, no. 133-155, p. 126, 2002.

[27] WK.Liu, S.Jun, "Multiple-scale reproducing kernel particle method for large deformation problems," *International Journal for Numerical Methods in Engineering ,* vol. 41, no. 7, pp. 1339-1362, 1998.

[28] Schwaiger, Hans F., "An implicit corrected SPH formulation for thermal diffusion with linear free surface boundary conditions," *INTERNATIONAL JOURNAL FOR NUMERICAL METHODS IN ENGINEERING,* pp. 647-671, 2008.

[29] Xing Zheng, Qingwei Ma and Songdong Shao, "Study on SPH Viscosity Term Formulations," *applied sciences ,* vol. 8, no. 2, p. 249, 2018.

[30] W.P.Graebel, Advanced fluid mechanics, Michigan: Elsevier, 2007.

[31] J.J. Monaghan,, "Simulating Free Surface Flows with SPH," *Journal of Computational Physics,* vol. 110, pp. 399-406, 1994.

[32] P.W. Cleary, J. Ha, M. Prakash, T. Nguyen, "3D SPH flow predictions and validation for high pressure die casting of automotive components," *Applied Mathematical Modelling,* vol. 30, p. 1406–1427, 2006.

[33] J.J. Monaghan, R. A. Gingold, "Shock Simulation by the Particle Method SPH," *journal of computational physics,* vol. 52, pp. 374-389, 1983.

[34] Adrian Bejan, John Wiley & Sons, Convection Heat Transfer, North carolina, 2013.

[35] Paul W. Cleary and Joseph J. Monaghan, "Conduction Modelling Using Smoothed Particle Hydrodynamics," *Journal of Computational Physics,* vol. 148, p. 227–264, 1999.

[36] J.J.Monaghan, "On the problem of penetration in particle methods," *Journal of computational physics,* vol. 82, pp. 1-15, 1989.

[37] G.R.Liu and M.B.Liu, Smoothed particle hydrodynamics a meshfree particle method, World scientific publishing , 2003.

[38] J.J. Monaghan, "Particle methods for hydrodynamics," *Computer physics report,* vol. 3, pp. 71-124, 1985.

[39] R.W. Hockney and J.W. Eastwood, Computer simulation using particles, New York: Adamhilger, 1988.

[40] Clifford E. Rhoades Jr, "A fast algorithm for calculating particle interactions in smooth particle hydrodynamic simulations," *Computer physics communications,* vol. 70, pp. 478-482, 1992.

[41] J.C.Simpson, "Numerical techniques for three-dimensional smoothed particle hydrodynamics simulations: applications to accretion disks," *The Astrophysical Journal, ,* vol. 448, pp. 822-831, 1995.

[42] A. krimi, "Modeling of multiphase fluid dlows with smoothed particle hydrodynamics approach," Paris, 2018.

[43] Joseph P. Morris, Patrick J. Fox, and Yi Zhu, "Modeling Low Reynolds Number Incompressible Flows Using SPH," *JOURNAL OF COMPUTATIONAL PHYSICS ,* vol. 136, pp. 214-226, 1997.

[44] P.N. Sun, A. Colagrossi, S. Marrone, A.M. Zhanga, "The δplus-SPH model: Simple procedures for a further improvement of the SPH scheme," *Comput. Methods Appl. Mech. Engrg.,* vol. 315, p. 25–49, 2017.

[45] M. Gomez-Gesteira, B.D. Rogers, R.A. Dalrymple, A.J.C. Crespo, "State-of-the-art of classical SPH for free-surface flows," *J. Hydraul. Res.,* vol. 48, pp. 6-27, 2010.

[46] D. Violeau, B.D. Rogers,, " Smoothed particle hydrodynamics (SPH) for free-surface flows: past, present and future," *J. Hydraul. Res,* vol. 54, pp. 1-26, 2016.

[47] M. Shadloo, G. Oger, D. Le Touze, "Smoothed particle hydrodynamics method for fluid flows, towards industrial applications: Motivations,current state, and challenges," *Comput. & Fluids,* vol. 136, pp. 11-34, 2016.

[48] E.Y. Lo, S. Shao, "Simulation of near-shore solitary wave mechanics by an incompressible SPH method," *Appl. Ocean Res.,* vol. 24, pp. 275-286, 2002.

[49] R. Xu, P. Stansby, D. Laurence,, "Accuracy and stability in incompressible SPH (ISPH) based on the projection method and a new approach," *J. Comput. Phys.,* vol. 228, pp. 6703-6725, 2009.

[50] H. Gotoh, A. Khayyer, H. Ikari, T. Arikawa, K. Shimosako,, "On enhancement of Incompressible SPH method for simulation of violent sloshing flows," *Appl. Ocean Res,* vol. 46, pp. 104-115, 2014.

[51] J. Vila,, "On particle weighted methods and smooth particle hydrodynamics," *Math. Models Methods Appl. Sci,* vol. 9, pp. 161-209, 1999.

[52] P. Koukouvinis, J. Anagnostopoulos, D.E. Papantonis,, "An improved MUSCL treatment for the SPH-ALE method: comparison with the standard SPH method for the jet impingement case," *Internat. J. Numer. Methods Fluids,* vol. 71, pp. 1152-1177, 2013.

[53] R. Fatehi, M. Manzari,, "A consistent and fast weakly compressible smoothed particle hydrodynamics with a new wall boundary condition," *Internat. J. Numer. Methods Fluids,* vol. 68, pp. 905-921, 2012.

[54] M. Antuono, A. Colagrossi, S. Marrone,, "Numerical diffusive terms in weakly-compressible SPH schemes," *Comput. Phys. Comm.,* vol. 183, pp. 2570-2580, 2012.

[55] Domenico D. Meringolo, Salvatore Marrone, Andrea Colagrossi, Yong Liua, "A dynamic δ-SPH model: How to get rid of diffusive parameter tuning," *Computers and Fluids,* vol. 179, p. 334–355, 2019.

[56] S.D. Chowdhury, S. Sannasiraj, "Numerical simulation of 2D sloshing waves using SPH with diffusive terms," *Appl. Ocean Res,* vol. 47, pp. 219-240, 2014.

[57] M. Antuono, B. Bouscasse, A. Colagrossi, S. Marrone, , "A measure of spatial disorder in particle methods," *Comput. Phys. Comm,* vol. 185, pp. 2609-2621, 2014.

[58] J.W. Swegle, D.L. Hicks, S.W. Attaway, "Smoothed particle hydrodynamics stability analysis," *J. Comput. Phys.,* vol. 116, pp. 123-134, 1995.

[59] J.P. Morris, "A study of the stability properties of smooth particle hydrodynamics," *Publ. Astron. Soc. Aust.,* vol. 13, pp. 97-102, 1996.

[60] M. Antuonoa, A. Colagrossi ,S. Marronea, "Numerical diffusive terms in weakly-compressible SPH schemes," *Computer Physics Communications,* vol. 183, p. 2570–2580, 2012.

[61] Domenico D. Meringolo, Yong Liu, Xin-Yu Wang, Andrea Colagrossi, "Energy balance during generation, propagation and absorption of gravity waves through the δ-LES-SPH model," *Coastal Engineering,* vol. 140, p. 355–370, 2018.

[62] A.Jameson, "Numericla solution of the Euler equations by finite volume methods using Runge Kutta time stepping schemes," in *AIAA 14th fluid and plasma dynamics conference*, California, 1981.

[63] Xiaofeng Niu, Jingyu Zhao, Baojian Wang, "Application of smooth particle hydrodynamics (SPH) method in gravity casting shrinkage cavity prediction," *Computational Particle Mechanics,* vol. 6, pp. 803-810, 2019.

[64] Liu, M.B. Liu · G.R., "Smoothed Particle Hydrodynamics (SPH): an Overview and Recent Developments," *Arch Comput Methods Eng,* vol. 17, pp. 25-67, 2010.

[65] A. Brent, V. Voller, and K. Reid,, "Enthalpy-porosity technique for modeling convection-diffusion phase change: application to the melting of a pure metal," *Numerical Heat Transfer, Part A Applications,* vol. 13, no. 3, p. 297–318, 1988.

[66] C.Prakash and V. R.Voller, , "A fixed grid numerical modelling methodology for convection-diffusion mushy region phase-change problems," *International Journal of Heat and Mass Transfer,* vol. 30, no. 8, p. 1709–1719, 1987.

[67] J. A. Mackenzie and M. L.Robertson,, "The Numerical Solution of One-Dimensional Phase Change Problems Using an Adaptive Moving Mesh Method," *Journal of Computational Physics,* vol. 161, p. 537–557, 2000.

[68] Huespe, Víctor D. Fachinotti Alberto Cardona Alfredo E., "A Fast Convergent and Accurate Temperature Model for Phase-change Heat Conduction," *Int. J. Numer. Meth. Engng.,* vol. 44, pp. 1863-1884, 1999.

[69] J. Crank, "Free and moving boundary problems,," 1984.

[70] G.H.Meyer, , "Multidimensional stefan problems," *SIAM Journal on Numerical Analysis,* vol. 10, no. 3, p. 522–538, 1973.

[71] P. W. Egolf and H.Manz,, "Theory and modeling of phase change materials with and without mushy regions," *International Journal of Heat and Mass Transfer,* vol. 37, no. 18, p. 2917–2924, 1994.

[72] I. Danaila, R. Moglan, F. Hecht, and S. Le Masson, "A newton method with adaptive finite elements for solving phase-change problems with natural convection," *Journal of computational physics,* vol. 274, p. 826–840, 2014.

[73] Abdelkader Krimi, Mehdi Rezoug, Sofiane Khelladi, Xesús Nogueira, Michael Deligant, Luis Ramírez, "Smoothed Particle Hydrodynamics: A consistent model for interfacial

multiphase fluid flow simulations," *Journal of Computational Physics,* vol. 358, pp. 53-87, 2018.

[74] J. J. Monaghan, "Simulating free surface flows with sph," *Journal of computational physics,* vol. 11, no. 2, pp. 399-406, 1994.

[75] J. P. Morris, "Simulating surface tension with smoothed particle hydrodynamics," *International journal for numerical methods in fluids,* vol. 33, no. 2, pp. 333-353, 2000.

[76] S. Marrone, A. Colagrossi, M. Antuono, G. Colicchio, and G. Graziani,, "An accurate sph modeling of viscous flows around bodies at low and moderate reynolds numbers," *Journal of Computational Physics,* vol. 245, pp. 456-475, 2013.

[77] S. Adami, X. Hu, and N. Adams, "A generalized wall boundary condition for smoothed particle hydrodynamics," *Journal of Computational physics,* vol. 231, no. 21, pp. 7057-7075, 2012.

Chapter 3: A rapid gravity casting test case for validating 2D numerical results of filling and solidification

Contents

3.1 Introduction

Different and sophisticated physics are involved in the casting process, all of which are extremely complex and challenging to replicate at the same time. It is particularly valuable to introduce test cases that could be employed to better understand the physics of the casting process. Filling and solidification are two key steps in the casting process modeling that must be completed in order to simulate the casting process. As part of the thesis objective, the 2D SPH code for modeling filling and solidification of the casting process is validated by the introduction of a universal test case. The system is considered open in a traditional casting process because the molten metal is poured in such a way that the metal level surface in the pouring basin remains constant throughout the filling process. The current code has a limitation when it comes to 2D modeling of the casting process utilizing the SPH approach to depict molten metal pouring from the ladle to the pouring basin. Due to the constraints of the current SPH code, the experimental test case is designed in such a manner that it should be considered a closed system. When performing the closed experimental system, a plug must be considered to prevent the material from moving within the sprue.

The third chapter's main goal is to present a new universal test case for gravity casting of AlSi13 using 3D-printed resin-bonded sand molds. Thanks to the experimental setup, this universal test case allows for modeling in 2D in terms of filling and solidification. Using this experimental test case, any two-dimensional simulation of casting process could be validated and compared. The first section covers universal test case design, geometric characteristics, data measurement, and collection tools, as well as the experimental setup and the experiment.

The SPH method is chosen to simulate the filling, cooling, and solidification of the casting process, as outlined in the second chapter, because of its strength in replicating fluid flow. Finally, the simulation results of SPH are presented, analyzed, and compared to the experiment regarding filling, cooling, and solidification. Moreover, ProCAST is used to model gravity casting process. Numerical data are compared to experimental data to show the strengths and weaknesses of the two simulation approaches to modeling the casting process. Figure (3-1) shows the current demands for fluid and thermal flow analysis utilizing experimental and numerical (SPH and ProCAST) data with the relevant classification.

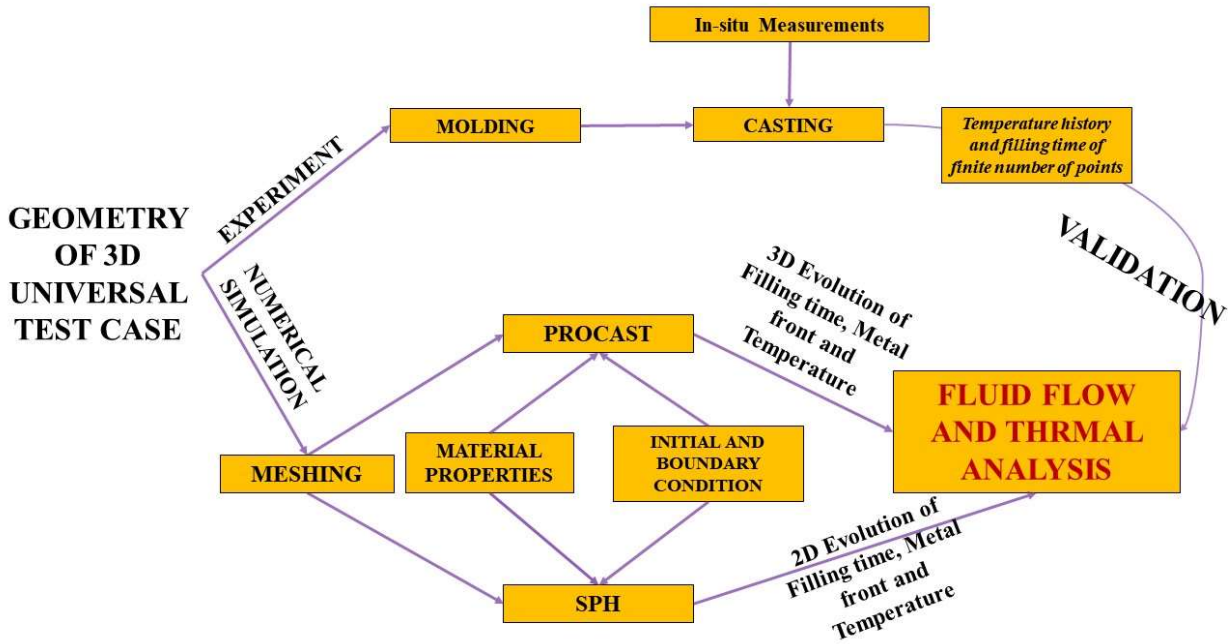

Figure 3-1 - The required elements for investigating fluid and thermal analysis using experimental and numerical data

Introduction

Différentes physiques sophistiquées sont impliquées dans le processus de coulée, qui sont toutes extrêmement complexes et difficiles à reproduire en même temps. Il est particulièrement utile de présenter des cas test qui pourraient être employés pour mieux comprendre la physique du processus de coulée. Le remplissage et la solidification sont deux étapes clés de la modélisation du processus de coulée qui doivent être réalisées afin de simuler le processus de coulée. Dans le cadre de l'objectif de la thèse, le code SPH 2D pour la modélisation du remplissage et de la solidification du processus de coulée est validé par l'introduction d'un cas test universel. Le système est considéré comme ouvert dans un processus de coulée traditionnel car le métal fondu est versé de telle sorte que la surface du niveau du métal dans le bassin de coulée reste constante tout au long du processus de remplissage. Le code actuel est limité lorsqu'il s'agit de modéliser en 2D le processus de coulée en utilisant l'approche SPH pour représenter le métal fondu qui coule de la poche de coulée vers le bassin de coulée. En raison des contraintes du code SPH actuel, le cas test expérimental est conçu de telle manière qu'il doit être considéré comme un système fermé. Lors de l'exécution du système expérimental fermé, un bouchon doit être envisagé pour empêcher le matériau de se déplacer à l'intérieur de la descente.

L'objectif principal du troisième chapitre est de présenter un nouveau cas d'essai universel pour la coulée par gravité de l'AlSi13 en utilisant des moules en sable à prise chimique et imprimés en 3D. Grâce au dispositif expérimental, ce cas d'essai universel permet une modélisation en 2D en termes de remplissage et de solidification. En utilisant ce cas d'essai expérimental, toute simulation bidimensionnelle du processus de coulée peut être validée et comparée. La première

section couvre la conception du cas d'essai universel, les caractéristiques géométriques, la mesure des données et les outils de collecte, ainsi que le dispositif expérimental et l'expérience.

La méthode SPH est choisie pour simuler le remplissage, le refroidissement et la solidification du processus de coulée, comme indiqué dans le deuxième chapitre, en raison de sa force dans la reproduction de l'écoulement des fluides. Enfin, les résultats de la simulation SPH sont présentés, analysés et comparés à l'expérience en ce qui concerne le remplissage, le refroidissement et la solidification. De plus, ProCAST est utilisé pour modéliser le processus de coulée par gravité. Les données numériques sont comparées aux données expérimentales pour montrer les forces et les faiblesses des deux approches de simulation pour modéliser le processus de coulée.

3.2 Gravity casting experimental test case

3.2.1 Geometry design

Figure (3-2) represents the overall geometry of the proposed experimental test case for gravity casting with a 3D-printed sand mold.

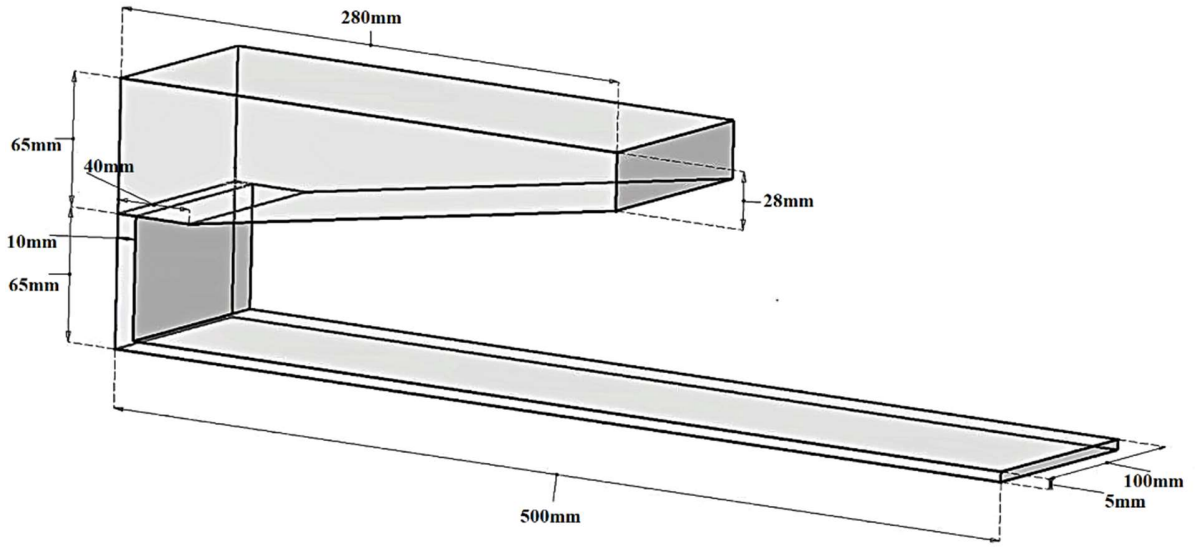

Figure 3-2 - Schematic of geometry intended for gravity casting

The casting geometry is composed of a pouring basin, a sprue and thin plate. In order to model the casting process in two dimensions even if it is not representative of traditional gravity casting geometry, the whole geometry has a fixed width. The aim is to create a design that enables temperature and velocity variations of the plate to be unaffected by the width direction except in the borders. Therefore, the width and the length of the plate should be deemed enough in comparison with the thickness. As a result, the plate width is 100mm, while the thickness is 5mm. Furthermore, in parallel having a large width size, the length of the test case should be regarded

long enough. The pouring basin is filled to a height of 37mm from the bottom in order to completely fill the sprue and plate. The plug is high enough that it can be easily taken out to begin the filling process. Approximately 13mm of molten metal from the pouring basin's bottom is existent there after the filling step. Hence, the height of the sprue is considered sufficient (65mm) to prevent the plate from being heated by molten metal left in the pouring basin after the filling phase. Furthermore, the sprue thickness is 10mm to prevent the molten material from solidification inside the sprue when filling. To reduce turbulence and sand entering the flow, the bottom of the sprue is assumed to be crescent-shaped where the fluid flow changes direction. The pouring basin's geometry is such that molten material on the ramp is gradually transported towards the sprue to fill the plate. In addition, it is designed in a way that additional processors could well be employed to decrease run time when employing the SPH method. In the SPH technique, solid and fluid particles are defined separately. To solve the governing equation, solid and fluid spaces are divided in the direction of x. The design of a "pouring basin" should be taken into consideration in order to have more fluid particles overlap with the solid particles of the plate in the direction of x. As a result, more processors can be used, substantially reducing on the simulation time. The CPU parallelization strategy used by our SPH algorithm is outlined in Appendix B.

3.2.2 Experimental setup

Figure (3-3) provides illustrations of the designed mold. The left side displays the CATIA-designed mold geometry, while the right side demonstrates the 3D-printed resin-bonded sand mold.

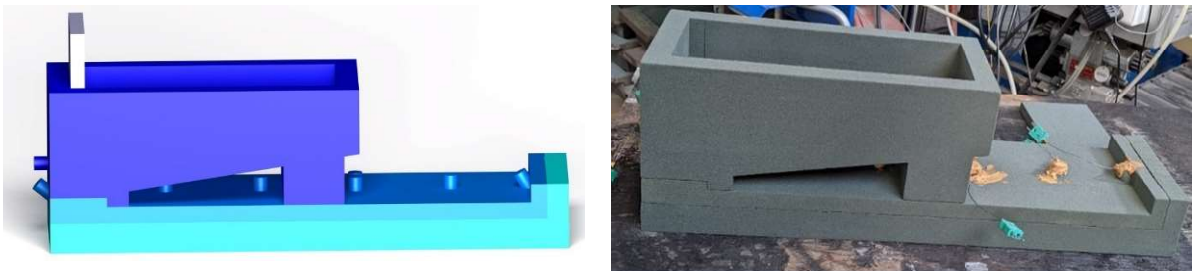

Figure 3-3 - Geometry of mold a) Left: designing by CATIA b) Right: 3D Printed resin - bonded sand mold

Both the pouring basin and the top of the sprue are included in the upper component. The upper surface of the plate and the rest of the sprue make up the mold's middle part. Finally, the last component of the mold is the plate underside, which completes the plate shape.

Using ProCAST simulation, the mold thickness is chosen. A temperature threshold should be selected in order to determine the mold's thickness. This threshold indicates that during the casting process, the mold's outside temperature never rises above 50 degrees. A very thick mold is used to numerically model the casting process in order to determine the mold's thickness. After the numerical simulation is complete, the temperature profile over time at various mold distances is examined. When the temperature is below the value of 50 degrees in every position of mold throughout this inquiry, the maximum thickness of sand is taken into consideration as the thickness of the mold. The thickness of the mold is assessed to be there 23 mm using this criterion.

A very thin gap is considered at the end of the plate to avoid having to take into account any backpressure induced by air entrapment. To prevent liquid metal from leaking on the measurement connections, an attachment with a proper height is also supplied. The metal is extracted from the

furnace with a ladle to cast, which leads to a pouring temperature 700°C corresponding to 130°C superheat. K-type thermocouples are inserted at 6 places to characterize temperature evolution in the melt, as shown in Figure (3-4). The maximum temperature is 700°C in the experiment, hence the thermocouples' precision is $\pm 5.25^{\circ} C$ $(0.0075 \times |T^{'}|)$. In parallel, to characterize the flow dynamics during filling, an acquisition system is employed. The acquisition system was put in nodes (N1, N2, N3, N4, N5, N6, and N7) and thermocouples in nodes (N1, N3, N4, N5, N6 and N8) to capture filling time and temperature, respectively (Figure (3-4)). Supports are provided on the mold for proper installation of thermocouples and measurement systems. These supports were used to prevent the rods from sliding inside the mold once they have been installed in a suitable location.

N1 is positioned at a distance of 5 mm from the top of the sprue. N2 is 2.5 mm from the bottom of the plate, at the bottom of the sprue in the central portion of its thickness representing time "t=0s". It should be noticed that the thermocouples N3, N4, N5, and N6 are 100mm, 200mm, 300mm, and 400mm away from the beginning of the plate, respectively. N7 is installed 5mm from the bottom of plate in the middle of thickness and width throughout the length to determine the final filling time. In the width direction, thermocouple N8 is inserted at a distance of 10mm from thermocouple N5. The goal of installing this thermocouple is to compare the temperatures associated with N5 and N8 in order to demonstrate that temperature variations in the center of the plate are independent of changes in the width direction. As a result, the temperature evolution of the 3D experimental test could be described in 2D.

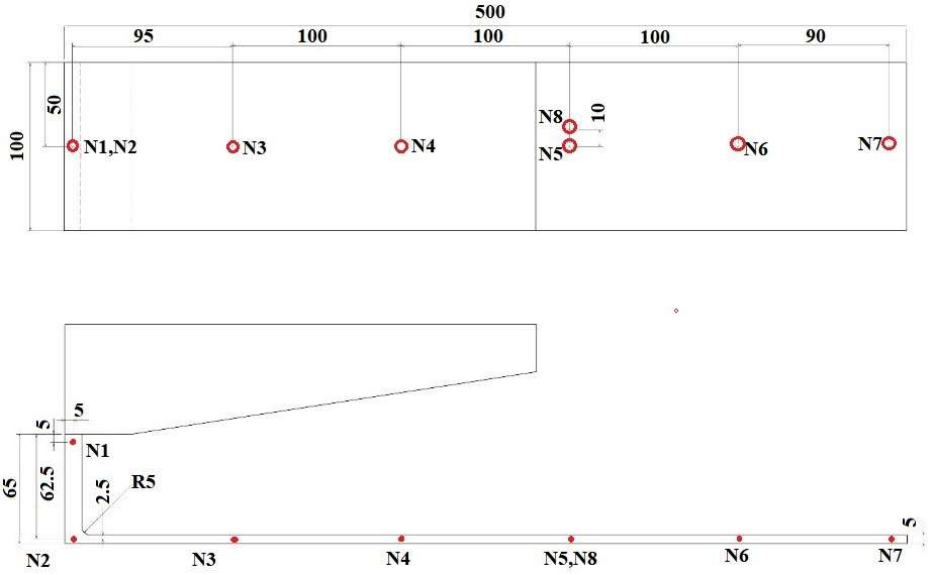

Figure 3-4 - Location of thermocouples and tracking of molten metal (mm)

3.2.3 Experimental results

3.2.3.1 Filling time

Figure (3-5) depicts the voltage decrease with time at seven places (N1 to N7). The filling times are 0.09s, 0.13s, 0.13s, 0.15s, and 0.14s between points (N2, N3), (N3, N4) (N4, N5), (N5, N6), and (N6, N7), respectively. Based on the distance between each point (in Figure (3-4)), average velocity can be deduced in these locations. The rate of change of velocity is linear with a very good approximation by representing the value 0.9944, as shown in Figure (3-6), thanks to linear regression and line equation. Given the linear slope obtained from the experimental data, this strongly suggests that the molten material's velocity is constant. Furthermore, the average velocity is calculated to be 0.7472m/s based on the line's slope. This constant velocity has two significant implications. The fluid is first at a temperature greater than 572°C and its viscosity is constant.

Second, the air trapped inside the plate is adequately evacuated and does not slow down the flow of the liquid. It should be mentioned that the Reynolds number in the plate is around 17600, and the flow is therefore turbulent.

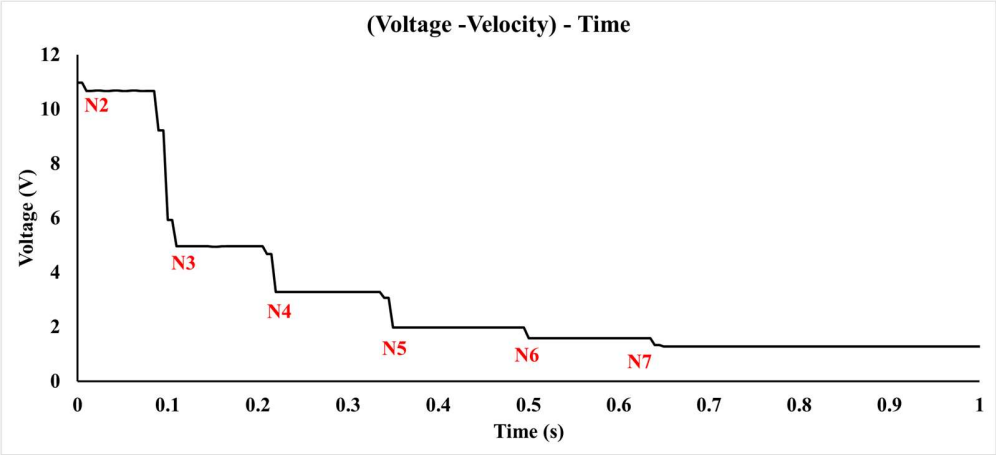

Figure 3-5 - Voltage and velocity versus filling time for different points of experimental test

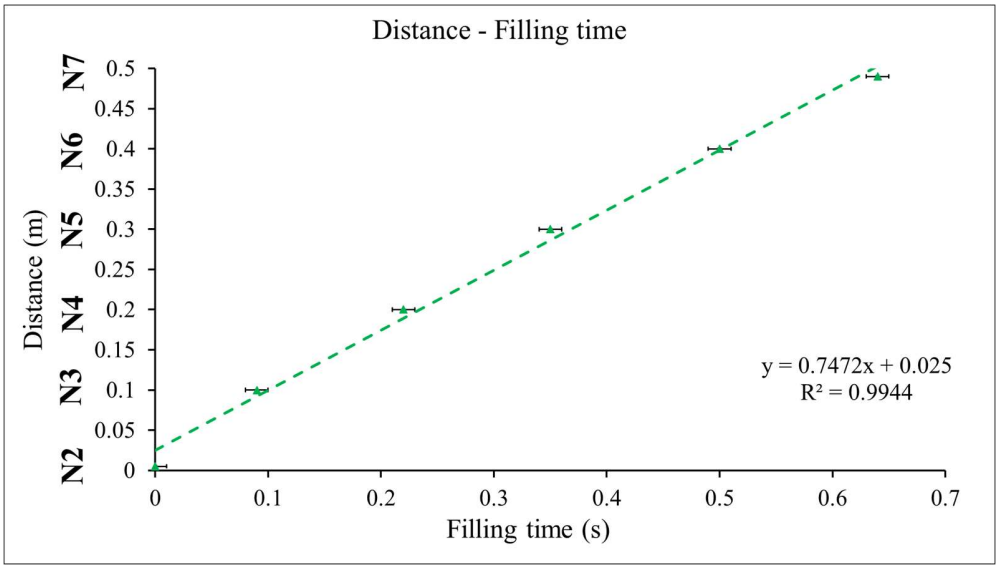

Figure 3-6 - Distance versus filling time for different points of experimental test

3.2.3.2 Temperature time curves

Figure (3-7) depicts the six temperatures evolution for (N1, N3, N4, N5, N6, and N8). The experimental results revealed temperature heterogeneities in the metal at the end of filling. The cooling curves have three domains. The temperature interval between the pouring temperature and the eutectic nucleation temperature is represented by the first domain. The alloy is in a liquid form during this period. A slope of this curve could be used to compute the "cooling rate" of the cast component. The solidification interval of the casting alloy is represented by the second domain. A solidification domain starts with an undercooling process that corresponds with the nucleation of the first eutectic germ and, as a result, the start of alloy solidification. After nucleation, eutectic germs grow, and this process is marked by a plateau of temperature at 570 °C. In eutectic alloys, the plateau duration is a significant correlate of the solidification time. Then in the third domain, the fully solid alloy is cooled until it approaches ambient temperature in the third and final domain. At time 0s in the graph, the acquisition system responds to metal for the first time during filling. As shown in the diagram, the thermocouples have a slight delay.

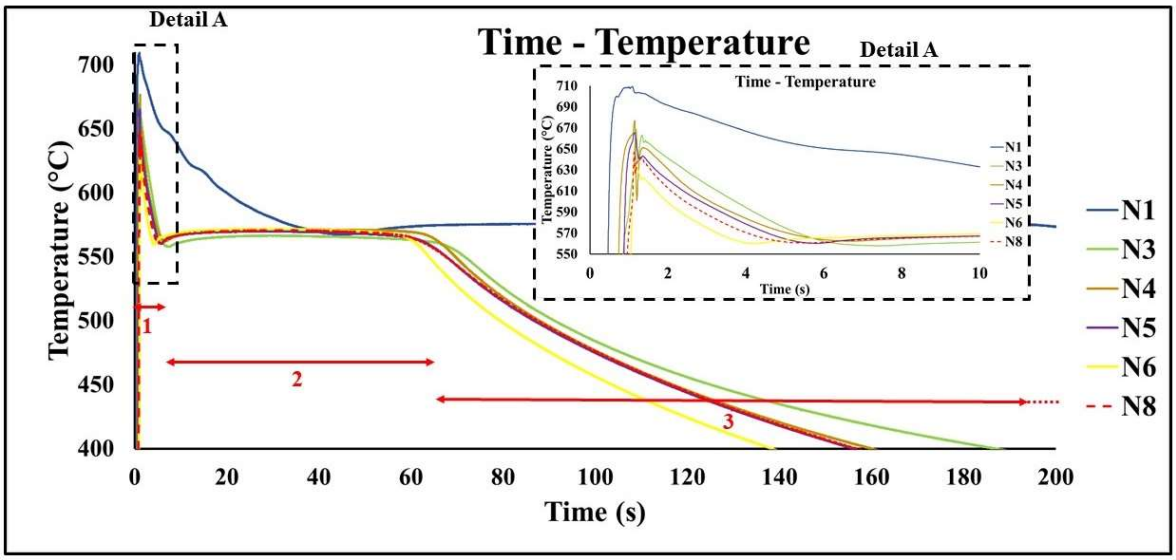

Figure 3-7 - Experimental cooling curves of AlSi13 alloy for points (N1, N3, N4, N5, N6, and N8)

N1 at the top of the sprue is used to estimate the initial temperature of casting. It should be noted that the molten material has been superheated to a temperature of 700 degrees with a good confidence interval, ensuring that the material is completely melted during the filling process. This ensures that the material remains in its liquid state throughout the filling process and does not solidify prematurely. Therefore, by superheating the material to the appropriate temperature, it is possible to achieve the necessary level of fluidity and viscosity for optimal filling. The solidification time at various sites is shown in Table (3-1). The temperature evolution trend for positions N3 through N6, as well as their solidification periods, is remarkably consistent. The cooling rate decreases as the influence of the end-of-plate boundary conditions reduces when we go farther from the plate's end. Similarly, as we get closer to the plate's end, the solidification time reduces gradually. Furthermore, the highest error percentage between the maximum and minimum

solidification times is expected 5.4 %. These results indicate that the length of the plate has little effect on the solidification time. The solidification times for locations N5 and N8 are 57s and 56.8s, respectively, with a 0.35% difference. It clearly indicates that the boundary conditions in the direction of the geometry's width have very little impact on the temperature change process, particularly the solidification time, which is negligible. Temperature changes at points N5 and N8 demonstrate that they have the same temperature process. Therefore, the solidification process can be regarded approximately as 1D.

Table 3-1 - Experimental solidification time for (N3, N4, N5, N6, and N8)

Position of thermocouples	Cooling rate (Liquid state) $(T.s^{-1})$	Solidification time (s)	Cooling rate (solid state) $(T.s^{-1})$
N3	**20.37**	**60.83**	**2.29**
N4	**21.08**	**57.5**	**2.52**
N5	**23.84**	**57**	**2.32**
N6	**21.30**	**57**	**2.73**
N8	**23.93**	**56.8**	**2.35**

3.3 Numerical simulation

In chapter two, a thorough explanation of the numerical simulation based on ProCAST commercial simulation and SPH approach is provided. Following are descriptions of the corresponding hydraulic and thermal boundary conditions mesh and convergence in ProCAST and SPH.

3.3.1 Initial and boundary conditions

3.3.1.1 Initial condition

Hydraulic: It should be highlighted that the fluid is initially motionless, as in the experiment done, while applying the initial and boundary conditions relevant to fluid dynamics. The fluid begins to flow as a natural consequence of gravity.

Thermal: The thermocouple (N1) is placed at the top of the sprue. The maximum temperature, relying on this, is roughly 700 °C, which is used as an initial condition for numerical simulation. The mold wall's initial temperature is about 20 °C, which is the same as the ambient temperature.

3.3.1.2 Boundary condition

Hydraulic: The WSHEAR (wall shear) method is used to account for a velocity boundary layer along the mold wall in ProCAST simulation. At the mold walls, it allows for non-zero or zero velocities. The velocity of the nearest core node is used to determine the velocity of the free surface at the mold wall (i.e. closest node in the volume). The velocity of this nearest node multiplied by a coefficient called WALLF equals the surface velocity at the free surface. The value of WALLF is set to 0.99, which correlates to more wall slips. In addition, Perfect slip is defined as the boundary condition between the wall and the fluid in SPH method. Furthermore, the symmetric boundary condition for walls in the direction perpendicular to the transverse axis is used in ProCAST simulation.

Thermal: In order to model cooling and solidification, the Neumann boundary condition (Conduction) is employed in both WCSPH and ProCAST simulations to estimate heat extraction ate metal/mold interface. The heat flux exiting the mold surface is supposed to be constant by three levels as illustrated in Table (3-2) and Figure (3-8).

The cooling of molten metal above liquidus temperature, the solidification process between liquidus and solidus temperature, and the cooling of solids at temperatures below solidus temperature are the three areas covered. The values are calculated based on experimental data using one-dimensional calculations in such a way those three zones (liquid metal cooling, phase transition, and solid metal cooling) were considered. The way for calculating the value of q using one-dimensional equations is shown below. It should be mentioned that T_0, T_L, T_S, and T_{end} represent initial, liquidus, solidus, and temperature at 100s. In addition, the average experimental periods $(t_{\exp})$ between corresponding temperatures in each location (N3 to N7) were utilized to derive these values.

Table 3-2 - One-dimensional equation to obtain Neumann boundary condition in three different zones

Zone (1)	$Q = -K\frac{\partial T}{\partial x} = \frac{\rho e C_p (T_0 - T_L)}{t_{\exp}} \approx 133000 \, W/m^2$
Zone (2)	$Q = -K\frac{\partial T}{\partial x} = \frac{\rho e L + \rho e C_p (T_L - T_S)}{t_{(\exp)}} \approx 61000 \, W/m^2$
Zone (3)	$Q = -K\frac{\partial T}{\partial x} = \frac{\rho e C_p (T_S - T_{end})}{t_{(\exp)}} \approx 19000 \, W/m^2$

In the first period, when the mold is still cold and the metal is liquid, the heat extraction is high owing to the thermal gradient between the mold and the molten material, q is equal to $(133000 \, W/m^2)$. The value of q then reduces to the value of $(61000 \, W/m^2)$ in the second stage, and to $(19000 \, W/m^2)$ in the third or final stage.

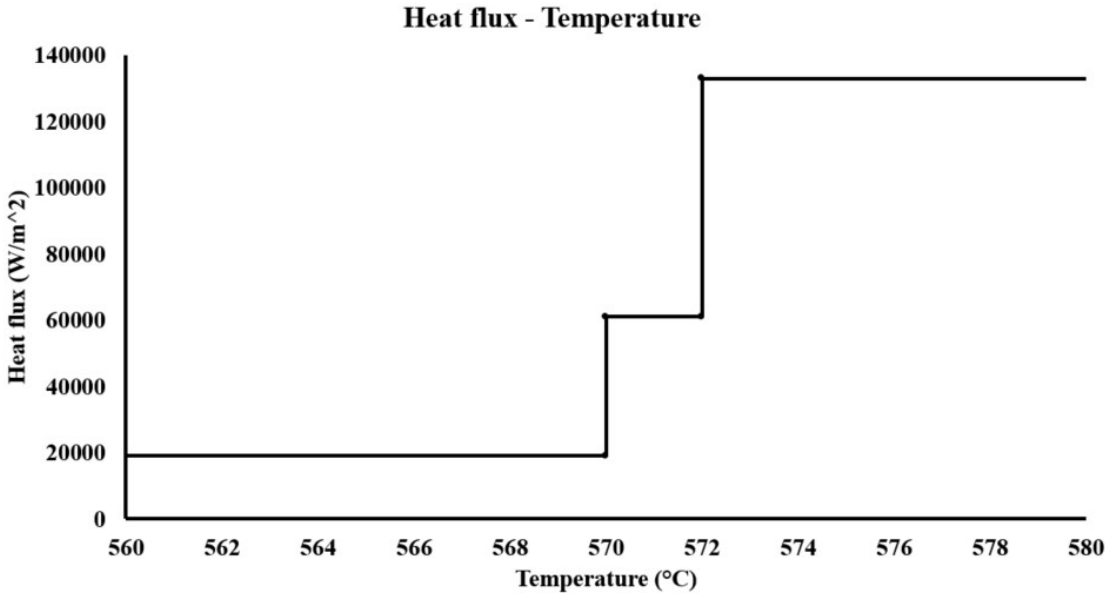

Figure 3-8 - q values of Neumann boundary condition versus temperature for WCSPH and ProCAST method

The ProCAST program has a limitation on the use of Neumann thermal boundary conditions. The Neumann boundary condition cannot be imposed as a function of temperature; therefore, in this software, it must be defined as a function of time. Because of this problem, it will be problematic if the casting geometry has different thicknesses. By applying this boundary condition, for example, Part A's solidification time could differ from Part B's, thus when the boundary condition is adjusted at a certain point in time, Part A could still be in the liquid cooling zone while Part B has into the solidification zone. The curves in one zone can subsequently have two different slopes, which is inappropriate. The average time of each zone is also calculated for ProCAST simulation in order to apply the Neumann boundary condition there.

In term of critical parameter of WCSPH to model filling of casting process, the value of artificial sounds speed is obtained by using criteria of choosing c_0 which is explained in following:

$$c_0^2 \geq \max\{\frac{U_0^2}{\delta\rho}, \frac{\| g \| L_0}{\delta\rho}, \frac{\mu U_0}{\rho_0 L_0 \delta\rho}\} \quad (3\text{-}1)$$

Based on experimental measurements, the average velocity of molten metal (1 m/s) is utilized to calculate the artificial sound speed. While the incompressible technique was used in ProCAST, the artificial sound speed value is obtained at 10 m/s. It should be mentioned that the maximum variation of density $(\delta\rho)$ is around 1%.

3.3.2 Mesh and convergence

CAD models of the part, the gating system, and the sand mold are generated using CATIA V5 software before being imported by ProCAST. The model is meshed using linear tetrahedral elements with mesh size 1.5mm for the part and mold. To check that ProCAST and SPH simulation are mesh-independent, the mesh size is determined through several mesh refinement trials. Figure (3-9) depicts the trend of mesh independence for filling of casting process. As shown in the figure, when filling simulations using ProCAST software with different numbers of cells provide results that are similar and do not change, we can say that the results are independent of mesh. The ProCAST simulation results show that while the cell size is high, a lower velocity value is predicted, which converges as the cell size decreases. The SPH approach reverses the trend of change. Velocity is overestimated and converges as the number of particles increases. As a result, the number of cells used in ProCAST simulation is chosen at 529133 corresponding to 1.5 mm in size. When the number of particles in the SPH technique exceeds 10491 corresponding to 1mm distance between each particle, the results become independent of the number of particles.

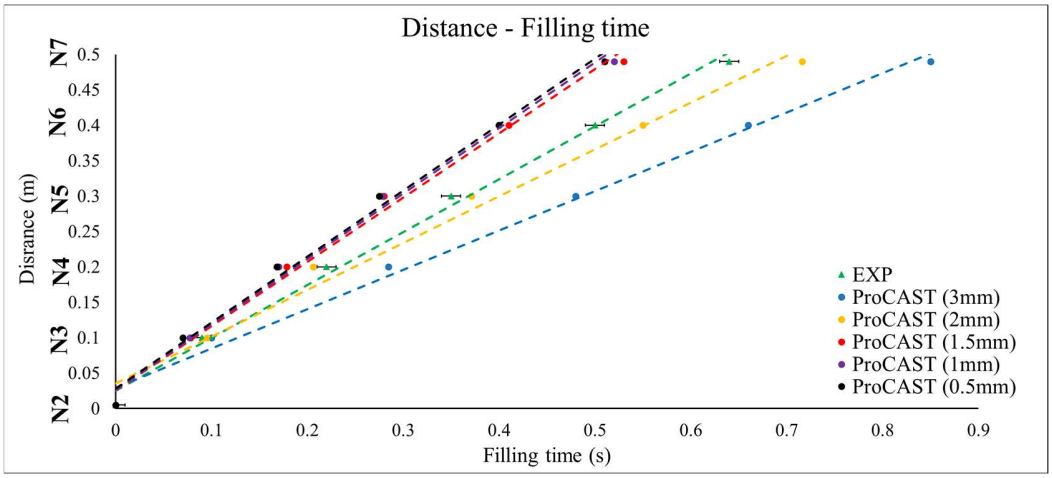

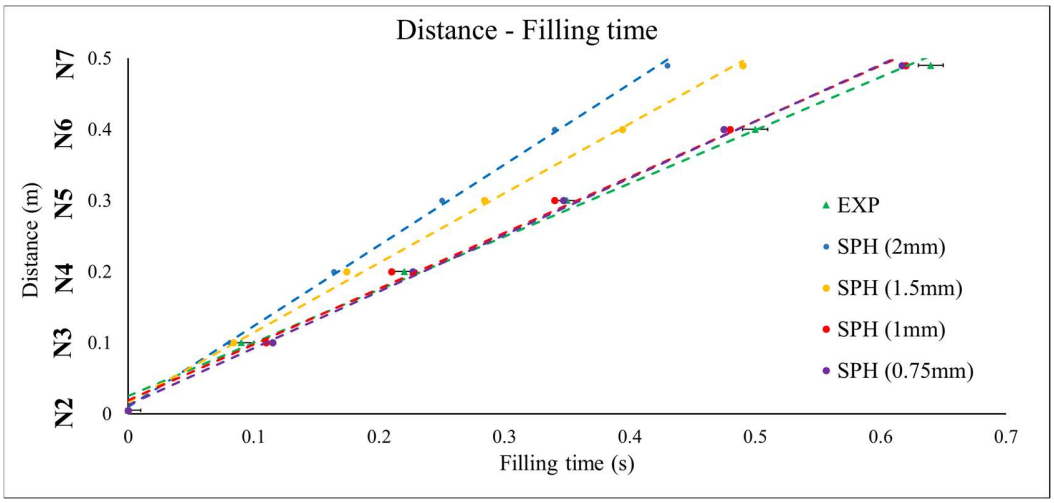

Figure 3-9 - Mesh independency of filling step for ProCAST and SPH simulation

Figures (3-10) and (3-11) illustrate the schematic mesh in ProCAST and the particle distribution using the 2D SPH approach. It should be noted that the calculation time for the 2D SPH method and 3D ProCAST simulation using the appropriate meshes is equivalent to roughly one day. It should be noted that for the SPH approach, the time step value is $2e^{-4}$ s.

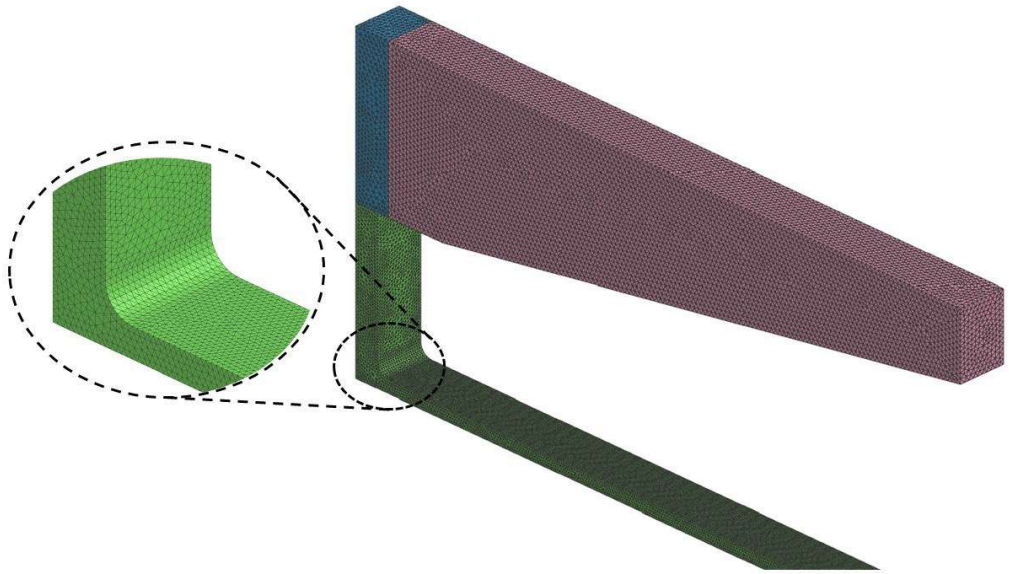

Figure 3-10 - Schematic of mesh of ProCAST simulation

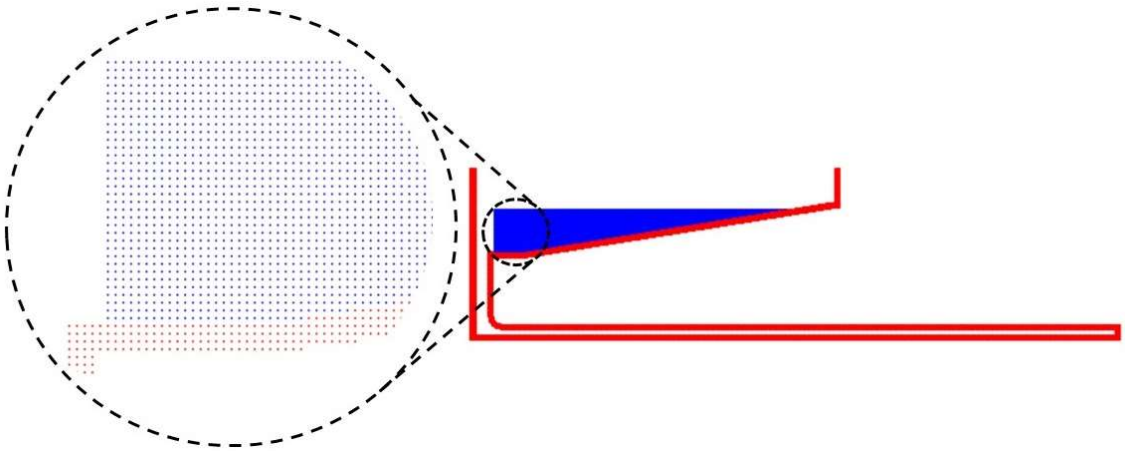

Figure 3-11 - SPH geometry schematic with 1mm distance between particles: blue (mold), red (molten metal)

3.4 Results

3.4.1 Study of filling step

The metal filling time at various positions in the part is shown in Figure (3-12) for experimental data, SPH, and ProCAST simulation. It should be mentioned that the time between filling N1 (top of sprue) and N2 (bottom of sprue) has been removed from the total filling time, and N2 is regarded as a reference point in Figure.

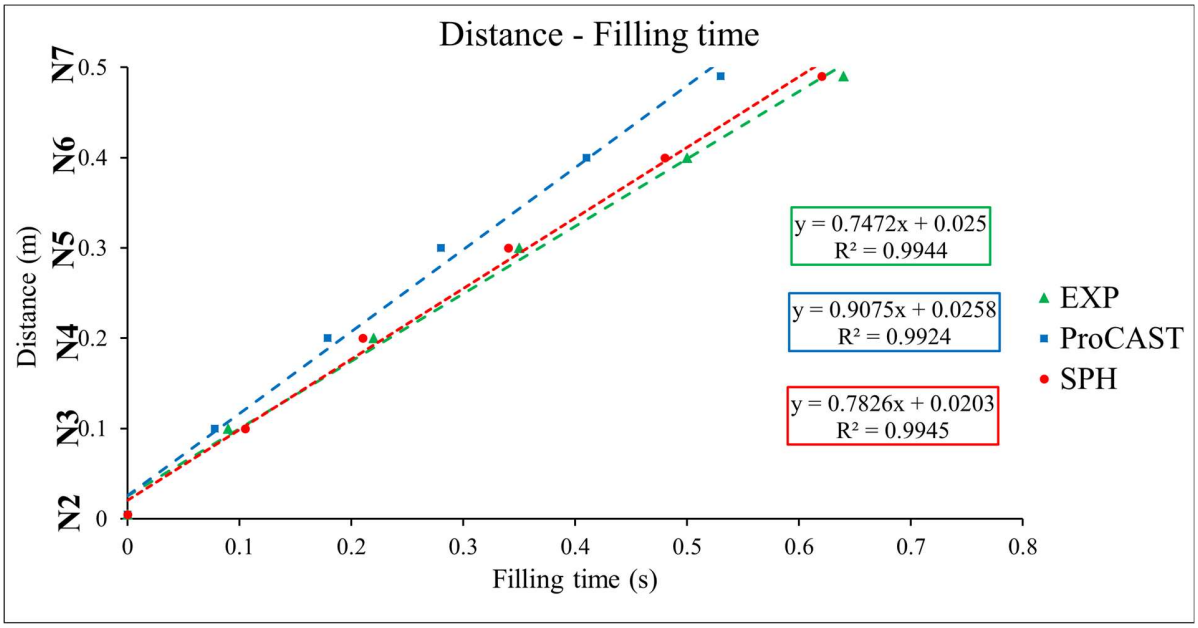

Figure 3-12 - Length of plate versus filling time for Experiment, ProCAST simulation and SPH method

Figure (3-12) shows that for all three techniques, the correlation between distance and time is linear, resulting in a constant velocity value. The discrepancy between the experimental velocity

(0.7472 m/s) and the velocity of ProCAST (0.9075 m/s) and SPH simulations (0.7826 m/s) is 21.4% and 4.63%, respectively.

N2 is 5mm distant from the start of the plate. The experimental analysis reveals that it takes 0.09s to go from N2 (5mm) to N3 (100mm), SPH approach overestimates it (0.105s), and the simulation using ProCAST underestimates it (0.078s). The experiment and SPH are increasingly consistent with each other as we go from N3 (100mm) to N4 (200m), and the SPH approach is able to replicate filling time (between N3 and N4) by 4.76% error. ProCAST and experimental filling time at N4 have a discrepancy of 25%. The gap between ProCAST and experimental data increases considerably by passing the N4 (200m) and reaching the N5 (300m), reaching 29.6% at this point. The filling time, does match well in N5 between the SPH technique and experimental data, by a variation of 2.94 %. The difference in filling time between ProCAST and SPH is 20.95 % while advancing to the end of the plate at position N6, which is 400 mm from the start of the plate. The SPH approach and the experiments have a roughly 4% variation in filling time. The filling time for the SPH method at location N7, which is 10 mm from the plate's end, is around 0.62s, whereas it is 0.64s in experiments and 0.53s in the ProCAST simulation. The experimental data and the SPH approach differ by 3.125 % and 14.5 %, respectively.

Despite the fact that the SPH solution is significantly closer to the experiment, both simulations indicate some errors. The difference between the experimental and SPH simulations is never more than 5%, demonstrating that the SPH approach successfully predicted fluid flow. SPH results show a slight over prediction on filling time until N4, and a corresponding under prediction beyond that. The trend line of filling time using ProCAST software is much lower than the experimental results

and the SPH technique. In a conclusion, the divergence between experimental and ProCAST simulation is larger than 15% in most positions.

The SPH method is a Lagrangian method that can more accurately simulate the filling of gravity castings by using artificial viscosity to increase stability. To keep the particles from separating, the viscosity level is set higher. Using the ProCAST simulation and SPH methodologies, Figure (3-13 to 3-19) depicts the temperature and velocity field of filling step at 0.1s, 0.2s, 0.3s, 0.4s, 0.5s, 0.6s, and 0.74s.

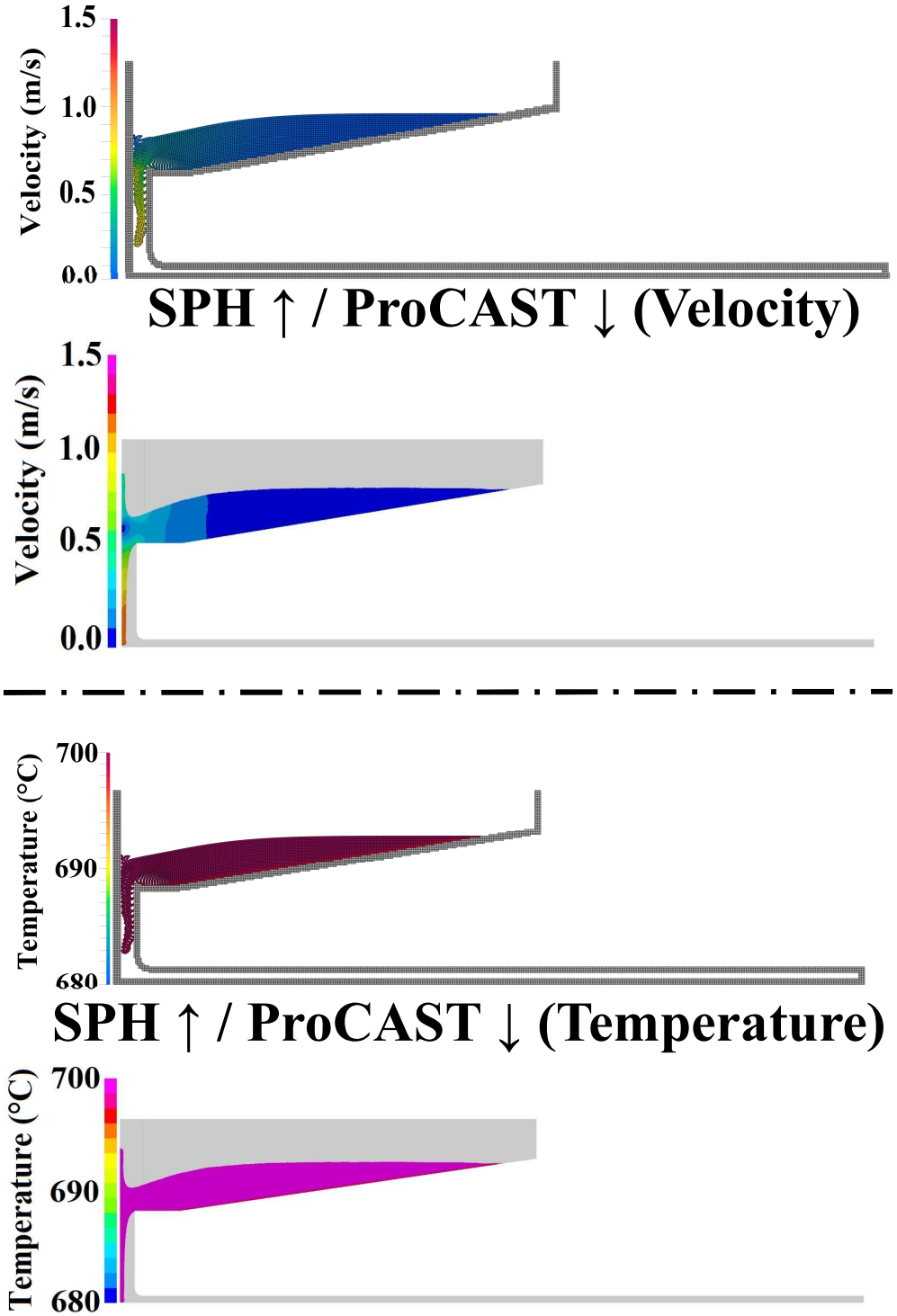

Figure 3-13 - Temperature and Velocity field during filling step of SPH and ProCAST simulation (0.1s)

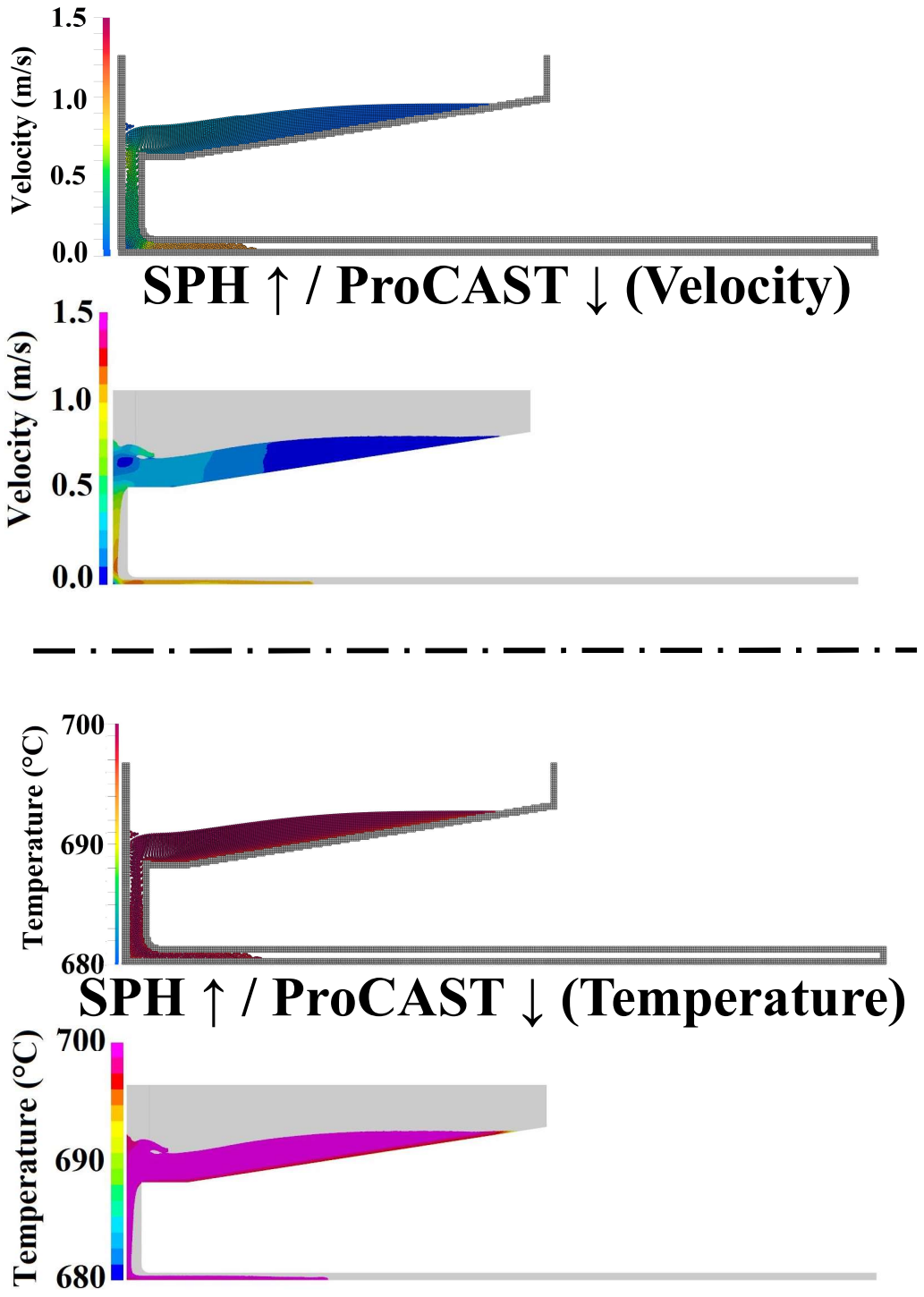

Figure 3-14 - Temperature and Velocity field during filling step of SPH and ProCAST simulation (0.2s)

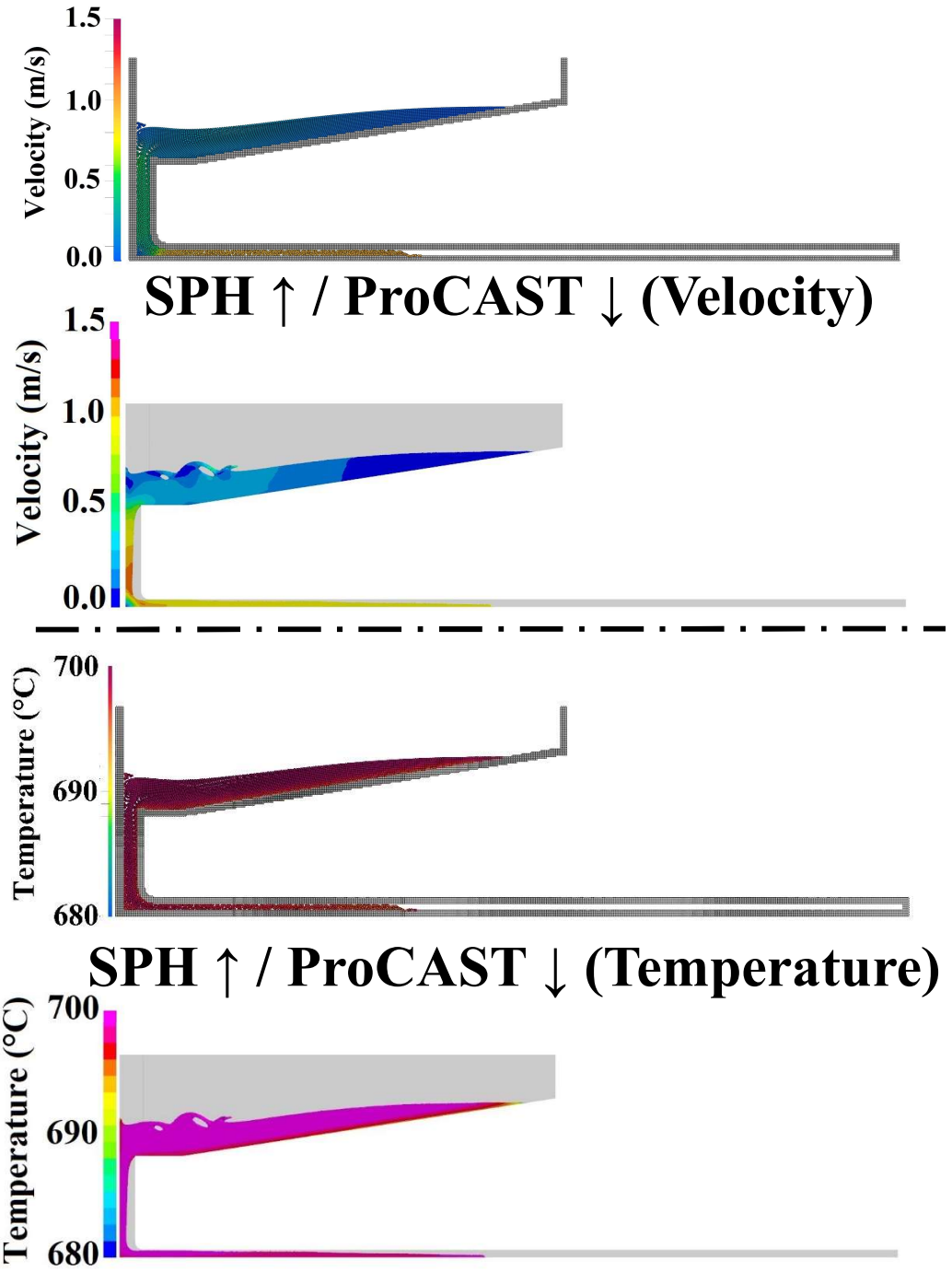

Figure 3-15 - Temperature and Velocity field during filling step of SPH and ProCAST simulation (0.3s)

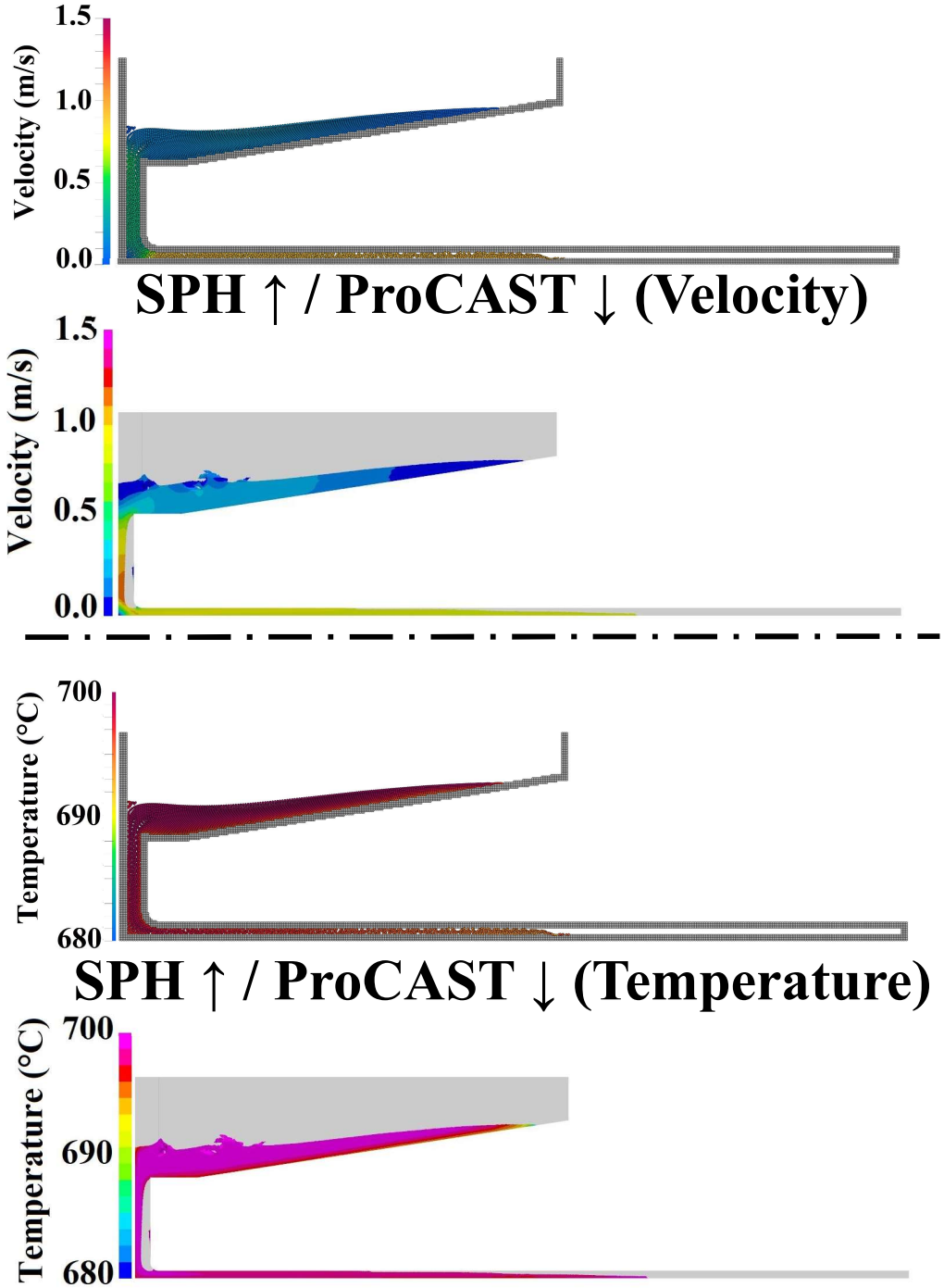

Figure 3-16 - Temperature and Velocity field during filling step of SPH and ProCAST simulation (0.4s)

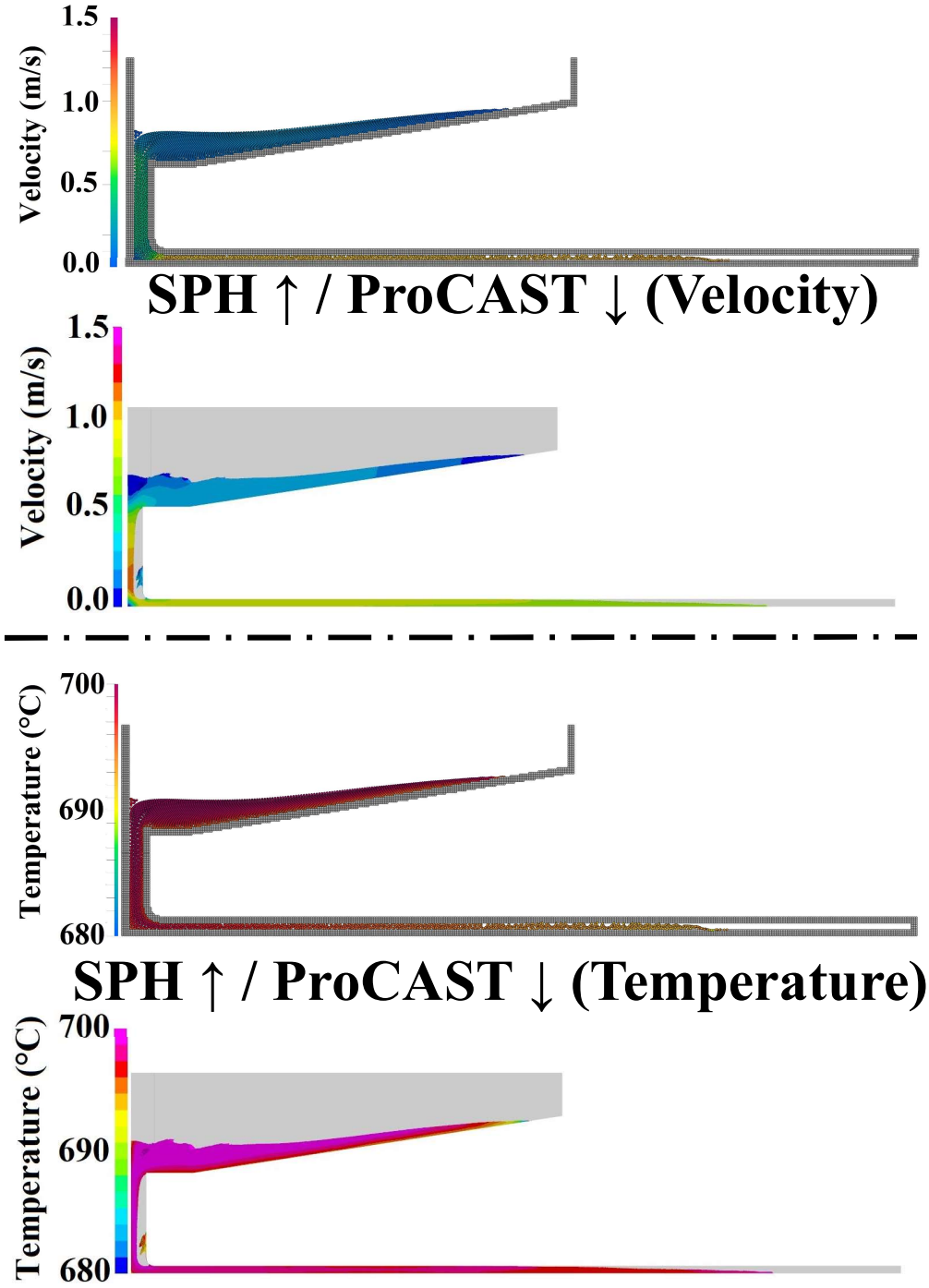

Figure 3-17 - Temperature and Velocity field during filling step of SPH and ProCAST simulation (0.5s)

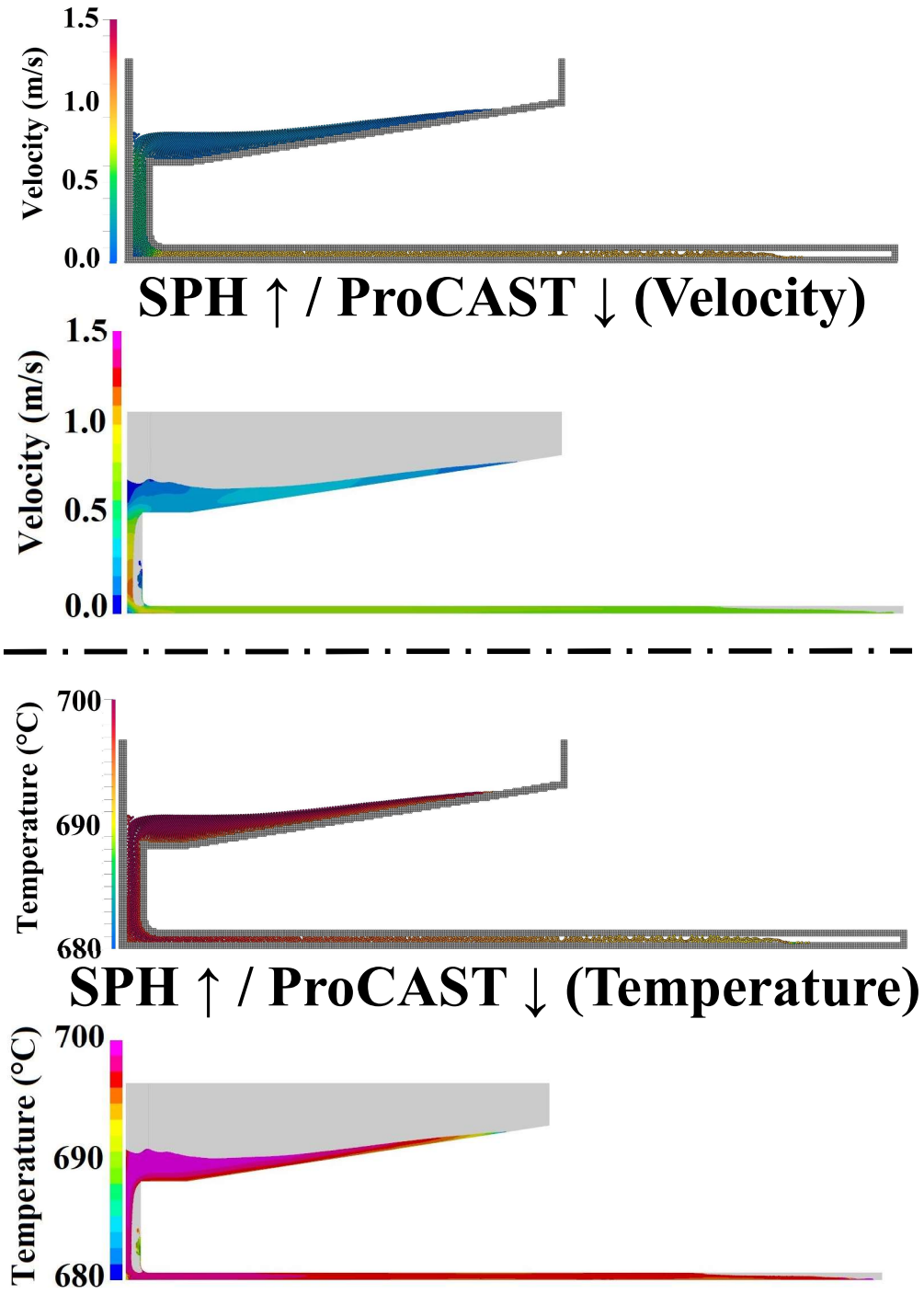

Figure 3-18 - Temperature and Velocity field during filling step of SPH and ProCAST simulation (0.6s)

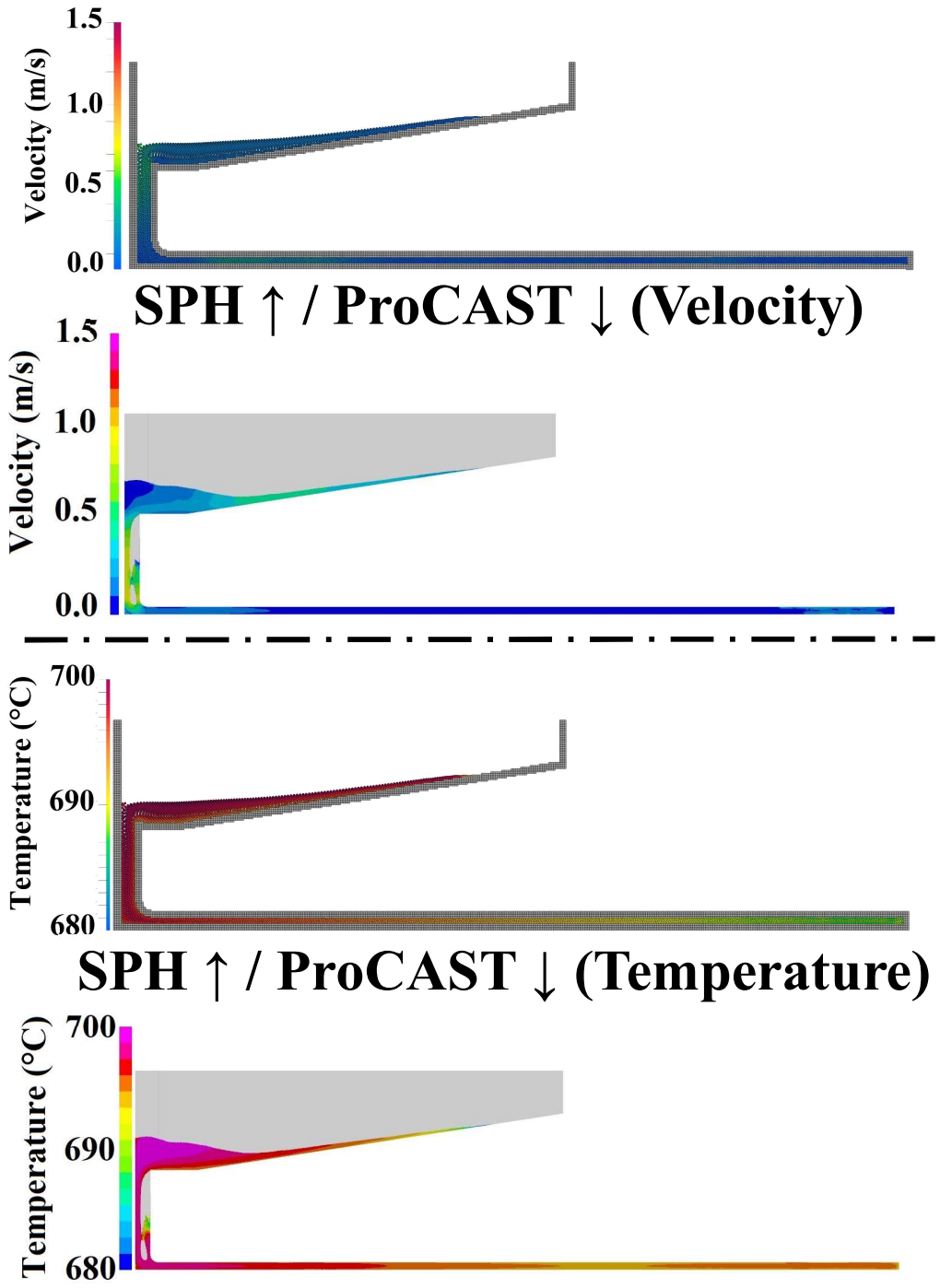

Figure 3-19 - Temperature and Velocity field during filling step of SPH and ProCAST simulation (0.74s)

In terms of velocity field, Figure (3-13) shows that the amount of molten metal entering the sprue in ProCAST is more than SPH at the beginning of filling (0.1s). In ProCAST simulation, the fluid going through the sprue sticks to one side and moves downward, having reached the bottom of the sprue after 0.1s. With SPH technique, on the other hand, approximately 2/3 of the sprue is filled by the maximum velocity of 0.9m/s. Regarding the temperature field, it should be underlined that the temperature in both simulations is 698°C at the end of 0.1s.

At (0.2s), the differences between ProCAST solution and the experiment get larger, while the SPH solution compares more favorably based on comparison with experimental results. The fluid has moved to a length of 100mm in the ProCAST approach, whereas it has advanced to a length of 75mm in SPH approach in 0.2s. A thin layer of molten material is flowing over the plate in the ProCAST process, approximately half the thickness of the plate, and as the flow continues, the thickness decreases. It is worth noting that half of the sprue in ProCAST is still empty at this point, while in the SPH method, it is entirely filled. The velocity of the molten metal is higher near the bottom of the plate than at the top of it in the SPH method due to gravity. This is assumed to be due to the simulation's absence of air. The temperature begins to reduce slowly after 0.2s, and variations in the molten metal are visible near the ramp's surface, with temperatures reaching 695°C in certain positions of SPH.

In the ProCAST technique, molten metal passe more than half the plate at time 0.3s, whereas in the SPH approach, it is still a long way from filling half the plate (Figure (3-15)). In the pouring basin and plate, temperature changes from the walls to the inside of the flow in 0.3s are clear for both numerical methodologies.

As demonstrated in Figure (3-16), half of the plate is filled in SPH method, whereas the filling process in ProCAST simulation approached 60% of the plate. Figure (3-16) indicates that temperature continues to drop in the plate when the temperature in the SPH technique approaches 692°C, whereas the minimum temperature in ProCAST approach remains 695°C along the plate.

Figure (3-17) shows that in SPH approach and ProCAST simulation at 0.5s, filling reaches over 65% and 75%, respectively. At 0.5s, advancing from the bottom of the sprue to the end of the plate using the SPH technique, it is clear that the temperature progressively decreases from 697°C to 690°C as we go closer to the end of the plate. Regardless of the fact that this pattern is less visible, the temperature gradient in the middle and even in front of flow utilizing the ProCAST approach is still 700°C.

The filling stage is practically complete in frame 0.6s and ends in time 0.62s, as seen in Figure (3-18). The SPH method fills 80 percent of the plate after 0.6 seconds.

To sum up, Figure (3-19) presents the state of filling using ProCAST and SPH at 0.74s. The period from the start of the filling to the completion of the filling corresponds to 0.62s in ProCAST method and 0.74s in the SPH corresponding to 19.3% gap. The highest velocity in the filling stage of the SPH approach is roughly 0.9m/s, while it is around 1.1m/s for ProCAST. It should be noticed that the SPH method's filling temperature balance is more homogeneous in 0.74s than ProCAST. The temperature in some areas of the plate is lower than the end of plate at the end of filling step in ProCAST simulation. The SPH shows sustainable agreement with experiment at all late stages of the filling process, with accurate estimates of the speed of fluid front propagation and filling

times. The ProCAST simulation, on the other hand, quickly diverges from the experimental flow, with considerable inaccuracies anticipated in the filling time estimate.

3.4.2 Study of solidification step

The cooling curves for points N3, N4, N5, and N6 as well as cooling rate and solidification time for three zones are presented in the Figure (3-20 to 3-23) and Table (3-3), respectively. Since the thermal properties of the sand and the alloy were not experimentally described, the comparison between experimental and numerical results is qualitative.

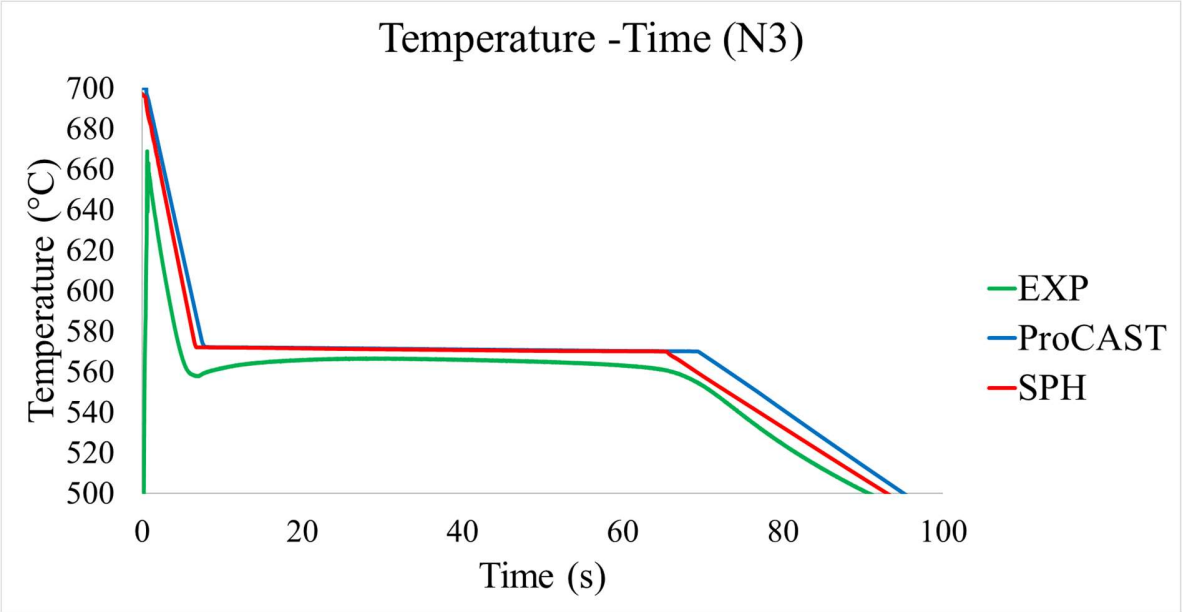

Figure 3-20 - Temperature evolution of point N3

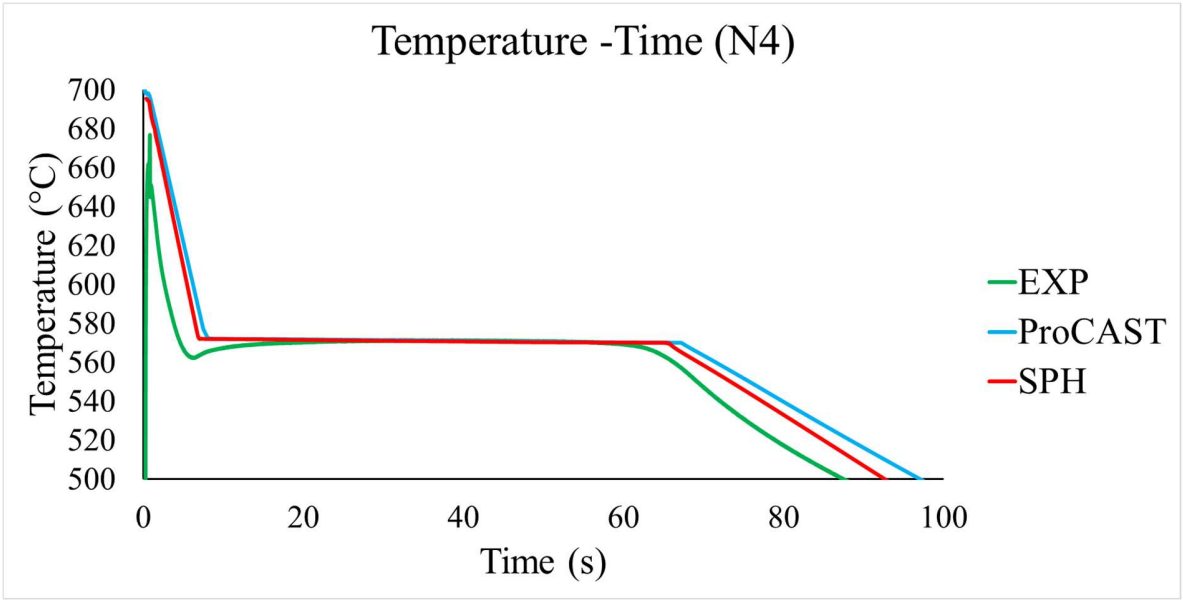

Figure 3-21 - Temperature evolution of point N4

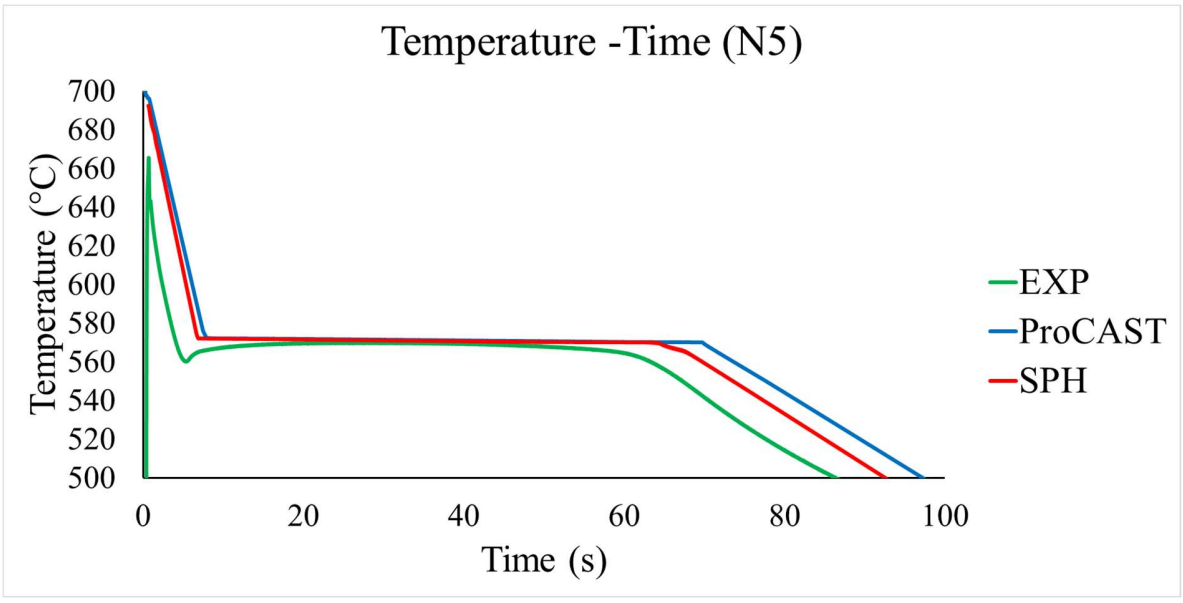

Figure 3-22 - Temperature evolution of point N5

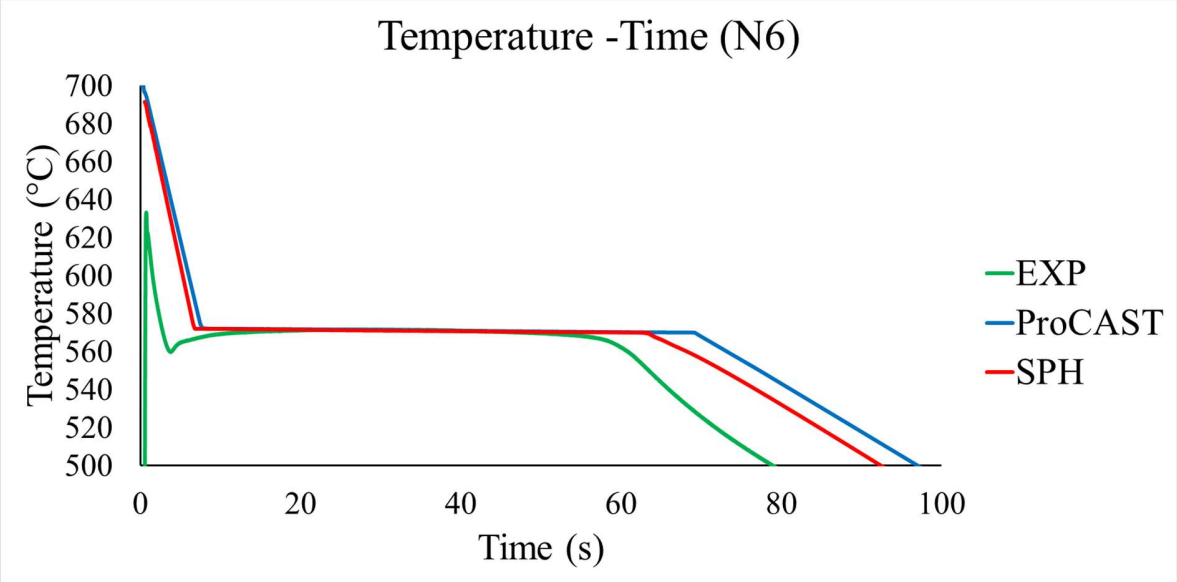

Figure 3-23 - Temperature evolution of point N6

Table 3-3 - Comparison of temperature drop rates (C°/s) in liquid (zone 1) and solid (zone 3) and solidification time (s) (zone 2) for N3, N4, N5 and N6 using experimental data, SPH and ProCAST

Methods/Points	N3			N4			N5			N6		
Zone	1	2	3	1	2	3	1	2	3	1	2	3
Experiment	20.37	60.83	2.29	21.08	57.5	2.52	23.84	57	2.32	21.30	57	2.73
SPH	19.44	59.32	2.12	18.65	58.18	2.57	19.05	56.54	2.45	19.02	56.1	2.43
ProCAST	15.61	60.64	2.18	15.01	58.51	2.34	14.7	60.75	2.55	15.38	60.37	2.51

Table (3-3) compares four measures at positions N3 to N6, the average cooling rate between maximum temperature and liquidus temperature (zone 1), the cooling rate at solid state (zone 3) and solidification time (zone 2). Cooling rates are given in degrees Celsius per second $(C^{\circ}/_{S})$ in zone 1 and 3, and solidification time for zone 2 in seconds.

N3: The results of Point N3, as shown in Table (3-3) and Figure (3-20), indicate that the values of cooling rate between experiment $(20.37\,C^{\circ}/_{S})$ and SPH $(19.44\,C^{\circ}/_{S})$ are consistent whereas there is a significant difference with the cooling curve of ProCAST $(15.61\,C^{\circ}/_{S})$. The solidification time between experiment and ProCAST, as well as between experiment and SPH, is consistent with a difference of 0.31% and 2.48%, respectively, according to the data in Table (3-3). ProCAST's rate of temperature $(2.18\,C^{\circ}/_{S})$ decline in the solid zone of N3 is closer to experiment than $(2.29\,C^{\circ}/_{S})$ the SPH technique $(2.12\,C^{\circ}/_{S})$ but cooling is underestimated in both simulations.

N4: Figure (3-21) shows the temperature evolution for N4 using experimental and numerical data. The rate of temperature drop for experimental data at liquid and solid states is larger compared to N3, whereas numerical simulations SPH and ProCAST have reduced at point N4 in the first zone. In first zone, the experimental data with SPH and ProCAST differ by 11.53% and 28.8%, respectively, due to this issue. By moving forward the boundary conditions at the end of the plate, the solidification time in all three methods has been slightly reduced in the second zone. The disparity between the solidification time of experimental data and numerical findings is less than 2%. The rate of cooling in the solid state of SPH for N4 is more valid than the ProCAST simulation. It should be noted that SPH overestimates solidification time, whereas ProCAST underestimated.

N5: In the first zone of N5 which is shown in Figure (3-22), the rate of temperature decrease is still higher in experimental data than in both numerical simulations. It should be noted that the SPH method is still much closer to the experimental data than ProCAST simulation. For experiment and SPH, solidification time decrease with a low slope, however, this value grows in ProCAST. In the third area, both numerical techniques underestimate the rate of temperature drop, with SPH being closer to experimental data.

Figure (2-24) illustrates the changes in solid fraction over time for N5 in the SPH model, where N5 has been chosen as a representative case. To achieve this, the Carman-Kozeny equation (2-57) has been integrated into the momentum equation, and the sine function of the solid fraction (2-63) has been utilized. The figure indicates that the solid fraction is one when the alloy is in a liquid state, 0 when it is in a solid state, and in the mushy region, the alloy lies between these two values. The slope of the curve demonstrates a relatively constant change from 1 to 0.1, followed by a gradual decrease from 0.1 to 0.

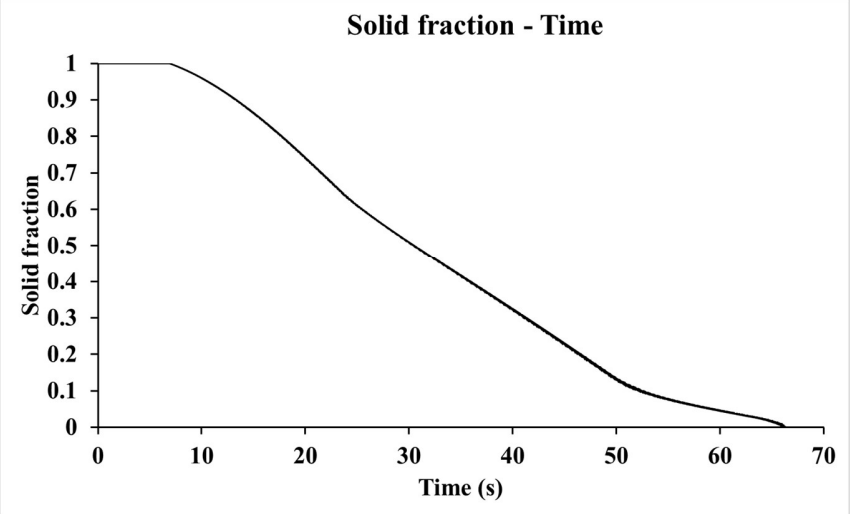

Figure 3-24 - Solid fraction versus time for N5 using SPH approach

N6: The rate of temperature drop in the experimental data remains higher than the simulation at point N6 in Figure (3-23); the difference between the experiments and SPH is 10.70 %. In addition, the gap between the experiments and ProCAST is 27.80%. It should be emphasized that experimental data and SPH show the shortest solidification time at this point. When compared to SPH, the ProCAST approach is more consistent with experimental data in the solid state of N6.

To summarize, the cooling rate for all positions in the first zone is greater for the experiment, while the SPH approach is significantly capable of predicting such temperature reduction rate with global maximal error of 11.73%. The gap between experiential data and ProCAST is higher, ranging between 24 and 39 %. It is worth mentioning that the experimental test exhibits a faster temperature decrease rate during the filling process compared to the two numerical methods. This is due to the fact that the free surface of the molten material comes in contact with air during the filling step. Upon initial observation of Figures (3-20) to (3-23), it might appear that the solidification time for the experimental method is shorter than that of the numerical methods. However, upon closer examination, it becomes apparent that the solidification time in the experimental method is nearly the same as that of the numerical methods. This is because the solidification process starts and finishes earlier in the experiment due to the presence of air during the filling process.

In the solidification zone, the solidification time should decrease, as one gets closer to the end of the plate, which is observed and well predicted in experimental data and the SPH technique, unlike ProCAST. It should also be highlighted that the highest difference between the maximum and minimum solidification time is 6.3 %, 5.4 %, and 3.7 % for experiment, SPH, and ProCAST. This clearly demonstrates that the boundary condition at the end of the plate has little impact on

solidification time. The most substantial variation among experimental data and SPH is 11% and experimental data and ProCAST is 9%.

It should be mentioned that in the third zone, the solid cooling rate value ranges from $(2.12\,{}^{C^\circ}\!/_{s})$ to $(2.73\,{}^{C^\circ}\!/_{s})$ for all four points and all approaches. Additionally, SPH technique predicted more accurately at points N4 and N5, and ProCAST approach performed better at points N3 and N6. It is therefore impossible to determine with certainty whether method models better cooling in zone 3.

In the whole zone 1 and 2, SPH is able to predict the trend of temperature evolution better than ProCAST. The results demonstrate that the two numerical approaches differ in the filling time and cooling during the filling stage as well as the cooling and solidification times during the solidification stage of the gravity casting process. The variations between the results of these two numerical modelings can be attributed to a two important factors. Firstly, it could well result from fundamentally different methods, especially during filling. ProCAST uses the Eulerian approach (Finite Element Method), while SPH uses the Lagrangian approach. It should be noted that the Navier-Stokes equation's pressure gradient and diffusion term are derived in different ways using the two different numerical approaches, which could lead to discrepancies during the filling of gravity castings. Moreover, continuity and momentum equations contain mathematical operators like gradient, divergence, and Laplace and the discretization methods used in FEM and SPH are different, the results may vary.

Secondly, different definitions of thermophysical parameters, such as heat capacity and density, lead to a rise in the difference between SPH and ProCAST in terms of cooling and solidification.

In comparison to SPH simulation, which uses the following equation to define heat capacity and density, ProCAST simulation uses predefined data bases for properties. Additionally, latent heat is added as an equivalent heat capacity to the solidification term in the energy equation of SPH, whereas it is added as a source term in ProCAST.

$$< . >= (1-\phi)(.)_s + \phi(.)_l \tag{3-2}$$

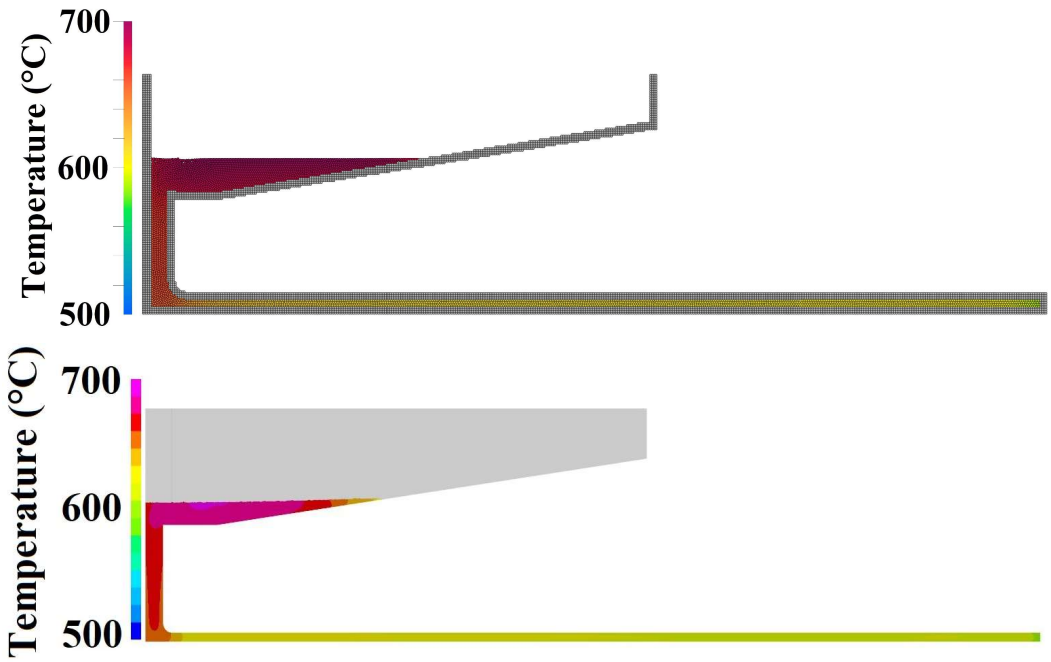

Figure 3-25 - Temperature field during cooling of simulation using SPH (top) and ProCAST (bottom) at 5s

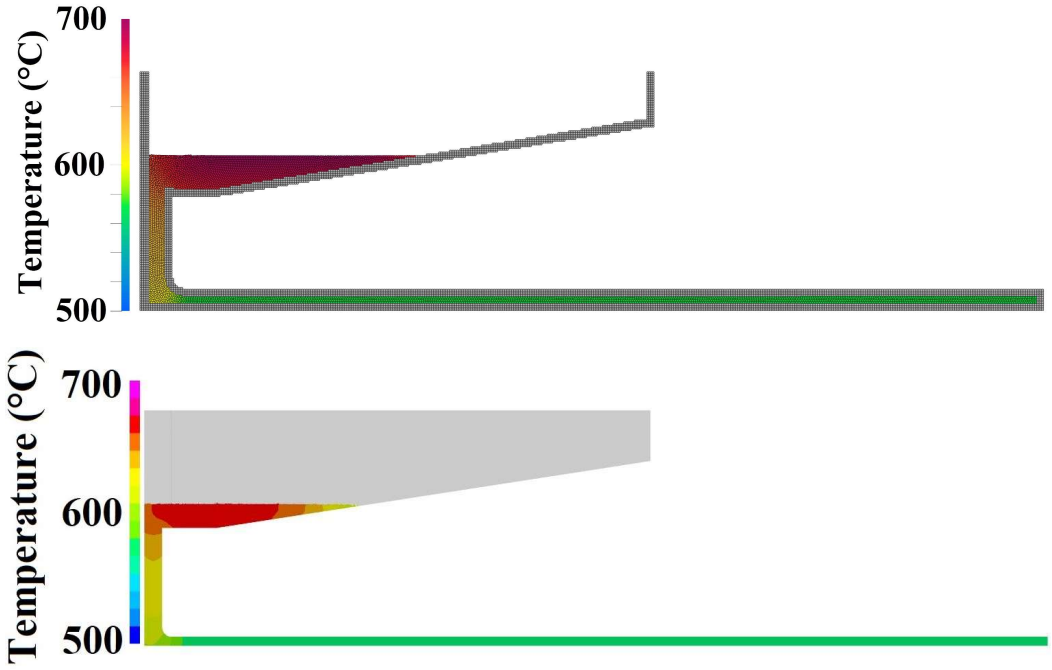

Figure 3-26 - Temperature field during solidification of simulation using SPH (top) and ProCAST (bottom) at 10s

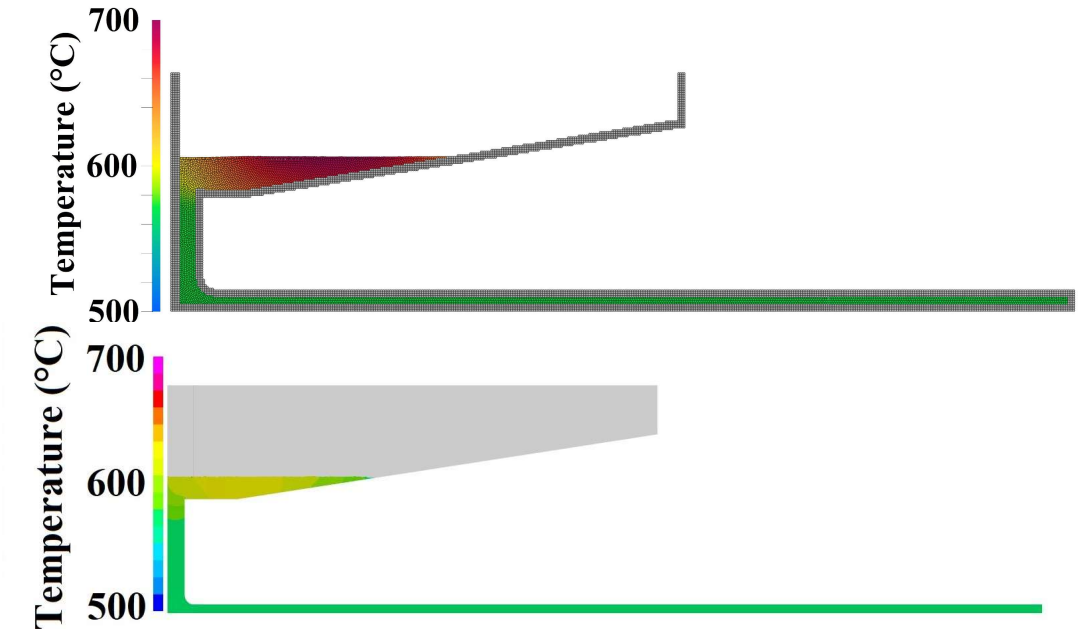

Figure 3-27 - Temperature field during solidification of simulation using SPH (top) and ProCAST (bottom) at 30s

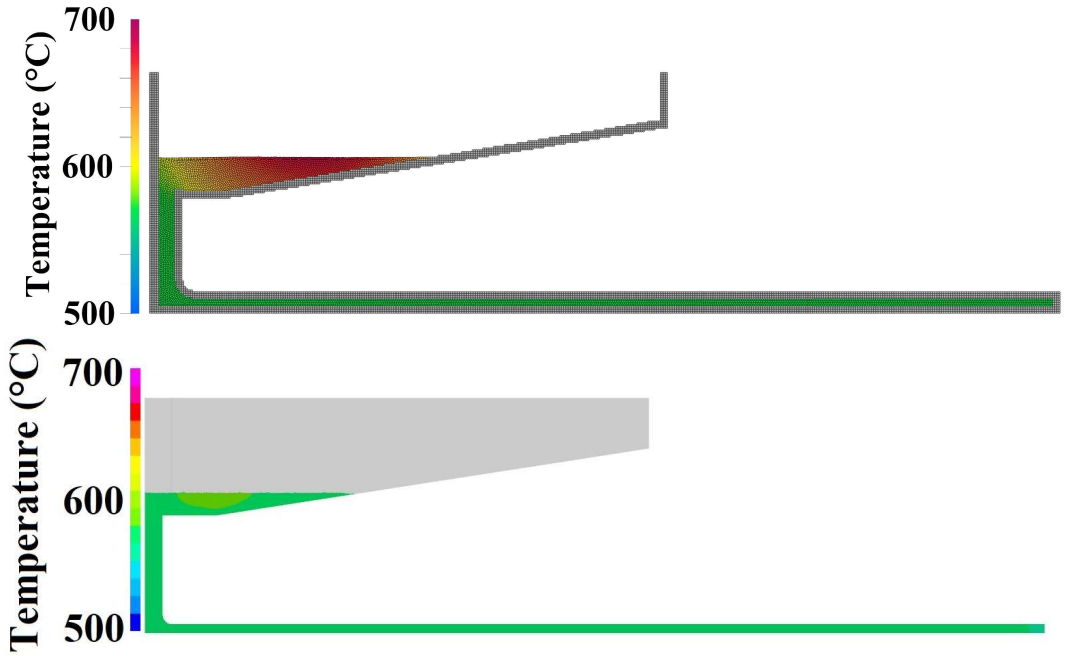

Figure 3-28 - Temperature field during solidification of simulation using SPH (top) and ProCAST (bottom) at 50s

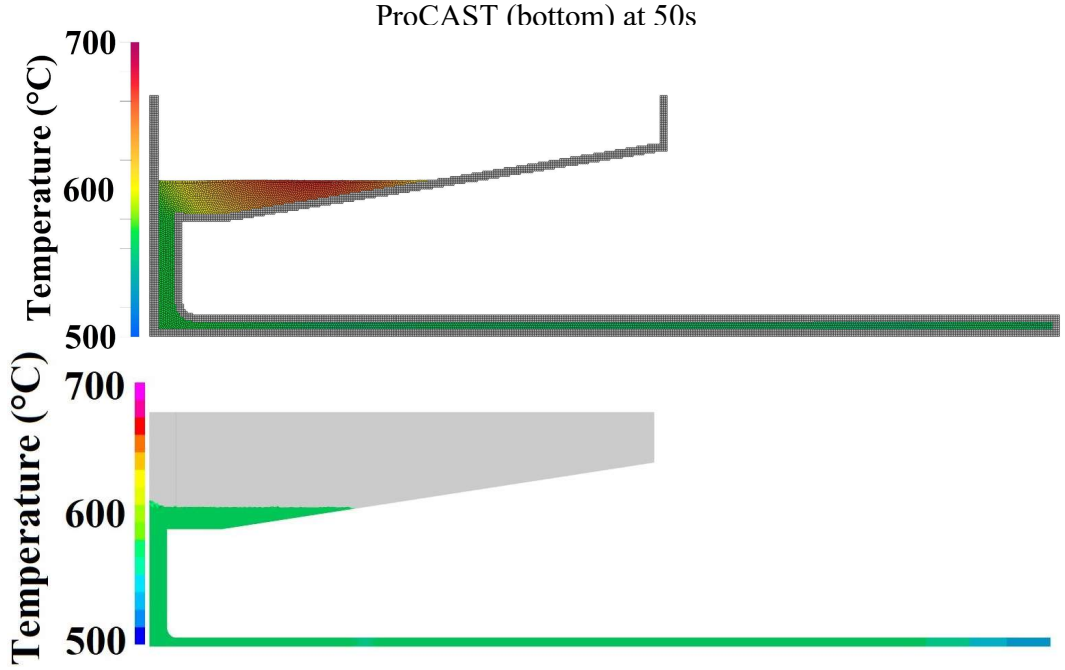

Figure 3-29 - Temperature field during solidification of simulation using SPH (top) and ProCAST (bottom) at 70s

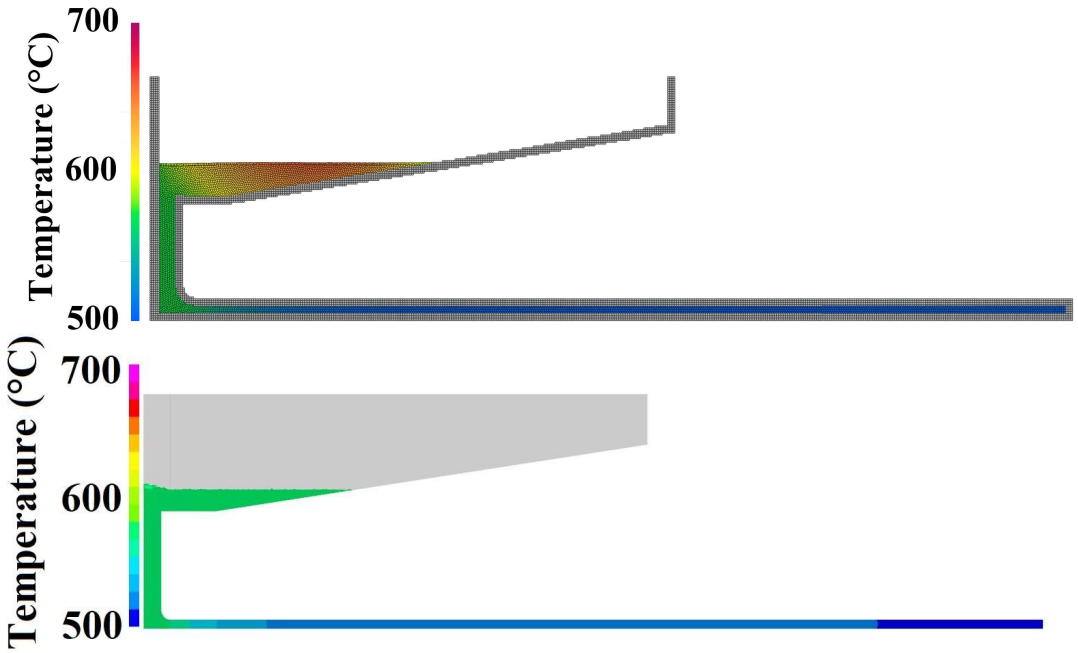

Figure 3-30 - Temperature field during solidification of simulation using SPH (top) and ProCAST (bottom) at 90s

Figure (3-25) shows the temperature change trend after 5s. The temperature of the plate starts around 640°C degrees and goes to 590°C in both techniques. In both methodologies, the temperature field follows the same pattern of temperature change over time and plate length. The solidification process for both simulations begins after 10s and the temperature on the plate is lower than 572°C in the whole plate and about 620°C in the sprue. A significant part of the sprue is solidifying after 30s (Figure 3-27), and the process of phase transition and temperature decrease on the plate. The solidification process at the end of the plate is complete both ways by the time it reaches 50s, as shown in Figure (3-28), and it propagates across the entire plate. At 70s, Figure (3-

29) displays the temperature field. The solidification process is complete for the entire plate, as indicated in the previous Tables and Figures. The temperature in a major part of the plate in both simulations is between 550°C and 500 °C after 90s, as illustrated in Figure (3-30). It is worth noting that as we move further to the plate's end, the temperature drops to around 100°C.

3.5 Conclusion

This chapter is undertaken to design an experimental test case for rapid gravity casting in a closed system that could be simulated in 2D. The simulation would include the filling, cooling, and solidification phases in order to analyze velocity and temperature fields. The experimental test case was designed in such a way that the effect of width was considered unimportant compared to the length and thickness for filling and cooling. Developing a universal test case of a closed system with the capability to replicate the two-dimensional filling, cooling, and solidification phases of the casting process is quite interesting when developing numerical approaches.

Consequently, the strength of the SPH technique to model filling and solidification of gravity casting in 2D could be analyzed and compared to the ProCAST commercial software. The experimental results of gravity casting of AlSi13 using a 3D printed mold were compared to numerical data via SPH and ProCAST commercial software in terms of filling and solidification.

The most interesting finding from this investigation is that the SPH approach could completely replicate casting filling by employing modeling using artificial viscosity. The thermal results suggest that using Neumann thermal boundary conditions, both methods could reproduce the cooling and solidification of the gravity casting process. It is important to note that this Neumann boundary condition is derived from experimental data. Comparisons between numerical and

experimental results show that the SPH approach can simulate cooling and solidification more accurately than ProCAST due to its fundamental methodology and thermophysical properties. SPH surpassed ProCAST in terms of modeling the rate of heat dissipation in the liquid state and the trend of solidification time along the plate's length. In conclusion, the introduction of an experimental test case for gravity casting of closed systems could make it possible to model filling and solidification in two dimensions and validate the results of numerical simulations like the SPH approach and ProCAST.

Conclusion

Ce chapitre a pour but de concevoir un cas expérimental de coulée par gravité rapide dans un système fermé qui pourrait être simulé en 2D. La simulation comprendrait les phases de remplissage, de refroidissement et de solidification afin d'analyser les champs de vitesse et de température. Le cas d'essai expérimental a été conçu de manière à ce que l'effet de la largeur soit considéré comme peu important par rapport à la longueur et à l'épaisseur pour le remplissage et le refroidissement. Le développement d'un cas universel d'un système fermé ayant la capacité de reproduire le remplissage, le refroidissement et la solidification du processus de coulée est très intéressant pour le développement d'approches numériques.

Par conséquent, la force de la technique SPH pour modéliser le remplissage et la solidification de la coulée par gravité en 2D a pu être analysée et comparée au logiciel commercial ProCAST. Les résultats expérimentaux de la coulée par gravité d'AlSi13 en utilisant un moule imprimé en 3D ont été comparés aux données numériques via SPH et le logiciel commercial ProCAST en termes de remplissage et de solidification.

Le résultat le plus intéressant de cette étude est que l'approche SPH pourrait complètement reproduire le remplissage du moule en employant une modélisation utilisant une viscosité artificielle. Les résultats thermiques suggèrent qu'en utilisant les conditions limites thermiques de Neumann, les deux méthodes peuvent reproduire le refroidissement et la solidification du processus de coulée par gravité. Il est important de noter que cette condition limite de Neumann est dérivée de données expérimentales. Les comparaisons entre les résultats numériques et expérimentaux montrent que l'approche SPH peut simuler le refroidissement et la solidification avec plus de précision que ProCAST en raison de sa méthodologie et de ses propriétés thermophysiques. SPH a surpassé ProCAST en termes de modélisation du taux de dissipation de la chaleur à l'état liquide et de la tendance du temps de solidification sur la longueur de la plaque. En conclusion, l'introduction d'un cas expérimental de coulée par gravité de systèmes fermés pourrait permettre de modéliser le remplissage et la solidification en deux dimensions et de valider les résultats de simulations numériques comme l'approche SPH et ProCAST.

Chapter 4: 3D numerical simulation and experimental validation of filling and solidification for rapid gravity casting

Table of Contents

4.1 Introduction

In contrast to the geometry suggested in the third chapter, which had a filling system different from the typical systems used in standard gravity casting, this chapter performs experiments using the actual filling system. The experiments were conducted while considering the actual filling system for casting a plate to validate the 3D SPH code and compare it with the ProCAST software. For the experiments, two different molds were printed. The first mold employed transparent glass installed in front of the plate to observe and record the filling morphology of AlSi13 into a 3D printed resin-bonded sand mold. For thermal analysis, the second mold just employed a 3D-printed resin-bonded sand mold without glass. The first section presents the experimental methods, molding design, data measurement, and data gathering equipment. The filling, cooling, and solidification phases of the casting process were simulated during the development of the 3D SPH approach, which is extensively discussed in the second chapter. The simulation results of the 3D SPH and ProCAST simulation are presented and compared with the experiment in terms of filling, cooling, and solidification. The numerical data is compared with experimental data to identify the strengths and weaknesses of the two simulation techniques for simulating the casting process. Figure (4-1) shows the current requirements for fluid flow and thermal analysis using experimental and numerical data (SPH and ProCAST) with the classification.

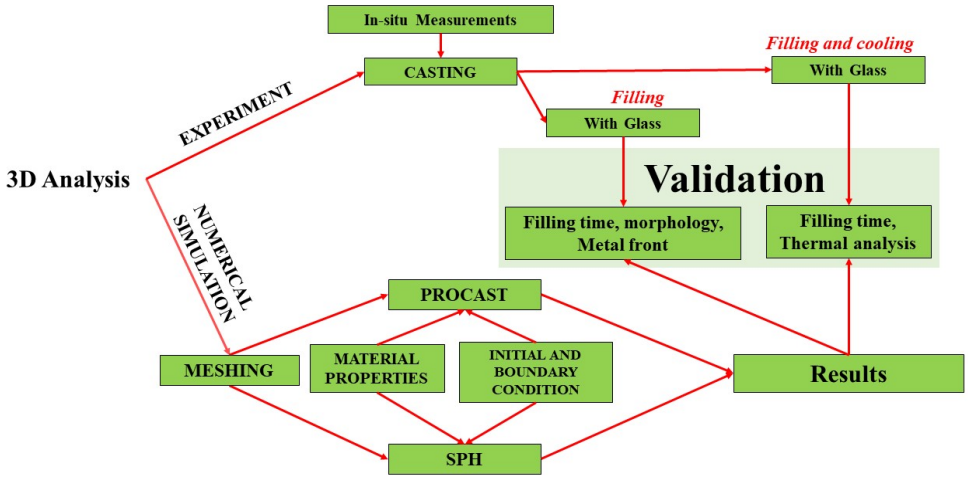

Figure 4-1 - The required elements for investigating fluid and thermal analysis using experimental and numerical data

Introduction

Contrairement à la géométrie proposée dans le troisième chapitre, qui avait un système de remplissage différent des systèmes utilisés dans la coulée par gravité standard, ce chapitre a pour but de présenter des expériences en utilisant le système de remplissage réel. Les expériences ont été menées en considérant le système de remplissage réel pour le moulage d'une plaque afin de valider le code SPH 3D et de le comparer avec le logiciel ProCAST. Pour les expériences, deux moules différents ont été imprimés. Le premier moule utilisait un verre transparent installé devant la plaque pour observer et enregistrer la morphologie du remplissage d'AlSi13 dans un moule en sable à prise chimique imprimé en 3D. Pour l'analyse thermique, le second moule n'a utilisé qu'un moule en sable à prise chimique et imprimé en 3D, sans verre. La première section présente les méthodes expérimentales, la conception du moulage, la mesure des données et l'équipement de

collecte des données. Les phases de remplissage, de refroidissement et de solidification du processus de moulage ont été simulées pendant le développement de l'approche SPH 3D, qui est largement discutée dans le deuxième chapitre. Les résultats de la simulation 3D SPH et de la simulation ProCAST sont présentés et comparés à l'expérience en termes de remplissage, de refroidissement et de solidification. Les données numériques sont comparées aux données expérimentales afin d'identifier les forces et les faiblesses des deux techniques de simulation pour la simulation du processus de coulée.

4.2 Gravity casting experiment

4.2.1 Casting design

The design of test case to study 3D SPH code validity in case of closed system gravity casting with a 3D printed sand mold is shown in Figure (4-2).

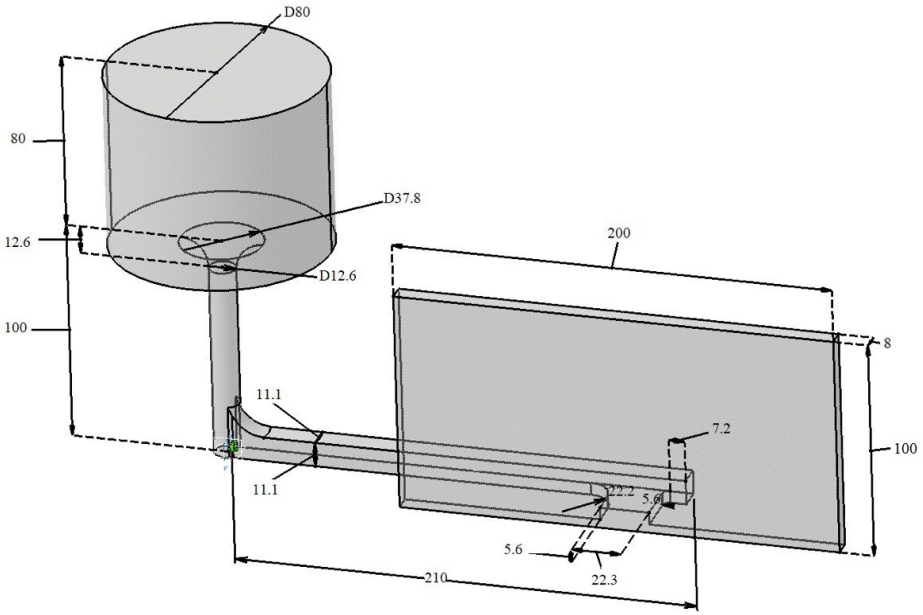

Figure 4-2 - Schematic of geometry intended for gravity casting (mm)

It should be noted that the proposed geometry is designed for a closed system since the SPH code suffers difficulty simulating open systems. All the components required for a traditional casting experiment are considered in the geometry, including a pouring basin, a circular sprue, a runner, and an ingate. The plate is filled from the bottom by the ingtate in the center of the plate. This plate measures 200mm in length, 100mm in height, and 8mm in thickness. It should be noticed that the top of the plate has an opening so that trapped air can escape and not affect the filling process. To ensure a homogeneous filling in thickness direction and to shorten the simulation's runtime, it should be noted that the plate's thickness is significantly lower than its length and height.

For the filling of plate, an ingate with 5.6mm height and 22.3mm length is considered. The ingate is designed by the distance of 10mm from the end of the runner to limit sand that could be transported at metal front. As a result, it is recommended to leave a space between the ingate and the end of the runner to avoid the ingot from being blocked from adequately filling the plate. The ingate is also positioned at the bottom of the runner to limit entering the float oxidation defects of the liquid during filling of the plate. It should be noted that the square runner used to connect the sprue to the ingate has a dimension of 11.1mm and a length of 210mm. The circular sprue is used with 12.6mm diameter and a 100mm height. The sprue has the same height as the plate to guarantee that it is fully filled. A cylindrical pouring basin with 80mm diameter and 80mm height is considered. The Crescent surface is also taken into account in the cross section between the pouring basin and the sprue, the sprue and the runner, and the runner and the ingate. This limits turbulence and the amount of wrestling sand that enters the liquid.

4.2.2 Mold design

The resin-bonded sand mold technology of 3D printing is used to fabricate the intended part for the gravity casting experiment using AlSi13. Furthermore, the use of transparent glass technology rather than a resin-bonded sand mold on the plate's front surface allows for the observation of the filling procedure. The morphology of the filling could well be examined and analyzed in addition to the filling time when the filling process is visible. On the other hand, the transparent glass in front of the plate, the open space above it, and the resin-bonded sand on the four other sides bring on non-homogeneous cooling. As a result, two experiments have been conducted. The first one uses the transparent glass and considers the camera that is positioned in front of the glass to evaluate the morphology of the filling in plate. The acquisition system is also used to measure the filling time at different points. In the second experiment, which is carried out without the use of glass, the filling time and thermal studies are obtained using thermocouples. Figure (4-3) shows illustrations of the designed molds. The mold geometry designed in CATIA for the experiment involving glass and the experiment omitting glass is displayed on the left and right sides, respectively. Additionally, the 3D-printed resin-bonded sand mold for the glass experiment is present at the bottom.

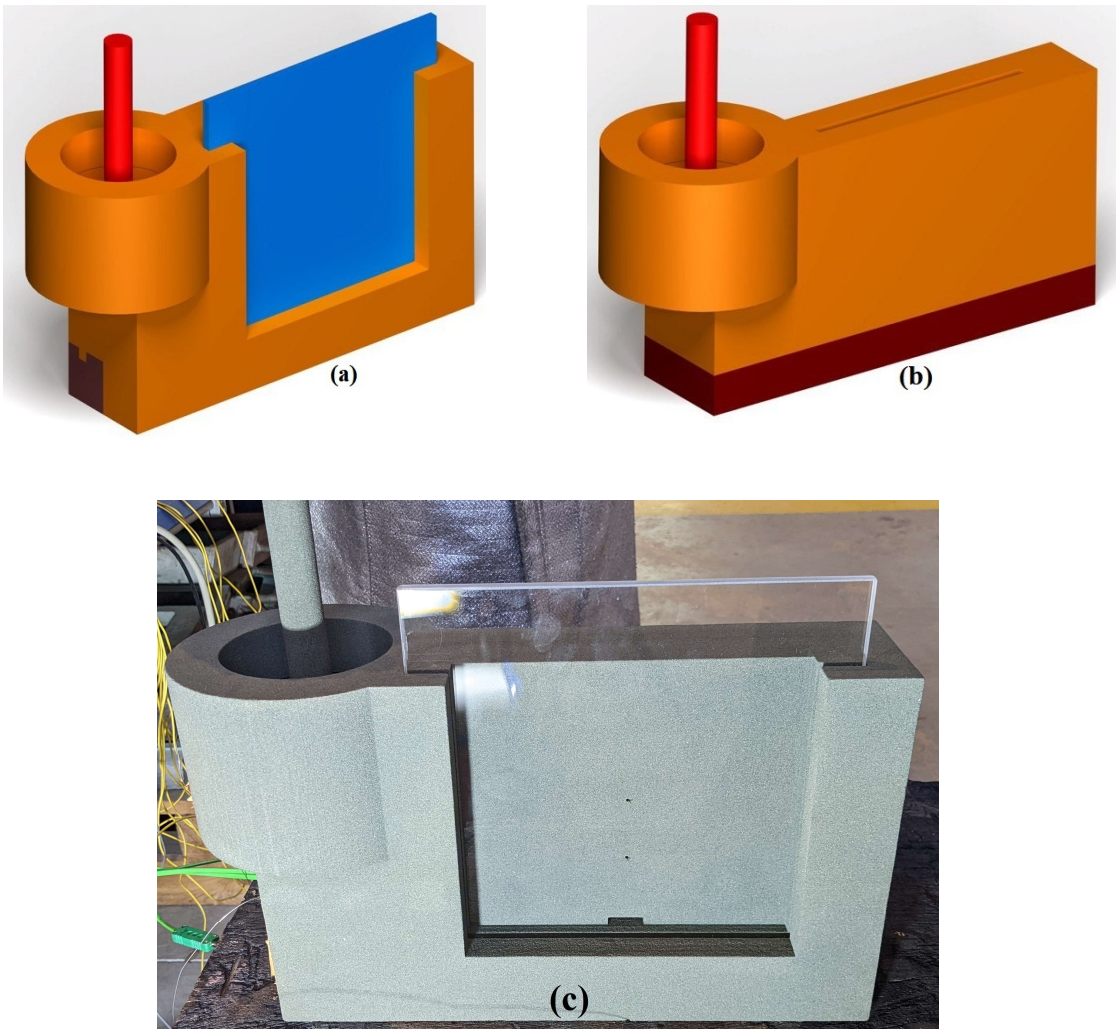

Figure 4-3 Geometry of mold a) Designing mold with glass by CATIA b) Designing mold without glass by CATIA c) 3D printing resin - bonded sand mold with glass

The experimental mold with glass contains three components (positive side, negative side, and the glass), while the mold without glass has just two parts (positive side and negative side). The positive side of the mold is larger in both cases and makes up the majority of the filling system, whereas the negative side is located in the lower part of the mold.

For ease of installation, the glass is deemed to be larger than the size of the plate, as seen in Figure (4-3). The analysis of the filling procedure is done until the metal reaches 100 mm above plate's bottom. With a maximum temperature threshold of 50 degrees on the mold's exterior surface, ProCAST numerical simulation is used to define the thickness of the mold. Using this criterion, the thickness of the mold is determined to be 27.1 mm. To avoid having to face any backpressure caused by air entrapment, a gap is thought to be appropriate at the top of the plate.

4.2.3 In-situ Measurement

In order to cast the metal, it was taken out of the furnace using a ladle, which resulted in a pouring top temperature of 655°C, or 75°C superheat. K-type thermocouples are inserted to characterize temperature evolution in the melt, as shown in Figure (4-4). The maximum temperature is 655°C in the experiment, hence the thermocouples' precision is $\pm 4.91^{\circ}C\ (0.0075\times|T^{'}|)$. In parallel, to characterize the flow dynamics during filling, an acquisition system is employed. For the experiment using glass the acquisition system was put in nodes (N1, N2, N3, N4, N6, N7) to capture filling time (Figure (4-4)). The acquisition system and thermocouples were placed respectively in the nodes (N1, N2, N3, N4, N6, and N7) and (N1, N5, N6, N7, N8, and N9) for the experiment without glass in order to record the filling time and temperature (Figure (4-4)).

N1 is positioned at a distance of 17.6mm from the top of the sprue. N2 is 5.55mm from the sprue bottom in the central portion of its thickness. It represents time “t=0s”. It should be noted that N3 is situated at the bottom of the runner, at the ingate entrance. N4 is in the middle of the ingate. By taking into account 20mm, 50mm, and 90mm heights from the bottom of the plate, respectively, N5, N6, and N7 are installed at the middle of the thickness and length of the plate. By considering

50mm and 25mm from the plate's border, two additional points, defined N8 and N9, are embedded at the middle thickness of the plate and 50mm height from the bottom of it.

It should be noted that the filling process of casting is visible thanks to the use of 8 mm thick heat-resistant transparent silicone glass. The high-speed CR1000x3 camera can record the casting process filling. The 1280 x 512 pixel camera's field of view enables the recording of images while the casting is being filled. The camera is configured to take pictures at a 100Hz frequency.

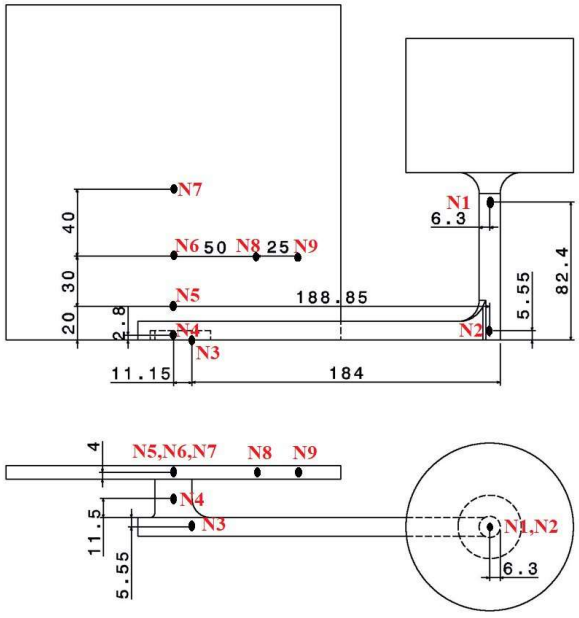

Figure 4-4 - Location of thermocouples and tracking of molten metal (mm)

4.2.4 Experimental results

The experimental data of gravity casting tests are divided into two groups which are the filling time curves and the time-temperature curves, which are obtained using an acquisition system and thermocouples, respectively as explained in Figures (4-5) to (4-8) and Table (4-1).

4.2.4.1 Filling time

Figure (4-5) illustrates the voltage decline over time for two different experiments using glass (N1, N2, N3, N4, N6, and N7) and without glass (N1 to N7). Figure (4-6) displays time the metal reaches the positions of the points N2 to N7 (bottom of sprue (N2), in the runner (N3), in the ingate (N4), and 20mm, 50mm and 90m height of plate (N5, N6, and N7) respectively). The results for the experiment with glass are shown in black, while the results for the experiment without glass are shown in red. Figure (4-7) uses image analysis from the metal to plot in detail the liquid level height against filling time in the experiment using glass.

Point by point filling time analysis: The filling times of N3 (at the runner) and N4 (at the middle of the ingate) for both experiments are fairly close to one another, as shown in Figures (4-5) and (4-6), with a relative error of less than 5%. Looking at the filling time results in point N5 reveals that there was no data for the experiment with glass; only the filling time for the experiment without glass was recorded. The difference in results for the point N6 (50mm height from the bottom of plate) between the two experiments is approximately 13%, and in the case of the glass, the liquid reaches the N6 more quickly. The glass used in the experiment has a higher sleeping coefficient than the sand mold, which helps it fill more quickly, which could make up for the shorter filling time. The experiments with and without glass would have filling times of 1.935s and 1.965s, respectively, according to an analysis of the filling time in N7.

Analysis of liquid level height: The results are shown in Figure (4-7), which depicts the height of the liquid level at the center of the 200 mm-long plate. At the beginning of filling the plate, the height between 15 mm and 40 mm is filled in a time interval of 0.2s, as is evident from the figure. This demonstrates that the filling vertical velocity, which is approximately 0.125m/s, is high at the

start of the filling process. It is clear from the experiment results that the liquid's height oscillates until it reaches a height of 40mm. When liquid reaches a height of 40 mm, it remains there for 0.3s (0.5s to 0.8s). The cause of this is the balance between liquid pressure and gravity, which causes the metal to keep moving vertically and begins to flow horizontally. Between 0.7s and 1.0s oscillations are visible between a height of 40mm and 55mm. Following a 1.0s timeframe, the liquid stays at a height of 55mm for about 0.1s before slowly beginning to rise. From 55mm height, the liquid gradually begins to rise linearly in height between the times 1.1s and 1.93s, with an average velocity of 0.042m/s, with very few oscillations.

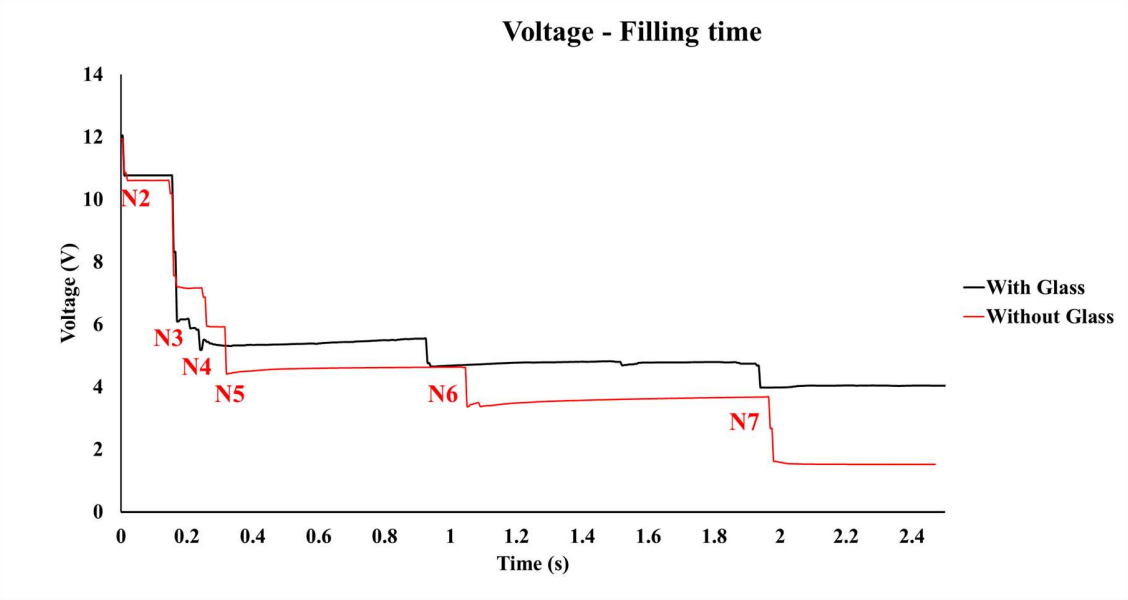

Figure 4-5 - Voltage and velocity versus filling time for different points of experimental test

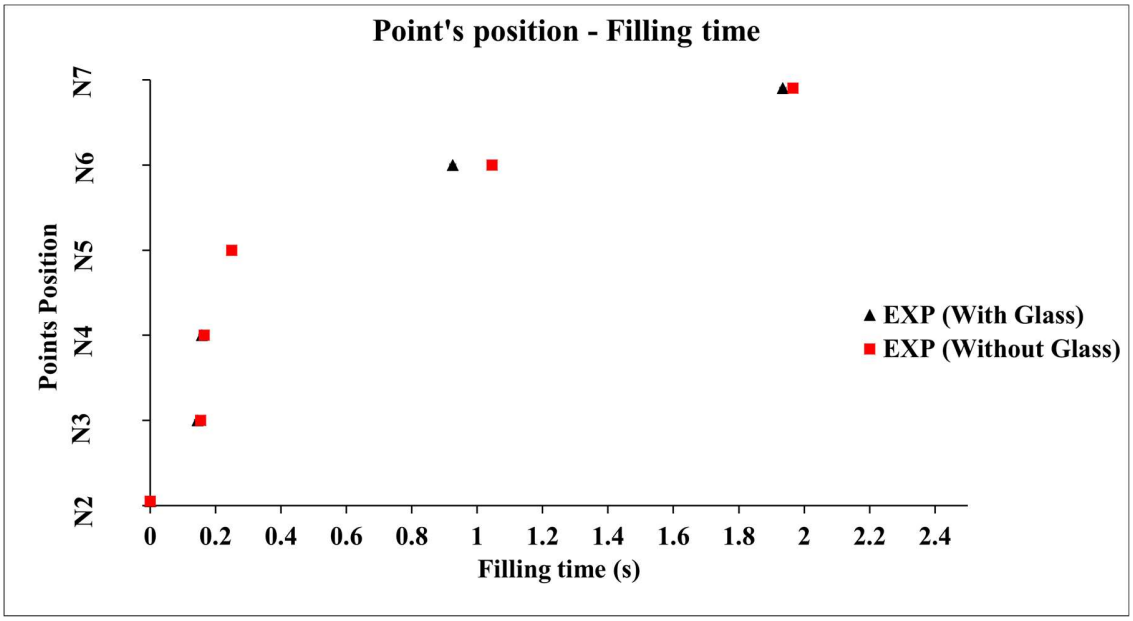

Figure 4-6 - Points position versus filling time for different points of experimental test for whole part

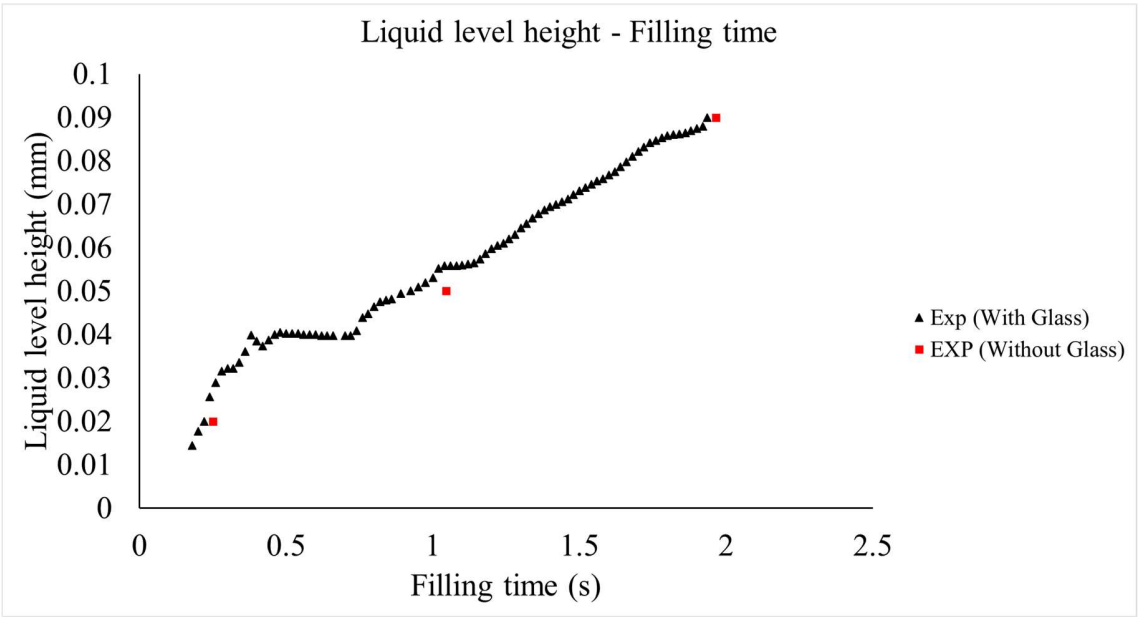

Figure 4-7 - Liquid level height versus filling time of experimental test for plate

4.2.4.2 Temperature time curves

Figure (4-8) shows the evolution of temperatures at 6 positions (N1, N5, N6, N7, N8, and N9). Three zones on the cooling curves, which match the alloy phase transition, are present. Additionally, Zones 1 and 3's experimental cooling rates and Zone 2's experimental solidification time are shown in Table (4-1). It should be noted that the maximum and minimum temperature values and corresponding times were used to calculate the slopes in each zone. Additionally, up to 200s of slope calculations have been performed in the third zone. The graph's zero time corresponds to the moment when the metal touches N1 during filling. The graph, however, makes it clear that the thermocouples have a delay in displaying the temperature. Because of this delay, the thermocouples N1 show their maximum temperature after 0.75s. The N1 at the top of the sprue is used to quantify the casting's initial temperature.

Two different directions on the plate are examined for temperature changes. The first analysis, which includes points N5, N6, and N7, looks into changes in temperature in the direction of height. The positions N5, N6, and N7 are 20mm, 50mm, and 90mm away from bottom of plate in the middle of thickness (4mm) and length (100mm). The second study of temperature involves the points N6, N8, and N9 and is aimed in the direction of the plate's length. Points N6, N8, and N9 are situated at the midpoint of height (50mm) and thickness by taking into account distances of 100mm, 50mm, and 25mm in the length direction.

Temperature analysis in height direction (N5, N6, and N7): Point N6 has a higher temperature drop in the liquid cooling area than points N5 and N7 by 12.41% and 5.43%, respectively. As can be seen in Figure (4-8) Detail A, N5, and N6 have nearly the same initial temperature. In addition, in about 5s, both of them simultaneously enter the solidification zone. Even so, because N5 is filled

before N6 and N7 has a higher rate of temperature decline. Comparing N6 and N7 reveals that, despite N7 being filled later, N6's rate of temperature changes is higher than temperature rate at N7 because of the lower initial temperature estimated at N7.

In solidification zone, N6 has the longest solidification in comparison to N5 and N7 because the impact of the boundary condition in height is minimal. The plate was filled to a height of more than 100mm during the experiment could be the cause of N7's longer solidification time than N5's. The air from the top of the plate therefore less affects the N7 because there is more molten metal above it.

In the third zone that is cooling of solid state, N6 has a higher rate of temperature decline than the other two points (N5 and N7). Furthermore, N7 has a higher rate of temperature drop than N5. The explanation could be that point N6 takes longer to solidify than points N5 and N7. When point N6 enters the solid cooling zone, the surrounding material has already gone through the solid phase. As a result, the rate of temperature drop at N6 accelerates since the material surrounding has a lower temperature (N5 and N7) in all directions.

On the other hand, when N5 and N7 enter zone 3, N6 remains in zone 2 for a few more seconds. As a result, the temperatures at the top area of N5 and the down area of N7 is higher than the temperatures at N5 and N7. It causes decreasing the cooling rate at N5 and N7. As a result, N6 cools more quickly than N5 and N7.

On the other hand, for example, when N5 enters zone 3, point N6 is still in zone 2 and remains there for more seconds. Hence, temperature in top area of N5 is higher than temperature at N5.

This phenomenon limits the cooling rate drop at N5. Therefore, cooling rate at N6 is higher than at N5 and N7.

Temperature analysis in length direction (N6, N8, and N9): It is evident from Detail A in Figure (4-8) that the thermocouples positioned at each of the three points all display the maximum temperature value at same time (1.8s). The maximum temperature at each of these three locations decreases as one moves in a lengthy direction toward the mold's boundary. Furthermore, N6 has a maximum temperature of 625°C, while N9 has a maximum temperature of 595°C. There are differences in the rate of cooling in the first zone due to the different maximum temperature values at these three points. Furthermore, it should be highlighted that N8 and N9 compared to N6 entered the solidification phase later and earlier, respectively. This could be a result of the thermocouples sliding or an error in the thermocouple, which could cause a significant drop in temperature at N6 during 4s to 5s of filling. In solidification zone solidification time of N6 is longer than N8 (1.57%) and N9 (20.81%), respectively. N6 takes slightly longer to solidify than N8, but significantly longer than N9. This demonstrates that the solidification time decreases more sharply by approaching the mold wall from the length direction. Similar to the first zone, N6 in the third zone undergoes a greater rate of temperature decline than N8 and N9. A comparison of the cooling drop values for N6 and N8 reveals a small difference between them of approximately 3.93%. This could be due to the similar solidification times of N6 and N8. It should be noted that N6, which is 100mm from the border, experiences a higher temperature drop than N9, which is 25mm from the border, by about 25.2%.

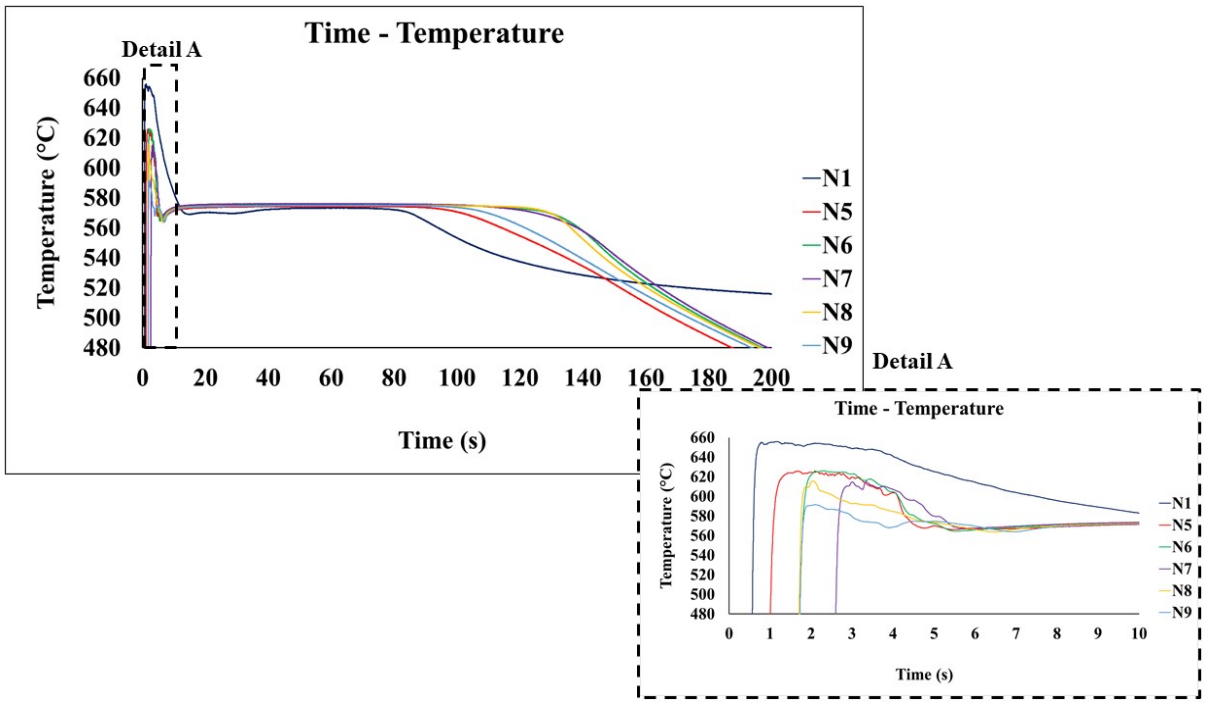

Figure 4-8 - Experimental cooling curves of AlSi13 alloy for points (N1, N3, N4, N5, N6 and N8)

Table 4-1 - Experimental cooling rate and solidification time for (N5, N6, N7, N8, and N9)

Position of thermocouples	Cooling rate (Liquid state) $(T.s^{-1})$	Solidification time (s)	Cooling rate (solid state) $(T.s^{-1})$
N5	**16.27**	**83.36**	**0.91**
N6	**18.29**	**119.5**	**1.27**
N7	**17.38**	**109.17**	**1.07**
N8	**13.91**	**117.62**	**1.22**
N9	**13.60**	**94.63**	**0.95**

4.3 Numerical simulation

In chapter two, a thorough explanation of the numerical simulation based on ProCAST commercial simulation and SPH approach is provided. Following are descriptions of the corresponding hydraulic and thermal boundary conditions, adopted mesh, and its convergence in ProCAST and SPH.

4.3.1 Initial and boundary conditions

4.3.1.1 Initial conditions

Hydraulic: It should be observed that at zero time, the molten material in the closed gravity casting system has been poured into the pouring basin and has become stationary. Air is also not considered throughout the simulation procedure. Gravity causes the fluid to begin to flow.

Thermal: The thermocouple (N1) that is positioned at the top of the sprue (highest temperature: about 655°C) is used as the initial temperature of the metal for the numerical simulation. The initial temperature of the mold wall is set to 20°C, which is the same as the exterior temperature.

4.3.1.2 Boundary conditions

Hydraulic: In ProCAST simulation and the SPH technique perfect slip boundary condition defines between the fluid and the wall.

Thermal: As mentioned in chapter (3), the Neumann boundary condition (Conduction) is used in both WCSPH and ProCAST simulations to estimate heat extraction at the metal/mold interface in order to replicate cooling and solidification. The heat flux exiting the mold surface is supposed to be constant by three levels as illustrated in Table (4-2). The three zones are the cooling of molten metal above liquidus temperature, the solidification process between liquidus and solidus

temperature, and the cooling of solid metal at temperatures below solidus temperature. The values were determined using one-dimensional calculations based on experimental data, taking into account the three zones. The process for determining q's value using one-dimensional equations is demonstrated below. It should be mentioned that T_0, T_L, T_S and T_{end} represent initial, liquidus, solidus, and temperature at 150s. In addition, the average experimental periods $(t_{\exp})$ between corresponding temperatures in each location (N5 to N9) were utilized to derive these values.

Table 4-2 - One-dimensional equation to obtain Neumann boundary condition in three different regions

Zone (1)	$Q = -K\frac{\partial T}{\partial x} = \frac{\rho e C_p (T_0 - T_L)}{t_{\exp}} \approx 195000 \, W/m^2$
Zone (2)	$Q = -K\frac{\partial T}{\partial x} = \frac{\rho e L + \rho e C_p (T_L - T_S)}{t_{(\exp)}} \approx 44000 \, W/m^2$
Zone (3)	$Q = -K\frac{\partial T}{\partial x} = \frac{\rho e C_p (T_S - T_{end})}{t_{(\exp)}} \approx 11300 \, W/m^2$

Due to the temperature gradient between the mold and the molten material in the first period, when the mold is still cold and the metal is liquid, q is equal $195000 \, W/m^2$, the heat extraction is high. Then, in the second and third stages, the value decreases to $44000 \, W/m^2$ and $11300 \, W/m^2$, respectively. Figure (4-9) shows q values of Neumann boundary condition versus temperature and time for SPH and ProCAST method,respectively.

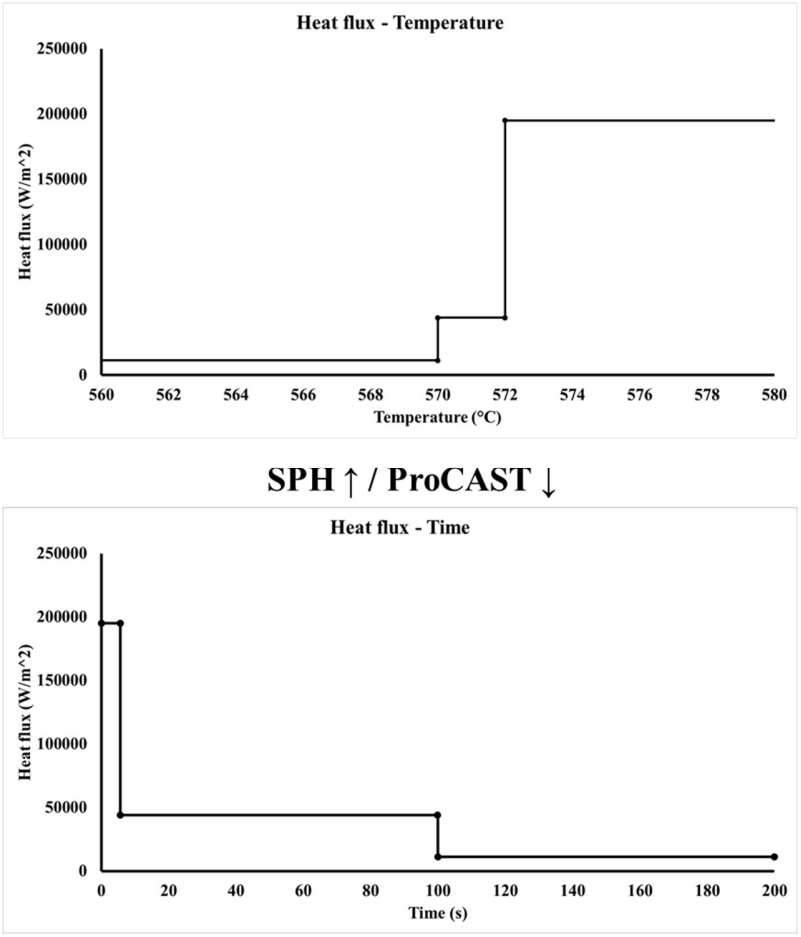

Figure 4-9 - q values of Neumann boundary condition versus temperature and time for SPH and ProCAST method.

4.3.2 Mesh and convergence

CATIA V5 software is used to create the CAD models of the part, the gating system, and the sand mold before being imported into ProCAST (Figure 4-2). For the part and mold, the model is meshed using linear tetrahedral elements with a mesh size of 2mm. The mesh size is established via a number of mesh refinement trials in order to confirm that ProCAST and SPH simulations are mesh-independent. The trend of mesh dependence for filling is shown in Figures (4-10) and (4-

11). According to ProCAST simulation results, a larger filling velocity value is expected when mesh is refined, and this value converges as the cell size goes down. Figure (4-10) shows that when the cells are 2mm in size or smaller, variation is less than 5% in total filling time with reducing cell size. As a result, mesh is generated in a 2mm size. This leads to the selection of 596578 cells, which correspond to 2mm in size.

With the SPH method, the trend is reversed. When there are more particles, the velocity is decreased. The results of the SPH technique are considered to become independent of the number of particles once the number of particles reaches 184839 corresponding to 1.8mm between each particle. Figure (4-10) shows that when the distance between each particle is between 1.7mm and 1.8mm, variation is less than 3% in total filling time.

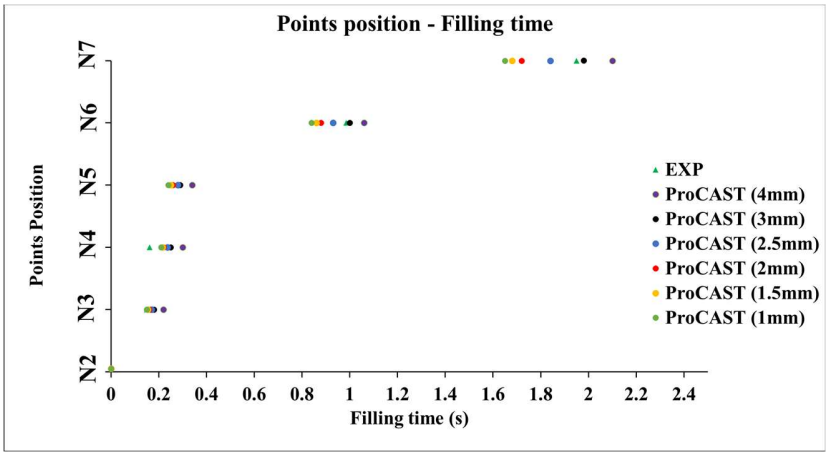

Figure 4-10 - Mesh independency of filling step for ProCAST Simulation

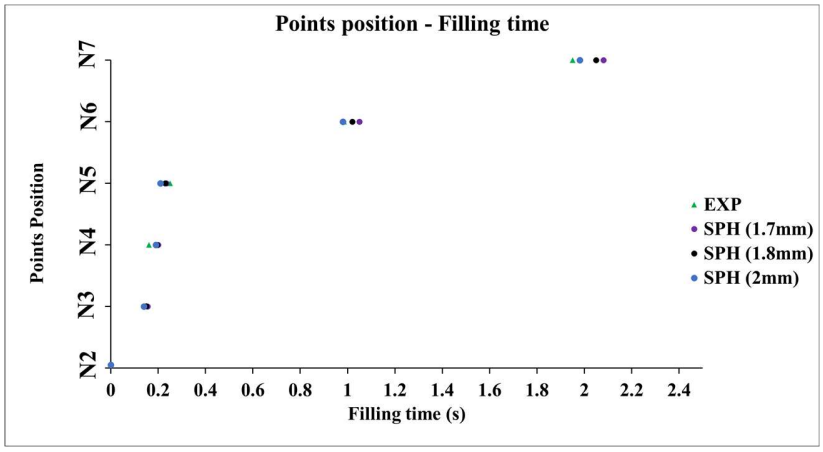

Figure 4-11- Mesh independency of filling step for SPH Simulation

Figure (4-12) represents the final mesh used for ProCAST simulation. Figure (4-13) also illustrates the SPH method's mesh generation. The geometry must be created using CATIA by designing the desired part's outer shell in order to generate mesh for the SPH method. Then, four particles should be positioned in the outer direction perpendicular to the shell, with an embedded thickness proportional to the space between each particle. The appropriate geometry file is given to a program that can generate a triangular mesh, such as ProCAST, QuikCAST, Abaqus, etc. The file is sent to MATLAB software because the generated triangular mesh may not have exactly 2mm between each point. The distance between the points is organized in MATLAB software, and an embedded geometry shell is created with a thickness equal to four times the distance between each particle. In the context of the SPH approach, it is worth mentioning that the time step has a value of $2.5e^{-4}$ s.

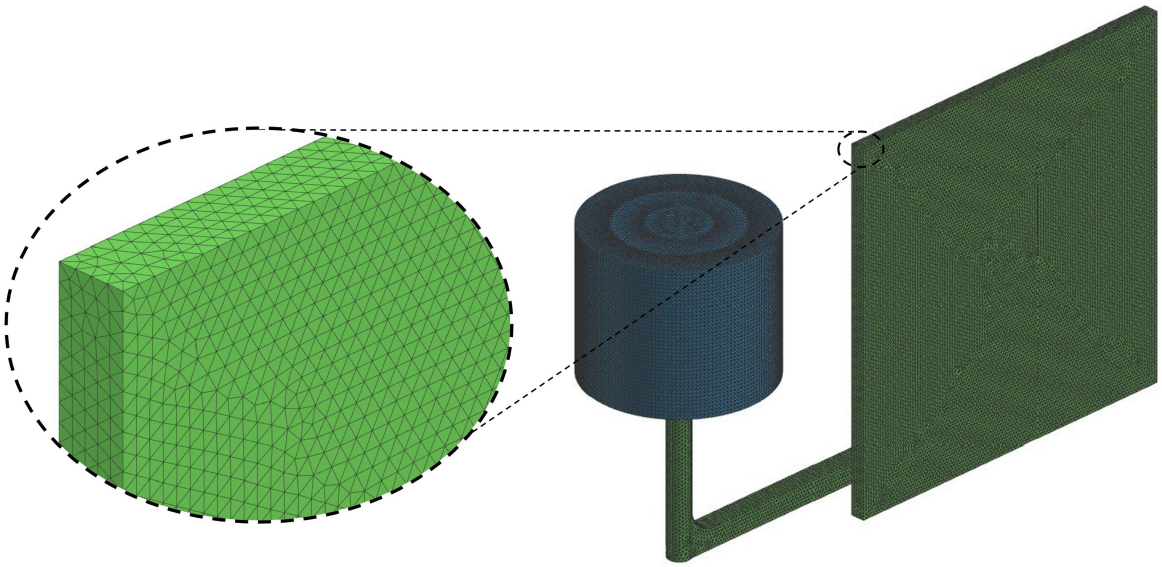

Figure 4-12 - Schematic of mesh of ProCAST simulation

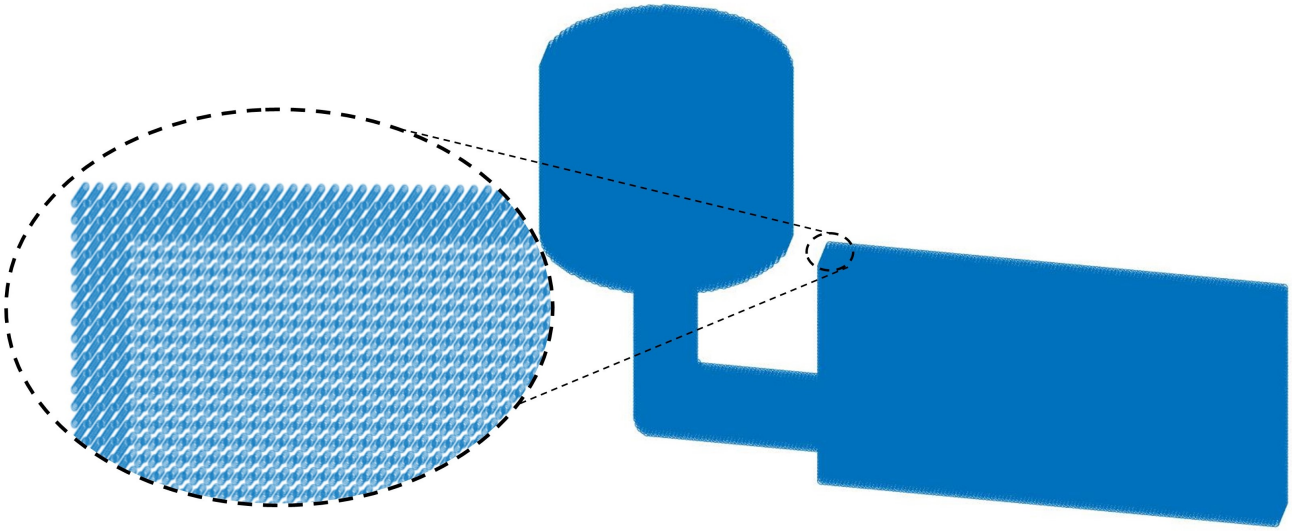

Figure 4-13 - SPH geometry schematic with 1.8 mm distance between particles

4.4 Results

4.4.1 Study of filling step

Three ways can be employed to analyze the filling results. In the first, filling time of 6 points into mold cavity are considered. Figure (4-14) displays experimental data (With and without Glass), SPH simulation, and ProCAST simulation of the metal filling time at some specific points. It should be noted that the filling results with and without glass are displayed in green with different markers. Secondly, in the experiment with glass, SPH simulation, and ProCAST, Figure (4-15) compares the filling time against the liquid level height in the plate. It should be noted that the middle of the plate is used for this analysis of liquid level height versus filling time in the length direction. In the third category of analysis, the morphology of the filling is examined experimentally in 2D by considering the plate thickness small enough (8mm) to neglect the third direction effect on flow. In this method, a camera is placed in the front of the plate.

A camera that is placed in front of the plate examines the morphology of the filling experimentally. Figure (4-16) compares the morphology of the filling for three different techniques (Experiment with glass, SPH, and PrOCAST). Additionally, Figure (4-16) compares the volume flow rate over time for each of the three methods by considering the flow in 2D only.

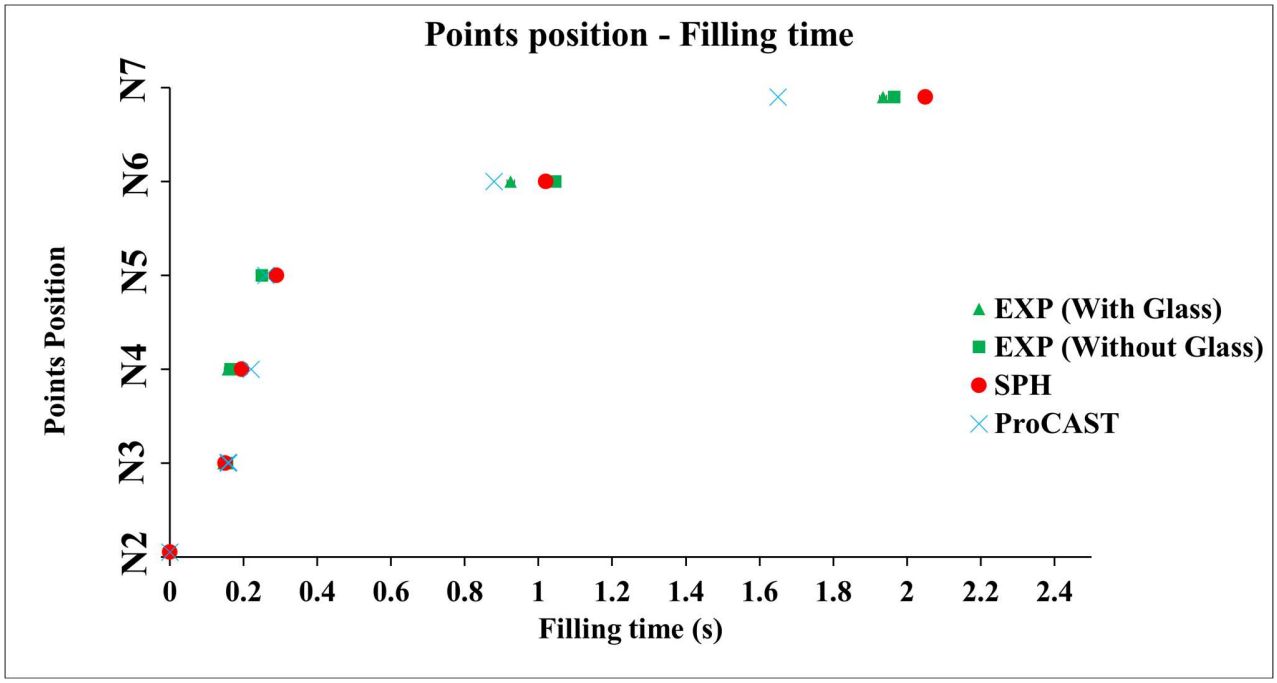

Figure 4-14 - Filling time of several points in the mold cavity for Experiment, SPH method and ProCAST simulation

4.4.1.1 Filling time analysis

The filling time for points N3, N4, N5, N6 and N7 in seconds for average values of two experiment with glass and without glass, SPH method and ProCAST simulation is shown.

Table 4-3 – Filling time (s) of N3 to N7 in the mold cavity for Experiment, SPH method and ProCAST simulation

Methods/Points	N3	N4	N5	N6	N7
Experiment	0.15	0.16	0.25	0.99	1.95
SPH	0.15	0.2	0.29	1.02	2.05
ProCAST	0.16	0.22	0.26	0.88	1.65

N2 is used as a reference point since the filling time between N1 (the top of the sprue) and N2 (the bottom of the sprue) has been subtracted from the overall filling time. The results using the acquisition system given in Figure (4-14) show that it takes 0.15s experimentaly to go from N2 (bottom of sprue) to N3 (beginning of ingate), SPH approach estimates it (0.15s) carefuly, and the simulation using ProCAST slightly overestimates it (0.16s). Only 0.012s are needed for the experimental filling time between N3 (beginning of ingate) and N4 (middle of ingate), and these values for SPH and ProCAST are 0.045s and 0.06s, respectively. According to the results of the experiment, the filling time between N4 and N5, which is 20mm above the plate's bottom, is equivalent to 0.088 seconds. Between N4 and N5, the filling times of SPH (0.045s) and ProCAST (0.04s) both show a negligible underestimation of the filling times. The filling time for N6 (50mm height from the bottom of plate) and N7 (90mm height from the top of plate) revealed that the numerical approaches SPH and ProCAST overestimate and underestimate filling time in comparison with experiment, respectively. The experimental filling time for point N6 is 0.985s, whereas it is 1.02s for SPH and 0.88s for ProCAST. Additionally, the experimental filling time for point N7 is 1.95s, compared to 2.02s and 1.65s for SPH and ProCAST, respectively. The outcome reveals that the discrepancies between the experiment and SPH for points N6 and N7 are about 3.43% and 3.58%, meanwhile the variations between the experiment and ProCAST for these two points are 10.65% and 15.38%, respectively. It should be noted that the flow is turbulent initially as the liquid enters the plate from the ingate due to the small ingate dimensions, high velocity, and changing cross section. The flow seems to continue to be turbulent until the free surface becomes flat. When the liquid becomes flat after 0.6s, the Reynolds number is less than 1000. It indicates that the flow has transitioned into the laminar phase.

4.4.1.2 Liquid level height

Figure (4-15) represents the level of liquid height in the center of the plate versus filling time for the experiment and numerical (SPH and ProCAST) results.

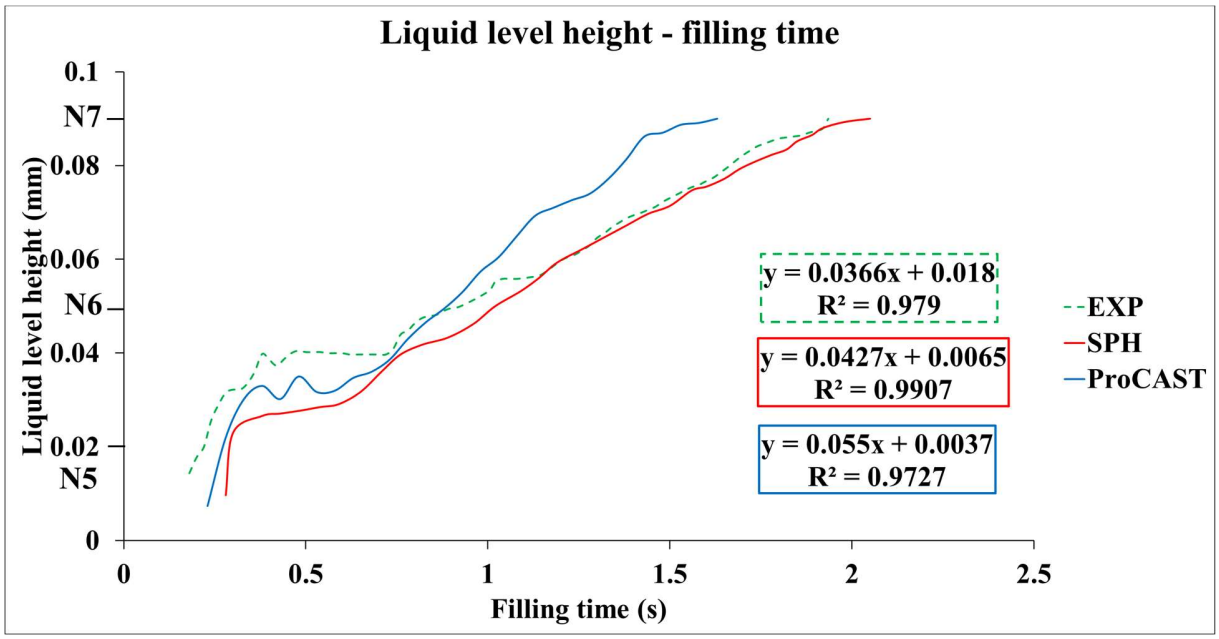

Figure 4-15 - Liquid level height in the center of plate versus filling time for Experiment, ProCAST simulation and SPH method

The starting location of each curve of the in Figure (4-15) for each of the three methods is at a different height and time due to different filling time. The approach to choosing the first point is that the first image recorded on the plate both numerically and experimentally is analyzed to select the initial point. Due to the embedded ingate in the plate's center, the liquid fills the plate first and rises to a height determined by its pressure before spreading out in a longitudinal direction. The simulation using ProCAST predicts more precisely the filling time, as evidenced by the comparison of the liquid level height up to 0.5s. The oscillations made during this time using

ProCAST should be noted as being appropriately predicted. However, it is not seen that the height of the liquid in the middle of the plate remains constant during the simulation using the ProCAST method; instead, it oscillates. The liquid level height in the SPH method, in contrast to ProCAST simulation, is nearly constant over the time range of 0.35s to 0.65s. The height of the liquid is approximately 27mm, and the plate is filled during this period in the longitudinal direction. The liquid level variations after that are then oscillatory in the experiment and ProCAST simulation but nearly linear in the SPH method. The SPH and experiment results are nearly identical after 0.75s, which is an important point. By comparing the SPH simulation's prediction to the experiment, it was found to have an error of less than 10% in predicting the height of the liquid level in relation to filling time between 0.75 and 2.05s.

4.4.1.3 Filling morphology:

Figure (4-16) displays the filling morphology of the sand gravity casting process for the SPH method, experiment, and ProCAST simulation with 0.1s time intervals from time 0s to 1.7s. It should be noted that the time that defines the zero reference time in this figure is the moment when the liquid enters the 200mm wide plate through the ingate. The calculations are evaluated up to a height of 90mm from the plate's bottom. Using image analysis, it is possible to determine the volume of the liquid entering the plate at any time by calculating the area of the liquid entering the plate and considering homogenous filling step along the thickness. Hence, volume flow rate vs time is depicted in Figure (4-17).

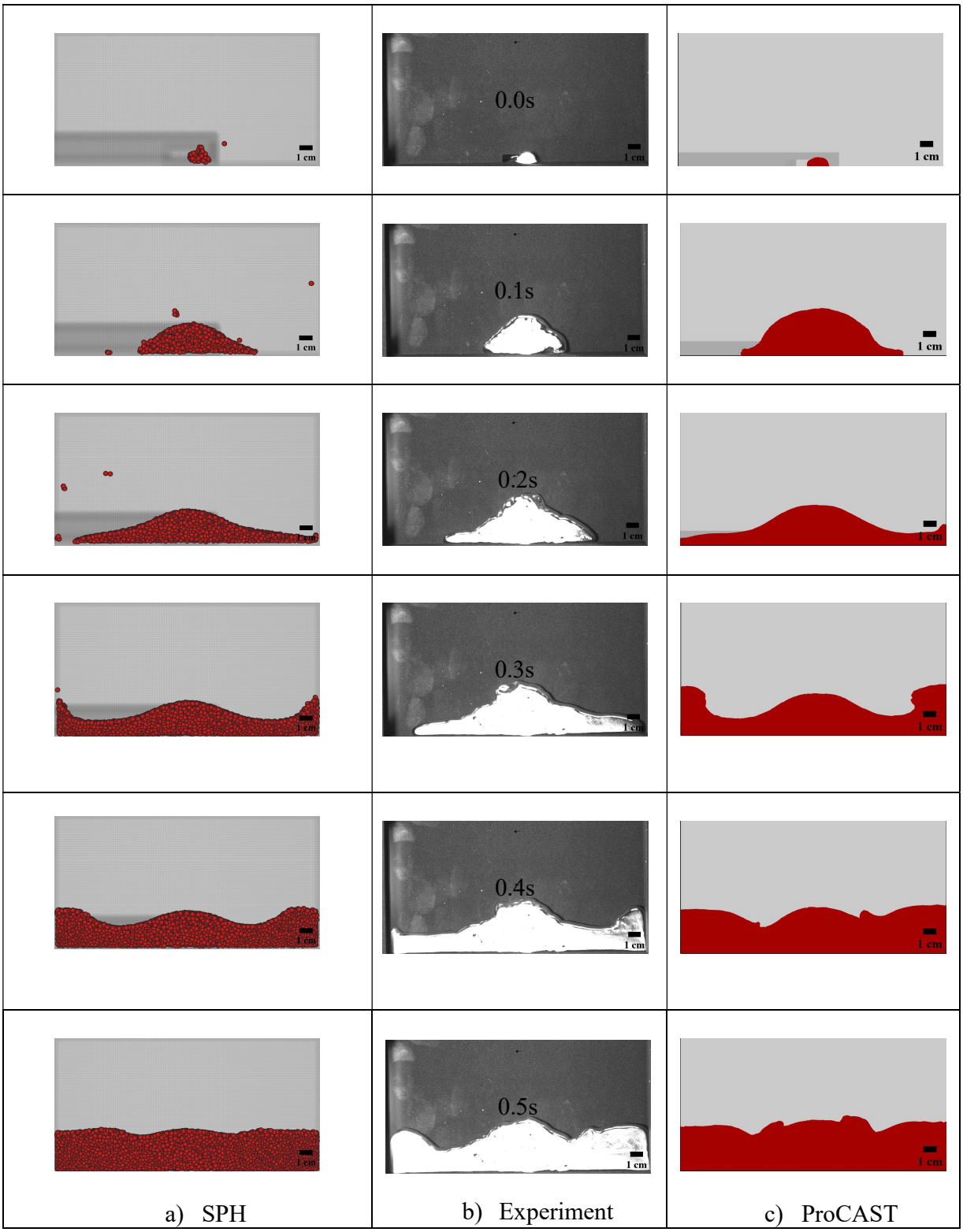
0.0s
0.1s
0.2s
0.3s
0.4s
0.5s
1 cm
a) SPH
b) Experiment
c) ProCAST

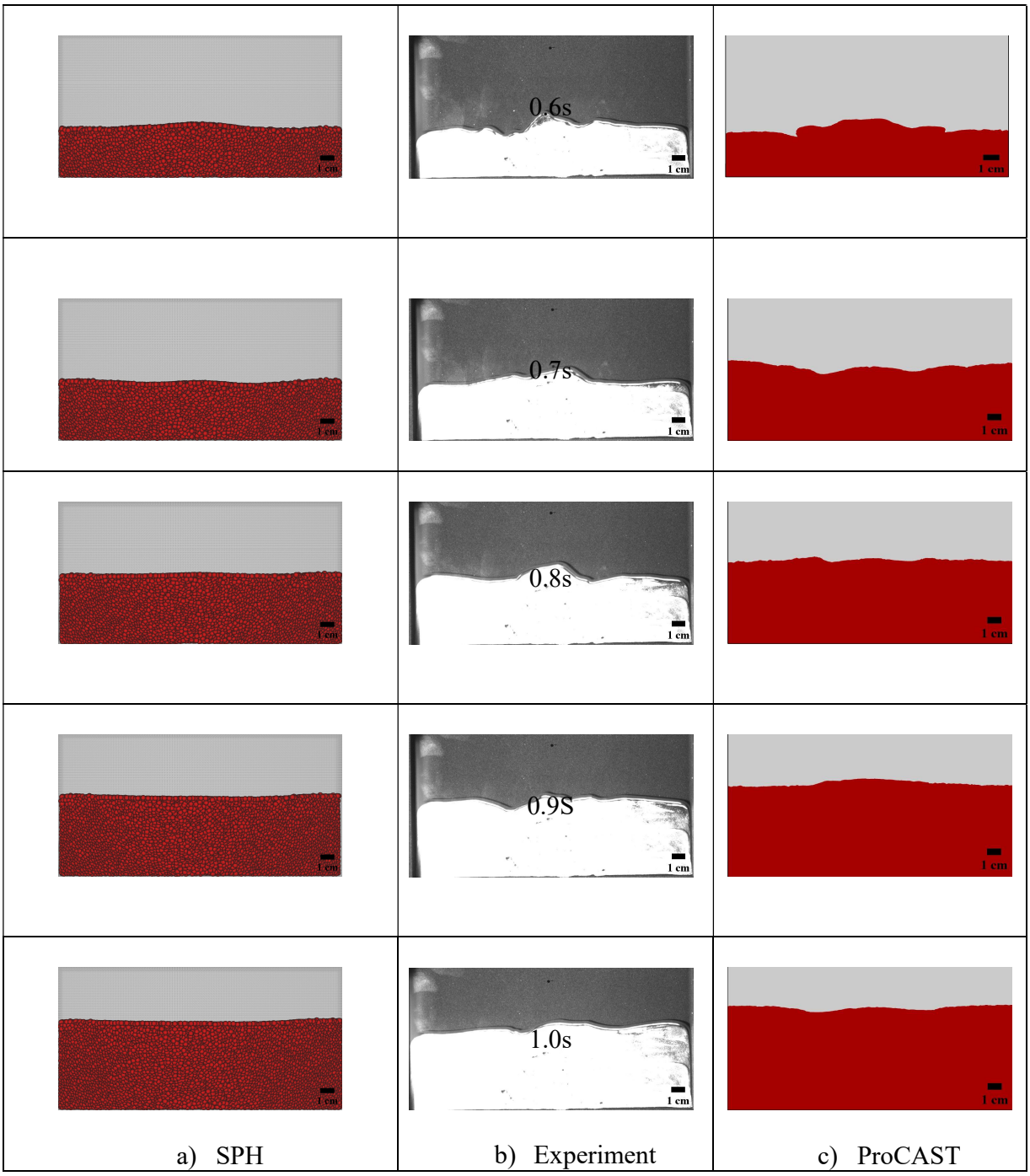

a) SPH b) Experiment c) ProCAST

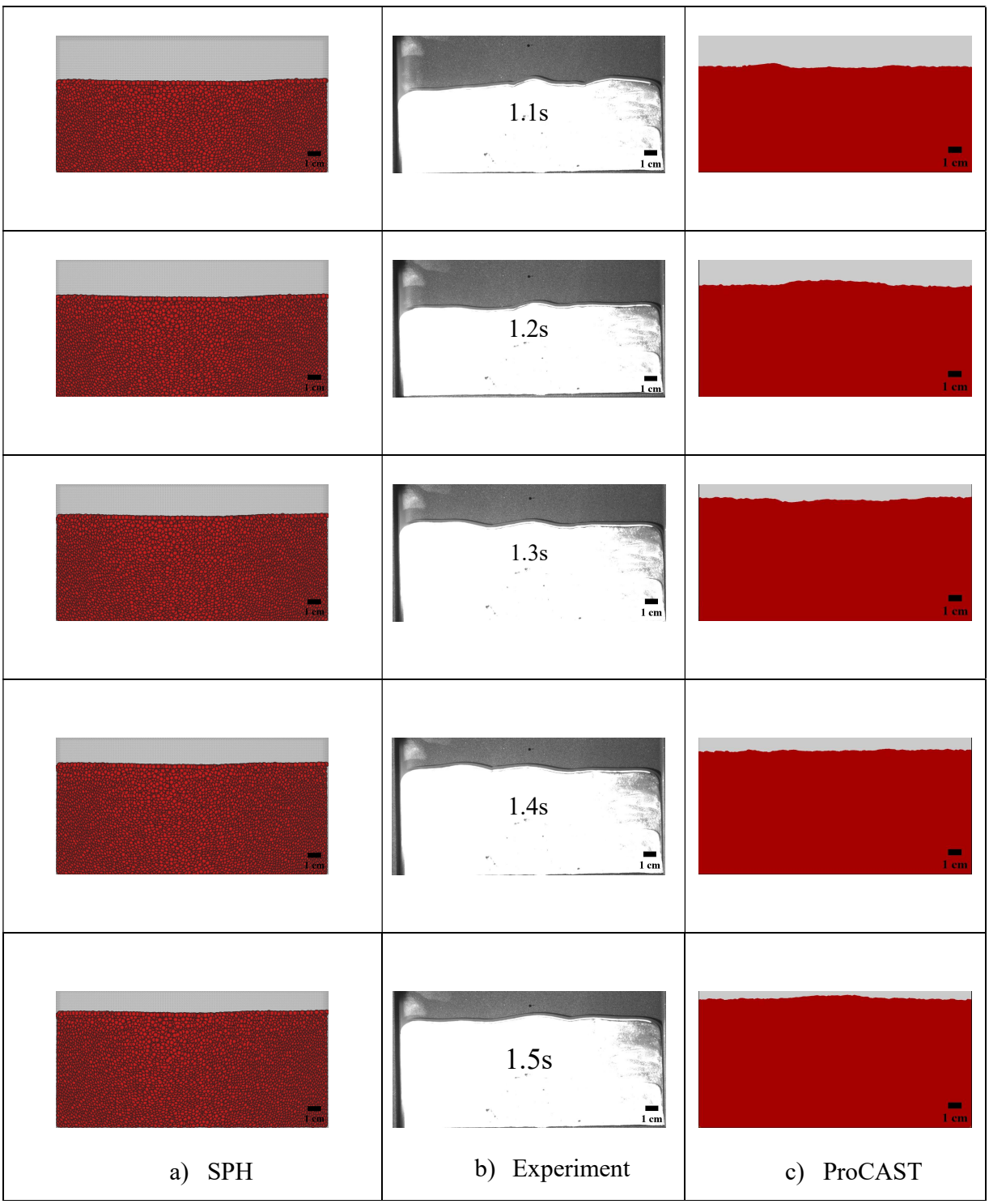

a) SPH b) Experiment c) ProCAST

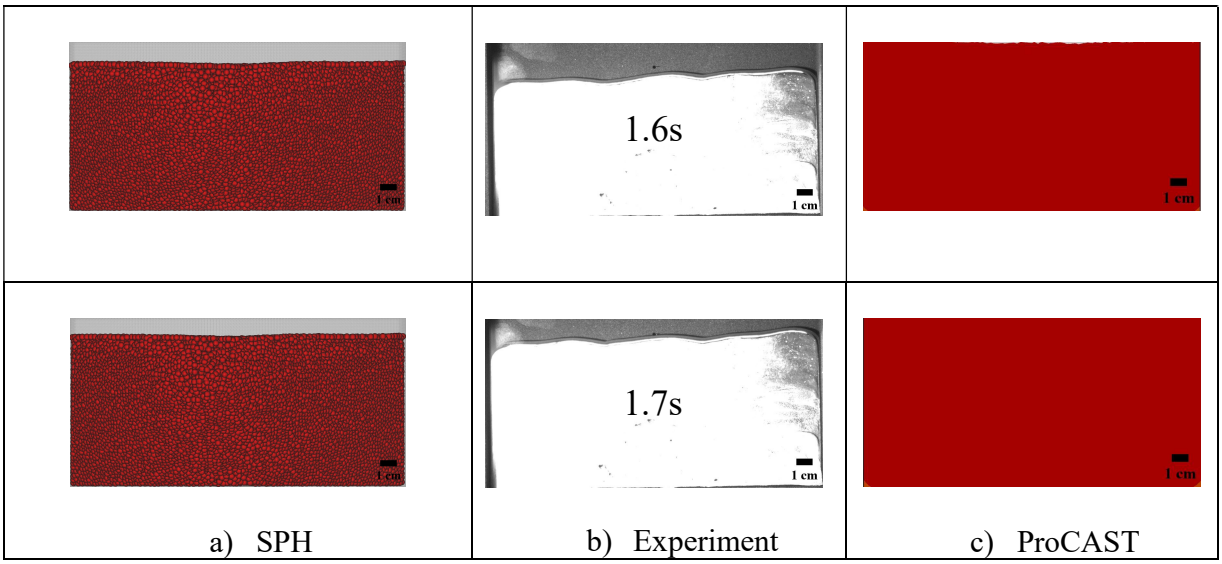

Figure 4-16 - Morphology of filling process versus time – a) SPH (Left) b) Experiment (middle) c) ProCAST (Right)

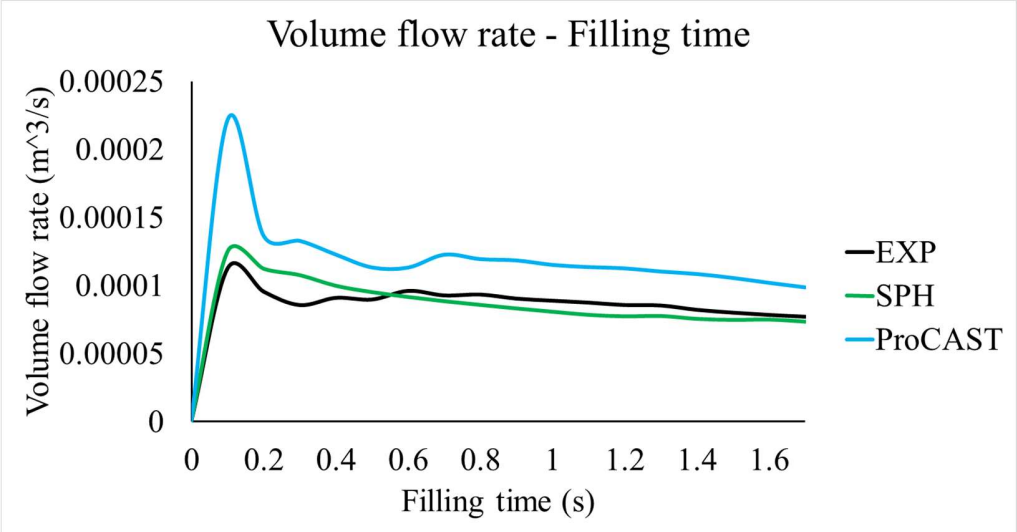

Figure 4-17 - Volume flow rate versus filling time into the plate for EXP, SPH and ProCAST method

0.0s: At zero time, the plate fills up from the bottom through the right side of the ingate, which is situated in the middle of the plate's width, according to the results of the three methods (SPH, Experiment, and ProCAST). Time zero is set by taking into account the requirement that in all three methods (Experiment, SPH, and ProCAST), a specific volume of liquid ($8\times10^{-7}m^3$) is entered into the plate at time zero.

0.1s: The vast volume of liquid ($2.21\times10^{-4}m^3/s$) entered the plate at a time of 0.1s in the ProCAST simulation, as illustrated in Figures (4-16) and (4-17), in strong contrast to the SPH and experiment, which are roughly $1.22\times10^{-4}m^3/s$ and $1.14\times10^{-4}m^3/s$ respectively. It should be observed that the liquid distributed in the experimental results in 0.1s was mostly in the direction of height (3.02cm), whereas in the SPH approach, it was mainly filled in the direction of the plate's length with a lower height (2.29cm).

0.2s: The volume flow rate is $0.93\times10^{-4}m^3/s$ at 0.2s in the experimental data, however, it is higher in the methods SPH and ProCAST by 17.59% and 42.52%, respectively. In addition, the filling morphology of two numerical techniques shows that the liquid has reached the wall in the longitudinal direction in contrast to the experimental data. It should be noted that compared to the SPH method, the ProCAST method distributes it more evenly along the wall. These differences between experimental and numerical results in terms of volume flow rate and morphology come from perfect slip boundary condition assumption that was applied in both numerical methods.

0.3s: According to the filling morphology of the experimental results, the fluid reached the wall on the right side of the plate at 0.3s, but not on the left. This contrasts with the other two numerical methods, where in ProCAST method the liquid rises higher to the wall than SPH approach. These

differences result from the fact that both simulations were run with perfect slip boundary conditions since the ProCAST method overestimates the velocity value. Moreover, the discrepancy between experimental results and SPH in terms of volume flow rate has reached its highest value. Volume flow rate for Experiment, SPH, and ProCAST are $0.81\times10^{-4}m^3/s$, $1.06\times10^{-4}m^3/s$, and $1.30\times10^{-4}m^3/s$, respectively.

0.4s: The morphology of the filling in the experimental approach and the two numerical methods are comparable at 0.4s, but it is significantly more comparable when compared to SPH. It is obvious by looking at the volume flow rate at 0.4s that the disparity between the experimental results using two numerical methods has been minimized. SPH and ProCAST overestimated the volume flow rates by 9.63% and 34.65%, respectively, compared to experimental volume flow rate.

0.5s: When comparing the free surface of the liquid in experimental results with the numerical data, it can be seen that the SPH method was successful in predicting the free surface of the liquid with two dips at 0.5s. Additionally, there are fewer differences between the experimental volume flow rates and the numerical simulations (SPH and ProCAST). It should be noted that the corresponding volume flow rates for the experiment, SPH, and ProCAST are $0.90\times10^{-4}m^3/s$, $0.94\times10^{-4}m^3/s$, and $1.10\times10^{-4}m^3/s$.

0.6s: The fluid surface is nearly flat at 0.6s using the SPH approach. Nevertheless, the liquid's free surface oscillates and is not smooth in the ProCAST methods and experiment. It should be mentioned that the current value of volume flow rate for experimental results is around $0.96\times10^{-4}m^3/s$. By comparing the SPH method with the experiment results, it can be concluded

that the volume flow rate was overestimated by the SPH approach up until 0.5s after filling and is now underestimated. Additionally, the difference between the ProCAST simulation's volume flow rate value and the outcomes of the experiment is equivalent to 17.61%.

0.7s: The liquid surface has nearly become horizontal in all three techniques within 0.7 seconds, and the experimental results show that the liquid has risen 5 cm beyond the plate's bottom. It should be highlighted that the volume flow rate is dropping in the experimental results and SPH technique, reaching values of $0.94\times10^{-4}m^3/s$ and $0.90\times10^{-4}m^3/s$, whereas increasing by a value of $1.22\times10^{-4}m^3/s$ in the ProCAST simulation.

0.8s to 1.7s: The liquid morphology changes only in the vertical direction between 0.8s and 1.7s. It should be observed that during this time, volume flow rate peaks at 0.8s for all three methods and then gradually declines until 1.7s, its minimum value. This demonstrates that the effects of decreasing height of metal in pouring basing and increasing the height of metal in plate have been properly modeled by the two simulation approaches. The maximum values for the experiment, SPH, and ProCAST Simulation are $0.94\times10^{-4}m^3/s, 0.90\times10^{-4}m^3/s$, and $1.22\times10^{-4}m^3/s$, respectively, whereas the minimum values for all three approaches are $0.77\times10^{-4}m^3/s$, $0.73\times10^{-4}m^3/s$ and $0.98\times10^{-4}m^3/s$. It should be noted that the minimum volume flow rate of ProCAST simulation (at time 1.7s) is higher than the maximum volume flow rate of SPH and Experiment (at time 0.8s). Hence, it is obvious that ProCAST simulation grossly overestimates volume flow rate during casting process filling.

The results demonstrate that the two numerical approaches differ in filling time, morphology of filling, and volume flow rate during the filling stage of gravity casting process. The variations

between the results of these two numerical simulations can be attributed to a number of factors like physical models and numerical methods.

In physical model, ProCAST is mesh-based method (Finite Element Method), while SPH is mesh-less method. Mesh-based techniques are typically Eulerian: they simulate fluid flows using a fixed grid. SPH, on the other hand, employs a Lagrangian approach. This simply shows that particles move in accordance with the flow rather than being fixed in space. SPH is a great method for examining casting process filling because there is no mesh distortion, which enables efficient simulation of the free surface. In general, the SPH allows for a better understanding of the fine details of the flow, such as the filling time and morphology.

When it comes to the numerical method, weakly compressible flow is taken into account in the SPH method, whereas incompressible flow is taken into account in the ProCAST method. The equation of state is used by the SPH method, whereas ProCAST does not. This means that each method has a different way of calculating pressure. Because of the various pressure and density equations, the characteristics of the flow change and are diverse in two ways.

Using the two distinct numerical approaches, the pressure gradient and diffusion term of the Navier-Stokes equation are derived and discretized in different ways. Due to this, the filling results of gravity cast parts for both numerical methods could differ. Examining mathematical operators such as gradient, divergence and Laplace and discretization methods used in FEM and SPH show that the discretization of Navier stocks and continuity equation is different.

4.4.2 Study of cooling and solidification step

Figure (4-18 to 4-23) and Table (4-4), respectively, show the cooling curves for points N5, N6, N7, N8, and N9 as well as the cooling rate and solidification time for three zones. The comparison between experimental and numerical results is qualitative because the thermal properties of the sand and the alloy were not experimentally characterized.

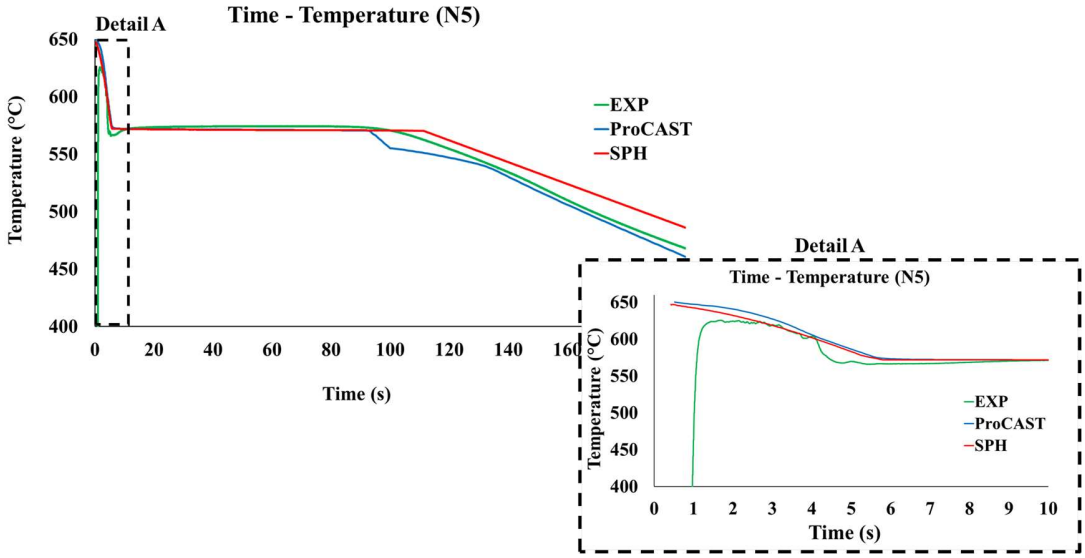

Figure 4-18 - Temperature evolution of point N5

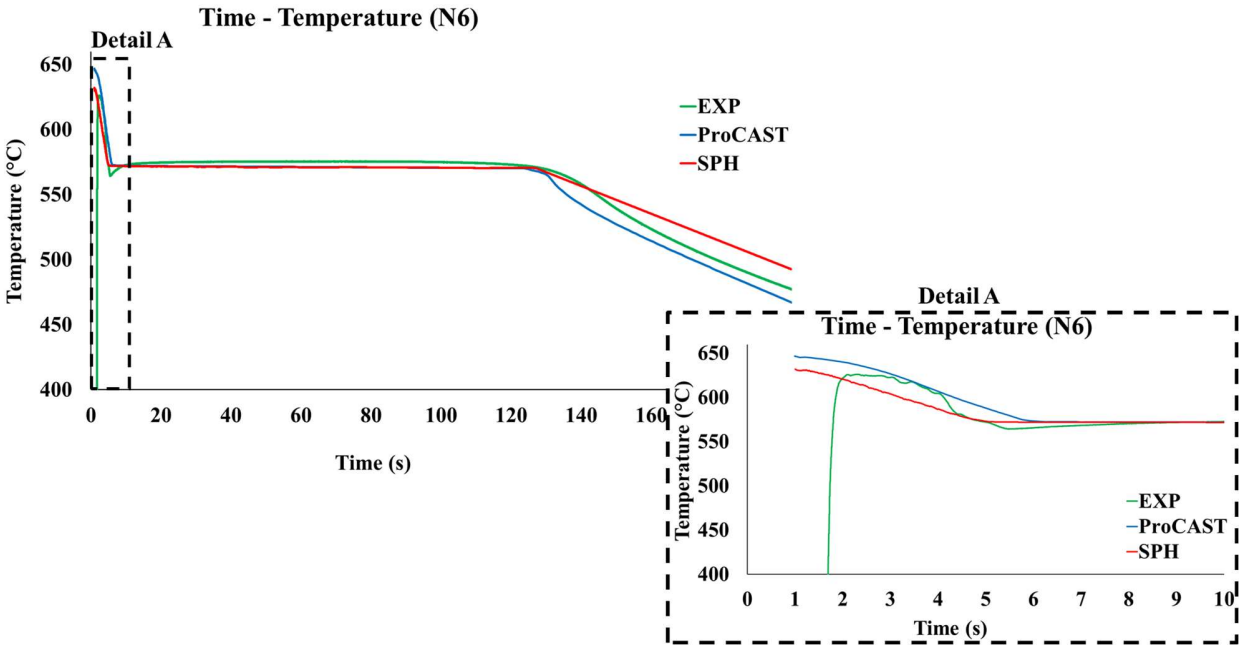

Figure 4-19 - Temperature evolution of point N6

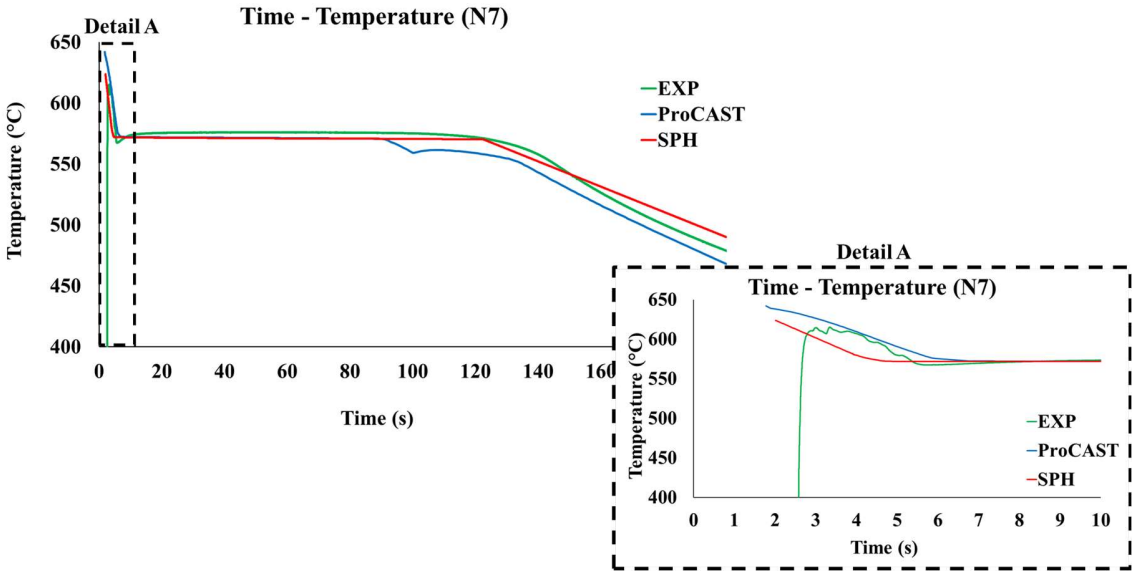

Figure 4-20 - Temperature evolution of point N7

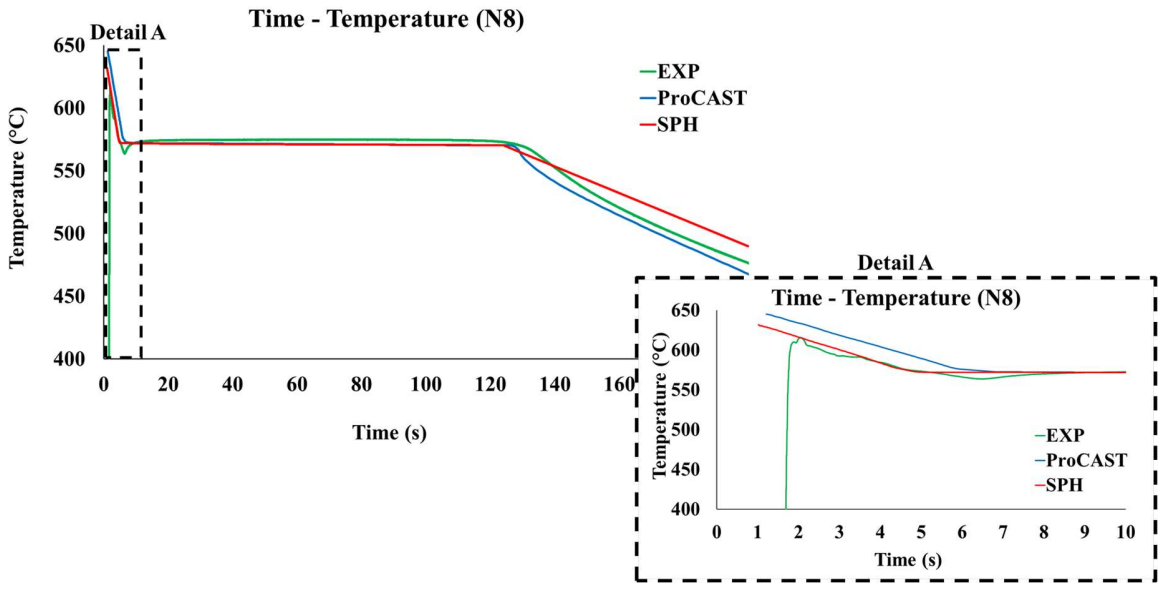

Figure 4-21 - Temperature evolution of point N8

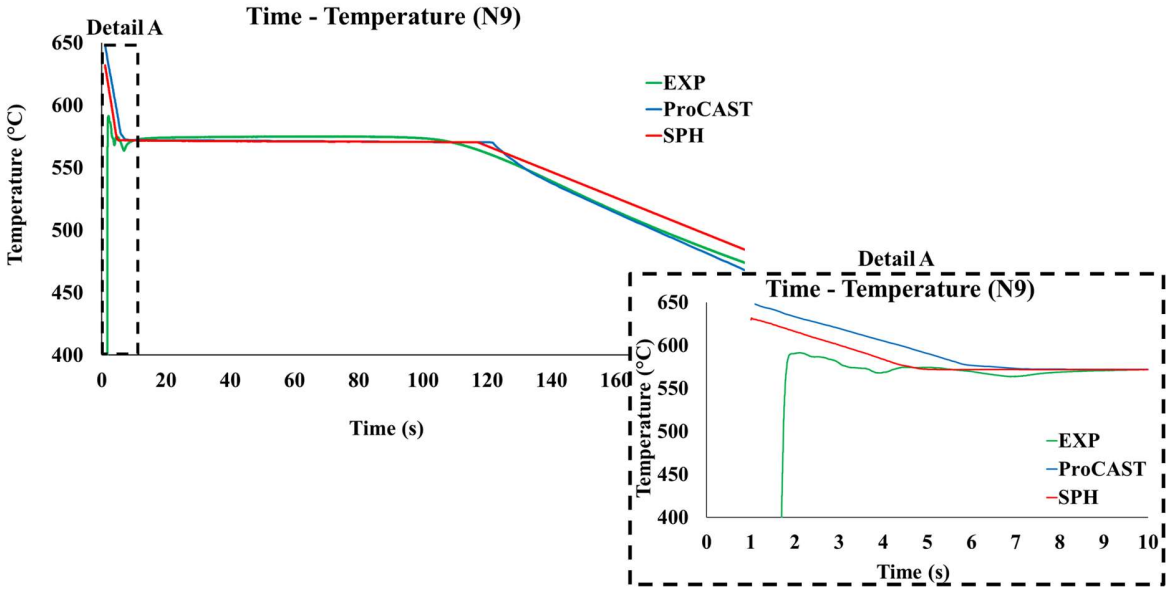

Figure 4-22 - Temperature evolution of point N9

Table 4-4 - Comparison of temperature drop rates (C°/s) in liquid (zone 1) and solid (zone 3) and solidification time (s) (zone 2) for N5, N6, N7, N8 and N9 using experimental data, SPH and ProCAST

Methods/Points	N5			N6			N7			N8			N9		
Region	1	2	3	1	2	3	1	2	3	1	2	3	1	2	3
Experiment	16.27	97.16	1.04	18.29	119.5	1.27	17.38	109.17	1.07	15.32	117.62	1.22	13.60	94.63	0.95
SPH	13.96	105.4	0.95	14.41	121.95	1.03	14.72	116.80	0.97	14.30	118.81	1.06	13.80	117.81	1.02
ProCAST	13.39	86.8	1.02	14.12	117.7	1.33	14.34	84.49	0.94	13.04	119.96	1.40	12.58	114.58	1.11

N5: By comparing the cooling rates in zone one of Figure 4-18 and Table 4-4 at N5, which is located in the middle of the width and thickness of the plate with a height of 20 mm, it can be demonstrated that the experimental cooling rates from the SPH and ProCAST are higher 14.19% and 17.70%, respectively. By examining the experimental and numerical data to the solidification time (zone 2), it is evident that the SPH approach is shown to overestimate it at this point whereas ProCAST underestimate it than experiment. Numerical simulations overestimates the rate of cooling in zone 3 (similarly to zone 1). Figure 4-18 shows that applying thermal boundary conditions as a function of time causes a step in the simulation of ProCAST to replicate temperature evolution in the third zone. At 100s, metal is still in the second zone in the middle of the plate but is in the third zone at the plate's boundary, close to the mold. The value of q in the boundary conditions suddenly changes at this moment, and the rate of heat exit at the mold borders gradually decreases. The metal in the middle of plate act as a heat source and begin to transfer heat to the metal near the borders. As a result of this process, the rate of heat transfer from the metal in the center to the boundaries tries to balance out. Consequently, the rate of temperature drop is almost zero.

N6: Given that the SPH method predicts 2% more closely to experiment than ProCAST, the rate of cooling in zone 1 is still higher for the experimental method at N6, which is located in the center of width, thickness, and height. The solidification time values for all three methods are very similar at N6. ProCAST predicts about 1.5% less than the experiment, while SPH predicts about 2% more. It should be noted that N6, which is situated in the center of the plate, has the longest solidification time. As in the first zone, the SPH method predicts a slower cooling rate in the third zone, whereas the ProCAST simulation shows a higher value, which is totally abnormal.

N7: Like other points, N7's cooling rate is higher in the experimental results than it is in the numerical ones. N7 is 90 mm from the plate's bottom and is in the middle of its width and thickness. The initial temperatures for the SPH and ProCAST methods are 625°C and 640°C, respectively, while the experimental results indicate a value of 614°C degrees. The SPH method predicts the solidification time more reliably than ProCAST about 7% gap with experimental results. While solidification time in ProCAST is 22.5% lower than those in experiments. Both methods predicts a lower cooling rate in the third zone, but the SPH method has a significantly better prediction. Additionally, it should be noted that, similarly to N5, the change boundary condition at 100s causes a temperature drop. In addition, a rise in temperature is observed from 100s to 140s. This demonstrates that using Neumann's temperature boundary conditions as a function of time is not recommended.

N8: The experimental cooling rate at N8, which is at a height of 50 mm, in the middle of the thickness, and 75 mm from the transverse wall, is higher than SPH and ProCAST by values of 6.6% and 14.8%, respectively. The predicted values of solidification time in the second zone are very close to N6 due to its location near the center of the plate, whereas both numerical methods

predicts a slightly higher value. In ProCAST simulation, solidification time at N8 is greater than N6 which is abnormal. In the third zone, the SPH method predicts a lower temperature drop of about 15.1%. ProCAST forecast cooling rate 12.9% higher than experimental results.

N9: The SPH method overestimate by 1.5% at N9, which is situated 50 mm from the mold in the width direction and in the center of height and thickness, while ProCAST under predicts by 12.5%. Both methods have significantly overestimates solidification time. In the final zone (3), both numerical methods represent a higher value for cooling. SPH and ProCAST methods predicts by 7.4% and 16.8% more than experiment, respectively. The significant discrepancy between the numerical and experimental results of the solidification time in the second zone could be the cause of this overprediction in zone 3.

In the first zone, it was observed that the experimental tests showed a higher rate of temperature reduction compared to the numerical simulations in most cases. This difference can be attributed to the presence of air in the experimental tests, which was not considered in the numerical simulations. In the second zone, the solidification time in experiments was consistently shorter than the predictions of the SPH method at all points. The reason for this discrepancy is the calculation of the "q" value in the Neumann boundary condition in the numerical simulations for each zone using an analytical equation that is based on certain assumptions. Specifically, these assumptions are that the liquid is in complete contact with the mold and that the thermal conductivity of the molten alloy is infinite. These assumptions lead to an underestimation of the "q" value in the boundary conditions, which in turn results in longer solidification times in the numerical simulations.

As was mentioned in chapter 3, Neumann boundary conditions cannot be applied as a function of time because this leads to different slopes in the cooling zone of liquid and solid for parts with different thicknesses. There are issues when Neumann's boundary conditions are applied in terms of temperature. The value of "q" decreases with three step jumps from zone 1 to zone 3, as is demonstrated in Figure (4-9) and Table (4-2). When temperature of metal close to the boundaries falls to a value below the solidus temperature, metal moves from zone 2 to zone 3. Therefore, the thermal boundary conditions in the walls are completely changed and the value of "q" suddenly drops. At this time, the metal in the plate's center is still in zone 2. This causes the solidification time in the middle of the plate to be predicted incorrectly.

Due to the application of the thermal Neumann boundary condition as a function of temperature, temperature evolution in the SPH method for all points of the plate is therefore more homogeneous than experimental results. As can be seen in Table (4-4), the value of solidification time for all points in the SPH method is closer to each other than it is to the experimental results. Regarding cooling rate, it still holds true for both the first and third zones. A comparison of results obtained by applying Neumann boundary conditions as a function of time and temperature revealed that applying boundary conditions in terms of temperature derives better results.

4.5 Conclusion

The objective of this chapter is to carry out a real 3D gravity sand casting test using two molds, one with glass and the other without, to validate the modeling of filling, cooling, and solidification by numerical simulations like SPH for the closed system. The design of the test case allows the filling stage of gravity sand casting in the plate to be observed via transparent glass. Glass allows

seeing the liquid morphology during filling and to compare it with numerical simulations during the casting process using image analysis. Furthermore, assuming that the plate's thickness is much smaller than its length and height and that the liquid's density remains constant, it can be argued that the filling process is homogeneous in this direction. This study demonstrates how casting filling could be replicated using SPH modeling by examining the shape of filling, filling time, and volume flow rate. By comparing numerical and experimental data, it is evident that the SPH approach can more accurately model filling time, filling morphology, and volume flow rate than ProCAST. In the second experiment without glass, SPH results show that applying Neumann's boundary conditions to temperature can more precisely predicted the trend of temperature evolution for all points in all three zones since it was modeled more homogeneously. By carrying out these real experimental gravity sand casting tests, the SPH 3D code is verified, which is developed in this thesis for modeling the filling and solidification process of gravity casting. As a result, the reliability of the SPH approach to simulate the filling, cooling and solidification of rapid gravity casting in 3D can be evaluated and compared with commercial software like ProCAST. In conclusion, real gravity casting experimental tests of closed systems using glass could enable the observation of the casting process' filling developed in order to verify the results of numerical simulations using the 3D SPH code and commercial software such as ProCAST.

Conclusion

L'objectif de ce chapitre est de réaliser un essai réel de coulée par gravité de sable en 3D à l'aide de deux moules, l'un avec verre et l'autre sans, afin de valider la modélisation du remplissage, du refroidissement et de la solidification par des simulations numériques de type SPH pour le système

fermé. La conception du cas d'essai permet d'observer la phase de remplissage de la coulée de sable par gravité dans la plaque à l'aide d'une vitre transparente.Le verre permet de voir la morphologie du liquide pendant le remplissage et de la comparer aux simulations numériques pendant le processus de coulée en utilisant l'analyse d'image. En outre, en supposant que l'épaisseur de la plaque est beaucoup plus petite que sa longueur et sa hauteur et que la densité du liquide reste constante, on peut affirmer que le processus de remplissage est homogène dans cette direction. Cette étude démontre comment le remplissage de la coulée pourrait être reproduit à l'aide de la modélisation SPH en examinant la forme du remplissage, le temps de remplissage et le débit volumique. En comparant les données numériques et expérimentales, il est évident que l'approche SPH peut modéliser plus précisément le temps de remplissage, la morphologie du remplissage et le débit volumique que ProCAST. Dans la deuxième expérience sans verre, les résultats de SPH montrent que l'application des conditions limites de Neumann En fonction de la température peut prédire plus précisément la tendance de l'évolution de la température pour tous les points dans les trois zones car elle a été modélisée de manière plus homogène. La réalisation de ces essais expérimentaux réels de coulée en sable par gravité permet de vérifier le code SPH 3D développé dans cette thèse pour modéliser le processus de remplissage et de solidification de la coulée par gravité. En conséquence, la fiabilité de l'approche SPH pour simuler le remplissage, le refroidissement et la solidification de la coulée par gravité rapide en 3D peut être évaluée et comparée avec des logiciels commerciaux comme ProCAST. En conclusion, des tests expérimentaux réels de coulée par gravité de systèmes fermés utilisant du verre pourraient permettre l'observation du remplissage du processus de coulée développé afin de vérifier les

résultats des simulations numériques utilisant le code SPH 3D et des logiciels commerciaux tels que ProCAST.

Chapter 5: Conclusion and perspective

Contents

5.1 Conclusion

Even though there is plenty of numerical software to model casting process it is very difficult to predict exactly filling and solidification steps of casting and defects like oxidation due to the complex physics of the gravity sand casting process. Since oxidation forms at the metal/air interface and can result in defects being trapped and moving into the melt, it is very challenging to predict. Additionally, there is typically a gap between simulation and experimental evaluation, which is why this thesis is done in partnership with two ENSAM laboratories. SPH is employed in this thesis to model filling, cooling, and solidification of casting process because it has several special advantages, including the capability to simulate the behavior of free surfaces and material interfaces. Moreover, it is interesting validate SPH code with experiments and compare it with commercial software like ProCAST in order to comprehend the physics and evaluate the differences.

Firstly, the 2D SPH code written by specialists in the LIFSE laboratory is developed during this thesis to model the casting process and simulates filling, cooling, and solidification. Meanwhile, a experimental test case that can validate 2D results of filling, cooling, and solidification is introduced to validate SPH outputs. Using this experimental test case brings the possibility to validate the results of any two-dimensional simulation in terms of filling, cooling, and solidification of a rapid gravity casting for closed system. The most exciting result of this experiment is the ability of the δ–*SPH* technique to accurately replicate casting using SPH modeling with artificial viscosity. It should be noted that numerical simulation used Neumann boundary condition based on experimental results. The SPH approach can model cooling and

solidification better than ProCAST thanks to comparison between numerical and experimental results. The second objective of this thesis is to develop the 2D SPH algorithm in 3D and validate the results by experimental test case. To achieve this, a geometry was designed to cast plate while taking into account a real filling system such that transparent glass could be used to observe the procedure. To figure out the strength of the numerical method in simulating the filling, cooling and solidification of the casting process, experimental results were compared with SPH and ProCAST. The results demonstrate that the SPH technique has a stronger ability to model the filling process effectively compared to ProCAST by calculating volume flow rate and examining filling morphology. According to the results of temperature evolution in three zones for SPH, this method could replicate cooling and solidification of AlSi13 more precisely than the ProCAST method by applying Neumann thermal boundary conditions as a function of temperature.

Conclusion

Bien qu'il existe de nombreux logiciels numériques pour modéliser le processus de coulée, il est très difficile de prévoir exactement les étapes de remplissage et de solidification de la coulée et les défauts comme l'oxydation en raison de la physique complexe du processus de coulée en sable par gravité. Étant donné que l'oxydation se forme à l'interface métal/air et qu'elle peut entraîner le piégeage de défauts et leur déplacement dans la masse fondue, il est très difficile de la prévoir. De plus, il y a typiquement un écart entre la simulation et l'évaluation expérimentale, c'est pourquoi cette thèse est réalisée en partenariat avec deux laboratoires de l'ENSAM. La SPH est utilisée dans cette thèse pour modéliser le remplissage, le refroidissement et la solidification du processus de coulée car elle présente plusieurs avantages particuliers, notamment la capacité de

simuler le comportement des surfaces libres et des interfaces entre matériaux. De plus, il est intéressant de valider le code SPH avec des expériences et de le comparer avec un logiciel commercial comme ProCAST afin de comprendre la physique et d'évaluer les différences.

Tout d'abord, le code SPH 2D écrit par les spécialistes du laboratoire LIFSE est développé au cours de cette thèse pour modéliser le processus de coulée et simuler le remplissage, le refroidissement et la solidification. Parallèlement, un cas test expérimental permettant de valider les résultats 2D du remplissage, du refroidissement et de la solidification est introduit pour valider les résultats SPH. L'utilisation de ce cas d'essai expérimental offre la possibilité de valider les résultats de toute simulation bidimensionnelle en termes de remplissage, de refroidissement et de solidification d'une coulée rapide par gravité pour un système fermé. Le résultat le plus intéressant de cette expérience est la capacité de la technique SPH à reproduire avec précision la coulée en utilisant la modélisation SPH avec une viscosité artificielle. Il convient de noter que la simulation numérique a utilisé la condition limite de Neumann basée sur les résultats expérimentaux. L'approche SPH peut modéliser le refroidissement et la solidification mieux que ProCAST grâce à la comparaison entre les résultats numériques et expérimentaux. Le deuxième objectif de cette thèse est de développer l'algorithme SPH 2D en 3D et de valider les résultats par un cas expérimental. Pour ce faire, une géométrie a été conçue pour couler une plaque en tenant compte d'un système de remplissage réel de telle sorte qu'un verre transparent puisse être utilisé pour observer la procédure. Pour déterminer la force de la méthode numérique dans la simulation du remplissage, du refroidissement et de la solidification du processus de coulée, les résultats expérimentaux ont été comparés avec SPH et ProCAST. Les résultats montrent que la technique SPH a une plus grande capacité à modéliser efficacement le processus de remplissage par rapport

à ProCAST en calculant le débit volumique et en examinant la morphologie du remplissage. D'après les résultats de l'évolution de la température dans trois zones pour SPH, cette méthode pourrait reproduire le refroidissement et la solidification de l'AlSi13 plus précisément que la méthode ProCAST en appliquant des conditions limites thermiques de Neumann en fonction de la température.

5.2 Perspective

The next step of this research is the easy application of the SPH approach to investigate oxidation prediction. It is feasible to determine how oxidation is formed, transported, and trapped by using Lagrangian modeling along with SPH simulation. As a result, by utilizing SPH numerical simulation to discover the factors that intensify oxidation production, the formation of oxidation could be decreased to manufacture parts of greater quality at a lower cost. As a perspective of this thesis, the upgraded 2D and 3D code developed during this thesis should be developed to model the filling, cooling, and solidification steps of the gravity casting process for any casting geometry with pure metal and alloys. Additionally, it is upgradeable to cover both closed and open systems. SPH 3D code can be used to replicate other casting processes, such as low-pressure casting and high-pressure casting, by setting the proper boundary conditions and generating the required geometry. This thesis provides a solid foundation for further exploration and investigation of casting processes, allowing for more accurate and efficient simulations of complex geometries and flow dynamics. The development of the SPH code in this thesis opens up numerous possibilities for future research in the field of casting as well as other areas of physics such as the simulation of rotational molding processes and 3D printing.

Perspective

L'étape suivante de cette recherche est l'application de l'approche SPH pour étudier la prédiction de l'oxydation. Il est possible de déterminer comment les oxydes sont est formés, transportés et piégés en utilisant la modélisation lagrangienne avec la simulation SPH. En conséquence, en utilisant la simulation numérique SPH pour découvrir les facteurs qui intensifient la production d'oxydation, la formation d'oxydes pourrait être réduite pour fabriquer des pièces de meilleure qualité à un coût moindre. Le code 2D et 3D amélioré développé au cours de cette thèse devrait être développé pour modéliser les étapes de remplissage, de refroidissement et de solidification du processus de coulée par gravité pour toute géométrie de coulée avec du métal pur et des alliages. De plus, il peut être amélioré pour couvrir les systèmes ouverts. Le code SPH 3D peut être utilisé pour reproduire d'autres processus de coulée, tels que la coulée basse pression et la coulée haute pression, en définissant les conditions limites appropriées et en générant la géométrie requise. Cette thèse fournit une base solide pour une exploration et une étude plus poussées des processus de coulée, permettant des simulations plus précises et efficaces de géométries complexes. Le développement du code SPH dans cette thèse ouvre de nombreuses possibilités pour des recherches futures dans le domaine du moulage ainsi que dans d'autres domaines de la physique tels que la simulation des processus de moulage rotatif et l'impression 3D.

Appendix A

Pseudo-code of δ-SPH gravity casting model

The summary of the δ-SPH gravity casting, using Runge-Kutta **(2D)** and predictor-corrector **(3D)** time integration algorithms is provided in this appendix in the form of a pseudo-code.

/* Initialization */ 2D

- The physical properties of fluid must be assigned;
- Linked list method is used in this work.
- For time integration, Runge kutta 4th order is used.
- The initial particles velocity and pressure are set to zero and liquid level height, respectively;

Set $c_0, \delta t, T_{end}$;

While $\delta t * i_t < T_{end}$; **do**

for $(ik = 4; \quad ik > 0; \quad ik--)$ **do**

Search for each particle $i \in \Omega = \Omega_f \bigcup \Omega_s$ and its neighboring particles j.

Ω_f and Ω_s denote the fluid and solid particles, respectively.

for $i \in \Omega_s$ **do**

Compute p_w and v_w using Equations (2-76) and (2-78), respectively.

end

for $i \in \Omega_f$

Momentum Equation: Compute $\nabla p_i, F^{Vis}$ and $F^{Carman-Kozney}$ using (2-55) and (2-57), respectively.

Energy Equation: Compute $\tilde{C}$ and $\nabla^2 T$ using (2-67) and (2-69), respectively.

$$V_i^{n+1} = V_i^n + \delta t\left(\frac{1}{ik * \rho_i}(-\nabla p_i + F^{Vis} + F^{Carman-Kozney} + \rho_i g)^n\right);$$

$$T_i^{n+1} = T_i^n + \frac{\delta t}{ik}(\nabla^2 T / \tilde{C});$$

$$r_i^{n+1} = r_i^n + \frac{\delta t}{ik}(V_i^n)$$

end

for $i \in \Omega_f$ **do**

In this loop, the predicted particle positions are used for the calculation of ρ_i and p_i.

Compute ρ_i and p_i using Equations (2-48) and (2-73), respectively.

end

end

$i_t = i_t + 1$

$n = n + 1$

end

/* Initialization */ 3D

- The physical properties of fluid must be assigned;
- Linked list method is used in this work.
- For time integration, predictor-corrector is used.
- The initial particles velocity and pressure are set to zero and liquid level height, respectively;
- Set $c_0, \delta t, T_{end}$;

while $\delta t * i_t < T_{end}$ **do**

Search for each particle $i \in \Omega = \Omega_f \bigcup \Omega_s$ and its neighboring particles j.

Ω_f and Ω_s denote the fluid and solid particles, respectively.

for $i \in \Omega_s$ **do**

Compute p_w and v_w using Equations (2-76) and (2-78), respectively.

end

/* prediction step */

for $i \in \Omega_f$ **do**

Momentum Equation: Compute $\nabla p_i, F^{Vis}$ and $F^{Carman-Kozney}$ using (2-55) and (2-57), respectively.

Energy Equation: Compute $\tilde{C}$ and $\nabla^2 T$ using (2-67) and (2-69), respectively.

$$\tilde{V}_i^{n+1} = V_i^n + \delta t\left(\frac{1}{\rho_i}(-\nabla p_i + F^{Vis} + F^{Carman-Kozney} + \rho_i g)^n\right);$$

$$\tilde{T}_i^{n+1} = T_i^n + \delta t(\nabla^2 T / \tilde{C});$$

$$\tilde{r}_i^{n+1} = r_i^n + \delta t(V_i^n);$$

end

for $i \in \Omega_s$ **do**

In this loop, the predicted particle velocities and positions are used for the calculation of p_w and v_w using Equations (2-76) and (2-78), respectively.

end

/* correction step */

for $i \in \Omega_f$ **do**

In this loop, the predicted particle velocities and positions are used for the calculation of $\nabla p_i, F^{Vis}, F^{Carman-Kozney}, \tilde{C}$ and $\nabla^2 T$

Momentum Equation: Compute $\nabla p_i, F^{Vis}$ and $F^{Carman-Kozney}$ using (2-55) and (2-57), respectively.

Energy Equation: Compute $\tilde{C}$ and $\nabla^2 T$ using (2-67) and (2-69), respectively.

$$V_i^{n+1} = \frac{1}{2}\{V_i^n + \tilde{V}_i^{n+1}\} + \frac{\delta t}{2}\left(\frac{1}{\rho_i}(-\nabla p_i + F^{Vis} + F^{Carman-Kozney} + \rho_i g)^n\right.$$

$$T_i^{n+1} = \frac{1}{2}(T_i^n + \tilde{T}_i^{n+1}) + \frac{\delta t}{2}(\nabla^2 T / \tilde{C})$$

$$\tilde{r}_i^{n+1} = r_i^n + \delta t(V_i^n)$$

end

for $i \in \Omega_f$ **do**

In this loop, the predicted particle positions are used for the calculation of ρ_i and p_i.

Compute ρ_i and p_i using Equations (2-48) and (2-73), respectively.

end

$i_t = i_t + 1$

$n = n + 1$

end

Appendix B

Parallelization technique on CPU of our SPH code

The domain decomposition method is used to parallelize the SPH code on the CPU. This approach is based on the idea of partitioning the physical computational domain Ω into N_d subdomains Ω_i which are initially load balanced $\Omega_1 \approx \Omega_2 \approx ... \approx \Omega_{N_d}$ and $\bigcup_{i=1}^{N_d} \Omega_i = \Omega$. It suppose that the global domain is divided into four sub-domains as an illustration $\Omega = \Omega_1 \cup \Omega_2 \cup \Omega_3 \cup \Omega_4$. For each subdomain, Ω_i a process of rank $proc_i$ is designated to handle its task of calculation. The physical domain is regarded as a continuous medium, which means that the subdomains depend on one another in terms of the characteristics of physical computation. Due to this, data is transmitted between subdomains using the MPI (Message Passing Interface) paradigm. The use of a specific method is required due to the fluid flow's Lagrangian movement. The division of computation loads among the processes using this method must be balanced. This study employed the average position interface detection method. For each iteration, this method calculates the minimum particle position $x_{\max i+1}$ that belongs to the x-axis of the subdomain Ω_{i+1} and the

maximum particle position $x_{\max i}$ that belongs to the x-axis of the subdomain Ω_i. The new position of the interface is determined in the middle of the positions $(x_{\max i}, x_{\max i+1})$ that can express as $In_i = \frac{x_{\max i} + x_{\max i+1}}{2}$. Particles must be distributed differently on the subdomains Ω_i and Ω_{i+1} so that all particles with abscissa coordinates less than or equal to the interface position are transferred to subdomain Ω_i and all particles with abscissa coordinates greater than the same interface are transferred to subdomain Ω_{i+1}. The MPI paradigm is used for communication between processes, and it works by having processes of even rank send information stored in buffer zones to processes of odd rank and vice versa. While the odd processes send information to the even processes, the information is then received by the odd processes. With this approach, the performance of parallelism is optimized and there is enough buffer memory to ensure communication continuity.

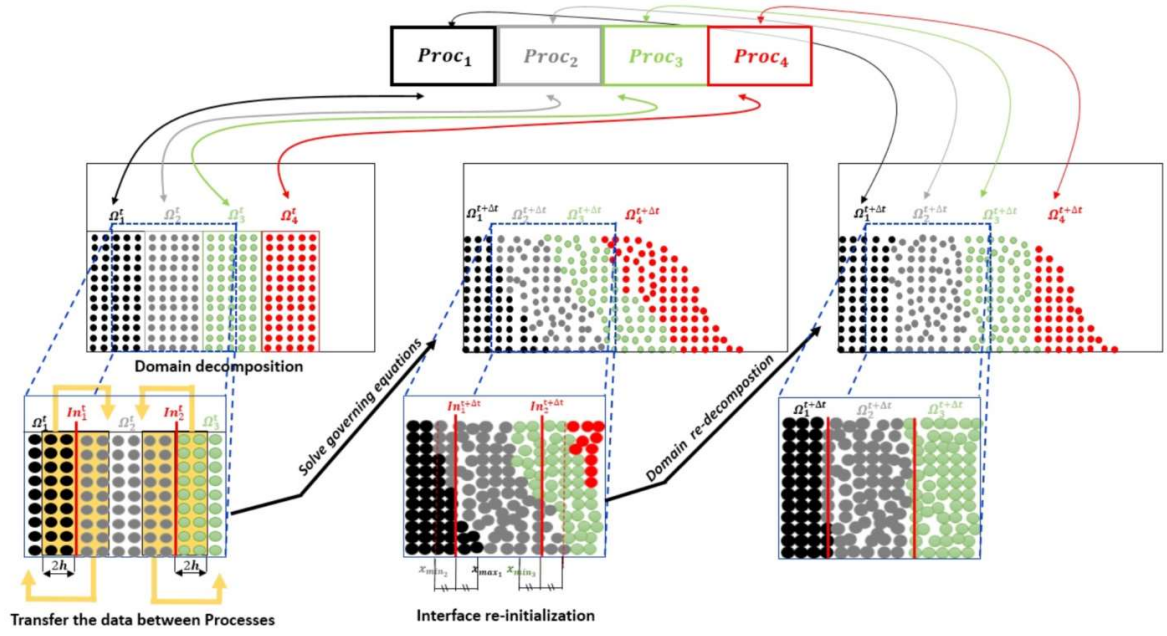

Figure Appendix 1- Parallelization technique of SPH code on CPU using MPI library

Arts et Métiers Sciences et Technologies	**Mohammad ZARBINI SEYDANI** **Smoothed particle hydrodynamics (SPH) modelling and experimental validation of filling and solidification processes of rapid gravity casting of AlSi13**	HESAM UNIVERSITÉ

Résumé : La simulation du processus de coulée en sable par gravité est complexe et implique des phénomènes multi-échelles et multi-physiques. Même si certains logiciels commerciaux sont disponibles, il est difficile de prévoir la dynamique de remplissage lorsqu'elle est couplée au refroidissement, à la solidification et aux défauts causés. En particulier, la prédiction de l'oxydation nécessite de suivre le front de fluide où se forme l'oxydation, donc leur mouvement par la suite dans la masse fondue est complexe avec les méthodes basées sur le maillage. La méthode "smoothed particle hydrodynamics" (SPH) est une approche de simulation lagrangienne qui est particulièrement bien adaptée pour modéliser l'étape de remplissage de la coulée. Le métal est modélisé par des particules en mouvement libre dans l'approche SPH, ce qui permet une prédiction fiable des écoulements fluides incorporant des mouvements complexes de surface libre. Cette thèse a pour objectif de développer l'approche SPH pour examiner les phases de remplissage, de refroidissement et de solidification de la coulée rapide par gravité d'AlSi13. Les résultats numériques SPH du remplissage, du refroidissement et de la solidification sont validés expérimentalement et comparés avec un logiciel commercial (ProCAST).
L'étape initiale pour atteindre l'objectif de cette thèse est le développement du code SPH de coulée en 2D, qui a été développé initialement par le laboratoire LIFSE. Tout d'abord, ce code SPH est développé au cours de cette thèse en 2D pour modéliser les processus de remplissage, de refroidissement et de solidification de la coulée par gravité en sable. Pour analyser le code SPH de la coulée par gravité en 2D pour un système fermé, un cas test expérimental est spécifiquement désigné. Ensuite, le code SPH est amélioré en 3D, et les résultats numériques du remplissage, du refroidissement et de la solidification sont étudiés dans le cas d'une coulée 3D plus réaliste et comparés à l'expérience. Enfin, le code SPH validé en 2D et 3D fournit la base pour la prédiction future des défauts de coulée tels que l'oxydation.

Abstract : The simulation of gravity sand casting process is complex and involves multiscale and multiphysics phenomena. Even though some commercial software is available, it is difficult to predict the filling dynamic when coupled with cooling, solidification, and the induced defects. In particular, oxidation prediction requires tracking the fluid front where oxidation forms, so their motion afterward in the melt is complex with mesh-based methods. Smoothed particle hydrodynamics (SPH) is a Lagrangian simulation approach that is particularly well adapted to model the filling step of casting. Metal is modeled by free-moving particles of SPH approach, allowing reliable prediction of fluid flow incorporating complex free surface motion. This thesis aims to develop SPH approach to examine the filling, cooling, and solidification phases of rapid gravity casting of AlSi13. SPH numerical results of filling, cooling and solidification are validated experimentally and compared with commercial software (ProCAST).
The initial step in achieving this thesis's goal is developing 2D casting SPH code, which was developed initially by LIFSE laboratory. Firstly, this SPH code is developed during this thesis in 2D to model the filling, cooling, and solidification processes of sand gravity casting. In order to analyze 2D gravity casting SPH code for a closed system, an experimental test case is specifically designed. Secondly, the SPH code is upgraded to 3D, and the numerical results of filling, cooling and solidification are studied in the case of a more realistic 3D casting and compared to experiment. Finally, the upgraded 2D and 3D validated SPH code provides the basis for future prediction of casting defects such as oxidation.